In-silico Trials with Human Modelling and Simulation for Guiding Optimal Stratification of Atrial Fibrillation Patients to Catheter Ablation and Pharmacological Therapy



Albert Dasí i Martinez

Wolfson College

University of Oxford

A thesis submitted for the degree of

Doctor of Philosophy

October 2023

This thesis is submitted to the Department of Computer Science, University of Oxford, for the degree of Doctor of Philosophy. This thesis is entirely my own work, and, except where otherwise indicated, describes my own research.

A Empar i Albert

ABSTRACT

Atrial fibrillation (AF) is the most prevalent sustained arrhythmia, affecting over 43 million people worldwide and one in 45 people in the UK. The modest efficacy of currently available therapies adds to the nature of the problem. Antiarrhythmic medication and catheter ablation are the two fundamental pillars of AF treatment, but both have limited efficacy, especially for persistent forms of the disease.

The general aim of this thesis is to provide digital evidence for the optimal stratification of AF patients to catheter ablation and pharmacological treatment, through in-silico trials in large cohorts of virtual patients. For this, a computational framework is developed based on multi-scale human modelling and simulation. The framework allows predicting and explaining how AF management can be modulated based on several patient characteristics, such as electrophysiology, tissue structure and anatomy of the human heart.

Throughout the thesis, AF inducibility and maintenance have been evaluated in large populations of virtual patients with variability in relevant clinical features. Different mechanisms of the arrhythmia (i.e., stable micro-re-entries, wavefront meandering, transient rotors and wave breakups) have been linked to specific ionic current dysregulations and their relationship with the structurally-remodelled substrate (i.e., presence of low voltage areas and atrial enlargement).

Besides influencing AF dynamics, I have provided evidence that the ionic current profile of the atria modulates the success of pharmacological treatment. Therefore, an accurate estimation of the ionic current substrate might be crucial to optimally stratify patients to antiarrhythmic drug therapy. In this sense, a non-invasive characterisation of the ionic profile of the atria results from the analysis of the electrocardiogram.

Moreover, the ionic current substrate also influences the outcomes of catheter ablation therapy, although the latter is mainly determined by the presence of heterogeneities in tissue structure (i.e., presence of low voltage areas) and the bi-atrial size (i.e., left and right atrial volume). In fact, analysis of nine state-of-the-art catheter ablation strategies suggests that the assessment of the latter patient characteristics could guide stratification of AF patients to optimal ablation therapies.

The digital evidence obtained from the in-silico trials has informed decision algorithms to guide optimal selection of AF treatment. Importantly, this thesis demonstrates overall agreement between simulated and clinical results, supporting the credibility of the in-silico trials, and provides novel insights for the evaluation of novel and existing treatments for AF, which facilitates translation into clinical practice.

Journal publications

First author

- Dasí A, Roy A, Sachetto R, Camps J, Bueno-Orovio A and Rodriguez B (2022), In-silico drug trials for precision medicine in atrial fibrillation: From ionic mechanisms to electrocardiogram-based predictions in structurally-healthy human atria. Front. Physiol. 13:966046. DOI: 10.3389/fphys.2022.966046.
- Dasí A, Pope MTB, Wijesurendra RS, Betts TR, Sachetto R, Bueno-Orovio A and Rodriguez B (2023), What determines the optimal pharmacological treatment of atrial fibrillation? Insights from in silico trials in 800 virtual atria. J Physiol. DOI: 10.1113/JP284730.
- Dasí A, Nagel C, Pope MTB, Wijesurendra RS, Betts TR, Sachetto R, Loewe A, Bueno-Orovio A and Rodriguez B (2023), in-Silico TRials guide optimal stratification of ATrIal FIbrillation patients to Catheter Ablation and pharmacological medicatION: The i-STRATIFICATION study. EP Europace: 10.1093/europace/euae150.
- Liu X*, Boycott HE*, **Dasí A***, Roy A, Vrellaku B, Carnicer R, Simon JN, Bueno-Orovio A, Gajendragadkar PR, Norris M, Sayeed R, Krasopoulos G, Srivastava V, Farid S, Rodriguez B and Casadei B (2023), Differential effects of nNOS-derived NO on human right and left atrial action potential duration: implications for atrial fibrillation. **Submitted**.
- Camargo-Ayala L*, Bedoya M*, **Dasí A***, Prüser M*, Prent-Peñaloza L, Adasme-Carreño F, Kiper A, Rinné S Camargo-Ayala PA, Peña-Martinez PA, Bueno-Orovio A, Varela D, Wiedmann F, Márquez-Montesinos JCE, Schmidt C, Rodriguez B, Ravens U, Decher N, Gutiérrez M, and González W (2024), Polypharmacological Modulation of Atrial Fibrillation: Rational Design, Synthesis, and Evaluation of Novel Compounds Targeting NaV1.5, KV1.5, and K2P Channels. ChemRxiv. 2024; doi:10.26434/chemrxiv-2024-v70lj.

Conferences attended and presentations

- **Oral talk:** First PersonalizeAF Meeting (October, 2020). Valencia, Spain.
- **Oral talk:** Second PersonalizeAF Meeting (March, 2021). Maastricht, The Netherlands.
- **Oral talk:** Third PersonalizeAF Meeting (June, 2021). Online.
- **Oral Talk**: Computing in Cardiology (September, 2021). Brno, Czech Republic
- **Attendee:** Atrial Signals 2021 (September, 2021). Karlsruhe, Germany
- **Oral talk:** Forth PersonalizeAF Meeting (January, 2022). Maastricht, The Netherlands.
- **Attendee:** Radcliff Department of Medicine Annual Symposium (April, 2022). Oxford, UK.
- **Poster:** European Working Group on Cardiac Cellular Electrophysiology Meeting (June, 2022). Toledo, Spain.
- **Attendee:** SmartHeart Conference (June, 2022). London, UK.
- **Oral talk:** Fifth PersonalizeAF Meeting (July, 2022). Bordeaux, France.
- **Moderated ePoster:** European Society of Cardiology Congress (August, 2022). Barcelona, Spain.
- **Two oral talks:** Computing in Cardiology (September, 2022). Tampere, Finland.
- **Oral talk:** Symposium Computational Cardiovascular Science (December, 2022). Oxford, UK.
- **Oral talk:** Sixth PersonalizeAF Meeting (Jenuary, 2023). Bologna, Italy.
- **Poster:** Gordon Research Seminar: Cardiac Arrhythmia Mechanisms (February, 2023). Galveston, US.
- **Oral talk:** Gordon Research Conference: Cardiac Arrhythmia Mechanisms (March, 2023). Galveston, US.
- **ePoster:** European Heart Rhythm Association Congress (April, 2023). Barcelona, Spain.
- **Oral talk:** Seventh PersonalizeAF Meeting (Jenuary, 2023). Karlsruhe, Germany.
- **Sandpit (5-min pitch):** Multi-scale & Multi-modality Digital Health Collaboration Workshop. London, UK.
- **Attendee:** European Society of Cardiology Congress (August, 2023). Amsterdam, The Netherlands.
- **Oral talk:** Computing in Cardiology (October, 2023). Atlanta, US.
- **Oral talk:** Eighth PersonalizeAF Meeting (October, 2023). Valencia, Spain.

Prizes

- 1st place poster award at Gordon Research Seminar: Cardiac Arrhythmia Mechanisms.
- Awarded oral talk at Gordon Research Conference: Cardiac Arrhythmia Mechanisms.
- Finalist of The Rosanna Degani Young Investigator Award (YIA). Computing in Cardiology 2023.
- Wolfson College travel grant to attend European Society of Cardiology Congress 2023.

ACKNOWLEDGMENTS

I would like to express my sincere gratitude

to Blanca and Alfonso, my supervisors, mentors, sponsors and role models. My right and left atrium. **Prof Alfonso Bueno Orovio**, who taught me to be precise and accurate, knowledgeable but humble. **Prof Blanca Rodriguez**, who taught me to enlarge and deepen any scientific approach. If only one day I could undertake research with the insight she does. I will never forget any lesson you both bestowed on me, especially those transcending Academia.

To **Dr Axel Loewe**, my offstage supervisor. Thanks for hosting me as one of your students, for your comprehensive feedback and for being always the first to release my work to social media.

To **Prof Ursula Ravens**, for so much guidance and support, and for a relentless drive to teach and discuss science, as well as for boosting experimental perspective into my research.

To the Computational Cardiovascular Science group. Thanks to **Luana**, for sharing this journey; to **Ruben**, for never missing a lunch together, to **Jakub**, for that insatiable thirst for knowledge, and to **Julià**, for being my support bubble during those COVID-19 lonely times. Lastly, special thanks to **Cristian**, my *life supervisor* and best friend.

To the Institut für Biomedizinische Technik in Karlsruhe, my second research lab. Thanks to **Claudia**, for completing my Dream Team Atria, to my *aunt* **Paty**, who taught me how to persevere in chasing my aims, and to you **Carmen**, for your unique gift of charming everyone around you.

To the Marie Skłodowska-Curie initiative and the European Union's Horizon 2020 research and innovation programme. For the amazing opportunity that **PersonalizeAF** offered to me, including the countless experiences I was allowed to live, as well as the great family that it built. A big thank to all ESRs, especially to Paty and Carmen, already mentioned, to **Alex** and **Lù**.

Lastly, I would also like to express my gratitude to everyone that has been by my side along this lengthy path. Thanks to **Prof Beatriz Trenor**, to **Prof Chema Ferrero** and to **Prof Javier Saiz**, for introducing me into cardiac modelling and simulation and encouraging me to pursued this PhD.

To my friends from Uni: **Sánchez**, **Edu**, **José** and, especially, **Andrés**, who still calls me regularly to ensure I am managing my stress levels.

A la colla de Bétera, perquè sempre em fa tornar als anys d'adolescència, quan la preocupació més greu era de no tenir prou gels per al cubata.

A **Empar** i **Albert**, perquè mai no els podré agrair prou tot.

E a **Giorgia**, la scoperta più importante di questi anni di ricerca

CONTENTS

Chapter 1

1.1. Atrial fibrillation: nature of the problem 1

1.2. Thesis goal 2

1.3. Thesis outline and statement of originality 3

Chapter 2

2.1. Atrial anatomy and electrophysiology: from organ to cell 4

2.1.1. Atrial anatomy and tissue structure 4

2.1.2. Atrial electrophysiology 6

2.2. Pathophysiology of atrial fibrillation 10

2.2.1. Atrial fibrillation 10

2.2.2. Contributors to the dynamic proarrhythmic substrate: electrical restitution 12

2.2.3. Contributors to the static proarrhythmic substrate: low voltage areas 13

2.3. Management of atrial fibrillation 15

2.3.1. Antiarrhythmic drug therapy 15

2.3.2. Catheter ablation 16

Chapter 3

3.1 Cellular electrophysiology: The action potential model 19

3.2. Cell coupling and propagation of the action potential 21

3.2.1. Finite volume method implemented in MonoAlg3D 22

Chapter 4

4.1 Population of human atrial cardiomyocyte models 25

4.1.1. Single (baseline) atrial cardiomyocyte model 25

4.1.2. Population of atrial cardiomyocyte models with variability in ionic currents 26

4.2 Population of human whole-atria models 28

4.2.1. Population of structurally-healthy atria: Electrophysiological variability 28

4.2.2. Population of structurally-remodelled atria: Anatomy and structural variability 30

4.3. Population of virtual atrial fibrillation patients 33

4.4. Validation of virtual atrial fibrillation patients 34

4.4.1. Validation against the patient data used to construct the models 34

4.2.3. Validation against external patient data 35

Chapter 5

5.1. Definition **37**

5.2. Pharmacological interventions **37**

5.2.1. Modelling and simulation of pharmacological treatment *37*

5.2.2. Validation of antiarrhythmic drug simulation *38*

5.3. Catheter ablation interventions **39**

5.3.1. Modelling and simulation of catheter ablation *39*

5.3.1. Validation of catheter ablation simulation *39*

Chapter 6

6.1. Summary of the study **41**

6.2. Introduction **41**

6.3. Methods **42**

6.3.1. Population of virtual AF patients *42*

6.3.2. In-silico trials *43*

6.3.3. Clinical decision support system *44*

6.4. Results **44**

6.4.1. Evaluation of human atrial cardiomyocyte action potential models shows that steep restitution is associated with long plateau and high cellular excitability *44*

6.4.2. AF is facilitated by discordant APD alternans, enabled by propagation at fast rates due to high excitability *46*

6.4.3. Analysis of 477 AF episodes reveals AF sustainability supported by high excitability, with enhanced up-regulation of I_{K1} and elevated I_{NaK} *49*

6.4.4. In-silico drug trials in over 200 AF episodes consistently reproduce cardioversion efficacy observed in clinical trials and identify key properties determining treatment success *51*

6.4.5. Optimal pharmacological treatments for individual ionic profiles are those that maximize prolonged refractoriness thus minimizing excitability *52*

6.4.6. Accuracy of prediction of AF cardioversion with specific treatments is 70% using both ECG metrics and ionic current profiles *54*

6.5. Discussion **55**

6.5.1. Precision medicine for AF management: In-silico drug trials *56*

6.5.2. Ionic current dysregulation and dynamic electrophysiological substrates in structurally-healthy atria *57*

6.5.3. Limitations and future perspectives *57*

6.6. Conclusion **58**

Chapter 7

7.1. Summary of the study **59**

7.2. Introduction **60**

7.3. Methods **60**

7.3.1. Population of virtual AF patients *60*

7.3.2. In-silico trials *61*

7.4. Results **62**

7.4.1. Compound 6f (100 μM) shows >70% efficacy for rhythm control of AF, following a dose-dependent prolongation of post-repolarization refractoriness *62*

7.4.2. The antiarrhythmic response of Compound 6f (100 μM) is modulated by Na^+ channel density *64*

7.5. Conclusions **65**

Chapter 8

8.1. Summary of the study **66**

8.2. Introduction **67**

8.3. Methods **67**

8.3.1. Population of virtual AF patients *67*

8.3.2. In-silico trials *68*

8.3.3. Clinical decision support system *68*

8.4. Results **70**

8.4.1. AF sustains in virtual atria presenting short refractoriness and high cellular excitability, the latter proportional to the extent of LVAs in the left atrium *70*

8.4.2. The ionic current dysregulation favouring AF maintenance is identified through ECG metrics, with I_{K1} being the main determinant of AF dominant frequency *72*

8.4.3. High frequency rotational activity in structurally-healthy areas coexist with rotors anchored around small and patchy LVAs *74*

8.4.4. In-silico drug trials in 494 virtual patients with 4 reference compounds identify the inward currents (I_{CaL} and I_{Na}) as critical for optimal stratification of AF patient to pharmacological treatment *75*

8.4.5. Decision algorithm for optimal pharmacological treatment selection *78*

8.5. Discussion **78**

8.5.1. Pharmacological treatment is influenced by the patients' ionic current substrate *79*

8.5.2. Fibrillation drivers are not exclusive of scarred areas *80*

8.5.3. Ionic current dysregulation is crucial for AF maintenance *81*

8.5. Conclusion **82**

Chapter 9

9.1. Summary of the study 83

9.2. Introduction 84

9.3. Methods 84

9.3.1. Overview of study design 84

9.3.2. Virtual AF patients 84

9.3.4. In-silico trials 86

9.4. Results 88

9.4.1. Primary outcome 88

9.4.2. Arrhythmia despite PVI 89

9.4.3. Catheter ablation as second procedure treatment 90

9.4.4. Antiarrhytmic drugs as second procedure treatment 93

9.4.5. Key patient characteristics and proposed decision algorithm 94

9.5. Discussion 98

9.5.1. In-silico trials using modelling and simulation for optimal AF treatment 98

9.5.2. Efficacy of Efficacy of in-silico vs. clinical trials 99

9.6. Conclusion 101

Chapter 10

10.1. Main thesis contributions 102

10.2. Summary of main findings 103

10.3. Limitations and future work 104

10.4 Thesis outlook 105

References

107

Annex I

I.1. Definition of the modified benchmark problem 119

I.2. Results 119

Annex II

II.1. Supplemental methods 121

II.1.1. APD and conduction velocity restitution 121

II.2. Supplemental results **122**

II.2.1. Discordant APD alternans and AF inducibility *122*

II.2.2. Comparison of drug effects between simulated and experimental result, and between simulated results obtained in different cell models *123*

II.2.3. Dynamic APD restitution and effective refractory period after drug action *123*

Annex III

III.1. Summary of the study **128**

III.2. Introduction **128**

III.3. Methods **129**

III.3.1 Population of virtual patients *129*

III.3.2 ECG analysis and regression with neural networks *129*

III.4. Results and discussion **130**

III.4.1 I_{Na} and I_{K1} modulate P- and T_a-wave duration, respectively *130*

III.4.2 I_{Kr} and I_{NaK} determine the amplitude and complexity of the T_a-wave *130*

III.4.3 ECG metrics identify ionic current dysregulation relevant to pharmacological AF management *131*

III.4.4 Both P- and Ta-wave are needed for characterizing the atrial ionic profile *133*

III.5. Conclusion **133**

LIST OF ABBREVIATIONS AND ACRONYMS

AF	atrial fibrillation
APD	action potential duration
CTI	cavo-tricuspid isthmus
ECG	electrocardiogram
LVA	low voltage area
Marshall-Plan	sequential elimination of the Marshall bundles, pulmonary vein isolation, and right and left atrial empirical lines of block
MI	mitral isthmus
MiLine	anterior mitral line
PVI	pulmonary vein isolation
PWI	posterior wall isolation

CHAPTER

1

INTRODUCTION

1.1. Atrial fibrillation: nature of the problem

Atrial fibrillation (AF) is the most prevalent sustained arrythmia, affecting over 43 million people worldwide (Hindricks *et al.*, 2021) and one in 45 people in the UK (BHF (2023) UK hospital data). The increasing AF incidence is, to a great extent, the result of a higher life expectancy (Kornej *et al.*, 2021). The better management of chronic conditions and the aging population are fuelling the growth of AF epidemic (Kany *et al.*, 2021). Advancing age is the primary risk factor (Kornej *et al.*, 2021), being half of AF patients in Europe older than 75 years (Krijthe *et al.*, 2013). However, hypertension, obesity, diabetes mellitus, chronic kidney disease, smoking, alcohol consumption and sedentarism, are well-documented AF-predisposing conditions too (Staerk *et al.*, 2017).

AF is a frequent cause of several cardiac and non-cardiac comorbidities. Dementia and, especially, stroke are the most common non-cardiac complications. Indeed, non-anticoagulated AF patients have 5-fold higher risk of thromboembolism and stroke (Jones *et al.*, 2020). Moreover, there exists a bidirectional relationship between AF and other forms of heart disease, such as myocardial infarction and heart failure, so that cardiac disease both drive and might derive from AF (Staerk *et al.*, 2017).

In fact, AF-derived complications comprise 5% of annual hospitalizations and cardiovascular death (Kany *et al.*, 2021). The overall economic burden in Europe is estimated to be over 10 billion Euros (Nattel *et al.*, 2021), with an individual 3-year cost per patient of 25.000 Euros. The annual cost per patients in the US is around 18.601 Dollars, resulting in a global US health care cost of 28.4 billion Dollars (Kornej *et al.*, 2021). Thus, AF represents a major public health problem with a substantial economic burden, and it is only expected to rise over time (Nattel *et al.*, 2021).

The modest efficacy of currently available therapies adds to the nature of the problem. Antiarrhythmic medication and catheter ablation are the two fundamental pillars of AF treatment. However, pharmacological agents have limited efficacy, substantial recurrence rates and undesired proarrhythmic effects (Heijman, Hohnloser and Camm, 2021). Similarly, while catheter ablation has shown promising results in patients with paroxysmal AF (i.e., AF that terminates within 7 days from onset), the success

rate is modest for persistent forms of the disease (i.e., AF sustained beyond 7 days). Ultimately, AF might become refractory to therapy in the most permanent stages (Heijman, Linz and Schotten, 2021).

Improving AF treatment, through tailored therapies that consider individual AF mechanisms and inter-patient characteristics (Heijman, Hohnloser and Camm, 2021; Heijman, Linz and Schotten, 2021), is therefore paramount. In this sense, in-silico trials with human modelling and simulation represent an effective means for treatment assessment (Passini *et al.*, 2017; Margara *et al.*, 2022). Widely accepted in engineering, in-silico trials are now emerging in medicine and biotechnology with strong regulatory backing (Viceconti *et al.*, 2021).

One of the major strengths of in-silico trials is the possibility of testing several therapies in large cohorts of virtual patients (i.e., virtual representation of human patients). Accordingly, optimal treatments can be identified for subgroups of subjects that share similar characteristics. The resulting stratification of patients to optimal therapies could boost the efficacy of AF treatment, and support the introduction of human-based multiscale modelling and simulation into precision medicine.

1.2. Thesis goal

The general aim of this thesis is to provide digital evidence for the optimal stratification of AF patients to catheter ablation and pharmacological treatment, through in-silico trials in large cohorts of virtual patients. For this, a computational framework is developed based on multi-scale human modelling and simulation. The framework allows predicting and explaining how AF management can be modulated based on several patient characteristics, such as electrophysiology, tissue structure and anatomy of the human heart.

To develop this framework, the specific goals considered in this thesis are:

1. Design a computational pipeline to generate large populations of whole-atria models that consider the patient variability encountered in clinical practice, including electrophysiological, structural and anatomical factors.
2. Identify the electrophysiological properties of the atria that favour AF even in the absence of structural remodelling and their relationship with successful pharmacological therapy.
3. Identify the role of electrophysiological and structural remodelling on AF maintenance and the key patient characteristics that could guide optimal pharmacological treatment.
4. Identify the extent of atrial enlargement, that combined with variability in electrophysiology and tissue structure, modulates AF dynamics and response to catheter ablation.
5. Ultimately, develop decision algorithms, based on key patient characteristics and in-silico results, for optimal stratification of patients with AF to optimal treatment strategies.

1.3. Thesis outline and statement of originality

This thesis presents the development of a human-based modelling and simulation framework for identifying optimal therapies for AF patients. The framework is based on in-silico clinical trials conducted in large cohorts of virtual AF patients. Therefore, dedicated chapters explain these two fundamental concepts (i.e., in-silico trials and populations of virtual patients).

First, **Chapter 2** covers the medical fundamentals that sustain the rational of this thesis.

Chapter 3 presents the human modelling and simulation methodologies underpinning this thesis.

Chapter 4 illustrates how I designed the construction of a large cohort of virtual AF patients to reproduce the human variability encountered in clinical practice, and **Chapter 5** explains how I implemented in-silico trials, based on human modelling and simulation, in this large cohort with state-of-the-art therapies for AF.

The chapters that follow, **Chapters 6-9**, present the in-silico trials results, with **Chapters 6-8** focusing on pharmacological treatment and **Chapter 9** additionally incorporating catheter ablation. The results presented in these chapters are entirely my own work, and, except where otherwise indicated, describe my own research. **Chapters 6**, **8** and **9** resulted in three journal publications of which I am first author. Therefore, I was responsible for the conception and drafting of the work, developing the computational modelling and simulation frameworks building on previous models and software (described in Chapter 3), conducting all simulations and analysis of results. **Chapter 7** is a multi-disciplinary work, involving experimental and computational methods, and many authors contributed to the writing of a journal publication. In the present thesis I have only included the section that I authored, consisting of a computational modelling and simulation study for which I designed, executed and analysed the simulated results.

Finally, **Chapter 10** presents the main thesis contributions, summary of the main findings, limitations and future lines of work.

CHAPTER

BASIS OF ATRIAL FIBRILLATION PATHOPHYSIOLOGY AND THERAPY

2

This chapter presents the medical fundaments of this thesis, and has been structured in three sections: the first one introduces the healthy human atria: their anatomical and electrophysiological properties; the second covers arrhythmia mechanisms, focusing on AF; and the third one provides an overview of AF therapies, their limitations and future directions.

2.1. Atrial anatomy and electrophysiology: from organ to cell

The heart is a hollow structure located within the thorax. It is formed by four chambers, but can be simply divided into the right heart, which pumps blood to the lungs, and left heart, which pumps it to peripheral organs (John Hall, 1946). The upper chambers, called the atria, are a weak primer pump, but enable a continuous blood circulation during the heart contraction.

2.1.1. Atrial anatomy and tissue structure

2.1.1.1. Gross anatomy

The atria are a continuum of muscular tissue that forms two chambers: the right and left atrium. While three basic components are common to both chambers (an appendage, a venous portion and a vestibule (Ho *et al.*, 2001; Ho, Cabrera and Sanchez-Quintana, 2012)), the atria present great heterogeneity in shape, muscle texture and thickness. **Figure 2.1** illustrates the anatomy of the human atria.

The right atrium has a triangular-shaped appendage in the anterior region. A venous wall expands from the appendage to the posterior region, and accommodates two big orifices. These orifices are terminations of the superior and inferior cava vein, located anteriorly and posteriorly, respectively. At the intersection of the superior cava vein with the appendage lays the sinoatrial or sinus node. The sinus node is detached from the right atrium, only connected through small cell pathways. One of these pathways converges in the crista terminalis, a muscular bundle that extends along the venous portion. Perpendicular bundles, called pectinate muscles, connect the crista terminalis to the right atrial vestibule, which contains the atrio-ventricular ring of the tricuspid valve.

The left atrium is characterised by a prominent rectangular-shaped body, called free wall. The free or posterior wall extends towards the venous portion, where the pulmonary veins converge. The rectangular shape of the wall enables differentiation between right and left, and superior and inferior pulmonary vein. The right pulmonary veins are in close proximity to the right atrium; and the left pulmonary veins to the left atrial appendage. The appendage presents varying size and shape, and it is located anteriorly, near the left atrial vestibule. In the vestibule, smooth musculature forms the atrioventricular ring of the mitral valve.

A prominent muscular structure, called Bachmann's bundle, connects both atrial chambers anteriorly. Small inter-atrial bridges can be observed in the posterior and inferior regions. The atria are also connected internally, through the margins of the septal wall that constitutes the fossa ovalis. This atrial septum prevents blood communication between the right and left atrium.

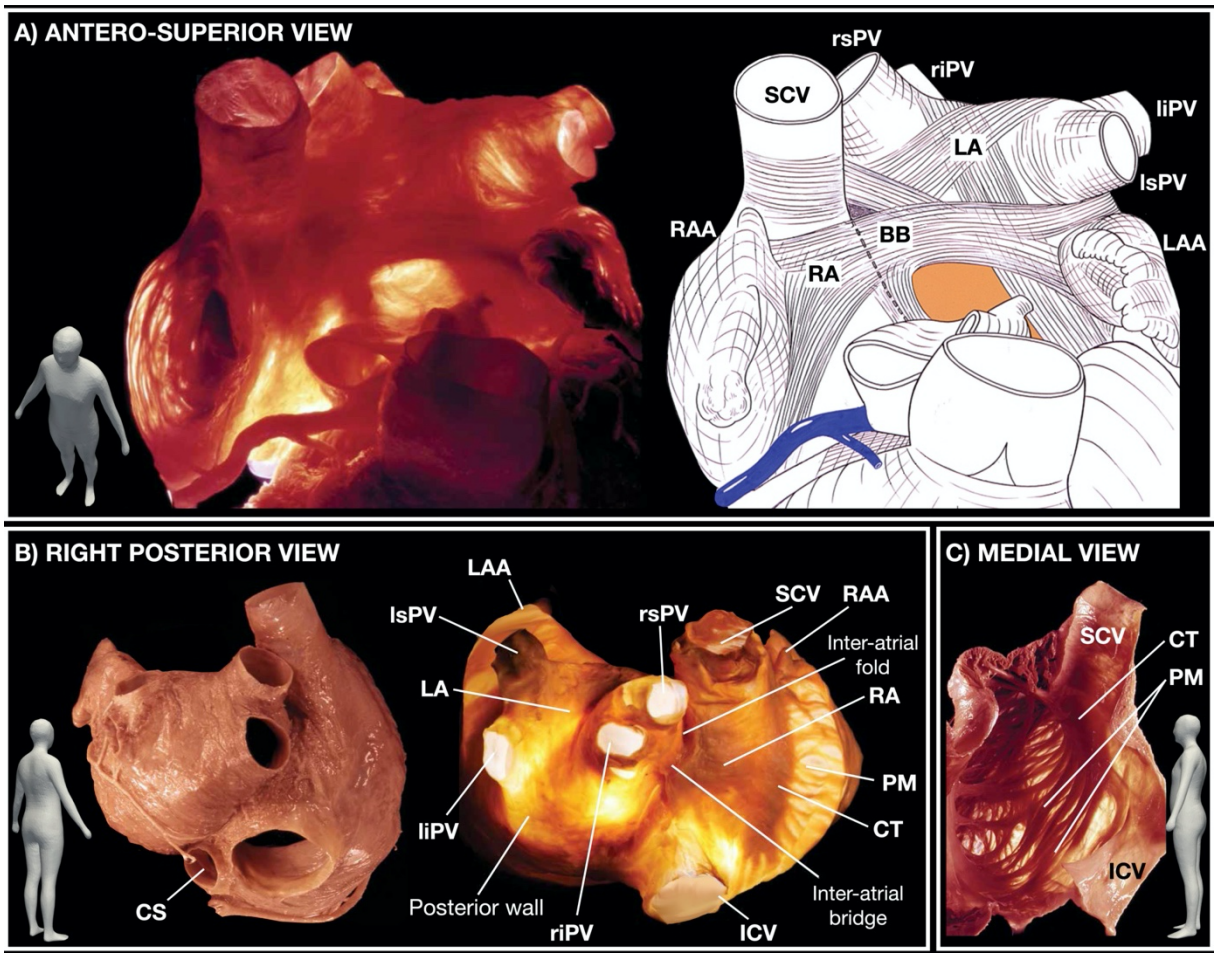


Figure 2.1. A) Antero-superior, B) right posterior and C) medial view of the atrial anatomy. The white human body schematically represents the point of view. Abbreviations: RA-LA: right and left atrium. RAA-LAA: RA and LA appendage. SCV-ICV: superior and inferior cava vein. rs-ri-ls-li-PV: right superior, right inferior, left superior and left inferior pulmonary vein. CT: crista terminalis. PM: pectinate muscles. BB: Bachmann's bundle. CS: coronary sinus. Adapted with permission from Cardiotext Publishing. Mori S, Shivkumar K. Atlas of Cardiac Anatomy. Vol 1. Minneapolis, MN: Cardiotext; 2022.

2.1.1.2. Tissue structure: atrial bundles, fibres and cardiomyocytes

The atrial walls are composed of muscular fibres. A fibre is a collection of atrial cardiomyocytes (i.e., atrial cells), and describes their macroscopic orientation within the tissue. The fibre architecture of the atria is schematically illustrated in **Figure 2.1A** and **Figure 2.2**.

The right atrium presents a large collection of longitudinal fibres in the crista terminalis. This crest intersects with the circumferential fibres that form the orifices of the superior and inferior cava vein. Non-uniform arrangements of junctional fibres connect the crista terminalis to the pectinate muscles; and the latter form intersections with the circular musculature of the atrio-ventricular ring.

The left atrium is formed by overlapping layers of fibres, which present mixed alignment and abrupt changes in orientation. In the posterior wall, longitudinal, oblique, and circumferential fibres intersect with the pulmonary veins (**Figure 2.2**). Similar to the right atrium, pectinate muscles can be observed in the lateral wall of the left atrium, but the absence of a crest makes their orientation less regular.

The largest collection of longitudinally-oriented fibres is found at the Bachmann's bundle. These fibres expand through the anterior wall and encircle the right and left atrial appendages (**Figure 2.1A**). Other groups of longitudinal fibres are observed in the posterior inter-atrial bridges.

2.1.2. Atrial electrophysiology

2.1.2.1. Atrial tissue: macroscopic conduction of the electrical impulse

The fibre architecture illustrated in **Figure 2.1A** and **Figure 2.2** determines the propagation of the electrical impulse. Pioneering work by Spatch and Dobler (Spach and Dolber, 1986) demonstrated that cardiac muscle had a preferential direction of propagation, faster along the fibre (i.e., longitudinal) than across the fibre (i.e., transversal). Therefore, alternations in the fibre architecture (i.e., fibre disarray) compromise the atrial activation pattern. **Figure 2.2** illustrates the normal activation sequence.

In the healthy heart, the electrical impulse is initiated at the sinus node. This is a small mass of specialized cells capable of firing electrical stimuli (i.e., automaticity; explained below). The stimulus is then propagated through the crista terminalis. The pectinate muscles enable a rapid propagation from the crista, located in the superior region, to the inferior vestibular region. Similarly, the longitudinal bundles of the crista enable a fast conduction from the anterior to the posterior region. Accordingly, while the sinoatrial node is located anteriorly, the propagation towards the left atrium is almost simultaneous through the Bachmann's bundle and the posterior inter-atrial bridges.

The posterior inter-atrial bridges yield a posterior-to-anterior propagation in the left atrium (Platonov, 2012). Since the Bachmann's bundle propagates anterior-to-posterior, both wavefronts intersect at the lateral wall of the left atrium (**Figure 2.2**). Interestingly, aging is associated with the fibrotic replacement of the posterior inter-atrial connections. The resulting fibre disarray prompts a longer and different activation pattern in the left atrium that can predispose to arrhythmias (Platonov, 2012).

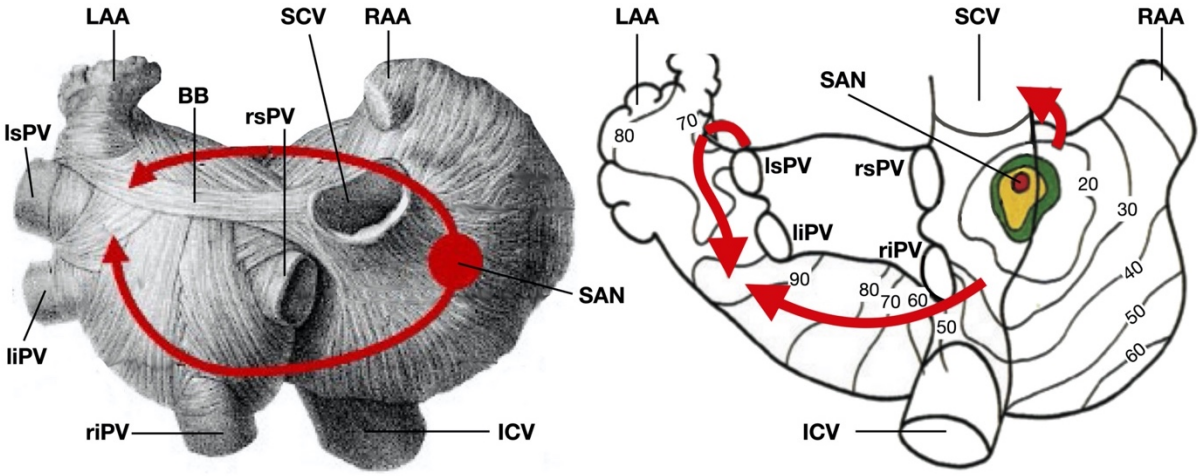


Figure 2.2. Left) schematic representation of the two pathways of electrical propagation form the right to the left atrium: anterior-to-posterior (top arrow) and posterior-to-anterior (bottom arrow). **Right)** isochronal map (in ms) showing the normal atrial depolarization. Abbreviations: RAA-LAA: right and left atrial appendage. SCV-ICV: superior and inferior cava vein. rs-ri-ls-li-PV: right superior, right inferior, left superior and left inferior pulmonary vein. BB: Bachmann's bundle. SAN: sinoatrial node. Adapted from Platonov, 2012 under permission.

2.1.2.2. Atrial cardiomyocytes: Generation of the action potential at single cell

The electrical propagation through fibres is facilitated by connexin proteins that form high-conductance gap junctions between adjacent cardiomyocytes (Mikhailov *et al.*, 2021). When one cell of the fibre is stimulated, the voltage difference between the excited and non-excited cell generates an axial current. This current is made of charged ions (i.e., sodium, Na^+, potassium, K^+ and calcium, Ca^{2+}) and propagates the electrical impulse by stimulating the un-excited cardiomyocyte.

Cardiomyocytes are therefore characterised by two properties: conductivity and excitability. The second one, excitability, is modulated by the flow of Na^+, K^+ and Ca^{2+} across the cell membrane. This movement is enabled by specific pore-containing proteins, called ion channels, that are embedded in the membrane. Since charged ions flow through different ion channels, a net electrogenic current can be derived from the contribution of all of them. This transmembrane ionic current, together with the ionic gradient at both sides of the membrane, generates a difference between the intracellular, V_i, and extracellular, V_e, potential. This difference is called transmembrane voltage, ($V_m = V_i - V_e$), and its time-course is known as the excitatory action potential.

Figure 2.3A illustrates a schematic representation of an atrial cardiomyocyte, showing ionic channels embedded in the cell membrane. **Figure 2.3B** illustrates the atrial action potential, and the contribution of all ionic currents entering (inward) or leaving (outward) the cell through ion channels. Since the extracellular potential is higher than the intracellular, inward currents are generally given a negative sign, and outward currents are considered positives.

The action potential can be divided into five phases (0 – 4), according to the time and voltage-dependent activation of specific ion channels (Ravens and Cerbai, 2008). Under physiological conditions, the ionic gradient resulting from the different K^+, Na^+ and Ca^{2+} concentrations at both sides of the cell membrane maintain the transmembrane voltage at a negative resting state, also called resting membrane potential. Under this state, the cell is said to be polarized.

Phase 0: In the presence of electrical activation coming from a neighbour cell, the fast Na^+ channels become activated. The influx of large amounts of Na^+ ions into the cell, known as the fast Na^+ current (I_{Na}), rises the transmembrane voltage to positive values. The elevation of the voltage activates the L-type Ca^{2+} channel, prompting an influx of Ca^{2+} (I_{CaL}). The sum of these inward currents, I_{Na} and I_{CaL}, and a small contribution of background currents, I_{bNa} and I_{bCa}, yields a fast cellular depolarisation.

Phase 1: The rise in the transmembrane voltage additionally activates a number of K^+ channels. The outflow of K^+ intends to return the cell to its resting state in a process called cellular repolarization. The transient outward K^+ current (I_{to}) is the first one in being activated, short after I_{Na}, yielding a rapid early repolarization.

Phase 2: I_{to} activation is followed by the ultra-rapid rectifier K^+ current (I_{Kur}), which is smaller in magnitude but remains activated for longer. A rapid I_{to} inactivation leaves I_{CaL} competing against I_{Kur}, in a phase characterised by a slow repolarization (i.e., plateau).

Phase 3: A fast late repolarization occurs after the activation of the rapid and slow rectifier K^+ currents (I_{Kr} and I_{Ks}, respectively). A number of small-magnitude K^+ currents contribute to shaping the action potential, such as the acetylcholine-activated K^+ current ($I_{K,ACh}$), ATP-dependent K^+ current ($I_{K,ATP}$), two-pore domain K+ current (I_{K2P}) and the small-conductance Ca^{2+}-activated K^+-current ($I_{SK,Ca}$). While their influence is lower in healthy conditions, they might play a pivotal role during AF (Heijman, Hohnloser and Camm, 2021).

Phase 4: In the last phase of the action potential, the inward rectifier K^+ current (I_{K1}) returns the transmembrane voltage to its resting state. The move of Na^+, Ca^{2+}, and K^+ ions across the cell membrane deviates their intra- and extracellular concentrations from the equilibrium. Regulatory currents, such as the Na^+/K^+ pump (I_{NaK}) or the Na^+/Ca^{2+} exchanger (I_{NaCa}), modulate the ion homeostasis since the beginning of Phase 0.

New phase 0: The inactivation of I_{Na} occurs at the end of Phase 0. Its re-activation is only enabled when the transmembrane voltage approaches the resting membrane potential. The period of time required between consecutive cellular depolarizations is called effective refractory period. The refractory period is similar to the action potential duration (APD) in the healthy heart, but might be very different during pathological conditions.

Different from ordinary atrial cardiomyocytes, cells from the sinoatrial node lack Phase 4 of the cellular repolarization. Instead, a gradual depolarization develops a new action potential (**Figure 2.3B**). Since the depolarization happens in the resting or diastolic phase, it is called diastolic depolarization. Numerous electrophysiological features account for this phenomenon. Firstly, sinus node cells present an inward Na^+/K^+ current (I_f, *funny* current) that activates when the transmembrane voltage reaches the resting membrane potential (Monfredi and Boyett, 2015). Secondly, a predominant contribution of I_{NaCa} rises the voltage to positive values. The elevation of the voltage activates I_{CaL} and the T-type calcium current (I_{CaT}) that, together with a minimal expression of I_{K1}, prevent the stabilization of a resting state.

The fast automaticity of sinoatrial node cells rules the initiation of the entire electrical impulse of the heart. Accordingly, the physiological cardiac rhythm is called normal sinus rhythm.

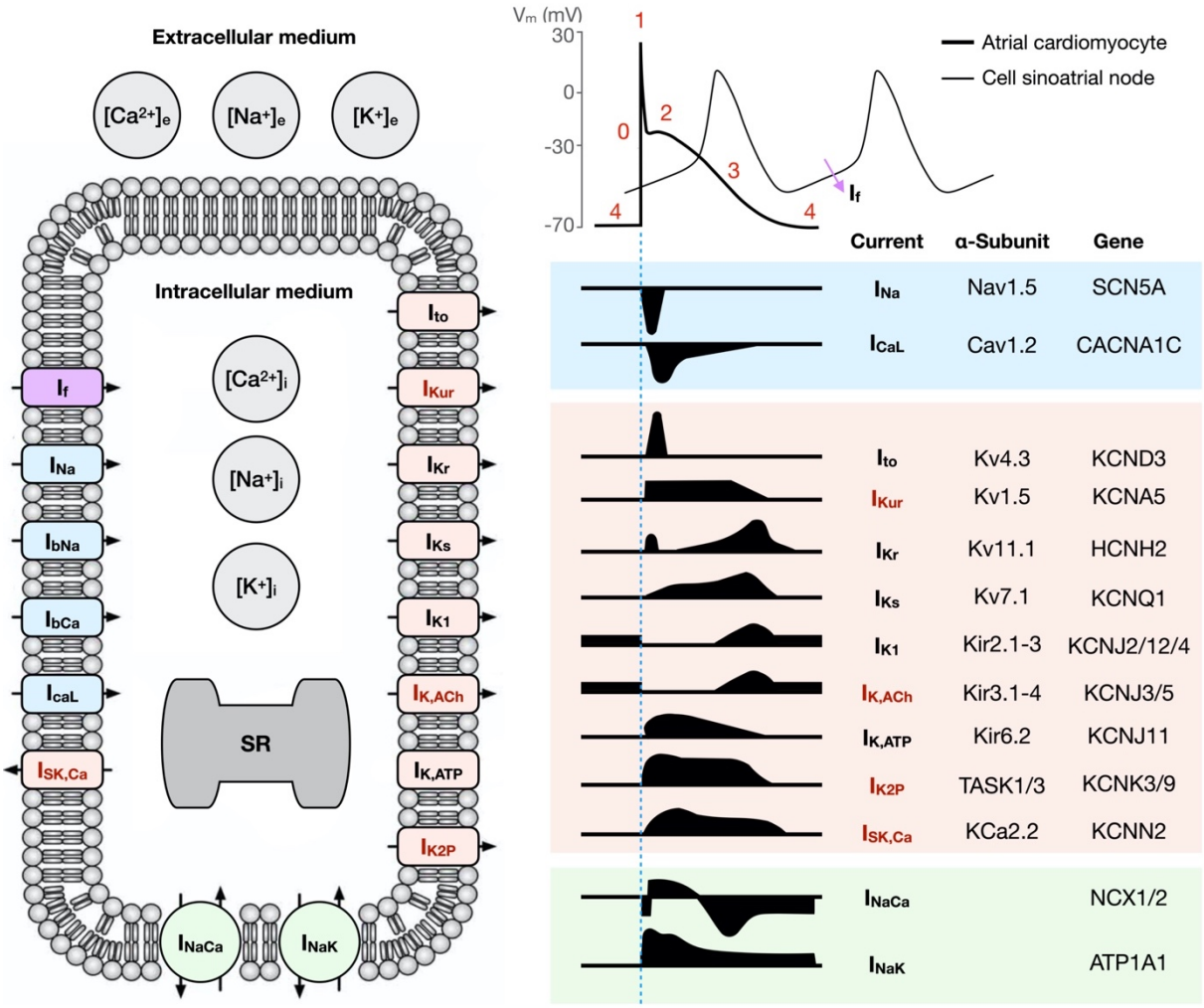


Figure 2.3. Electrical activity in the atrial myocardium. **Left)** schematic representation of different families of ion channels embedded in the lipid bilayer forming the cell membrane. I_f is mainly expressed in cells from the sinoatrial node. **Right)** time-course of the action potential and ionic currents. The currents presented in red (I_{Kur}, $I_{K,ACh}$, I_{K2P}, and $I_{SK,Ca}$) are mainly expressed in the atria. Adapted from Ravens & Cerbai, 2008 under permission.

2.2. Pathophysiology of atrial fibrillation

2.2.1. Atrial fibrillation

During sinus rhythm, the heart rate is regulated according to the metabolic demand (Nattel, 2002). Several regulatory systems tune the pacing frequency of the sinoatrial node, maintaining it between 60-200 beats per minute (Nattel, 2002). During AF, however, the stimulation is no longer ruled by the sinus node and the atrial activation follows a rapid and irregular pattern.

The initiation of this chaotic rhythm is promoted by functional and structural changes occurring in the healthy atria. These changes are rarely presented alone but interact with each other, characterising AF as a multifactorial disease (Heijman, Linz and Schotten, 2021). AF has also been documented in patients without structural abnormalities (Staerk *et al.*, 2017), highlighting its complex pathophysiology.

2.2.1.1. Onset and perpetuation of atrial fibrillation

Numerous mechanisms have been proposed to describe the onset and perpetuation of AF (reviewed by (Jalife, 2011; Nattel and Dobrev, 2017)). Among them, abnormal ectopic foci and the re-entrant circuits are acknowledged drivers of AF (Nattel and Dobrev, 2017). An ectopic focus releases electrical stimuli in the form of a single beat or a burst of very rapid depolarizations (340 beats per minute, (Haïssaguerre *et al.*, 1998)). Although ectopy can appear in multiple regions of the atria, Haïssaguerre et al., 1998 demonstrated that 94% of foci were located in the pulmonary veins, owing to their specific electrophysiological and structural properties (Nattel, 2013).

The propagation of this abnormal stimuli in the form of micro re-entries constitutes the basis of AF (Nattel and Dobrev, 2017). **Figure 2.4** compares the normal activation of the atria against different scenarios of re-entrant sources of electrical activity.

Re-entry formation requires a favourable substrate. The term substrate refers to any tissue heterogeneity, structural or electrophysiological; static or dynamic; physiological or pathological, that translates into conduction abnormalities. For instance, the abrupt changes in fibre orientation, the heterogeneous wall thickness, enlarged atria, or fibrosis infiltration (Mikhailov *et al.*, 2021). Fibrosis is considered the primary promotor of AF, and both the intersection of fibrotic regions with cardiac muscle (Haissaguerre *et al.*, 2016, **Figure 2.4E**), and the endocardium-epicardium disassociation caused by endomysial fibrosis (Verheule *et al.*, 2013; de Groot *et al.*, 2016, **Figure 2.4F**) are preferred locations for rotors.

Rotors may as well anchor in regions without structural heterogeneities (i.e., absence of static substrate). In these cases, dynamic substrates might prompt re-entry formation. Multiple regulatory systems, capable of tuning the atrial electrophysiology, have been associated with AF (Heijman, Linz and Schotten, 2021). The autonomic nervous system (Hanna *et al.*, 2021), the endocrine control (Aguilar *et al.*, 2021) or the inflammatory response (Scott Jr *et al.*, 2021), are among the most studied. The transient

and localised effect of these regulatory systems yields heterogeneous electrophysiological properties in adjacent atrial regions. The resulting electrical substrate is prone to re-entry formation and AF initiation.

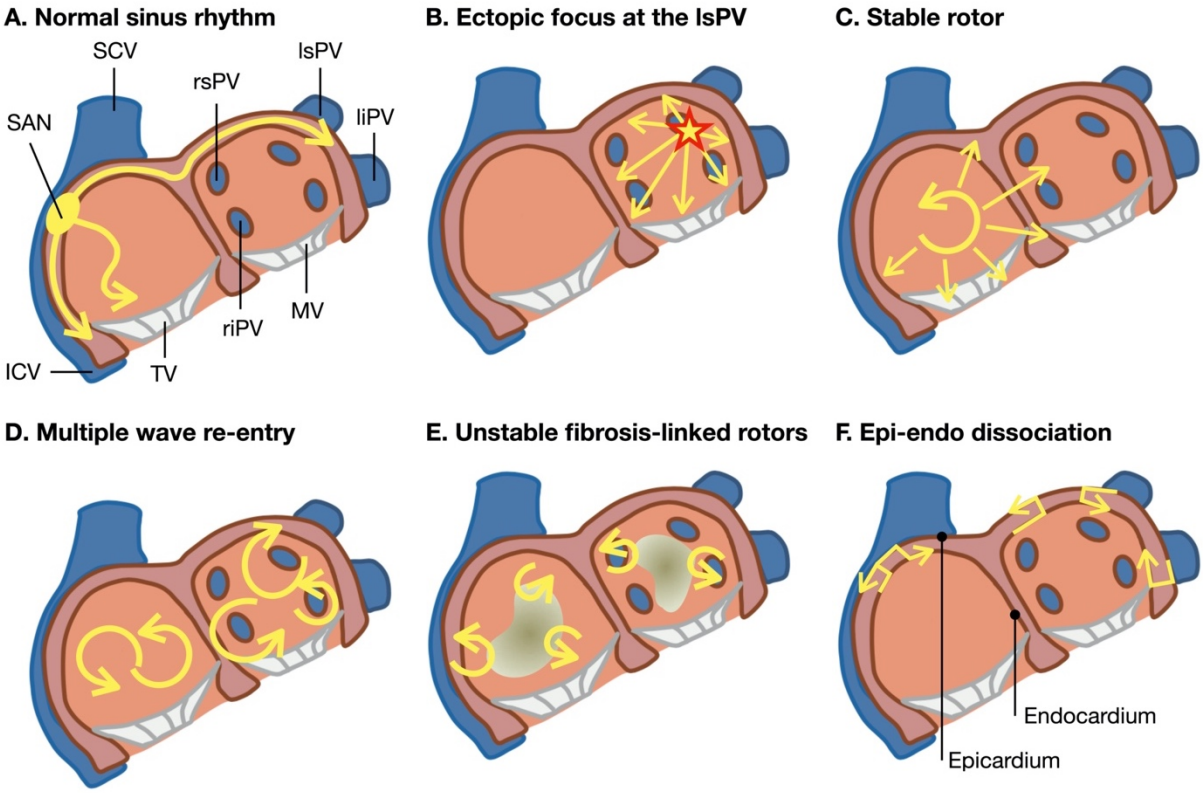


Figure 2.4. Representation of atrial activation during **A)** normal sinus rhythm and **B-F)** different scenarios of atrial arrhythmia. The grey areas in E) represent fibrotic regions. Abbreviations: SCV-ICV: superior and inferior cava vein. rs-ri-ls-li-PV: right superior, right inferior, left superior and left inferior pulmonary vein. SAN: sinoatrial node. TV-MV: tricuspid and mitral valve. Adapted from Nattel & Dobrev, 2017 under permission.

AF itself contributes to the development of electrical and structural substrate. High-frequency activity sustained for a period of time promotes oxidative stress. The production of reactive oxygen species has multiple implications, both electrical and structural. On the one hand, it decreases I_{CaL} and increases I_{K1}, which shortens the APD and effective refractory period (Jalife and Kaur, 2015). Mitochondrial reactive oxygen species additionally alters the Ca^{2+} dynamics in the sarcoplasmic reticulum, favouring Ca^{2+} release into the cytosol. Because Ca^{2+} influx through I_{CaL} happens in every action potential, a substantial intracellular Ca^{2+} loading occurs during AF (Nattel, 2002). The resulting Ca^{2+} overload compromises cell viability, so that an immediate defence mechanism further decreases I_{CaL}. The consequent shortening of the refractory period favours re-entry stabilization.

On the other hand, the production of reactive oxygen species down-regulates the production of connexin proteins and activates profibrotic signalling pathways (Wang *et al.*, 2019). Gap junction loss and increased fibrosis deposition start to happen within a week from AF onset, and further stabilize AF (Nattel, 2002). Thus, the electrical and structural remodelling continue as time progresses (Jalife and

Kaur, 2015). The atria enter a vicious cycle, "*AF begets AF*" (Wijffels *et al.*, 1995), which promotes severe structural and electrophysiological changes, re-entry stabilization and AF progression.

2.2.2. Contributors to the dynamic proarrhythmic substrate: electrical restitution

Some of the electrophysiological changes induced by AF, such as APD shortening, might be reversed upon restoration of sinus rhythm (Schüttler *et al.*, 2020). The APD accommodates to the pacing rate, and even changing the time interval between two consecutive beats (i.e., cycle length) produces an APD variation. This phenomenon is called restitution. The APD restitution curve is therefore the representation of APD changes with varying cycle length. **Figure 2.5A** illustrates the APD response to premature stimuli, and the corresponding APD restitution curve is shown in **Figure 2.5B**.

The implications of restitution for arrhythmias were first investigated by (Nolasco and Dahlen, 1968). The authors schematically illustrated how a premature stimulus could produce an APD alteration that deviated the cell from its equilibrium. In the event of flat APD restitution curves, the APD would oscillate until reaching a new equilibrium (**Figure 2.5C, left**). Conversely, steep APD restitution curves would make the cell enter an unstable state, characterised by persistent APD variations (**Figure 2.5C, right**). These variations were called alternans, referring to the presence of beat-to-beat alternation in a short-long APD pattern. The authors observed that persistent APD alternans would appear for an APD restitution "slope equal to one", what became known as the restitution hypothesis.

The restitution hypothesis was soon after associated with unstable tachycardia (Karma, 1994). The authors showed that wave break-up resembling fibrillation could occur for steep APD restitution (**Figure 2.5D**), even for structurally-healthy substrates (e.g., absence of fibrosis; (Karma, 2000)).

Nevertheless, Cytrynbaum and Keener (Cytrynbaum and Keener, 2002) proved that travelling waves could be stable for restitution slopes greater than one. Qu et al., (Qu, Weiss and Garfinkel, 1999) suggested that the range of diastolic intervals over which the slope was greater than unity was more important than the maximum steepness of the curve. Fox et al., (Fox, Bodenschatz and Gilmour, 2002) stated that alternans were a complex phenomenon, not only determined by the previous cycle length. Koller et al., (Koller, Riccio and Jr., 1998) introduced the concept of cardiac memory, and showed that the APD restitution was also influenced by the rate at which cells were previously paced.

A parallel study by (Pastore *et al.*, 1999) elegantly showed that discordant alternans (i.e., APD alternating with opposing phase in neighbouring regions, **Figure 2.5E**) were responsible for fibrillation. Therefore, following studies (Qu, 2010) observed that besides steep APD restitution, steep conduction velocity restitution was required to induce discordant alternans and fibrillation.

The restitution hypothesis, and its many derivates, rose great scepticism. For many years, it was seen as a theoretical idea, that could only happen in experimental preparations under very specific conditions. Nevertheless, subsequent studies conducted with AF patients (Narayan *et al.*, 2008; Krummen *et al.*,

2012) proved that steep APD restitution near the pulmonary could facilitate AF following fast stimulation, even in structurally-healthy atria.

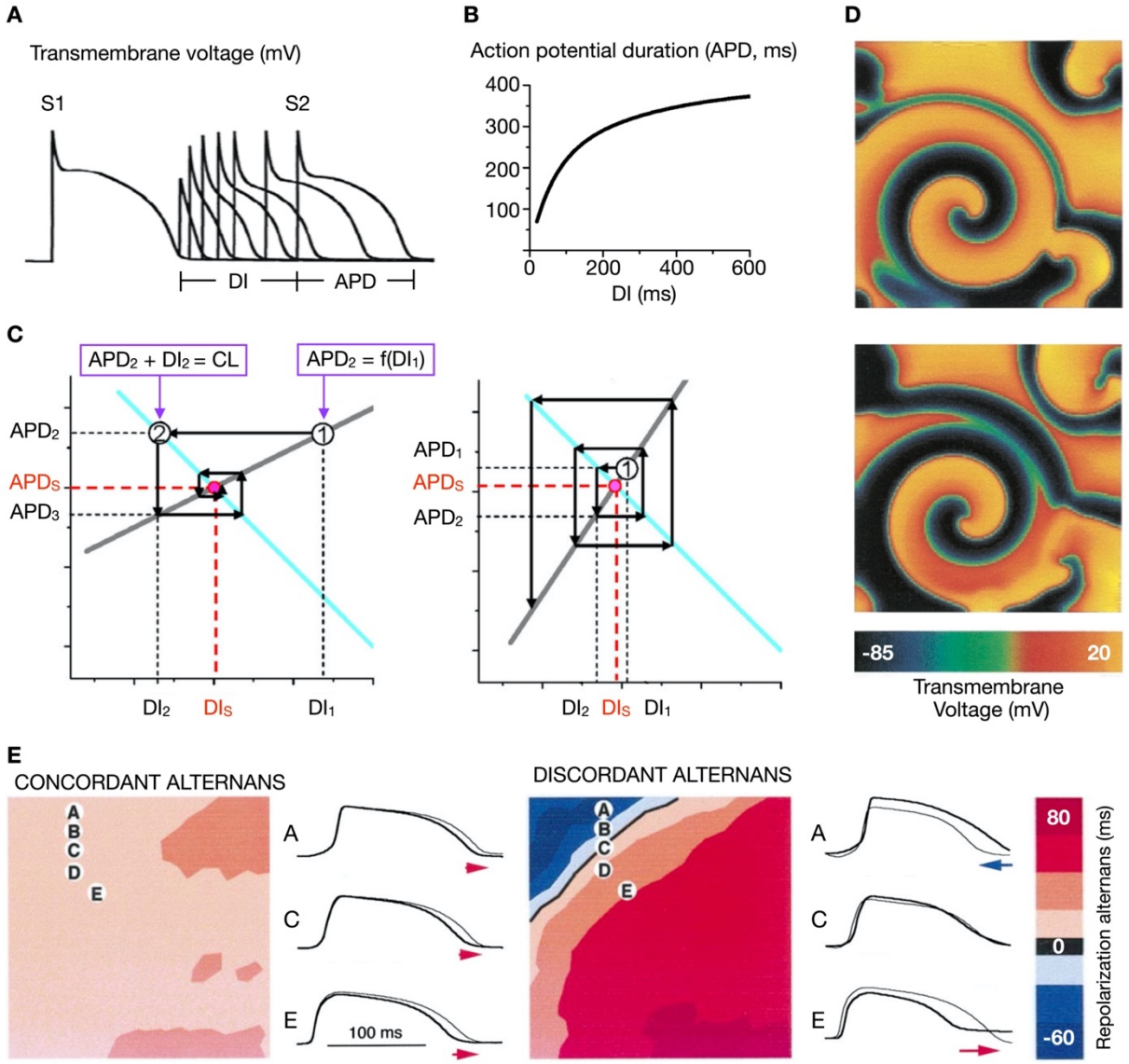


Figure 2.5. Cardiac restitution properties and repolarization alternans. **A)** Effects of applying a premature stimulus (S2) at decreasing diastolic intervals (DI) on the APD. **B)** APD restitution curve. **C)** Cobweb diagram illustrating stable (left) and unstable (right) equilibrium for an APD restitution slope flatter and steeper than one, respectively. The grey line represents the APD restitution curve. The cyan line satisfies CL (cycle length) = $APD_n + DI_n$. At the same time, APD is determined by the previous DI, $APD_n = f(DI_{n-1})$. The intersection of the two lines is the equilibrium point at which APD = APD_s and DI = DI_s. **D)** Simulated wave break-up and fibrillation due to steep APD restitution. **E)** Graphic representation of concordant and discordant alternans. Concordant: the entire tissue alternates with a short-long cadence. Discordant: part of the tissue alternates with short-long cadence (red) and the other with long-short (blue). **A-C)** adapted from Qu et al., 2010. **D)** Adapted from Karma et al., 2000. (Copyright (2000) National Academy of Sciences, U.S.A.) **E)** Adapted from Pastore et al., 1999 under permission.

2.2.3. Contributors to the static proarrhythmic substrate: low voltage areas

Realistically, structurally-healthy atria are not completely homogenous. Fibroblast represent the largest proportion of cells in the heart (Jalife and Kaur, 2015). While they primarily conform the fibrous

architecture that sustains the cardiac muscle, fibrosis may intermingle with cardiomyocytes and separate myocardial bundles. Thus, an extensive fibrotic substrate might impair the electrical propagation of the atria and facilitate fibrillation. In fact, some authors (Kottkamp, 2013) believe that AF is only the consequence of an underlying fibrotic atrial cardiomyopathy.

This arrhythmogenic substrate can be identified using voltage mapping (Jadidi *et al.*, 2016), since the bipolar voltage is considered a marker of atrial (dys)function (Miyamoto *et al.*, 2009). Low voltage areas (LVAs, bipolar voltage lower than 0.5 mV in sinus rhythm; (van Schie *et al.*, 2021)) represent regions of atrial damage, often characterised by conduction abnormalities (Kishima *et al.*, 2020), prolonged atrial activation times and slowed conduction velocity (van Schie *et al.*, 2021). LVAs are frequently observed in AF patients, but they might appear at late stages of the disease (Masuda *et al.*, 2020), since the atrial bipolar voltage is thought to decrease parallelly with AF progression.

Figure 2.6 illustrates the bipolar voltage map of two representative AF patients. While the atria on the left-hand side have a clear pro-arrhythmic substrate, characterised by high LVA density, the atria on the right-hand side have a minimal LVA extension. Yet, both atria belong to AF patients, illustrating that several factors, not only the remodelling of the tissue structure, can predispose to AF. Moreover, intra-cardiac voltage data should be interpreted with caution, given the following limitations of this mapping modality. The bipolar voltage in the mapping system is subjected to temporal variation and quality of contact between the cardiac tissue and the catheter (Jadidi *et al.*, 2016). Moreover, a decrease in the electrogram amplitude is not exclusively indicative of impaired atrial myocardium, but may reflect differences in tissue thickness or fibre orientation (Miyamoto *et al.*, 2009). Thus, a different bipolar voltage might be obtained depending on the wavefront direction. Furthermore, the cut-off value of 0.5 mV to delimit healthy from scar tissue depends on the atrial rhythm, and might reflect scar better in sinus rhythm than AF (Nairn *et al.*, 2020). Ideally, electro-anatomical mapping should be complemented with additional clinical information and mapping modalities for a more accurate tissue characterisation.

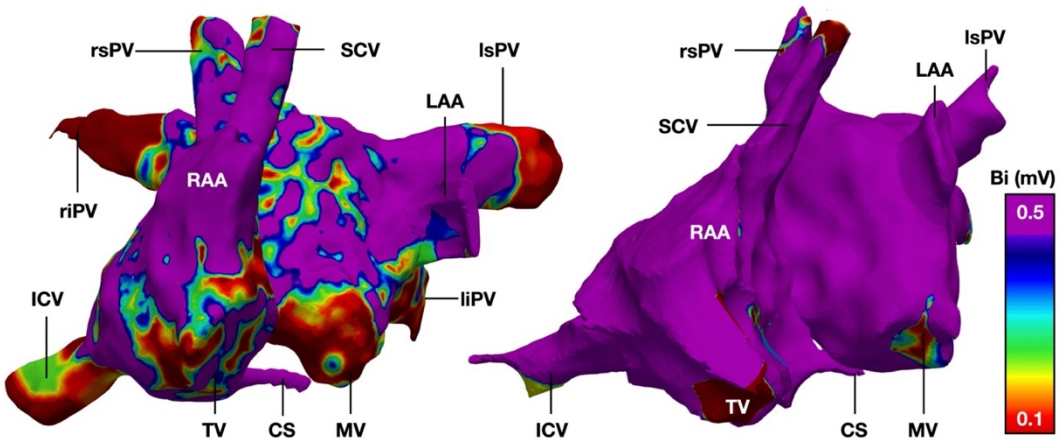


Figure 2.6. Electro-anatomical map of the bi-atrial endocardial surface. Comparison of the intracardiac bipolar voltage (Bi) between a patient with low (right) and high (left) presence of LVA (regions of Bi < 0.5 mV mapped during sinus rhythm).

2.3. Management of atrial fibrillation

AF management follows the integrated ABC pathway: 'A' Anticoagulation/Avoid stroke, 'B' Better symptom control, and 'C' Cardiovascular and Comorbidity optimization (Hindricks *et al.*, 2021). This thesis focuses on 'B' and, specifically, in strategies attempting to terminate fibrillation and restore the normal sinus rhythm, also called rhythm control of AF.

Rhythm control strategies comprise catheter ablation and pharmacological treatment. Recent technological advances, such as the use of cryogenic energy (Kuck *et al.*, 2016) and electroporation (i.e., field pulse ablation, (Verma *et al.*, 2022)) have boosted the efficacy of ablation, especially in patients with paroxysmal AF. Its higher methodological and economic impact, however, keep pharmacological therapy as a fundamental pillar of AF management (Heijman, Hohnloser and Camm, 2021).

2.3.1. Antiarrhythmic drug therapy

Antiarrhythmic drugs are commonly classified according to the Vaughan-Williams system (Lei *et al.*, 2018). Class I comprises Na^+ channel blockers, with a mild (Ia), middle (Ib) or strong effect (Ic) on the action potential upstroke and cellular excitability. Class II includes β-adrenergic blockers, which inhibit the sympathetic nervous system and thus, decrease the pacing rate. Class III drugs exert a predominant K^+ inhibition, prolonging the APD and refractory period; and Class IV, Ca^{2+} channels blockers, modify the heart rate and cellular excitability. Most drugs inhibit multiple ion channels (reviewed by Vagos *et al.*, 2018), so their classification is based on their primary effect.

Five drugs are suggested by the current AF guidelines for sinus rhythm restoration (i.e., amiodarone, flecainide, propafenone, ibutilide and vernakalant; (Hindricks *et al.*, 2021)). Flecainide and propafenone are Class Ic antiarrhythmics. Amiodarone is a multi-channel blocker, and while initially considered as Class III, nowadays is not included in any specific class. Vernakalant is a Class III agent, but exerts a rate-dependent Na^+ channel block similar to that observed by Class Ic antiarrhythmics (Wettwer *et al.*, 2013). Thus, only ibutilide is considered a pure K^+ blocker (Tamargo *et al.*, 2004).

Three additional drugs are commonly employed for AF management: dronedarone, digoxin and ranolazine. Dronedarone was developed to overcome the toxicity of amiodarone, and early trials (EURUDIS and ADONIS (Singh *et al.*, 2007) and ATHENA (Hohnloser *et al.*, 2009)) reported reduced arrhythmia recurrence in patients with paroxysmal and persistent AF. This prompted the PALLAS trial (Connolly *et al.*, 2011), which only included patients with persistent AF. The trial was however stopped due to an increase risk of heart failure, stroke and cardiovascular death with dronedarone therapy. The arrhythmic deaths were, in part, attributed to the interactions between dronedarone and digoxin (Heijman, Hohnloser and Camm, 2021). Digoxin had been widely used for rhythm control (The Digitalis in Acute Atrial Fibrillation (DAAF) Trial Group, 1997). However, nowadays it is only used for controlling the heart rate, due to its elevated cardiotoxicity and inconclusive potential for terminating

AF (Hindricks *et al.*, 2021). Finally, ranolazine is a Class Ib antiarrhythmic, safe but with a modest efficacy (Peyronnet and Ravens, 2019).

Despite the multiple available drugs, the success of pharmacological treatment is currently suboptimal, and only 45% of patients remain free of AF (Wazni *et al.*, 2021) The choice of an antiarrhythmic drug is based on the patient's associated heart disease, due to the risk of ventricular proarrhythmia (Hindricks *et al.*, 2021). This cardiotoxicity prevents the adoption of high-dose therapies, which limits drug efficacy. Many authors have conveyed the importance of targeting atrial-specific ion channels, to maximize drug efficacy while reducing the cardiotoxic risk. I_{K2P}, which is thought to be up-regulated during AF (Heijman, Hohnloser and Camm, 2021), $I_{SK,Ca}$ (study completed: NCT04571385), and I_{Kur}, are promising targets. I_{Kur} inhibition, however, has shown limited efficacy in clinical trials (DIGRAF-IKUR (Camm *et al.*, 2019)), potentially due to I_{Kur} down-regulation in patients with AF.

Nevertheless, even if successful therapies based on blocking atrial-specific ion channels were discovered, these most likely would still be based on a "one-size fits all" approach (Kany *et al.*, 2021). Patients present different clinical responses to drugs (Capucci *et al.*, 2018), which emphasizes the suitability of personalizing drug treatment (Capucci *et al.*, 2018; Kany *et al.*, 2021). Pharmacological agents target specific ion channels, and since humans present inter-subject variability in channel density (Britton *et al.*, 2013), different subjects are expected to respond differently to the same drug (Capucci *et al.*, 2018). Nevertheless, the interplay between inter-patient variability in electrophysiological and the response to pharmacological AF treatment is currently unknown.

2.3.2. Catheter ablation

Catheter ablation is the most effective therapy for preventing arrhythmia recurrence in patients with paroxysmal AF (Wazni *et al.*, 2021). Since most ectopic triggers originate in the pulmonary veins (Haïssaguerre *et al.*, 1998), their electrical isolation (i.e., pulmonary vein isolation, PVI) can impede the propagation of abnormal stimuli to the atrial body and prevent fibrillation. Therefore, PVI is the cornerstone of ablation therapy in paroxysmal AF.

Challenges remain for persistent AF, where patients experience 50% recurrence after PVI (Verma *et al.*, 2015). Persistent AF is associated with a sparser distribution of ectopic triggers beyond the pulmonary veins. Other regions, such as the superior and inferior cava vein, crista terminalis, and the posterior wall of the left atrium, have been reported as common foci (Schmitt *et al.*, 2002). The posterior wall shares a common embryological origin with the pulmonary veins (Kistler *et al.*, 2023), which might explain its predisposition for generating triggered activity. However, the CAPLA clinical trial ((Kistler *et al.*, 2023), **Figure 2.7A**) observed no incremental benefit of posterior wall isolation compared to PVI alone. In fact, modest rates of arrhythmia-free survival were reported in the PARTY-PVI study (Benali *et al.*, 2023), which assessed the systematic elimination of all triggered activity in the atria.

Therefore, other clinical trials have attempted to eliminate the substrate maintaining fibrillation (i.e., substrate modification approach) instead of potential ectopic foci. **Figure 2.7** shows a schematic representation of ablation procedures highlighted in recent clinical trials and studies.

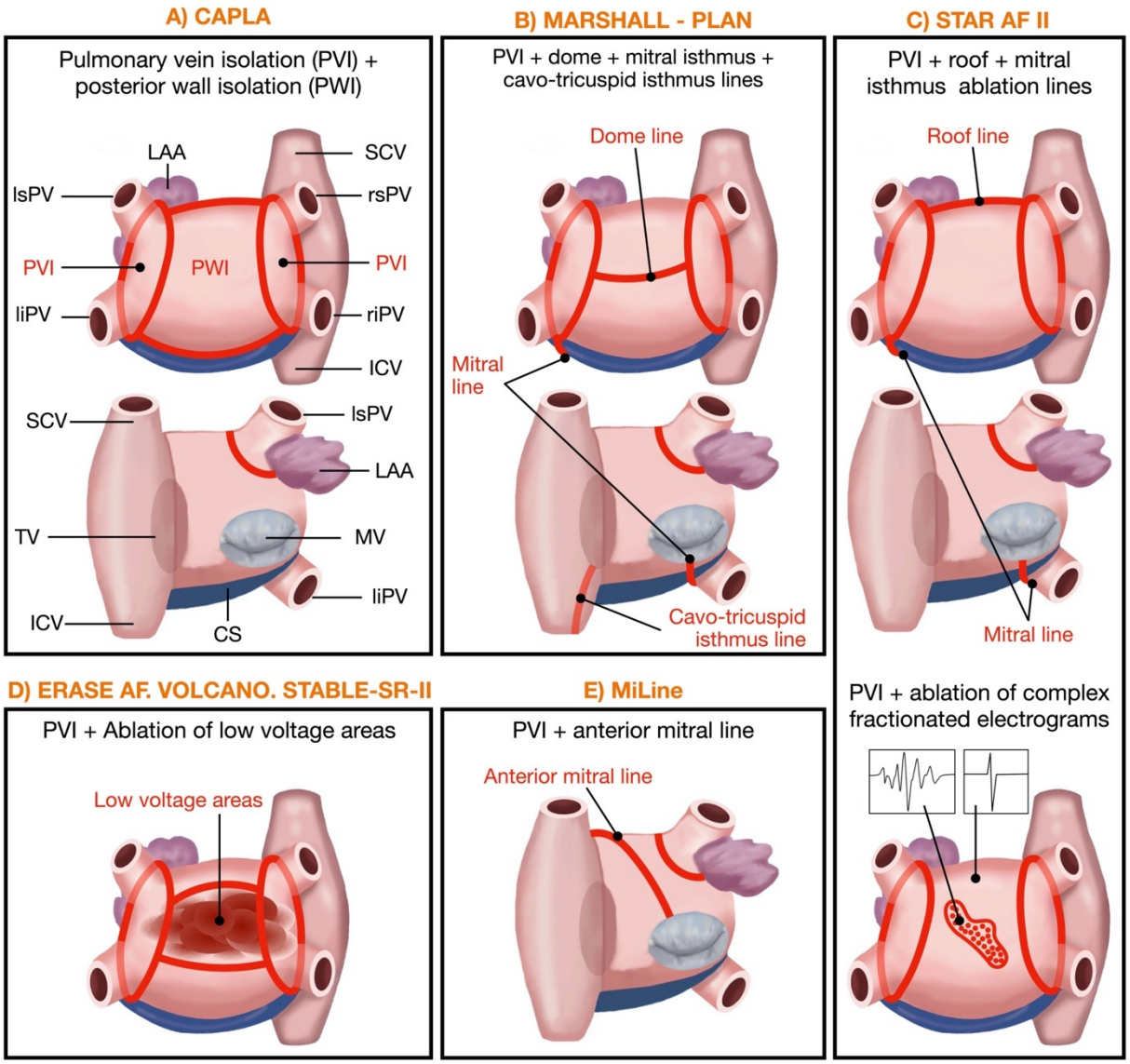


Figure 2.7. Schematic representation of ablation strategies featured in recent clinical trials and studies. **A)** CAPLA (Kristler et al., 2022). **B)** Marshall-Plan study (Derval et al., 2021). **C)** STAR-AF-II (Verma et al., 2015). **D)** ERASE-AF (Huo et al., 2023), VOLCANO (Masuda et al., 2020), and STABLE-SR-II (Yang et al., 2022). **E)** MiLine study (Bergonti, Spera, Ferrero, Nsahlai, Bonomi, Boris, et al., 2023). Abbreviations: LAA: left atrial appendage; SCV-ICV: superior and inferior cava vein. rs-ri-ls-li-PV: right superior, right inferior, left superior and left inferior pulmonary vein. TV-MV: tricuspid and mitral valve. CS: coronary sinus.

STAR-AF-II ((Verma *et al.*, 2015) **Figure 2.7C**) independently tested the ablation of complex fractionated atrial electrograms (CFAE; i.e., fractionated signals obtained during electro-anatomical mapping, **Figure 2.7C**) and the application of empirical lines of block. Electrogram fractionation has been consistently associated with regions of severe fibrosis and conduction abnormalities (Verma *et al.*, 2015). Similarly, numerous anatomical structures, such as the orifices of the atrio-ventricular rings, are

acknowledged perpetuators of atrial arrhythmia. Thus, both strategies presented convincing evidence for their assessment in large clinical trials and yet, failed to demonstrate superiority to PVI.

The ablation of LVAs is another technique widely investigated in clinical trials (**Figure 2.7D**). As mentioned above, LVAs might propitiate AF initiation and maintenance, which make them an attractive ablation target. Nevertheless, contrasting results have been reported in clinical trials. ERASE AF (Huo *et al.*, 2022) showed for the first-time superiority to PVI in persistent AF patients, after VOLCANO (Masuda *et al.*, 2020) and STABLE-SR-II (Yang *et al.*, 2022) reported no beneficial impact in neither paroxysmal nor persistent AF, respectively. Moreover, only 36% of patients presented LVAs in ERASE AF, which might have influenced the results of the trial.

LVAs ablation represents a functional ablation (i.e., patient-specific strategy), and thus a more tailored approach than empirical ablation. In this sense, the RECOVER AF study (Betts *et al.*, 2023) has shown that functional ablation can be very effective in preventing recurrent AF. Instead of LVAs, the authors assessed the elimination of pathological conduction patterns, and reported success rates as high as 91%. The ablation of pathological conduction patterns is yet to be tested in a large randomized clinical trial.

Similarly, novel ablation approaches, such as MiLine (anterior mitral line, (Bergonti, Spera, Ferrero, Nsahlai, Bonomi, Boris, *et al.*, 2023) **Figure 2.7E**) and Marshall-Plan (sequential elimination of the Marshall bundles, PVI, and right and left atrial empirical lines of block, (Derval *et al.*, 2021) **Figure 2.7B**), have obtained promising results in multicentre retrospective and prospective studies, respectively. While effective and approved for testing in larger trials, these strategies rely on extensive ablation lesions, potentially over-treating patients.

Therefore, the ability to accurately stratify patients with AF recurrence after PVI to those requiring extensive versus minimal substrate modification, those benefitting from empirical versus functional ablation, and those who may be optimally treated only with additional antiarrhythmic drug therapy, would be of tremendous clinical value but remains a major challenge. Moreover, since clinical trials have not provided convincing evidence for selecting an optimal ablation strategy, only PVI is suggested for first procedure treatments (Betts *et al.*, 2023). In this sense, when AF recurs despite durable PVI (Benali *et al.*, 2023), no consensus is established for further treatment strategies.

Due to their multiscale nature and scalability, human-based computer modelling and simulation offers the possibility of identifying key modulators of successful AF therapy. Novel and available treatments can be tested in virtual patients, with perfect control over the parameters of interest and high spatio-temporal resolution. Similar to other disciplines, such as aerospace or industrial research, nowadays, computer modelling and simulation represents a power tool in the field of medicine.

CHAPTER

MODELLING AND SIMULATION OF ATRIAL ELECTROPHYSIOLOGY

3

This chapter covers the human atria modelling and simulation methodologies used in this thesis. The mathematical equations that are presented here for electrical propagation encompass experimental knowledge from in-vitro and in-vivo research, and have undergone consistent calibration and validation to ensure that modelling and simulation constitute a reliable representation of living cells, tissue and whole-organ atrial electrophysiology.

3.1. Cellular electrophysiology: The action potential model

In the process of simulating the electrical behaviour of the human heart, the first step consists of modelling and simulating the cardiac action potential.

The first cardiac action potential model was published in 1962 by Denis Noble (Noble, 1962). The model was an adaptation of the seminal work by Hodgkin & Huxley on the squid giant axon (Hodgkin and Huxley, 1952a, 1952d, 1952c, 1952b). The authors proposed a system of ordinary differential equations to describe the axon's electrical propagation and its underlying ionic mechanisms. While the model reproduced the action potential of a neuron, their equations are still the basis of most cardiac electrophysiological models developed to date. Indeed, the contribution of Denis Noble to the broader understanding of excitable cells beyond neurons, building on the Hodgkin & Huxley formalism, demonstrated that the principles of excitable cell physiology stated by Hodgkin & Huxley could be generalised to many fields. Subsequent studies (Carbonell-Pascual *et al.*, 2016) additionally demonstrated that the Hodgkin & Huxley formulation yielded identical results as more complex models, such as the Markov model, both in control conditions and in the presence of ionic current mutations.

In their original manuscript, Hodgkin & Huxley hypothesized that the electrical activity of the cell could be represented by an electrical circuit. The cell membrane, which forms an electrical insulator separating two conductive media, the intracellular and extracellular, was schematically presented as a capacitor. The membrane proteins, such as ion channels and pumps, were described as electrical impedances in parallel with the membrane capacity. Therefore, ionic current could flow either through the cell

membrane, charging the capacitor, or through the impedances, in the form of transmembrane current. The voltage difference caused by the latter current, called transmembrane voltage, was formulated as:

$$C_m \frac{dV_m}{dt} + I = 0, \quad (1)$$

where C_m is the membrane capacitance; V_m is the transmembrane voltage; and the total current density, I, is the sum of the transmembrane ionic current (I_{ion}) and additional stimulation currents (I_{stim}).

In the original model by Hodgkin & Huxley, I_{ion} was the balance of three components: one carrying Na^+ ions (I_{Na}), one K^+ (I_K) and one carrying non-specific ions (I_{leak}). In the most recent atrial cardiomyocyte models, the total ionic current is the balance of the currents and fluxes presented in **section 2.1.2.2**:

$$I_{ion} = I_{Na} + I_{to} + I_{CaL} + I_{Kur} + I_{Kr} + I_{Ks} + I_{K1} + I_{K,ACh} + I_{K,ATP} + I_{K2P} + I_{SK,Ca} + I_{NaK} + I_{NaCa}. \quad (2)$$

For every family of ionic channels in the equation, the movement of ions across the cell membrane is favoured by two forces: the diffusive (osmolarity law) and the electric field (electrical charge law) force. The diffusive force appears when two media have different ionic concentrations. The electric field force is due to the difference between the intracellular, V_i, and extracellular, V_e, potential ($V_m = V_e - V_i$).

If free diffusion is enabled, ions will move according to the electric and diffusive forces. If both forces have the same magnitude but opposing direction, the transmembrane voltage will reach an equilibrium potential where there is no ionic movement. This equilibrium potential, E, is computed through the Nernst law, that considers the intra- and extracellular concentration of an ion S, $[S]_i$ and $[S]_e$, respectively, the temperature, T, the Faraday constant, F, the gas constant, R, and the ion valence, Z_S:

$$E_S = \frac{R\ T}{Z_S\ F} \cdot \ln \frac{[S]_i}{[S]_e}. \quad (3)$$

Conversely, if the electric and diffusive forces have a different magnitude, their difference ($V_m - E_s$) will rule the direction of movement. This difference is called driving force, and is a key element of each individual ionic current (I_S) that constitutes the total I_{ion}:

$$I_S = g_S \cdot (V_m - E_S) \quad (4)$$

The other term of the equation, g_S, is the maximal conductance, which refers to the ion channel density (i.e., channel expression per unit surface of the cell membrane). It is readily understood that a higher channel density would lead to a higher current magnitude. However, Hodgkin & Huxley realized that ion channels were not always open, but instead, maximal conductances experienced transient changes over time. The authors observed up to three channel states: open, closed and inactivated. The transition between states was described by different variables, nowadays called channel gates, that obeyed a first-order differential equation dependent on the transmembrane voltage.

The dynamics of the Na^+ conductance, g_{Na}, perfectly illustrate the transition between channel states upon changes in the transmembrane voltage. Experiments on the squid nerve showed that the voltage exerted

a dual effect on g_{Na}. While a large increase in g_{Na} followed a sudden depolarization of the membrane, a more rapid decrease occurred if the depolarization was maintained. Hodgkin & Huxley described this phenomenon by the presence of two variables, *m* and *h*, which behaved with different time constants and in opposite direction (i.e., *m* activating the Na^+ channel, and *h* inactivating it). Thus, g_{Na} was formulated as the product of a constant term, $\bar{g}_{Na}$, and the variables *m* and *h*:

$$g_{Na} = m^3 h\, \bar{g}_{Na}, \tag{5}$$

$$\frac{dm}{dt} = \alpha_m \cdot (1 - m) - \beta_m m, \tag{6}$$

$$\frac{dh}{dt} = \alpha_h \cdot (1 - h) - \beta_h h. \tag{7}$$

The gating variables *m* and *h* varied in the range of 0 (completely closed) and 1 (completely open), and were governed by the voltage-dependent transition rates α and β:

$$\alpha = value_1 \cdot \exp\left(\frac{value_2 - V_m}{value_3}\right), \tag{8}$$

$$\beta = \left[\exp\left(\frac{value_4 - V_m}{value_5}\right) + 1\right]^{-1}, \tag{9}$$

where "values" are scalars obtained from experimental measurements.

Accordingly, Hodgkin & Huxley derived the complete I_{Na} formulation as:

$$I_{Na} = \bar{g}_{Na} \cdot m^3 h \cdot (V_m - E_{Na}) \tag{10}$$

and similar equations were obtained for the rest of ion channels.

Improvements in experimental techniques and in the understanding of cellular electrophysiology have led the most recent atrial cardiomyocyte models to incorporate several ion channel families, as well as a cytosolic and sarcoplasmic representation of the Ca^{2+} diffusion.

3.2. Cell coupling and propagation of the action potential

Cardiomyocyte models can provide a rough estimate of the proarrhythmic risk (Passini *et al.*, 2016). However, only whole-atria models can capture the great mechanistic complexity of AF (Vagos *et al.*, 2018). These multi-scale representations allow simulation of the electrical propagation in healthy and disease conditions, considering the complex anatomical structures described in **section 2.1.1**.

This electrical propagation is enabled by gap junctions, which couple adjacent cardiomyocytes. The resulting wave of excitation can be described by a reaction-diffusion equation, called the monodomain model of the transmembrane voltage. The monodomain model has the following form:

$$\beta C_m \frac{dV_m}{dt} + \beta I_{ion}(V_m, \boldsymbol{\eta}) = \nabla \cdot (\boldsymbol{\sigma}\, \nabla V_m) + I_{stim}, \tag{11}$$

$$\frac{d\boldsymbol{\eta}}{dt} = (V_m, \boldsymbol{\eta}), \tag{12}$$

where the reactive part (left hand side of Equation 11) has been explained in the previous section; β is the cardiomyocyte surface-volume ratio, and η is a vector of state variables (e.g., gating variables) that depend on the transmembrane voltage, V_m. In the diffusive part (right hand side of Equation 11), the divergence of ∇V_m represents the diffusion of the transmembrane voltage throughout the tissue, governed by the conductivity tensor $\boldsymbol{\sigma}$.

To solve the monodomain model, the reactive and diffusive system need to be discretized in time and space, respectively. Accordingly, a solution is obtained in each time-step for the nonlinear system of ordinary differential equations (Equation 13), and the parabolic system of partial differential equations (Equations 14):

$$\frac{dV_m}{dt} = \frac{1}{C_m}[-I_{ion}(V_m, \boldsymbol{\eta}) + I_{stim}], \tag{13}$$

$$\beta\left(C_m \frac{dV_m}{dt}\right) = \nabla \cdot (\boldsymbol{\sigma}\, \nabla V_m). \tag{14}$$

Many numerical methods allow discretization of these differential equations. In this thesis, I have employed MonoAlg3D, which is a software based on the finite volume method. MonoAlg3D uses parallel computing through graphic processing units (GPUs) to enable a very fast computation of the electrical propagation in the heart. In fact, the authors (Sachetto Oliveira *et al.*, 2018) reported a reduction in the computing time by 165x in a realistic heart geometry presenting spiral wave re-entries.

Thus, the following section briefly summarizes the finite volume method, implemented in MonoAlg3D. A detailed explanation can be found in (Sachetto Oliveira *et al.*, 2012, 2018; Sachetto Oliveira, Alonso and dos Santos, 2018).

3.2.1. Finite volume method implemented in MonoAlg3D

The finite volume method is based on the idea that a continuum can be discretised into finite volumes (i.e., discretised mesh). Thus, a given quantity, such as mass or energy, can flow through the surface area of adjacent volumes. The integration of this quantity over the boundaries of a control volume yields a net flux, resulting from the difference of flows entering and leaving the volume.

Monodomain discretization using the finite volume method

Space discretization. To spatially discretize the diffusion of the electrical impulse, an intracellular current density J (μA/cm^2) can be defined as:

$$J = \boldsymbol{\sigma}\, \nabla V_m, \tag{15}$$

Thus, taking into account Equation 14, the following relation can be stablished:

$$I_v = \nabla J, \tag{16}$$

where I_v ($\mu A/cm^3$) is a volumetric membrane current.

According to the principle of the finite volume method, Equation 16 can be spatially integrated over the continuum delimited by boundaries of the heart, if the latter is discretized into control volumes:

$$\int_\Omega I_v \, dv = \int_\Omega \nabla J \, dv \, . \tag{17}$$

Applying the divergence theorem and using Equation 14, Equation 17 can be written as:

$$\beta C_m \int_\Omega \frac{dV_m}{dt} dv = \int_{\partial\Omega} J \, \mathbf{n} ds \, . \tag{18}$$

Equation 18 represents the basic formula for deriving the linear system of equations that enables the discretization of the monodomain model. For example, in a uniform mesh of regular hexahedra with surface area A^2, the intracellular current density, J, could be computed as the sum of the fluxes over the 6 faces of a hexahedra:

$$A^3 \beta C_m \frac{dV_m}{dt} = A^2 \sum_{f=1}^{6} J_f \, . \tag{19}$$

Considering Equation 16, the flux on each face, J_f, could be calculated by assessing the spatial derivatives of the transmembrane voltage. The latter could be obtained by finite differences, considering the conductivity values between adjacent volumes described by the conductivity tensor, $\boldsymbol{\sigma}$.

Time discretization. The time derivative of the transmembrane voltage (i.e., reactive part of the monodomain model) is calculated at the centre of each control volume. This derivative can be approximated at the time-step *n+1* by the explicit Euler method:

$$\frac{dV_m}{dt} = \frac{V_{m,n+1} - V_{m,n}}{\Delta t} . \tag{20}$$

The first-order Euler method has been widely employed for solving the system of ordinary differential equations of cell models. However, a very small time-step needs to be taken to satisfy numerical stabilities. To overcome this problem, an adaptive time-step Euler method is commonly employed. The latter compares the solutions obtained using the explicit Euler method (first-order method) and the second-order Runge-Kutta (or Heun) method (Sachetto Oliveira *et al.*, 2018).

Parallel implementations using GPUs

When discretized in time and space, both systems can be solved independently. MonoAlg3D uses the Godunov operator splitting, and **Algorithm 1**, adapted from (Sachetto Oliveira *et al.*, 2018), describes the sequential steps applied by the solver.

The reactive system of ordinary differential equations is computed at the centroid of each control volume of the discretised mesh. Since there is no data dependency between different reactive systems, the code can be parallelized. Moreover, as mentioned before, a considerable speed-up is achieved if the parallelization considers a GPU implementation with CUDA.

In this case, a different GPU thread solves the system of ordinary differential equations of each volume centroid. Therefore, line 5 in **Algorithm 1** runs in the GPU. Solving the linear system of partial differential equations requires information of the transmembrane voltage in every control volume. Thus, line 7 in **Algorithm 1** runs in the CPU. Accordingly, after computing line 5, the GPU communicates to the CPU to share the updated values of the transmembrane voltage. Once the system of partial differential equations is solved, the opposite communication (i.e., CPU to GPU) is established for computing line 4, and a new iteration starts.

Algorithm 1	Sequential steps applied by MonoAlg3D for solving the monodomain model. Iterative steps (i_step) are computed until reaching final number of steps (n_steps)
1:	set the cell model initial conditions
2:	assemble the monodomain matrix (linear system of partial differential equations)
3:	**while** i_step < n_steps **do**
4:	Update the transmembrane voltage (V_m) for cell model
5:	solve cell model (reactive system of ordinary differential equations)
6:	update V_m for the diffusive system of partial differential equations
7:	solve the linear system of partial differential equations
8:	i_step = i_step + 1
9:	**end while**

A detailed verification of MonoAlg3D in the framework of the cardiac electrophysiology Benchmark (Niederer *et al.*, 2011) can be found in (Sachetto Oliveira *et al.*, 2018). A modified version of the Benchmark problem, for the purpose of this thesis, has been included in **Annex I**. The modifications were applied to the longitudinal conduction velocity, the transversal to longitudinal anisotropy ratio and the cellular model (see **Annex I**), in order to replicate the setting used for multi-scale atrial simulations. All simulations were run using Cray XC50 (2.60GHz (12 cores, 64GB RAM) and NVIDIA Tesla P100, 16GB), located in the Swiss National Supercomputing Centre (Switzerland). When MonoAlg3D was implemented in this massively parallel multiprocessor supercomputer, the computational cost of running 7 seconds of simulated AF on a mesh of one million regular hexahedra was 2 hours and 30 minutes. The high performance of the solver enabled simulations in large cohorts of virtual AF patients.

CHAPTER

LARGE COHORTS OF VIRTUAL AF PATIENTS

4

In this chapter I present how I constructed a large cohort of virtual AF patients (also referred as population of virtual atria or whole-atria models). The concept of virtual AF patient refers to the virtual representation of the patient's atria during AF. Thus, besides including accurate patient characteristics (i.e., atrial anatomy, electrophysiology and tissue structure), virtual atria simulate the irregular electrical activity occurring during AF. The population of virtual AF patients, together with the in-silico trials presented in ***Chapter 5****, constitutes the central paradigm of the framework developed in this thesis.*

4.1. Population of human atrial cardiomyocyte models

In the process of constructing a large cohort of virtual AF patients, the first step comprises the development of a population of human atrial cardiomyocyte models using a baseline cellular model.

4.1.1. Single (baseline) atrial cardiomyocyte model

Numerous biophysically-detailed (baseline) models of the human atrial action potential have been published (reviewed by (Vagos *et al.*, 2018) and benchmarked by (Wilhelms *et al.*, 2013)). While all of them comprise a system of ordinary differential equations that essentially follows the Hodgkin-Huxley formulation, the models differ in the number, magnitude and kinetics of their ionic components. Adopting one model or another is therefore dependent on the research question being addressed (Muszkiewicz *et al.*, 2016).

In this thesis, I have used the CRN model (Courtemanche, Ramirez and Nattel, 1998), since it has been expanded to study drug effects in single-cell (Loewe *et al.*, 2014; Sutanto *et al.*, 2019) and, after appropriate ionic current modifications, reproduces both the long plateau observed in paroxysmal AF patients with steep restitution (Narayan *et al.*, 2008), and the more triangular shape of persistent AF. To circumvent model-dependent bias, simulations with the CRN model have been repeated, as necessary, using the Grandi-Bers (Grandi *et al.*, 2011) and Maleckar-Trayanova (Maleckar *et al.*, 2009) models.

4.1.2. Population of atrial cardiomyocyte models with variability in ionic currents

These mathematical models were originally developed using a subset of *in-vivo* or *in-vitro* data, so that their differential equations reproduced the average behaviour observed in the data (Britton *et al.*, 2013). Since the models did not include electrophysiological variability, they were unable to capture the wide range of disease phenotypes observed in humans or an accurate treatment response (Passini *et al.*, 2016). Thus, following simulation studies (Romero *et al.*, 2009; Sarkar, Christini and Sobie, 2012) conveyed the importance of incorporating inter-subject variability in cardiac electrophysiology. Ultimately, (Britton *et al.*, 2013) developed an efficient methodology, called population of models, that enabled simulation of the electrophysiological variability observed in a (clinical, experimental, etc.) dataset.

Figure 4.1 illustrates the development of a representative population of atrial cardiomyocyte models. The methodology consists of scaling a subset of model parameters, which are thought to vary in the human population, over a specified range. By using sampling techniques (e.g., Latin hypercube sampling), every cardiomyocyte model of the population has a unique combination of parameters, which results in a unique electrophysiological profile and thus, action potential. It is commonly assumed that variability in cellular electrophysiology is mainly expressed at the level of the ion channel density (Britton *et al.*, 2013; Muszkiewicz *et al.*, 2016). **Figure 4.1A** illustrates how scaling the density of I_{CaL} by ±50% modifies the action potential shape. Following this principle, a population of cardiomyocyte models can be developed by scaling the maximal conductance of all ionic currents and fluxes of the CRN model, including I_{Kur}, I_{Kr}, I_{to}, I_{K1}, I_{Ks}, I_{CaL}, I_{NaK}, I_{NaCa} and I_{Na}, as well as the sarcoplasmic reticulum Ca^{2+} release (J_{rel}), leak (J_{leak}) and uptake (J_{up}).

The generated population (**Figure 4.1B**), called candidate population of cardiomyocyte models, undergoes a calibration step. The calibration is performed against human experimental data, and ensures that cardiomyocyte models accurately reproduce human electrophysiological properties. For this, action potential recordings from human patients (Sánchez *et al.*, 2014) are compared to the in-silico signals. **Figure 4.1C** shows characteristic action potential biomarkers that are used for the comparison, such as duration at 20, 50 and 90% of cellular repolarization, the amplitude, resting membrane potential and maximum upstroke velocity. The experimentally-calibrated population, illustrated in **Figure 4.1D**, comprises all the atrial cell models which biomarkers are within the ranges delimited by the minimum and maximum value observed experimentally (**Figure 4.1E**). In this thesis, only those cardiomyocytes which all biomarkers were within the experimental ranges were kept for further analysis.

Another approach to refine the calibration considers limiting the boundaries within 2 standard deviations (i.e., adopting a Gaussian distribution; Muszkiewicz *et al.*, 2016). While this criterion has not been used in this thesis, it may prevent over-representing extremes of physiology, at the expense of not capturing the broadest range of possible physiological variability or missing important data points related to the disease of interest. Other approaches have been proposed in order to calibrate the populations to data

densities (i.e., specific data distributions, Lawson *et al.*, 2018). While a priori these approaches have been argued to allow the extraction of additional information from the calibration, previous studies of atrial electrophysiology have observed no differences between using Latin hypercube sampling or more advanced sampling methods (Muszkiewicz *et al.*, 2018). The size and variability of the experimental data available ultimately dictates the calibration criteria employed (Muszkiewicz *et al.*, 2016).

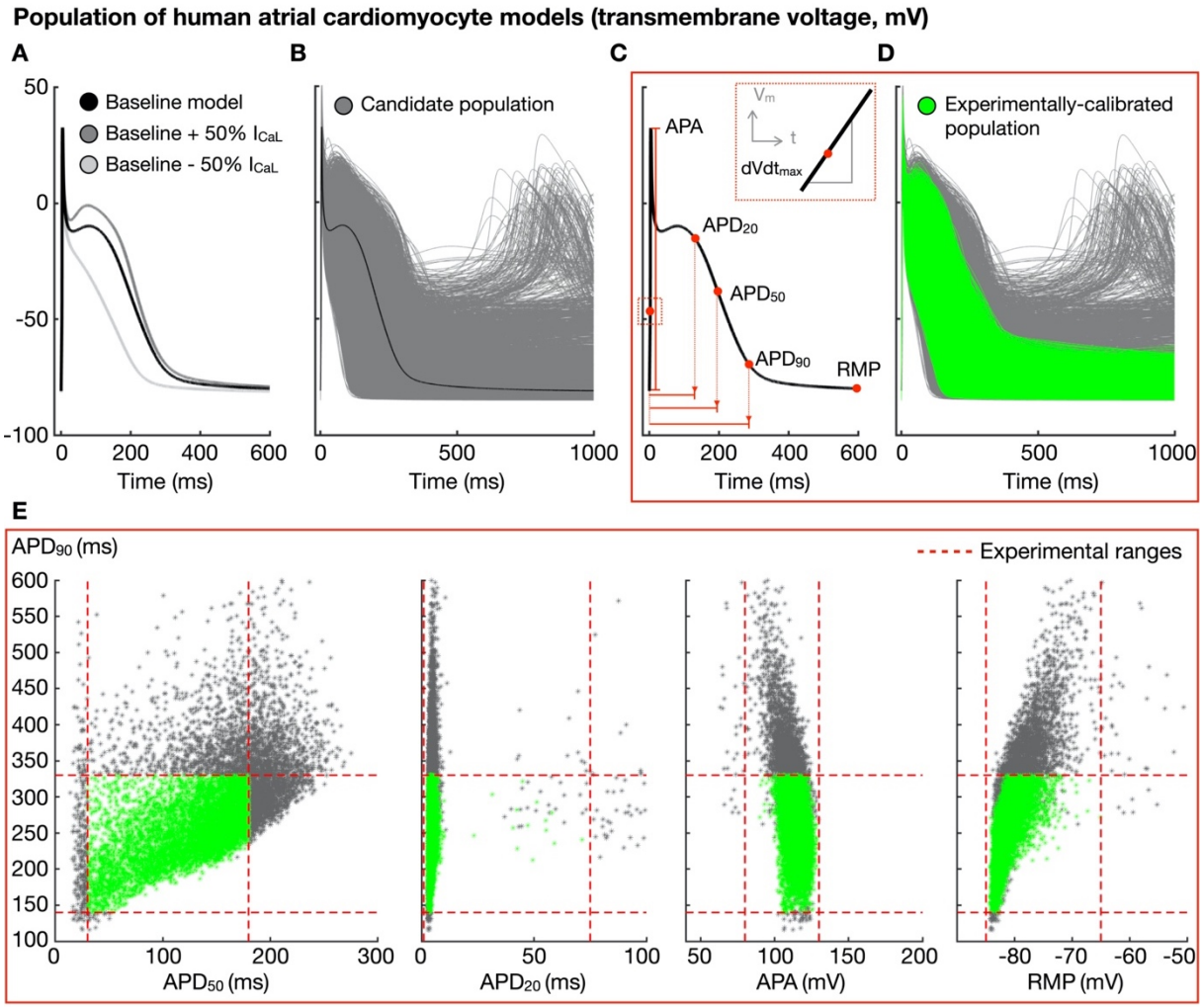


Figure 4.1. Generation of a population of human atrial cardiomyocyte models. **A)** Effects of scaling the maximal conductance of I_{CaL} in the CRN model (baseline model). **B)** Candidate population of cardiomyocyte models, developed scaling all ionic conductances by ±50%. **C)** Action potential biomarkers: action potential duration at 20% (APD_{20}), 50% (APD_{50}) and 90% (APD_{90}) of cellular repolarization, action potential amplitude (APA), resting membrane potential (RMP) and maximum upstroke velocity ($dVdt_{max}$). **D)** Calibrated population using the human experimental ranges presented in **E)** (Sanchez et al., 2014), for the action potential biomarkers.

4.2. Populations of whole-atria models

4.2.1. Population of structurally-healthy atria: Electrophysiological variability

Similar to populations of cardiomyocytes models, a population of whole-atria models can capture inter-subject variability in electrophysiology. The higher dimensional complexity of whole-atria models,

moreover, enables variation of other relevant characteristic, such as atrial volume and tissue structure. In this thesis, the first step in constructing a large population of virtual patients considered the case of structurally-healthy atria. These whole-atria models are characterised by absence of heterogeneities in tissue structure (e.g., absence of fibrosis), but might include electrophysiological and anatomical variability. They represent a common phenotype of early AF stages.

Structurally-healthy atria were developed by combining one cardiomyocyte model with one atrial anatomy. In studies that considered a single anatomy (e.g., **Chapter 6**), the number of whole-atria models was the same as the original number of cardiomyocyte models in the population. In studies that considered anatomical variability (e.g., **Chapter 9**), the number of whole-atria models was the number of cardiomyocyte models multiplied by the number of atrial geometries (see below).

While every whole-atria model was developed with a single cardiomyocyte model, the latter was scaled in different atrial structures to reflect regional heterogeneities in electrophysiology. These regional heterogeneities have been considered by assigning the single-cell properties of each atrial cardiomyocyte model to the left or right atrial tissue, depending on the chapter, and modifying them in the right or left atrium, crista terminalis, pectinate muscles, left atrial appendage and atrio-ventricular rings. The resulting action potential models (i.e., the original cardiomyocyte model and the scaled versions) constituted an ionic current profile. **Figure 4.2** illustrates one ionic current profile used to construct one whole-atria model. **Table 4.1** gathers the scaling factors applied in each atrial region.

Table 4.1. Regional electrophysiological heterogeneities. Adapted from (Sánchez *et al.*, 2017). The original cardiomyocyte model can be included either in the LA or RA. When included in the RA, the scaling factors for I_{Kr} are "1" in the RA and "1.6" in the LA. Conversely, when the cardiomyocyte model is included in the LA, the I_{Kr} scaling factors are "1/1.6" in the RA and "1" in the LA.

Region	Anisotropic ratio Transversal-Longitudinal	CV (cm/s)	I_{to}	I_{CaL}	I_{Kr}
Left atrium (LA)	1:2	60 – 80	1	1	1 or 1.6
Right atrium (RA)	1:2	60 – 80	1	1	1 or 1/1.6
Sinoatrial node	1:1	31 – 42	1	1	1
Crista terminalis	1:10	116 – 157	1.35	1.6	0.9
Pectinate muscles	1:2	98 – 133	1.05	0.95	0.9
Bachmann's bundle	1:2	98 – 133	1	1	1
Left atrium appendage	1:2	59 – 80	0.65	1.05	2.75
Atrio-ventricular rings	1:2	59 – 80	1.05	0.65	3

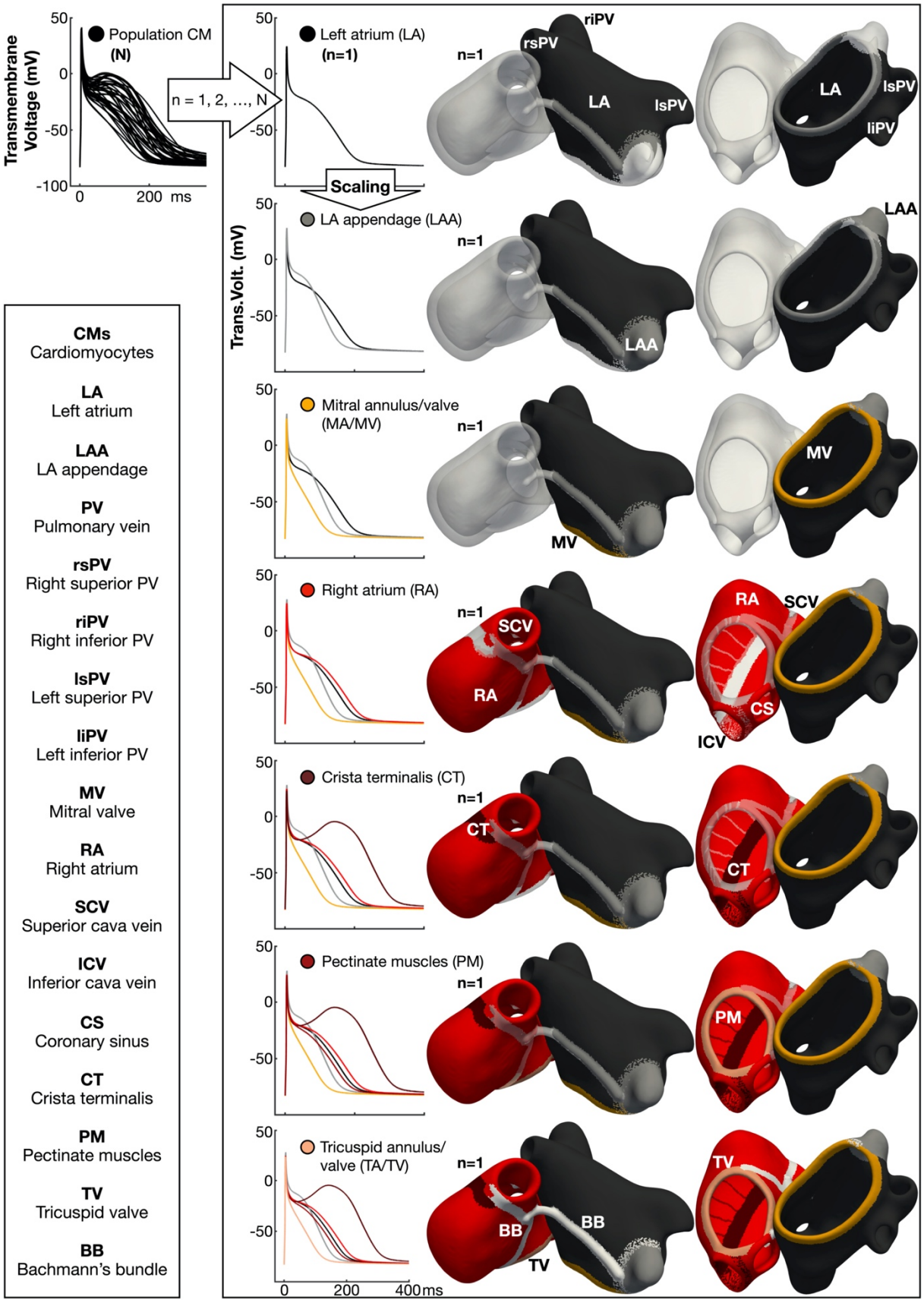


Figure 4.2. Generation of human whole-atria models using a population of cardiomyocyte models. One whole-atria model is developed with one cardiomyocyte model, by assigning its single-cell properties to the left atrial tissue and scaling them in other atrial regions.

4.2.2. Population of structurally-remodelled atria: Anatomy and structural variability

4.2.2.1. Remodelling of the atrial anatomy: Bi-atrial enlargement

The first human whole-atria model that incorporated regional heterogeneities was published by (Seemann *et al.*, 2006). The atrial anatomy was obtained from the ex-vivo Visible Human Project and included realistic wall thickness, fibre architecture, and defined atrial regions. This atrial anatomy, commonly referred as the Visible Female atria, has been adopted for conducting multi-scale simulations.

To consider anatomical variability, 10 additional geometries were generated from a bi-atrial statistical shape model (Nagel, Schuler, *et al.*, 2021). The bi-atrial shape model was developed with 47 CT and MRI datasets from control and AF patients, and its development and the generation of the 10 anatomies was performed by Dr Claudia Nagel. These 10 atrial anatomies (right and left atrium, 127±51 mL and 105±39 mL, respectively; mean ± SD) covered the volumes associated clinically with AF recurrence. **Table 4.2** compares the volume of the 10 atrial anatomies with the Visible Female atria and clinical data.

Table 4.2. Volume of the atrial anatomies considered in this thesis to conduct multi-scale simulations. Comparison with the atrial volumes associated with AF recurrence clinically.

		Atrial volume (mL)	
		Left atrium	**Right atrium**
Atrial volumes associated with AF recurrence clinically	(Lang *et al.*, 2015)	65 – 112	80 – 148
	(Njoku *et al.*, 2018)	96 – 210	–
Visible Female atria		62	83
Bi-atria statistical mean shape model		93	109
Atrial anatomy 1 (AA1)		102	58
Atrial anatomy 2 (AA2)		59	64
Atrial anatomy 3 (AA3)		44	91
Atrial anatomy 4 (AA4)		146	96
Atrial anatomy 5 (AA5)		85	122
Atrial anatomy 6 (AA6)		110	135
Atrial anatomy 7 (AA7)		169	145
Atrial anatomy 8 (AA8)		94	162
Atrial anatomy 9 (AA9)		142	194
Atrial anatomy 10 (AA10)		99	205

In studies that considered several geometries, the construction of the population also followed the principles illustrated in **Figure 4.2**, in which one whole-atria model was developed with one ionic current profile (i.e., one cardiomyocyte model scaled in different atrial regions). However, since this ionic profile was included in every atrial anatomy, the number of virtual AF patients developed was the number of cardiomyocyte models multiplied by the number of atrial anatomies.

4.2.2.2. Remodelling of the tissue structure: Patient-specific distribution of low voltage areas

The number of whole-atria models that were developed also increased with the addition of tissue heterogeneities (i.e., remodelling of the tissue structure). In this thesis, tissue heterogeneities were modelled based on invasive electro-anatomical mapping, that identified the patient-specific distributions of LVAs. As mentioned in **Section 2.2.3**, cardiac tissue characterisation should be based not only on voltage mapping but, ideally, on several mapping modalities and clinical data. This has been acknowledged in **Section 10.3** (limitations and future work). After adding structural heterogeneities, the resulting number of whole-atria models was the number of structurally-healthy atria multiplied by the number of LVA distributions considered. The inclusion of LVAs in whole-atria models is schematically illustrated in **Figure 8.1** (**Chapter 8**) and **Figure 9.1** (**Chapter 9**).

The electro-anatomical maps of AF patients were obtained at the John Radcliffe Hospital in Oxford, by Dr Rohan S. Wijesurendra, Dr Michael T.B. Pope and Dr Timothy R. Betts. All studies were conducted according to the principles of the Declaration of Helsinki, and all patients gave written informed consent.

High density mapping of the atria was performed using an Abbott Advisor HD grid (SE) catheter while pacing at the coronary sinus at a cycle length of 800 ms. The patient electro-anatomical maps were registered to a common atrial surface, through a rigid and non-rigid registration.

In the study presented in **Chapter 8**, left atrial maps of 8 AF patients were registered to the left atrium of the Visible Female atria. The 8 patients had a median age of 64 (59–70; interquartile range, IQR) and 58% were male (Pope *et al.*, 2022). A median number of 5399 points (3279–8677; IQR) was obtained per electrogram map. After the total reconstruction of the patients' anatomy, the left atrial meshes had a median of 11819 (10300–14184; IQR) and 23632 (20595–28366; IQR) points and elements, respectively, for a total atrial surface of 191.96 (174.50–273.73; IQR) cm^2.

In **Chapter 9**, bi-atrial maps were obtained from 20 (85% persistent) AF patients and were registered to the endocardial surface of the bi-atrial statistical shape model. The 20 patients had a median age of 61 (56–66; IQR) and 59% were male (Pope *et al.*, 2021). A similar number of points were obtained per electrocardiogram map. The left atrial meshes had a median of 10817 (9348–12452; IQR) and 21630 (18696–25083; IQR) points and elements, respectively. The right atrial meshes had a median of 41386 (20547–57343; IQR) and 78616 (42268–92206; IQR) points and elements, respectively. The total atrial surface was 188.69 (161.37–217.01; IQR) cm^2 and 180.07 (155.85–262.68; IQR) cm^2 for the left and right atrial chambers, respectively.

After registration, the patients' voltage data were subsequently interpolated to the target surface using the nearest neighbour algorithm. LVAs were simulated as regions of 30% decreased conductivity, increased anisotropy (i.e., 8:1 longitudinal to transversal ratio) and 50%, 40% and 50% reductions in I_{CaL}, I_{Na} and I_{K1}, respectively (Azzolin *et al.*, 2023). This remodelling was applied on top of the individual electrophysiological properties of each virtual patient.

In this thesis, the registration was performed using MeshMonk (White *et al.*, 2019), which is an open-source toolbox implemented in MATLAB. MeshMonk was chosen since it supports different image registration techniques (e.g., rigid, affine, non-rigid), provides accurate surface alignments in a few seconds (rigid registration) or in less than a minute (non-rigid), it has a user-friendly interface that provenance of the registration, it supports several image formats and, importantly, the publicly available code integrates various workflows and tutorials for an effective utilisation of the software.

The program first orients, repositions, and scales a template surface (i.e., in this case the patients' endocardial surface) to a target surface (e.g., the endocardial surface of the Virtual Female atria), during a rigid registration step. Subsequently, the template surface was further transformed to fit the specific shape of the target surface, using a non-rigid deformation. To perform the rigid and non-rigid registration, common landmarks need to be placed in the target and template surfaces. For the registration of the patient-specific maps, nine landmarks were placed in the left atrium, namely, the intersection of the four veins with the left atrial posterior wall, the tip of the appendage and four equally-spaced point around the mitral ring. Similarly, seven points were placed in the right atrial surfaces: the intersection of the superior and inferior cava vein with the venous portion of the chamber, the tip of the appendage and four equally-spaced point around the tricuspid ring.

Noteworthy, while landmark-based registration is effective for applications that deal with images containing well-defined landmarks (e.g., the veins converging in the right and left atrium), the registration might rely on the accuracy of landmark placement. This, at the same time, depends on a correct manual annotation (i.e., operator error). **Figure 4.3** quantifies the registration error obtained when a different subset of landmarks is used for the registration. Three different left atrial surfaces, with a different LVA extension, have been used for the analysis (**Figure 4.3A**). Moreover, for each patient surface, four different subsets of landmarks were employed, namely, the original subset (used in this thesis for the registration of all patient surfaces) and three additional ones, each of them comprising variations in all nine landmarks placed in the left atrium (**Figure 4.3B**).

After registering the patient surface to the mean shape model, the patient voltage data was interpolated. Voltage maps were subsequently binarized into LVA (bipolar voltage lower than 0.5 mV) and non-LVA ($\geq$ 0.5 mV). For the purpose of analysing the error resulting from variability in landmark placement, the binary map derived from using the original subset of landmarks was defined as ground truth. Thus, the error was computed as the percentage of points that being originally defined as LVA (or non-LVA) were defined as non-LVA (or LVA) when another subset of landmarks was employed.

Figure 4.3C illustrates the error in LVA classification obtained in three different patients when three different subset of landmarks are used for the registration. A higher error was observed for medium size LVA (patient #2), since small deviations in space translated into bigger error accumulation. However, in any case the error was lower than 0.2%, and all four maps (using the original and modified landmarks)

yielded imperceptible differences to the human eye. As mentioned above, this is likely due to the perfectly-defined cardiac structures (i.e., valves, veins and appendages).

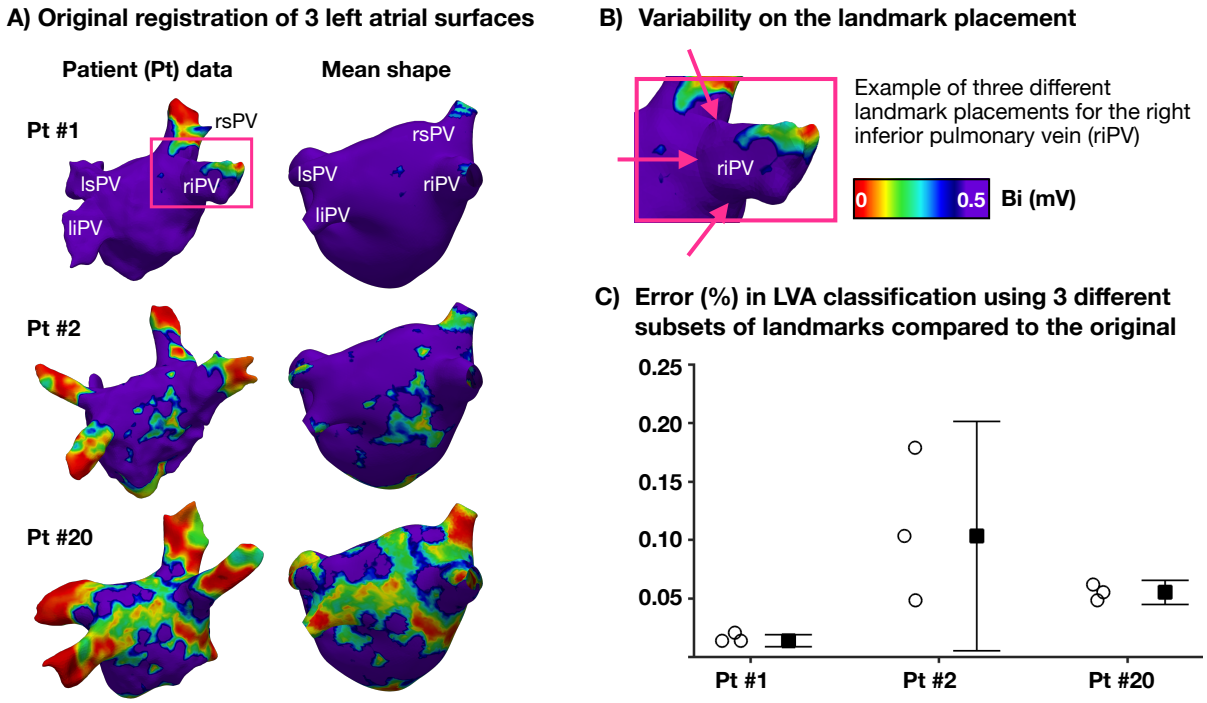


Figure 4.3. A) Left atrial electro-anatomical map of three AF patients and original registration to the left atrial endocardial surface of the statistical mean shape model. Abbreviations: rs-ri-ls-li-PV: right superior, right inferior, left superior and left inferior pulmonary vein. **B)** Example of three different landmark placement for the riPV. Abbreviations: Bi: bipolar voltage. **C)** Error (%) obtained comparing the original registration of the patient surface (Panel A) against three further registrations obtained using three different subsets of landmarks.

4.3. Population of virtual atrial fibrillation patients

Following the construction of the population, an AF induction protocol was applied to create a cohort of virtual AF patients. In this thesis, two different protocols were used to induce AF.

The first one replicated accurate AF initiation conditions and evaluated how a given substrate facilitated AF induction. The protocol mimicked the spontaneous ectopic beats reported in human AF patients (Haïssaguerre *et al.*, 1999). As such, a burst of five to eight periodic stimuli was applied at the left or right pulmonary veins, the most common foci origin sites. To account for repetitive discharges with irregular cycle length, different intervals were tested for the burst. **Figure 6.5** in **Chapter 6** illustrates that upon application of the burst, appropriate atrial substrates (e.g., in the form of discordant alternans; see **section 2.2.2**) can propitiate AF induction.

The second protocol considered the arrhythmia as already present in the tissue, and assessed AF maintenance under different patient characteristics. For this, spiral wave re-entries were imposed as the initial conditions of the simulation (Matene and Jacquemet, 2012; Roney *et al.*, 2022). Three spiral

waves were applied in each atrial chamber. In the left atrium, one spiral wave was induced in the anterior wall, one in the posterior, and another in the inferior wall. In the right atrium, two spiral waves were induced in the venous portion, one around the proximity of the superior cava vein and one close to the inferior cava vein, and a third one in the inferior wall. The direction of rotation was clockwise for two spiral waves in each chamber and counter-clockwise in the third one, ensuring that adjacent re-entries rotated with opposing phase (Matene and Jacquemet, 2012; Roney *et al.*, 2022). **Figure 8.2** in **Chapter 8** illustrates a representative example.

Virtual atria presenting sustained AF, commonly defined in this thesis as 7 s of uninterrupted arrhythmia (Matene and Jacquemet, 2012), were considered virtual AF patients. To ascertain the proportion of virtual patients that, being initially defined as sustained (>7 s) AF patients, presented uninterrupted arrhythmia over a meaningful duration in the clinics, AF was further analysed for 30 s (i.e., duration used clinically for AF diagnosis). This served to demonstrate that all virtual patients presenting sustained arrhythmia over 7 s additionally had uninterrupted arrhythmia for 30 s (a representative example is shown in **Figure 4.4**).

4.4. Validation of virtual atrial fibrillation patients

The development of virtual AF patients was subjected to consistent calibration, and human data were used from single cell to organ levels. First, the population of cardiomyocytes models was calibrated with human recordings from AF patients; second, the atrial anatomies considered the volumes associated with AF recurrence; and finally, LVAs distributions were directly extracted from patient images.

Similarly, the cohort underwent extensive validation. The validation of virtual AF patients considered two steps: the first one, internal validation, was carried out with the data used to develop the models. The second step, external validation, was performed with data not used during the model generation.

4.4.1. Validation against the patient data used to construct the models

Virtual patients with structurally-remodelled atria were developed considering patient-specific distributions of LVA. As mentioned above, the electro-anatomical maps were obtained while pacing at the coronary sinus. Thus, besides the bipolar voltage, the atrial mapping intrinsically obtained the sequence of electrical activation (i.e., atrial depolarization). This local activation of the atria was used to estimate the local and global conduction velocity (Coveney, Cantwell and Roney, 2022), identify regions of conduction abnormalities, and associate them with presence of LVA.

Accordingly, the internal validation of virtual patients assessed whether the simulated local activation times agreed with those obtained with the human patient. This validation process ensured that the parameters of the virtual patient (i.e., conduction velocity and modelling of LVA) accurately reproduced the conduction properties of human tissue. **Figure 4.4A** illustrates a comparison of the bipolar voltage and local activation time maps from a human patient and the corresponding virtual patient model.

4.4.2. Validation against external patient data

Virtual AF patients were externally validated through the analysis of the electrocardiogram (ECG; **Figure 4.4B**). The ECG was computed in virtual patients presenting sustained AF as in (Gima and Rudy, 2002). The resulting signals were standardized and processed using pass-band filtering with cut-off frequency of [0.5–50] Hz (Alcaraz *et al.*, 2011). Five biomarkers, namely, dominant frequency, organization index, Shannon's spectral entropy, sample entropy and relative harmonic energy, were extracted from each lead (a detailed explanation can be found in (Zeemering *et al.*, 2018)). Briefly, the dominant frequency is a surrogate of the main AF frequency, and describes how fast the atrial tissue (or a specific region) is depolarized. The organization index considers the strength of the main AF frequency within the spectrum of frequencies. Thus, a low organization index (i.e., a weaker main frequency) is observed for numerous fibrillatory processes with different frequencies. A similar interpretation can be obtained from the relative harmonic energy or the spectral entropy, which are measures of complexity. Low values of these biomarkers indicate a dominant role of the main atrial wave (e.g., one single frequency resulting from a single re-entrant or focal source). Finally, the sample entropy is a surrogate of predictability and repetitiveness, also observed when a single driver governs the arrhythmia.

These biomarkers provide a characterisation of AF complexity in the frequency domain. Thus, the credibility of simulation results was assessed by comparing the morphology and complexity of the signals, and the ranges of the simulated and clinical biomarkers. In this sense, **Figure 4.4B** illustrates a comparison between clinical and simulated ranges of AF dominant frequency.

The in-silico data in **Figure 4.4B** comprises the 494 and 522 (1016 in total) virtual patients with sustained AF obtained in the studies presented in **Chapter 8** and **9**, respectively. Especially in **Chapter 9**, which considered the most complex population of virtual patients (i.e., 522 virtual patients with electrophysiological, anatomical and structural variability), the ECG dominant frequency was 6.9±3.4 Hz, consistent with the average 6-8 Hz reported in many clinical studies (Mikhailov *et al.*, 2021). Further comparisons of the morphology and complexity of the simulated ECGs against clinical recordings are illustrated in **Figure 6.2** and **Figure 8.2** (**Chapters 6** and **8,** respectively).

The development and validation of virtual AF patients was the starting point for assessing the virtual application of treatments. The so-called *in-silico* trials are hereunder introduced.

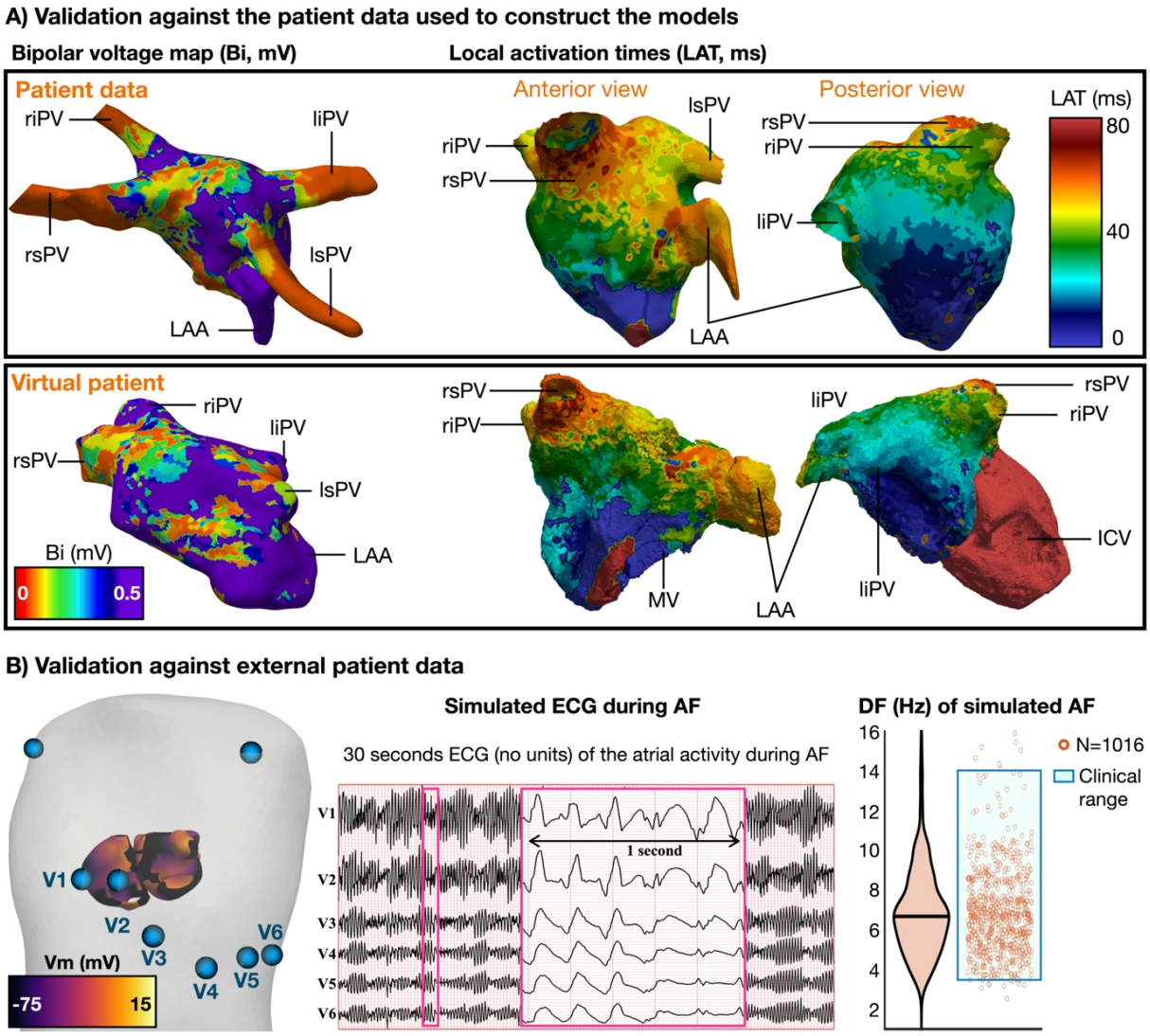


Figure 4.4. A) Comparison of the bipolar voltage and local activation time maps obtained in a human patient (top) and in a representative virtual patient (bottom). Abbreviations: LAA: left atrial appendage. ICV: inferior cava vein. rs-ri-ls-li-PV: right superior, right inferior, left superior and left inferior pulmonary vein. MV: mitral valve. **B)** Representative virtual AF patient with the atria inside the torso. Screenshot of the simulated transmembrane voltage and 30 seconds ECG (dimensionless, only showing atrial activity). Comparison between clinical and simulated ranges of AF dominant frequency. The clinical ranges are extracted from Sanders *et al.*, 2005.

CHAPTER

CONCEPTUALIZATION OF IN-SILICO TRIALS

5

This chapter covers the methodologies I implemented for the second pillar of this thesis: in-silico clinical trials.

5.1. Definition

Clinical trials are implemented to test the safety and efficacy of medical interventions on human patients. They consist of four carefully designed phases that undergo thorough evaluation. Since new treatments need to be tested in large populations and in different countries before approval, clinical trials are both expensive and long.

In-silico trials resemble clinical trials, and medical interventions are assessed in a population of study. However, the subjects of study are virtual patients that consider key human characteristics. In-silico trials offer a range of advantages over clinical trials, namely, they are conducted faster and with a lower economic burden, they are not subjected to ethical constraints, numerous interventions can be applied in the same virtual patient, and there is perfect control over the parameters of interest (i.e., less impact of confounding variables). Moreover, since in-silico trials can explore novel treatments and define a better use of existing ones in a cost-effective manner, they represent a powerful aid to clinical trials.

In this thesis, in-silico trials are conducted in large cohorts of virtual AF patients to assess two medical interventions: pharmacological treatment and catheter ablation.

5.2. Pharmacological interventions

5.2.1. Modelling and simulation of pharmacological treatment

As described in **section 2.3.1**, pharmacological agents inhibit specific ionic currents by binding to channel proteins. This complex process can be modelled using numerous methods. In this thesis, drug action was simulated as simple pore-block models, since the data required were available for the compounds investigated, and it resembles the characterisation performed by the pharmaceutical industry. Accordingly, ion channel inhibition was described by the Hill's equation (Hill, 1910):

$$\Theta = \left[1 + \left(\frac{D}{IC_{50}}\right)^{nH}\right]^{-1}, \quad (21)$$

$$g_{S,Block} = \Theta \cdot g_S, \quad (22)$$

where Θ, in the range of [0,1], is the degree of ion channel block. Θ multiplies the maximal conductance of the ion channel family S, g_S, generally resulting in a lower value after drug application, $g_{S,Block}$. The equation considers the 50% inhibitory concentration (IC_{50}), the Hill coefficient (nH) and effective plasma drug concentration (D). IC_{50} is a quantitative measure that describes the drug concentration needed to achieve a 50% inhibition of a biological process (e.g., flow of ions through channels), nH quantifies the interaction of the drug with the ion channel for different drug concentrations, and D considers the concentration of the compound at the receptor site.

When modelling the effect of a compound on different ion channels, the effective plasma concentration is common for all of them. The IC_{50} and nH, however, depend on the binding affinity between the ion channel and the agent and thus, is different for each family of ion channels. These values are usually extracted from in-vitro and in-vivo studies. Nevertheless, the lack of studies on human atrial cardiomyocytes have led different simulation studies to adopt disperse values for the same compound. **Table 5.1** gathers IC_{50}, nH and D values adopted in different simulation studies for different drugs.

5.2.2. Validation of antiarrhythmic drug simulation

The adoption of different values for modelling drug effects might yield very different results. Thus, a validation process is needed to ensure that the set of values adopted, and the simulated drug effects, correspond with the effects observed in the experimental and clinical setting.

In this thesis, the validation of simulated antiarrhythmic drug effects was performed at different scales and considered three steps. As detailed in **section 2.3.1**, antiarrhythmic drugs can modify electrophysiological properties of the cell and tissue (i.e., excitability, action potential characteristics, conduction velocity, etc.). Therefore, a first validation step comprised the comparison of single-cell and tissue characteristics between simulated and experimental data, before and after drug application. Numerous biomarkers can be used for the comparison, namely, the APD, conduction velocity and maximum upstroke or rise rate; as well as the changes of these parameters with varying pacing rate (i.e., rate-dependence alterations).

The second validation step compared drug effects in different cellular models (e.g., Maleckar-Trayanova model vs. Grandi-Bers model). This step ensures that the results obtained in the simulations are not unique to bias associated with one cellular model (i.e., model independence of key results).

Finally, the validation process included the assessment of the results obtained at whole-organ level. In-silico trials tested the virtual application of antiarrhythmic drugs to prevent AF. Thus, similar to clinical

trials, the efficacy of a compound (i.e., percentage of AF episodes prevented) was quantified in-silico. In interventional clinical trials, this cardiac efficacy is usually the primary endpoint of the study. Thus, the comparison of primary endpoints between in-silico and clinical trials constituted the third fundamental step in the validation.

5.3. Catheter ablation interventions

5.3.1. Modelling and simulation of catheter ablation

Catheters can apply different sources of energy (i.e., radiofrequency, cryoenergy, pulsed electrical field) to kill the cardiac tissue underneath. When successfully applied, the ablation creates scar tissue unable to conduct electrical signals. Therefore, in this thesis, the ablation lesions were simulated by making cells from the atrial mesh unexcitable. The lesions reproduced those of the associated clinical studies. **Figure 5.1** shows a comparison between the schematic representation illustrated in **Figure 2.7**, the ablation lesion featured in a clinical study (Liang *et al*., 2021), and the simulated ablation.

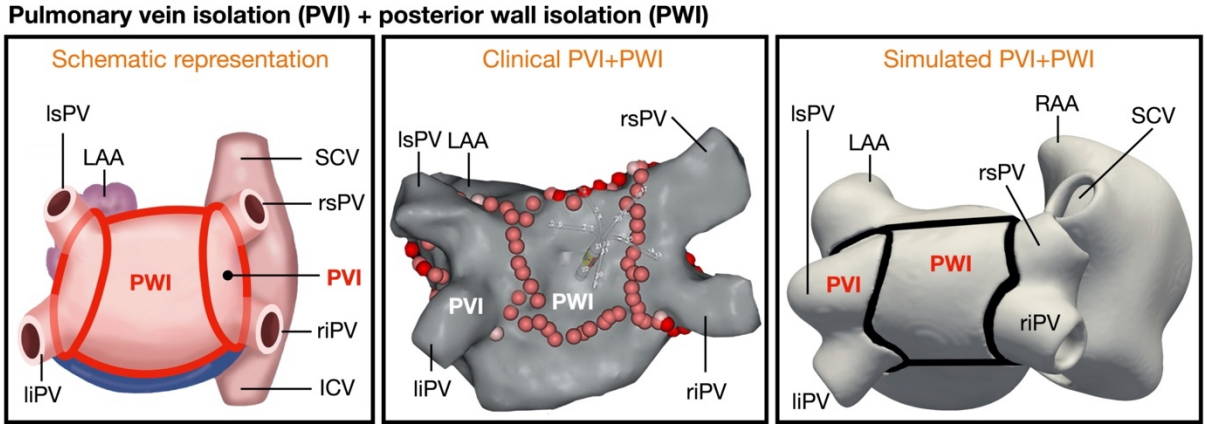


Figure 5.1. Pulmonary vein isolation and posterior wall isolation. Comparison between a schematic representation of the ablation lesion (left), a representative left atrium of a human patient enrolled in a clinical study (middle), and the simulated lesion (i.e., in-silico trials) performed in this thesis (right). Abbreviations: RAA-LAA: right and left atrial appendage. SCV-ICV: superior and inferior cava vein. rs-ri-ls-li-PV: right superior, right inferior, left superior and left inferior pulmonary vein. Adapted from Liang *et al.,* 2021 with permission.

5.3.2. Validation of catheter ablation simulation

Similar to the virtual application of pharmacological treatment, the efficacy of virtual ablation for preventing AF was quantified in-silico and compared against clinical data. A comparison of the primary outcomes between the simulations and clinical trials are presented in following chapters, when showing the results of the in-silico trials.

Table 5.1. List of antiarrhythmic drugs with their IC_{50} (μM) and hill coefficient (in brackets) used in previous simulation studies.

Drug	Concentration (study)	Ionic current IC_{50} (nH)								
		I_{Na}	I_{to}	I_{CaL}	I_{Kur}	I_{Kr}	I_{Ks}	I_{K1}	I_{NCX}	I_{NaK}
Amiodarone	**2.33 μM** (Loewe *et al.*, 2014)	4.84 (0.76)	–	5.80 (1.0)	–	2.8 (0.91)	3.84 (0.63)	–	3.3 (1.0)	15.6 (1.0)
	10.0 μM (Sutanto *et al.*, 2019)	5 (1.0)	3.8 (0.4)	1.5 (0.6)	–	3.0 (1.0)	100 (1.0)	–	3.4 (1.0)	–
	1.55 μM (Bai, Lu and Zhang, 2020)	4.84 (0.76)	4.90 (1.0)	0.4 – 5.8 (1.0)	132.86 (1.0)	10 (1.0)	3.84 (0.63)	–	3.6 (1.0)	15.6 (1.0)
Dronedarone	**0.205 μM** (Loewe *et al.*, 2014)	0.54 (2.03)	–	0.83 (2.75)	1.0 (1.0)	0.0591 (0.8)	5.6 (0.51)	–	–	–
	10.0 μM (Sutanto *et al.*, 2019)	1 (1.7)	–	4 (1.0)	–	2 (1.0)	10 (1.0)	–	–	–
Flecainide	**3.0 μM** (Sutanto *et al.*, 2019)	6.5 (1.0)	10.0 (0.8)	27.1 (1.0)	2.9 (1.0)	1.6 (1.0)	–	–	–	–
	2.0 μM (Bai *et al.*, 2020)	84 (1.0)	–	–	–	1.5 (1.0)	–	–	–	–
Propafenone	**1.5 μM** (Sutanto *et al.*, 2019)	2.5 (1.0)	7.2 (1.0)	1.55 (1.0)	–	0.44 (1.0)	16 (1.0)	–	–	–
	0.2–0.8 μM (Bai *et al.*, 2021)	1.2 (1.0)	4.8 (1.0)	1.7 (1.0)	4.4 (1.0)	2.0 (1.0)	–	16.8 (1.0)	–	–
Ranolazine	**10.0 μM** (Sutanto *et al.*, 2019)	200 (1.0)	–	250 (1.0)	–	12 (1.0)	100 (1.0)	–	91 (1.0)	–
Vernakalant	**30 μM** (Sutanto *et al.*, 2019)	90 (1.0)	15 (1.0)	84 (1.0)	15 (1.0)	20 (1.0)	–	–	–	–
	30 μM (Loewe *et al.*, 2015)	15.07 (0.95)	30 (0.82)	84 (1.0)	13 (0.92)	21 (0.92)	–	–	–	–
Ibutilide	**0.01 μM** (Sutanto *et al.*, 2019)	–	–	–	–	0.02 (1.0)	–	–	–	–
Digoxin	**1.0 nM** (Bai, Lu and Zhang, 2020)	–	–	–	–	0.054 (1.0)	–	–	–	0.12 (1.0)

CHAPTER

IN-SILICO DRUG TRIALS FOR PRECISION MEDICINE IN STRUCTURALLY-HEALTHY ATRIA

6

In this chapter, I present the first in-silico trial conducted in this thesis. The study assessed pharmacological treatment in virtual patients with structurally-healthy atria, and the original work can be found in: "Dasí et al., (2022), Front. Physiol. DOI: 10.3389/fphys.2022.966046".

6.1. Summary of the study

As mentioned in **section 2.3.1**, patients present different clinical responses to drugs. Pharmacological agents target specific ion channels and, since humans present inter-subject variability in channel density, different subjects are expected to respond differently to the same drug. Thus, this study assessed whether the ionic current profile of the atria modulates the response to pharmacological treatment.

To test this hypothesis, 477 AF episodes were induced in a population of 75 virtual patients with structurally-healthy atria and varying ionic current properties. AF was facilitated by steep APD restitution (which elicited APD alternans) and high excitability (which enabled the fast pacing transforming alternans into discordant). Forty-nine virtual patients developed sustained AF (211 AF episodes), and were subjected to in-silico trials with 10 drugs. The results of the in-silico trials reproduced the outcome of previous clinical trials, and identified optimal drug treatments for individual electrophysiological properties of the atria. Thus, decision algorithms trained on the 211 simulated AF episodes exhibited >70% accuracy for predicting successful pharmacological treatment using ionic current profiles and ECG metrics.

6.2. Introduction

As mentioned in **section 1.1**, in-silico trials with human modelling and simulation represent an effective means for studying drug safety and efficacy (Passini *et al.*, 2016; Margara *et al.*, 2022). They offer the possibility of identifying key modulators of successful treatment and guide tailored AF therapies. This

is especially relevant in complex AF scenarios, where the source of the arrhythmia is difficult to identify (e.g., in structurally-healthy atria).

As described in **section 2.2.1.1**, many regulatory systems can transiently modify the electrical substrate (Heijman, Linz and Schotten, 2021) and facilitate AF in structurally-healthy atria. For instance, steep electrical restitution near the pulmonary veins has proven to facilitate AF in human patients (Narayan *et al.*, 2008). Steep restitution has been widely associated with elevated I_{CaL} (Gong *et al.*, 2007). However, other ionic current properties, mechanisms or channel dysregulations, resulting from imbalanced regulatory systems (Heijman, Linz and Schotten, 2021) or natural inter-subject variability in ionic densities (Muszkiewicz *et al.*, 2018), may also engage with restitution and facilitate AF in patients with structurally-healthy atria. The mechanisms are however unknown.

Early detection of AF in patients with structurally-healthy atria is crucial, given their higher eligibility for pharmacological treatment (Hindricks *et al.*, 2021). Indeed, absence of structural heart disease is an independent predictor of successful cardioversion to normal sinus rhythm (Boriani *et al.*, 2004). Yet, the success rate of pharmacological treatment is currently suboptimal (Heijman, Linz and Schotten, 2021), and little is known about how inter-subject variability in channel densities (Muszkiewicz *et al.*, 2018) determines the response of individual AF patients to antiarrhythmic drugs (Capucci *et al.*, 2018).

Therefore, the aim of this study was to exploit human-based multiscale modelling and simulation to (1) identify the ionic current profiles that favour AF inducibility in structurally-healthy atria, (2) understand their relationship with pharmacological cardioversion, and (3) quantify the prognostic significance of ionic current densities versus ECG metrics for identifying successful therapies.

6.3. Methods

6.3.1. Population of virtual AF patients

A population of cardiomyocyte models was developed as described in **section 4.1.2**. Key conductances and permeabilities of the CRN model were sampled up to ±70%. Experimental calibration was subsequently applied, using action potential characteristics obtained from human subjects in sinus rhythm (dataset available in (Sánchez *et al.*, 2014)). No AF remodelling was applied to the calibrated population of atrial cardiomyocyte models.

The APD restitution curves of the experimentally-calibrated population were computed by both standard S1S2 and dynamic restitution protocols. The standard S1S2 protocol consisted of a train of S1 stimuli applied at a fixed cycle length, followed by a single extra-stimulus with coupling interval S2. For the dynamic restitution protocol, the train was applied until steady-state at constant S1, for decreasing cycle lengths. Conduction velocity restitution was measured for models yielding APD restitution steeper than unity for both APD protocols (a detailed explanation is provided in **section II.1.1** of **Annex II**).

Ninety-seven atrial cardiomyocyte models presented steep APD restitution and conduction velocity restitution, and were used to populate two whole-atria models, one with homogeneous and one with heterogeneous ionic current properties. The population of 97 homogeneous whole-atria models was constructed by assigning one cardiomyocyte model to all atrial regions. The population of 97 heterogeneous models was constructed considering the regional heterogeneities detailed in **section 4.2.1**. A baseline conduction velocity of 60 cm/s was set in the bulk tissue (Sanchez et al., 2017).

AF was induced in virtual atria by burst pacing. Five periodic stimuli were applied at 10 different cycle length, ranging from 170 to 260 ms ((Haïssaguerre *et al.*, 1998); mean CL of focal discharges 175±30 ms) with 10 ms increment. AF episodes longer than 3 seconds were considered sustained, and recorded through a simulated 8-lead (leads I, II, V1-V6) ECG.

6.3.2. In-silico trials

Sustained AF episodes (> 3 s) were subjected to the virtual administration of 10 pharmacological treatments: five drugs currently approved for restoring sinus rhythm (i.e., flecainide, propafenone, vernakalant, amiodarone, and ibutilide; (Hindricks *et al.*, 2021)), dronedarone, ranolazine and digoxin. Two additional treatments considered single I_{NaK} and I_{K1} inhibition, respectively.

Drug action was simulated as simple pore-block models (described in **section 5.2.1**). **Table 6.1** collects the ionic current blockade of each treatment. Drug administration was modelled 3 s from AF induction (Sánchez *et al.*, 2017), and the episode was recorded for another 4 s. AF was considered successfully cardioverted by the drug if the atria were free of arrhythmic activity before the completion of the 7 s. Drug efficacy was defined as the percentage of AF episodes cardioverted by a given drug. Moreover, to evaluate whether pharmacological AF prevention and cardioversion followed the same restitution mechanisms, the AF-induction protocol was repeated in sinus rhythm after drug application. For this, only the two drugs that steepened/flattened the APD restitution curve the most were considered.

Table 6.1. Ionic current block (%) exerted by the antiarrhythmic drugs modelled in this study.

Drug	**Dose**	**Ionic current block (%)**								
		I_{Kur}	**I_{Kr}**	**I_{to}**	**I_{K1}**	**I_{Ks}**	**I_{CaL}**	**I_{NaK}**	**I_{NCX}**	**I_{Na}**
Amiodarone	2.000 µM	-	40	44	-	2	54	-	37	29
Dronedarone	0.205 µM	17	73	-	-	16	2	-	-	12
Flecainide	2.500 µM	46	61	25	-	-	8	-	-	28
Propafenone	0.800 µM	-	65	10	-	5	34	-	-	24
Ranolazine	10.000 µM	-	45	-	-	9	4	-	10	5
Vernakalant	10.000 µM	40	33	40	-	-	11	-	-	10
Ibutilide	0.015 µM	-	45	-	-	-	-	-	-	-
Digoxin	0.040 µM	-	43	-	-	-	-	25	-	-
Single I_{NaK} block	-	-	-	-	-	-	-	25	-	-
Single I_{K1} block	-	-	-	-	30	-	-	-	-	-

Section II.2.2 (Annex II) provides further validation of simulated drug effects against in-vitro experiments. The comparison of the rate-dependence alterations in APD, conduction velocity, and maximum upstroke show corresponding results between simulated drug action and experimental data. A further comparison of APD variation after drug action between the CRN, Grandi-Bers and Maleckar-Trayanova models can be also found in **section II.2.2**. The latter models showed a higher sensitivity to I_{Kur} inhibition than the CRN model, which presented a greater APD prolongation after I_{Kr} block.

6.3.3. Clinical decision support system

An algorithm for predicting the likelihood of pharmacological cardioversion (equivalent to a clinical decision support system) was built using ECG metrics and ionic current properties as inputs. Every antiarrhythmic drug was described by a dataset comprising the information of the AF episodes and the outcome of drug application. The AF episode was characterised by M=55 features, including 15 derived from the electrophysiological properties of the atria (i.e., baseline conduction velocity, APD, resting membrane potential, and 12 ionic current densities) and 40 from the ECG analysis (i.e., the 5 biomarkers presented in **section 4.4.2**, obtained from each lead, 8-lead ECG). The outcome of drug application was labelled either as 1, if AF was successfully cardioverted by the drug, or 0, otherwise.

Clinical decision support systems were built by elastic-net logistic regression (Zeemering *et al.*, 2018), using the Glmnet toolbox (available at http://hastie.su.domains/glmnet_matlab/). This machine learning tool was selected for enabling simultaneous regularisation and feature selection, which is especially useful for datasets with many correlated features (e.g., eight dominant frequency values, one per lead, for the same ECG). Most importantly, elastic-net logistic regression enhances interpretability, since it selects dominant parameters, with high predictive values, while diminishing less important ones (Zeemering *et al.*, 2018). Parameter selection was done by stepwise logistic regression with $\alpha = 0.05$ and 100 values for λ. The performance of the predictive models was validated through 5-fold cross-validation, repeated 20 times, randomly allocating 70-30% of data for training and testing, respectively.

6.4. Results

6.4.1. Evaluation of human atrial cardiomyocyte action potential models shows that steep restitution is associated with long plateau and high cellular excitability

From the calibrated population, 451 cardiomyocyte models showed steep APD restitution for both restitution protocols, and 97 additionally presented steep conduction velocity restitution. **Figure 6.1** illustrates the action potential (**Figure 6.1A**), representative APD and conduction velocity restitution curves (**Figure 6.1B-E**) and the ionic current distribution (**Figure 6.1F**) of the subpopulations considered for analysis. **Figure 6.1G** shows the generation of the population of whole-atria models, using one cardiomyocyte model to develop two whole-atria models: one with homogeneous and one with heterogeneous ionic current properties.

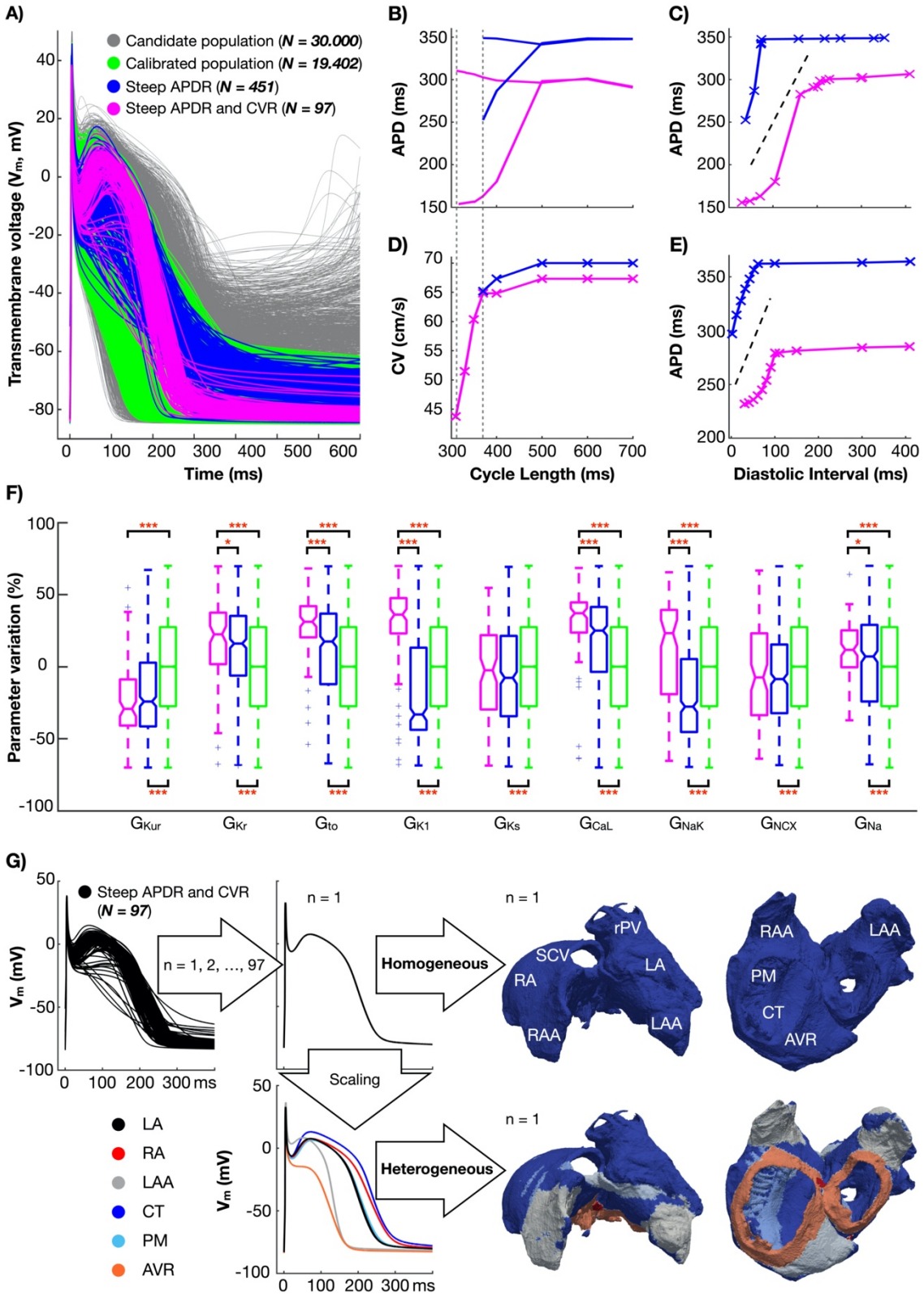


Figure 6.1. A) Simulated action potential traces for human atrial cardiomyocyte models in the population before (grey) and after (green) experimental calibration. **B-E**. Comparison of the electrical restitution between a representative cardiomyocyte model characterised by steep action potential duration restitution (APDR) alone (blue) and additional steep conduction velocity restitution (CVR, pink). **B)** Dynamic APDR plotted against the cycle length, showing transient alternation, and **C)** against the diastolic interval. **D)** CVR. **E)** Standard S1S2 APDR. **F)** Ionic density distribution (colour-code as per panel A). Data analysed using Wilcoxon test. * P<0.05, **P<0.01, *** P<0.001.

Steep APD restitution occurred for longer plateau phases (triangulation: (APD_{90}–APD_{50}) of 72.6±18.1 vs. 126.9±61.3 ms, steep vs. flat APD restitution). Models additionally yielding steep conduction velocity restitution had a more negative resting membrane potential (-82.4±1.7 vs. -74.5±3.3 mV; steep vs. flat conduction velocity restitution) (**Figure 6.1A**, pink versus blue traces). The more negative resting membrane potential allowed propagation for shorter cycle lengths (307±15 vs. 538±152 ms; steep vs. flat conduction velocity restitution), increasing the magnitude of APD alternans (**Figure 6.1B**) and favouring a greater modulation of the conduction velocity (**Figure 6.1D**).

Steep APD restitution alone was found in models with significantly high I_{CaL} and low I_{Kur} compared to flat restitution (**Figure 6.1F**, blue vs. green boxes). Models with steep APD and conduction velocity restitution (**Figure 6.1F**, pink boxes) were associated with even greater I_{CaL}, elevated I_{Na}, and high I_{NaK}, I_{K1}, I_{Kr} and I_{to} density. The 97 atrial cardiomyocyte models exhibiting steep APD and conduction velocity restitution were used to develop whole-atria models (**Figure 6.1G**).

6.4.2. AF is facilitated by discordant APD alternans, enabled by propagation at fast rates due to high excitability

The 97 whole-atria models were subjected to burst stimulation with 10 different cycle lengths. Seventy-five out of the 97 whole-atria models were prone to AF inducibility, resulting in 212 and 265 AF episodes when considering the homogeneous and heterogenous ionic current setting, respectively. More AF episodes were induced with the heterogeneous ionic substrate, but the same 22 whole-atria models (i.e., 22 ionic current profiles) failed to induce AF for both homogeneous and heterogeneous properties.

Figure 6.2 illustrates a representative virtual AF patient, showing multiple rotors in the atria (**Figure 6.2A**, left), the time-course of the transmembrane voltage (**Figure 6.2A**, right), and similarities between the simulated and a clinical ECG (atrial activity, **Figure 6.2B-C**, respectively).

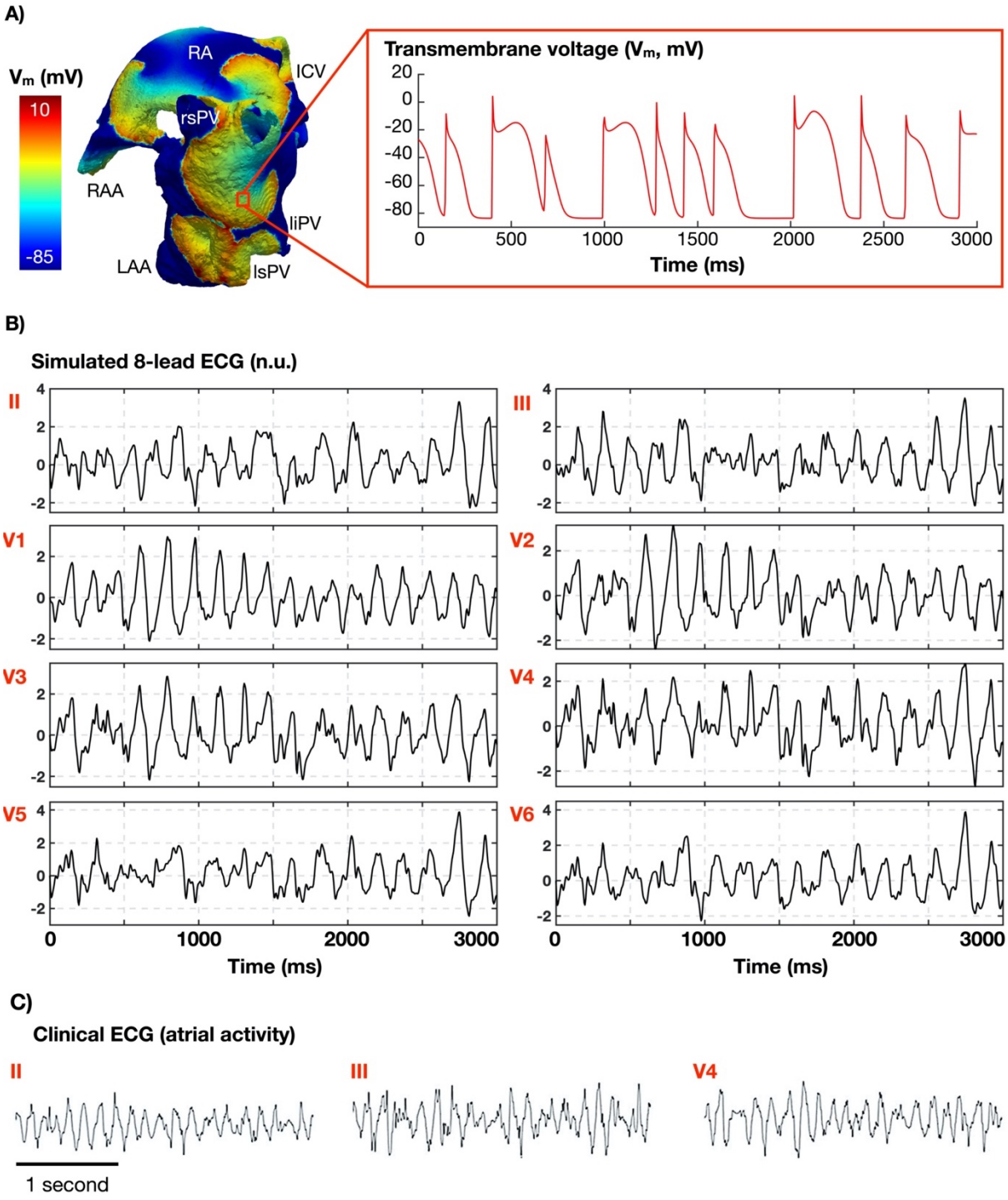


Figure 6.2. Representative AF episode. **A)** Simulated AF in the whole atria model (left), and time course of the transmembrane voltage (V_m) in one cell (right). **B)** Simulated atrial electrocardiogram (normalized ECG; no units). **C)** Clinical ECG obtained in AF patient (adapted from Lankveld *et al.*, 2016 under permission).

Figure 6.3 illustrates a comparison of the ionic current densities (**Figure 6.3A**), effective refractory period (**Figure 6.3B**), and APD restitution curves (**Figure 6.3C**) between the 75 virtual AF patients and the 22 non-inducible whole-atria models. The dynamic restitution curves in **Figure 6.3C** are plotted against the cycle length used for burst pacing (170-260 ms), and show the magnitude of APD alternans.

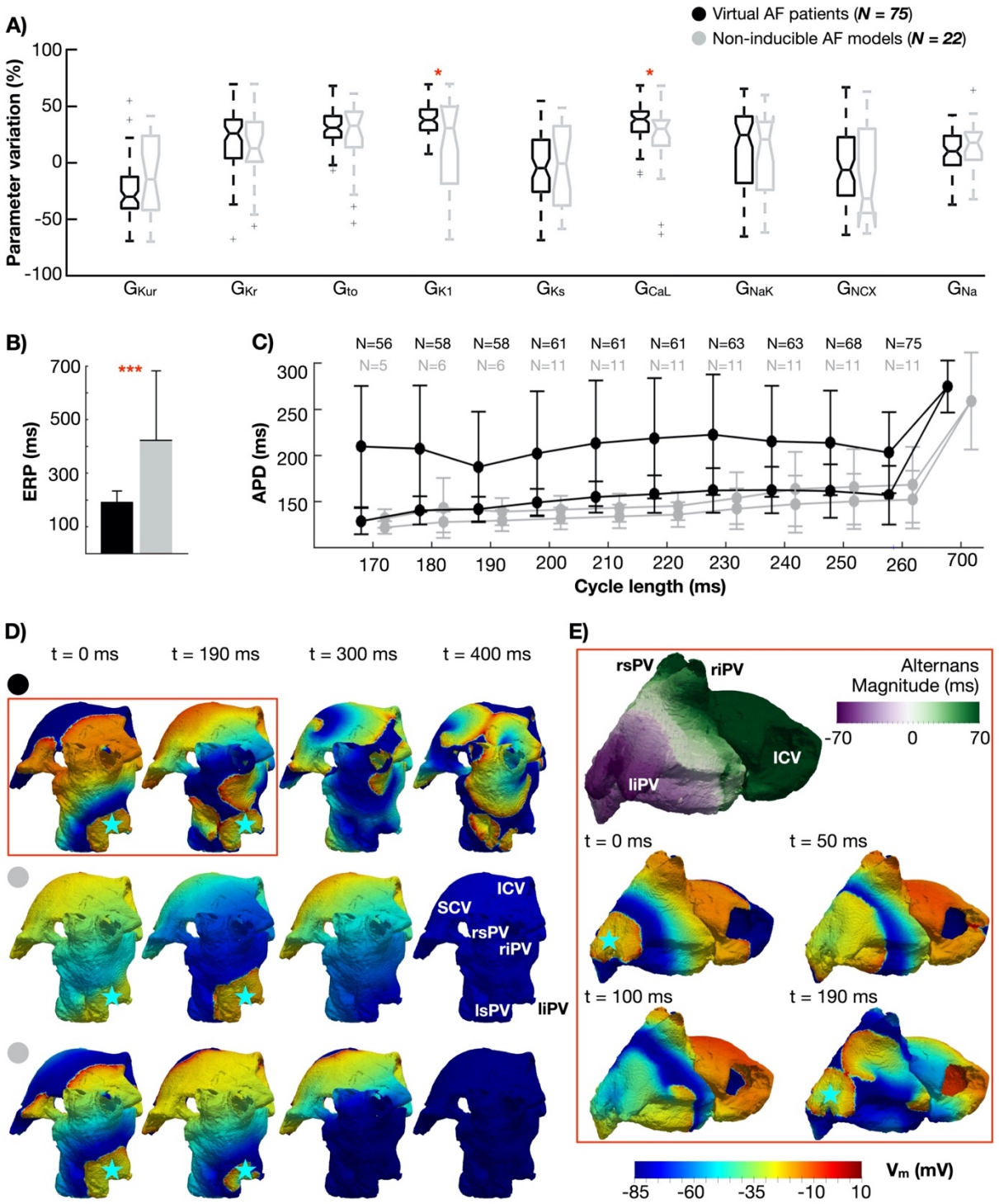


Figure 6.3. Ionic properties of virtual AF patients (in black) and non-inducible whole-atria models (in grey): **A)** Ionic density distributions. **B)** Effective refractory period (ERP). **C)** Dynamic APD restitution curves plotted against the cycle length used for burst pacing (170–260 ms). Two consecutive beats are considered (i.e., long and short APD), showing magnitude of APD alternans. Number (N) of models able to propagate all stimuli. **D)** Comparison of propagation dynamics between a virtual AF patient (top), and two non-inducible models: one showing a 1:2 conduction pattern (middle row), the other propagating all stimuli without AF induction (bottom row). Burst stimulus applied at a cycle length of 190 ms. The blue star represents the location of the burst. **E)** Discordant alternans favouring conduction block and re-entry. The snapshots in E) are an expansion of the red box in D). Abbreviations. S-ICV: superior and inferior cava vein; rs-ri-ls-li-PV: right superior, right inferior, left superior and left inferior pulmonary vein. Data are expressed as medians and IQR and analysed using Wilcoxon Test. *P<0.05, **P<0.01. ***P<0.001.

A higher AF inducibility was observed for ionic profiles presenting high I_{CaL}, which increased APD alternans, and I_{K1}, which conferred high cellular excitability (**Figure 6.3A-C**). Indeed, all virtual AF patients exhibited propagation at 260 ms, while this only occurred in 11 (50%) whole-atria models free of arrhythmia (**Figure 6.3C**). Moreover, 56 (75%) AF-inducible and 5 (23%) non-inducible models enabled propagation at 170 ms (i.e., shortest cycle length tested for the burst).

Figure 6.3D compares the response to burst stimulation between one virtual AF patient (top row) and two non-inducible models (one of them belonging to the 11 models that failed to propagate burst stimulation at 260 ms (middle row), the other belonging to the 5 models that propagated at 170 ms without inducing AF (bottom row)). Whole-atria models unable to propagate all stimuli in the burst exhibited a 1:2 conduction pattern (i.e., propagation of one every two stimuli). This conduction pattern prevented the engagement of restitution properties and thus, fibrillation (**Figure 6.3D, middle row**).

However, even when all burst stimuli propagated, some whole-atria models were resistant to AF (**Figure 6.3D, bottom row**). Analysis of their associated APD restitution curves revealed that virtual AF patients presented greater magnitude of APD alternans (67.3±92.5 vs. 8.9±6.6 ms, AF-inducible vs. non-inducible models; **Figure 6.3C**). The latter developed into discordant alternans following rapid burst stimulation, causing unidirectional block and re-entry at different sites of the left atrium (**Figure 6.3E**). An extended explanation of discordant alternans formation after burst pacing is provided in **section II.2.1** (Annex II). Discordant alternans were not observed in whole-atria models free of AF.

Restoring the baseline I_{CaL} density in virtual AF patients (i.e., reducing I_{CaL} to its original value) recapitulated the magnitude of APD alternans observed in non-inducible models (67.3±92.5 vs. 8.3±6.0 ms, virtual AF patients with elevated vs. control I_{CaL} density). Similarly, the magnitude of alternans was reduced after decreasing I_{K1} density (67.3±92.5 vs. 18.2±12.1; virtual AF patients with increased vs. control I_{K1}). This owed to a reduction of whole-atria models propagating at short cycle lengths.

6.4.3. Analysis of 477 AF episodes reveals AF sustainability supported by high excitability, with enhanced up-regulation of I_{K1} and elevated I_{NaK}

AF sustainability was evaluated in the 75 virtual AF patients with homogeneous and heterogeneous ionic current properties. Overall, 211 episodes sustained AF (> 3 s) were obtained in 49 virtual AF patients. The heterogeneous ionic current substrate favoured AF maintenance: 154 (58%) and 57 (27%) AF episodes were sustained in the heterogeneous and homogeneous substrate, respectively.

Figure 6.4 shows the ionic density distribution (**Figure 6.4A**), refractory period (**Figure 6.4B**), APD restitution curves (**Figure 6.4C**), and I_{Na} dynamics (**Figure 6.4D**) of the 49 and 26 virtual AF patients with sustained and unsustained AF, respectively.

Higher I_{NaK} and I_{K1}, and lower I_{Na} were associated with sustained AF. Analysis of Na^+ inactivation gates revealed that, in spite of a lower I_{Na} density, Na^+ availability was higher in the sustained AF group

(**Figure 6.4D, right**). This was accentuated as the pacing rate increased: the maximum Na^+ current peak, which was greater in the unsustained AF group for lower rates, became higher in models yielding sustained AF when stimulated at short cycle lengths (**Figure 6.4D, left**). This was due to the higher I_{NaK} and I_{K1}, which led to a more negative resting membrane potential (-82.6±0.7 vs. -81.5±0.6 mV, sustained and unsustained AF, respectively). Accordingly, these atrial cardiomyocyte models had higher cellular excitability (and shorter effective refractory period, **Figure 6.4B**).

At slow rates (700 ms), a lower conduction velocity was found in whole-atria models leading to sustained AF (60.3±5.7 vs. 62.5±4.5 cm/s), as a result of lower I_{Na}. At fast rates (260ms), the opposite trend was observed (56.4±9.8 vs. 50.7±5.7 cm/s; sustained vs. unsustained AF). The magnitude of APD alternans was similar across groups.

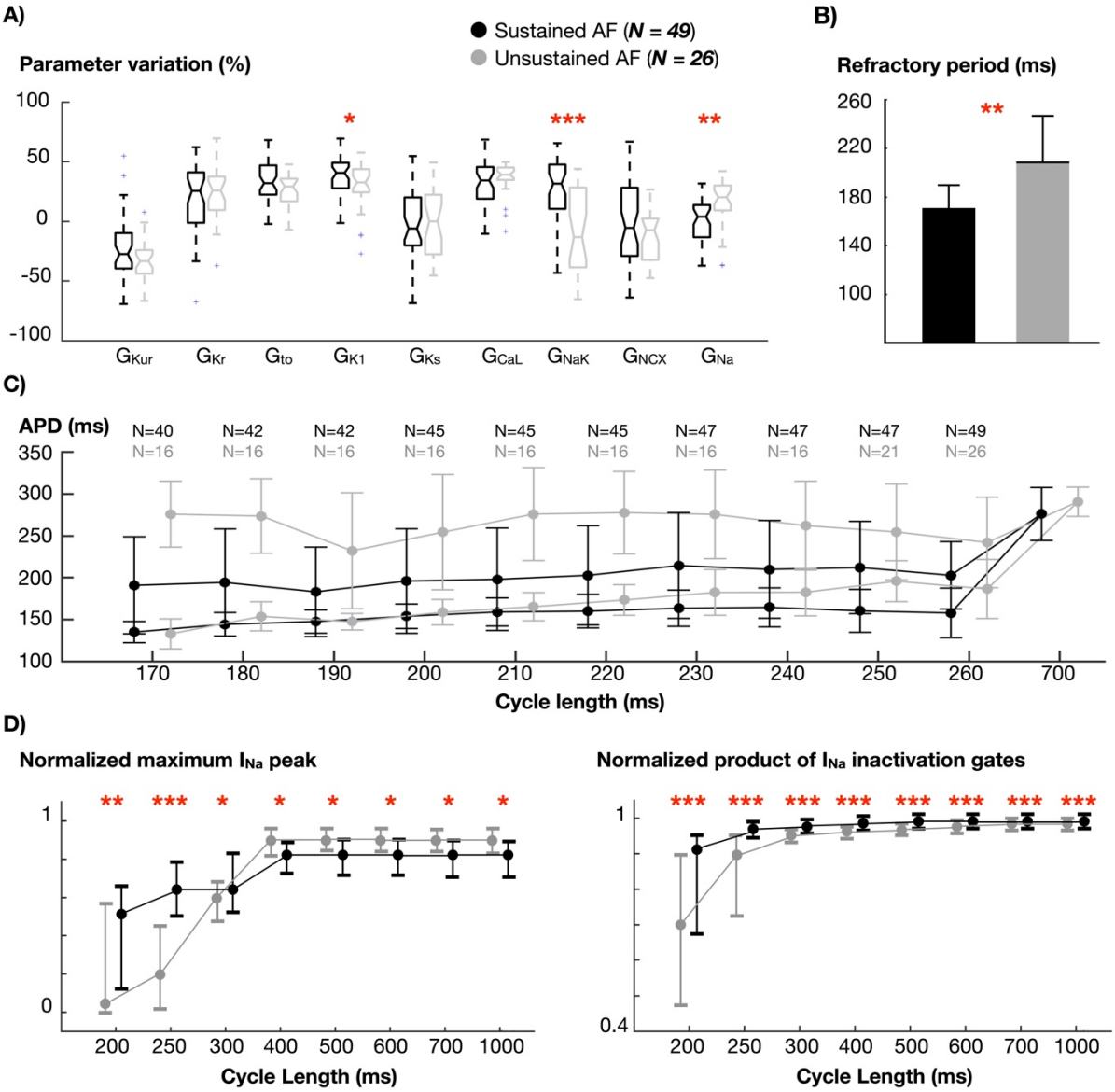


Figure 6.4. Comparison between virtual patients with sustained and unsustained AF. **A)** Ionic current density distribution (%). **B)** Effective refractory period (ERP). **C)** Dynamic APD restitution (as in Figure 5.3C). Number (N) of models able to propagate all stimuli. **D)** Normalized I_{Na} peak and product of I_{Na} inactivation gates. Data are expressed as medians and IQR and analysed using Wilcoxon Test. *P<0.05, **P<0.01, *** P<0.001.

6.4.4. In-silico drug trials in over 200 AF episodes consistently reproduce cardioversion efficacy observed in clinical trials and identify key properties determining treatment success

In-silico drug trials with 10 compounds were attempted in the 211 sustained AF episodes induced in both populations of virtual AF patients (homogeneous, 58 episodes; heterogeneous, 153 episodes). **Figure 6.5A** compares the efficacy of each treatment in-silico (colour bars) and in human clinical trials (black bars). Antiarrhythmic drugs are displayed according to their preferential ionic channel target.

Higher cardioversion efficacy derived from class III (i.e., dronedarone and vernakalant) and class V (i.e., digoxin) antiarrhythmic drugs. Drugs resulting in I_{Kr} inhibition (i.e, ranolazine, ibutilide, and dronedarone) showed an increase in cardioversion efficacy proportional to the extent of I_{Kr} block. However, higher success rates resulted from blocking multiple K^+ channels, even for lower percentages of I_{Kr} inhibition. For instance, a 25% I_{NaK} and 40% I_{Kr} block (i.e., digoxin) was more effective than 45% I_{Kr} (i.e., ibutilide, efficacy in-silico matching clinical trials) or 70% I_{Kr} block (i.e., dronedarone).

The high efficacy of digoxin, in agreement with some clinical trials, owed to I_{NaK} inhibition. Blocking I_{NaK} or I_{K1} alone raised the resting membrane potential and decreased I_{Na} availability. The subsequent prolongation of post-repolarization refractoriness was sufficient to terminate AF. Indeed, single I_{K1} block and digoxin were the pharmacological approaches that provided the highest cardioversion rates.

Combined I_{Kr} and I_{Kur} block (i.e., flecainide and vernakalant, whose cardioversion efficacies matched clinical trials) was also more effective than I_{Kr} inhibition alone, especially in the population with heterogeneous ionic current properties. In general, the heterogeneous substrate hampered pharmacological cardioversion, since antiarrhythmic drugs had an inhomogeneous effect on different atrial regions. In particular, the heterogeneous ionic substrate was characterised by a lower I_{Kr} in the right atrium compared to the left atrium (**Table 4.1**, **Chapter 4**), so that I_{Kr} inhibition lost cardioversion efficacy in this setting. Thus, the efficacy of dronedarone, but not of vernakalant, dropped significantly in the heterogeneous ionic substrate.

Low cardioversion rates stemmed from targeting inward currents. I_{Na} block was effective when complemented with I_{Kur} and I_{Kr} inhibition (i.e., flecainide and vernakalant). However, combined I_{Na} and I_{CaL} block (i.e., amiodarone and propafenone) shortened the APD, yielding the formation of local and stable re-entries (**Figure II.3** in **Annex II**). The cardioversion efficacy decreased proportionally to I_{CaL} block, with acute amiodarone (i.e., 50% I_{CaL}) showing the lowest cardioversion rate. The efficacy of amiodarone and propafenone differed from the efficacy reported in clinical trials (see Discussion).

Nevertheless, amiodarone-induced APD shortening significantly flattened the APD restitution curved (**Figure II.3**). Thus, investigations on AF prevention instead of cardioversion showed that amiodarone prevented 100% of recurrent AF episodes, with only atrial flutter (i.e., regular and periodic activation)

remaining in 2% of cases. In contrast, dronedarone prolonged the APD, steepening the APD restitution. Therefore, while effective in preventing AF induced at very short cycle lengths (i.e., 170-200 ms), 49% of AF episodes were still inducible in dronedarone pre-treated substrates.

6.4.5. Optimal pharmacological treatments for individual ionic profiles are those that maximize prolonged refractoriness thus minimizing excitability

To assess optimal pharmacological treatment according to the ionic current substrate of the atria, a sub-analysis considered those AF episodes only cardioverted by a single antiarrhythmic drug. Thus, from the 211 AF episodes sustained in 49 virtual AF patients, 49 AF episodes, sustained by 40 virtual patients, were successfully cardioverted only by a single drug.

Eleven episodes sustained in 9 virtual AF patients were only cardioverted by dronedarone; 14 episodes in 13 virtual patients by flecainide, and 24 episodes in 18 virtual patients by vernakalant. **Figure 6.5B** and **Figure 6.5C** illustrate the ionic density distribution of virtual patients responding favourably only to dronedarone, flecainide, or vernakalant, and how the refractory period of these models, grouped according to successful treatment, was modified after applying each drug.

Virtual patients showing a favourable response to dronedarone (N=9) also presented a greater prolongation of refractoriness after dronedarone application. Similarly, flecainide prolonged the refractory period more than dronedarone or vernakalant in virtual patients cardioverted by flecainide (N=13), and the same applied for vernakalant (**Figure 6.5B**).

Analysis of the ionic current profiles revealed that virtual patients with a successful response to vernakalant had high I_{Kur} and low I_{Kr}. This agrees with vernakalant action, with the strongest I_{Kur} inhibitory profile within the tested drugs. By contrast, dronedarone cardioverted AF in virtual patients presenting the opposite situation: higher I_{Kr} and lower I_{Kur}. Flecainide resulted more effective for an intermediate scenario, since it blocked I_{Kur} and I_{Kr}, but to a lesser extent than vernakalant and dronedarone, respectively (**Figure 6.5C**).

Virtual patients with high I_{K1} and I_{NaK}, and therefore high excitability, responded better to vernakalant and flecainide than to dronedarone. While none of them blocked these ionic currents, vernakalant and flecainide yielded a greater inward current block, and thus, a greater post-repolarization refractoriness.

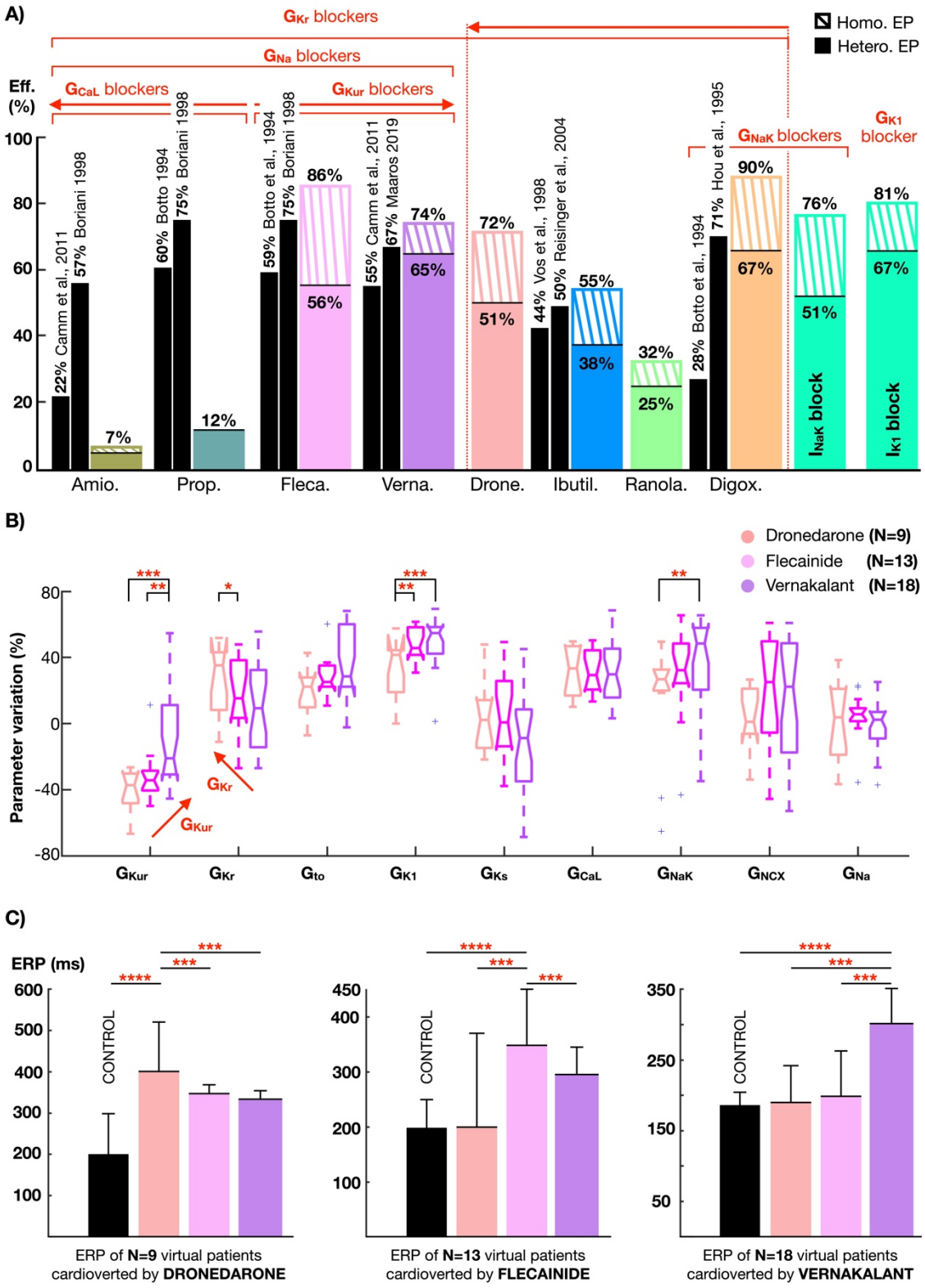


Figure 6.5. A) Comparison between the cardioversion efficacy (Eff.) obtained in-silico (colour bars) in whole-atria models with homogeneous (Homo.) and heterogeneous (Hete.) electrophysiology (EP) and human clinical trials (black bars). Drugs are grouped according to the ionic channels they target. A threshold of 25% block at therapeutic plasma concentration has been considered to denote ion current block. The arrows point towards greater ionic density block. **B)** Comparison of the ionic density distribution of virtual AF patients showing a favourable response only with dronedarone, flecainide or vernakalant. **C)** Effect of the three antiarrhythmic drugs on the effective refractory period (ERP), stratifying virtual patients according to the pharmacological treatment that produced successful cardioversion. Data are expressed as medians and IQR and analysed using Wilcoxon Test. *P<0.1, **P<0.05, ***P<0.01. ****P<0.001.

6.4.6. Accuracy of prediction of AF cardioversion with specific treatments is 70% using both ECG metrics and ionic current profiles.

Clinical decision support systems were built based on the information of virtual AF patients (i.e., ionic current properties) and the ECG metrics obtained during AF. **Figure 6.6** and **Table 6.2** show the prediction accuracy and receiver operating characteristics (ROC) curves of successful cardioversion for the drugs illustrated in **Figure 6.5B-C**.

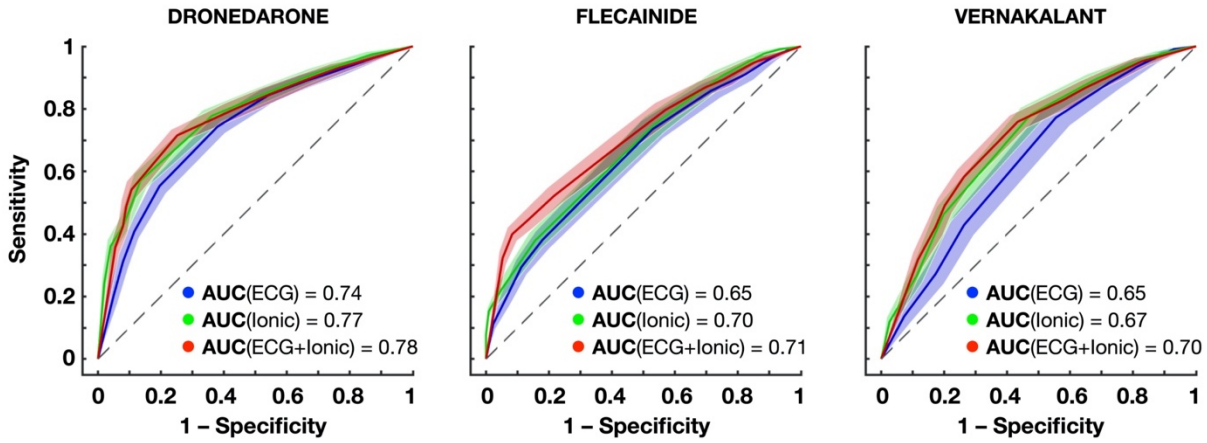


Figure 6.6. Receiver operating characteristics (ROC) curves for the prediction of successful cardioversion with dronedarone, flecainide and vernakalant using the ECG, ionic properties and both. The confidence interval around each ROC is obtained repeating 5-fold cross-validation 20 times. Abbreviations: **AUC:** Areas under the curve.

Table 6.2. Prediction accuracy (mean and confidence interval). Most relevant features selected by the elastic-net logistic regression. Abbreviations: DF: dominant frequency; SaE: sample entropy. RHE: relative harmonic energy.

Drug	Data	Best predictive biomarkers	Accuracy (%)
Dronedarone	ECG	DF (Leads V2–V6), SaE (Leads V2, V6)	**0.72** [0.70, 0.74]
	Ionic properties	G_{K1}, G_{Kur}, G_{NaK}, G_{Na}, G_{Kr}, G_{CaL}	**0.76** [0.74, 0.78]
	Both	CV, DF (Leads V2, V4)	**0.77** [0.75, 0.79]
Flecainide	ECG	SaE (Lead V1), RHE (Lead III), SaE (Lead III)	**0.69** [0.67, 0.71]
	Ionic properties	G_{NaK}, G_{K1}, G_{Ks}, G_{to}	**0.71** [0.69, 0.73]
	Both	G_{to}, G_{K1}, G_{NaK}, G_{Ks}, SaE (Lead V1)	**0.72** [0.70, 0.74]
Vernakalant	ECG	RHE (Lead V4, V5), SaE (V6)	**0.68** [0.66, 0.70]
	Ionic properties	G_{to}, G_{Kur}, G_{NaK}	**0.70** [0.68, 0.72]
	Both	G_{to}, G_{Kur}, SaE (Lead V6), RHE (Lead V4, V5)	**0.70** [0.68, 0.72]

Both the information of the ionic densities and the ECG biomarkers yielded high-accuracy predictions of successful AF cardioversion, with the former being slightly superior to the latter. Higher accuracies were obtained for dronedarone, due to a higher specificity (**Figure 6.6**). Dronedarone cardioverted around 50% of episodes, so that the dataset was more balanced (i.e., similar proportion of episodes cardioverted and not cardioverted). By contrast, the lowest specificity was obtained for vernakalant (70% cardioversion efficacy), with random oversampling slightly improving the prediction.

Three ionic densities were consistently selected as relevant features: G_{K1}, G_{Kur}, and G_{NaK}. As illustrated in **Figure 6.5C**, these ionic densities differed to a greater extent in virtual patients responding to flecainide, vernakalant or dronedarone, and thus, were revealing of the most favourable treatment. The dominant frequency, sample entropy and the relative harmonic energy were selected as relevant ECG metrics, suggesting that AF dynamics also had a crucial role on cardioversion efficacy.

When predicting dronedarone's cardioversion efficacy, the dominant frequency and sample entropy appeared as the most relevant ECG metrics (**Table 6.2, dronedarone–- first row**). Similarly, G_{K1}, G_{Kur}, G_{NaK}, G_{Na}, G_{Kr} and G_{CaL} were selected as the most informative ionic current densities (**Table 6.2, dronedarone–- second row**). Although at present there is no clear correlation between the two, we will see in **Chapter 8** (**Table 8.2**) that these ionic current densities are indeed related to both ECG metrics. **Table 8.2** evidences that low G_{CaL} and high G_{NaK} are associated with an elevation of the sample entropy, a measure of predictability and repetitiveness. Low G_{CaL} shortens tissue refractoriness and high G_{NaK} increases excitability. Both alterations promote the formation of localized re-entrant sources and thus, increase AF repetitiveness. Similarly, the ECG dominant frequency is mainly modulated by G_{K1}, with other ionic currents, such as G_{NaK}, G_{Na} and G_{CaL} having a secondary effect (**Table 8.2**). As discussed in detail below (and in posterior chapters), the relationship between ionic currents and ECG metrics consistently aroused throughout the thesis. For the present chapter, it helps to understand why no ionic current density was selected as a relevant feature for predicting dronedarone's cardioversion efficacy when all available features were used for the prediction (**Table 6.2, dronedarone–- third row**). The analysis conducted in posterior chapters reveals that the ionic densities were implicitly selected through the dominant frequency and conduction velocity, since the dominant frequency is mainly influenced by G_{K1}, G_{NaK}, G_{Na}, and G_{CaL}, and G_{Na}.

6.5. Discussion

Key features underlying AF inducibility, maintenance and pharmacological cardioversion were identified in a population of structurally-healthy atria with varying ionic current properties. In-silico trials with 10 antiarrhythmic treatments were consistent with clinical trials, and identified mechanisms and predictors of successful cardioversion. Specific findings are: (i) AF inducibility in structurally-healthy atria might be explained by discordant APD alternans resulting from steep electrical restitution and high excitability (occurring for elevated I_{CaL} and I_{K1}); (ii) AF maintenance is also enabled by high excitability, for profiles with high I_{K1} and I_{NaK}; (iii) pharmacological cardioversion is optimal for treatments minimizing excitability, through maximal prolongation of refractoriness, which is dependent on individual ionic profiles; (iv) successful pharmacological cardioversion is predicted in virtual AF patients with >70% accuracy using both ionic current profiles or ECG metrics.

6.5.1. Precision medicine for AF management: In-silico drug trials

As discussed in **section 2.3.1**, rhythm control therapy for AF follows a "one-size fits all" approach. However, the response of individual patients to rhythm control therapy is highly variable, and predicting its success is still a challenge (Kany *et al.*, 2021). Previous studies demonstrated that analysing AF complexity through the ECG might help predicting the cardioversion efficacy (Zeemering *et al.*, 2018). Others proposed that pharmacogenetics would bring the best tailored approach (Capucci *et al.*, 2018). In this study, pharmacological cardioversion could be predicted with over 70% accuracy using either ionic or ECG metrics in virtual AF patients. This is important as it points towards the possibility of predicting the response of pharmacological treatment using both non-invasive markers and ionic current properties. Moreover, it highlights the integral part of multi-scale modelling and simulation for AF treatment personalization (Roney *et al.*, 2022).

In this in-silico trial, I_{K1} was identified as one of the most informative properties for predicting AF cardioversion. The importance of I_{K1} in regulating AF inducibility and maintenance has been proven by previous experimental and computational studies (Atienza *et al.*, 2006; Sánchez *et al.*, 2017). However, I_{K1} inhibition might have opposing effects on triggers and substrates. While effective in terminating fibrillatory activity, as shown in this study, blocking I_{K1} might promote triggered activity and focal excitations (Filgueiras-Rama *et al.*, 2012). In this sense, safe restoration of sinus rhythm resulted from I_{K1} inhibition in goats with persistent AF (Ji *et al.*, 2017). Moreover, as observed here, higher cardioversion efficacies resulted from applying chloroquine (I_{K1} blocker, among others) than flecainide in sheep models (Filgueiras-Rama *et al.*, 2012).

Flecainide cardioverted 56% of the simulated AF episodes, matching the efficacy observed in clinical trials with AF patients (Boriani *et al.*, 1998; Reisinger *et al.*, 2004). Compared to flecainide, a higher proportion of AF episodes (i.e., 65%) were terminated after the virtual application of vernakalant. Similarly, a retrospective study (Pohjantähti-Maaroos *et al.*, 2019) observed higher number of patients cardioverted to sinus rhythm with vernakalant than flecainide (67% vs. 46%, respectively).

In this study, amiodarone showed the lowest cardioversion efficacy. Nevertheless, cardioversion rates as high as 87% are observed after 24 hours from its administration (Bash *et al.*, 2012). Amiodarone inhibits multiple ionic channels, including I_{CaL} and I_{Na}. Blocking both channels reduces cellular excitability (Loewe *et al.*, 2014; Liberos *et al.*, 2016) and amiodarone-induced I_{Na} inhibition has been suggested as the main mechanism underlying rotor termination (Wilhelms *et al.*, 2013). In the present study, however, virtual AF patients presented increased I_{Na} and I_{CaL} compared to the baseline model. Consequently, the inward current block induced by amiodarone was not sufficient to reduce excitability and terminate AF. This is in agreement with previous simulations studies, which showed that the antiarrhythmic effects of I_{Na} and I_{CaL} block depended on their basal ionic densities (Liberos *et al.*, 2016). It has been also suggested that amiodarone metabolites, such as desethylamiodarone, which accumulates

after long-term therapy with amiodarone, might be the actual responsible for the increased atrial refractory period (Talajic, DeRoode and Nattel, 1987).

Furthermore, amiodarone-induced I_{CaL} inhibition flattened the APD restitution curve, reduced the frequency and amplitude of APD alternans and prevented AF inducibility in the structurally-healthy atria. Therefore, while ineffective for AF termination, amiodarone hindered the formation of dynamic substrates derived from steep electrical restitution.

6.5.2. Ionic current dysregulation and dynamic electrophysiological substrates in structurally-healthy atria

Steep electrical restitution was the mechanism adopted in this study to induce AF, as observed in human patients (Narayan *et al.*, 2008). Unlike previous simulation works that changed single ionic currents (Garfinkel *et al.*, 2000), steep electrical restitution in this study resulted from specific multivariate ionic density distributions. These distributions were obtained by scaling uniformly all ionic densities of the cellular model, which mimicked inter-patient variability in ionic densities. Moreover, accurate AF-initiation conditions were replicated in a detailed atrial geometry with realistic anisotropy ratios and conduction velocity, as opposed to using monolayers (Virag *et al.*, 2002) or isotropic conduction (Gong *et al.*, 2007).

As such, it was observed that increased I_{CaL}, I_{K1} and I_{NaK} characterised AF inducibility and maintenance in structurally-healthy atria. Previous simulation studies observed that increasing I_{CaL} steepens the APD restitution slope, potentially leading to wave break-up and fibrillation (Garfinkel *et al.*, 2000). In this study, however, steep restitution was only engaged for high I_{K1}, which conferred high cellular excitability.

Likewise, elevated I_{K1} facilitated AF maintenance. Increased inward rectifier K^+ current has been extensively associated with the AF-induced electrophysiological remodelling (Dobrev and Ravens, 2003), and proven essential for rotor stabilization (Pandit *et al.*, 2005). In this population of virtual patients, high I_{K1} was additionally required for AF inducibility. Other computational studies have also observed that in the absence of fibrosis, I_{K1} inhibition hindered AF initiation (Gharaviri *et al.*, 2021). A genetic analysis reported missense mutations in KCNJ2, encoding I_{K1} channels, in human patients with paroxysmal AF (Deo *et al.*, 2013). Therefore, as shown in this study, increased I_{K1} constitutes an AF predisposing condition that additionally favours AF perpetuation.

6.5.3. Limitations and future perspectives

Drug action was simulated as simple pore-block models as the data required were available for the compounds investigated. However, it is possible that this might have increased the model sensitivity to repolarization prolonging effects, explaining the grater efficacy of class III antiarrhythmic drugs compared to class Ic. Neglecting the rate dependence of class Ic agents and thus, potentially

underestimating I_{Na} inhibition, might explain the different results obtained for propafenone and flecainide. Similarly, increasing the resting membrane potential through I_{K1} inhibition, therefore hampering I_{Na} (in)activation, resulted more effective than direct I_{Na} block. This might reflect the importance of class Ic agents for binding with different affinities to the different Na^+ channel states.

Moreover, pharmacological treatment and the performance of the predictive model should be further investigated, considering not only electrophysiological but also anatomical and structural variability. Even the electrophysiological variability considered can be weighed as relatively small. The 97 models selected, which presented the ionic current properties required to induce AF in structurally-healthy atria, had similar morphologies (i.e., a rapid phase 3 repolarization and relatively hyperpolarized resting membrane potential). Therefore, a wider range of action potentials has to be considered in future studies.

Restricting the study to similar action potential morphologies could also explain why the accuracy of the clinical decision support system was not higher than 70%. A better stratification of the ionic current properties that respond to specific antiarrhythmic drugs would result from considering a wider ionic current distribution in the first place (i.e., wider range of action potential morphologies). The latter could improve the prediction accuracy and boost associated prediction metrics. In this sense, employing other machine learning algorithms might also add extra predictive power.

Most of these limitations are covered in the following chapters.

6.6. Conclusion

In structurally-healthy atria, AF inducibility and maintenance are enabled by steep restitution and high excitability, due to I_{CaL} and I_{K1} up-regulation. Accordingly, decreasing excitability through prolonged refractoriness, results in pharmacological cardioversion. Maximal prolongation of refractoriness depends on the interaction between the ionic current substrate of the atria and the ionic currents targeted by the antiarrhythmic drug, highlighting optimal pharmacological treatments for individual ionic current profiles. Therefore, successful cardioversion is predicted in virtual human atria with 70% accuracy from both ionic current and ECG properties.

The finding that similar accuracies are obtained with the ECG and ionic metrics for predicting successful AF cardioversion suggests that the ECG already contains information of the ionic current properties. This is further investigated in **Chapter 8** and **Annex III**. Before that, **Chapter 7** complements the in-silico trials in structurally-healthy atria presented in this chapter by covering another crucial aspect about optimal antiarrhythmic drug treatment: drug repurposing.

CHAPTER

IN-SILICO TRIALS FOR DRUG REPURPOSING

7

Drug repurposing consists of identifying new uses for drugs already approved. For example, local anaesthetics have proven to possess antiarrhythmic properties. This has immediate implications for cardiac research, since novel molecules can be synthesized, based on the chemical structure of local anaesthetics, to target specific ionic currents while preserving a safe drug profile.

In ***section 2.3.1*** *I have explained two strategies to increase the success rate of pharmacological treatment: to make a better use of existing drugs, or to develop new ones that block atrial-specific ion channels. In this sense,* ***Chapter 6*** *shows how the assessment of the atrial ionic current profile could be used to guide optimal pharmacological treatments, and thus, promote a better use of currently available drugs.*

In this chapter, I will focus on assessing the antiarrhythmic effects of a new pharmacological agent, Compound 6f, which targets atrial-specific ion channels. This study has been conducted in collaboration with Prof Wendy Gonzalez and Ursula Ravens, and a journal publication has been submitted: "Lorena Camargo-Ayala, Mauricio Bedoya, Albert Dasí et al., (2023)".

7.1. Summary of the study

Compound 6f is a new molecule, based on the structure of a local anaesthetic, that inhibits three ion channels: NaV1.5 (which mediates I_{Na}), KV1.5 (I_{Kur}), and TASK-1 (I_{K2P}). Accordingly, it constitutes an attractive pharmacological agent for rhythm control of AF. This study aims to investigate the efficacy of Compound 6f for both acute AF cardioversion and long-term AF prevention.

For this, 45 virtual AF patients with structurally-healthy atria and varying ionic current densities were virtually treated with three doses of Compound 6f (1, 10 and 100 μM). The drug exerted a dose-dependent prolongation of post-repolarization refractoriness (increase in the refractory period by 16.3±12.3 ms, 29.3±29.5 ms and 177.6±143.0, respectively, compared to control conditions). The increase in refractoriness caused a proportional increase in its prevention efficacy (0%, 20% and 72% prevention efficacy after 1, 10 and 100 μM, respectively). The high prevention rate at 100 μM owed to

a strong I_{Na} inhibition. Therefore, virtual patients with I_{Na} up-regulation were less likely to respond to Compound 6f (I_{Na} density: 6.2±2.5 vs. 9.5±1.9 mS/F; virtual responders vs. non-responders).

Overall, in-silico trials with Compound 6f show high success rates when applied at high concentrations, and identify I_{Na} density as critical for determining those patients more likely to benefit from the drug.

7.2. Introduction

Local anaesthetic compounds have been long used as antiarrhythmic agents, since they can inhibit ion channels preferentially expressed in the atria, such as the two-pore domain (K_{2P}) channel (TASK-1) and the potassium voltage-gated channel KV1.5. These families of K^+ channels mediate I_{K2P} and I_{Kur}, respectively. As explained in **section 2.3.1**, both ionic currents are attractive targets, and their inhibition might increase the efficacy of pharmacological treatment while reducing the number of cardiotoxic events. Since local anaesthetics might also inhibit voltage-dependent sodium channels (NaV1.5), the combined I_{Na}, I_{Kur} and I_{K2P} block represents a promising poly-pharmacological strategy for AF.

Thus, the aim of this study was to conduct in-silico trials with Compound 6f, a new agent with the structure of a local anaesthetic, to assess its efficacy for rhythm control of AF.

7.3. Methods

7.3.1. Population of virtual AF patients

The CRN model was modified as in (Wiedmann *et al.*, 2020) to include the two-pore-domain potassium (K_{2P}) channel family, which comprises the TASK-1 channel (I_{K2P}).

A population of 100 atrial cardiomyocyte models was generated with the modified CRN model by varying all ionic current densities up to ±50%, including TASK-1. To incorporate a wider range of action potential morphologies (i.e., a limitation of the previous chapter), the calibration considered data from patients in sinus rhythm and AF (i.e., longer and shorter APD, respectively) (Sánchez *et al.*, 2014). A representative sample of the overall ionic current variability, consisting of 45 atrial cardiomyocyte models, was used to populate whole-atria models.

Whole-atria simulations were performed using the mean bi-atrial anatomy generated by Dr. Claudia Nagel (Nagel, Schuler, *et al.*, 2021). Similar to **Chapter 6**, this study considered one atrial anatomy and structurally-healthy atria. Thus, 45 virtual patients were developed using one atrial cardiomyocyte model to generate one whole-atria model. Regional electrophysiological heterogeneities were included as explained in **section 4.2.1**, setting the longitudinal velocity in the bulk tissue to 80 cm/s.

AF was induced in virtual atria by imposing spiral wave re-entries as the initial conditions of the simulation, and AF dynamics were analysed for 7 s of activity.

7.3.2. In-silico trial

Virtual patients with sustained (>7s) AF were subjected to the virtual administration of three doses of Compound 6f (i.e., 1, 10 and 100 µM). Drug action was simulated as a simple-pore block model. **Table 7.1** collects the ionic current block of each dose based on the inhibitory curves presented in **Figure 7.1**.

Efficacy for acute AF cardioversion was investigated by applying each dose 2 seconds from AF induction and the episode was recorded for another 5 seconds. Long-term AF prevention was modelled by repeating the AF initiation protocol after drug application. Drug therapy was considered successful if the atria were free from any form of arrhythmic activity before the completion of the 7 seconds.

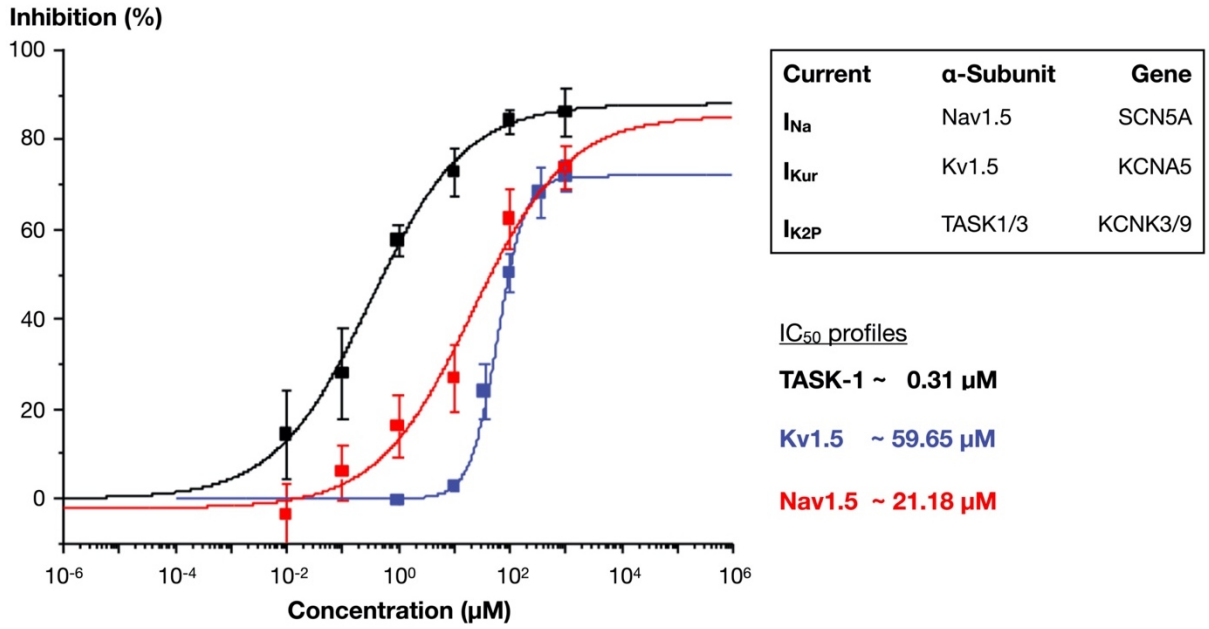


Figure 7.1 Inhibition curves of compound 6f for TASK-1, Kv1.5 and Nav1.5 channels. Nav1.5 block was determined at -30 mV and TASK-1 and Kv1.5 at +40 mV. The concentration range was from 0.01 µM to 1000 µM for TASK-1 and Nav1.5, and from 1 µM to 1000 µM for Kv1.5.

Table 7.1. Ionic current block (%) exerted by three doses of Compound 6f.

Drug	Dose	Ionic current block (%)		
		I_{Kur}	I_{Na}	I_{K2P}
Compound 6f	1 µM	0	16	58
	10 µM	2.5	30	75
	100 µM	50	65	85

7.4. Results

7.4.1. Compound 6f (100 μM) shows >70% efficacy for rhythm control of AF, following a dose-dependent prolongation of post-repolarization refractoriness

Sustained AF developed in all 45 virtual patient models. **Figure 7.2** illustrates the impact of three doses (i.e., 1, 10 and 100 μM) of Compound 6f on the APD (**Figure 7.2A-B**) effective refractory period (**Figure 7.2C**), and on the efficacy for rhythm control of AF (**Figure 7.2D-E**).

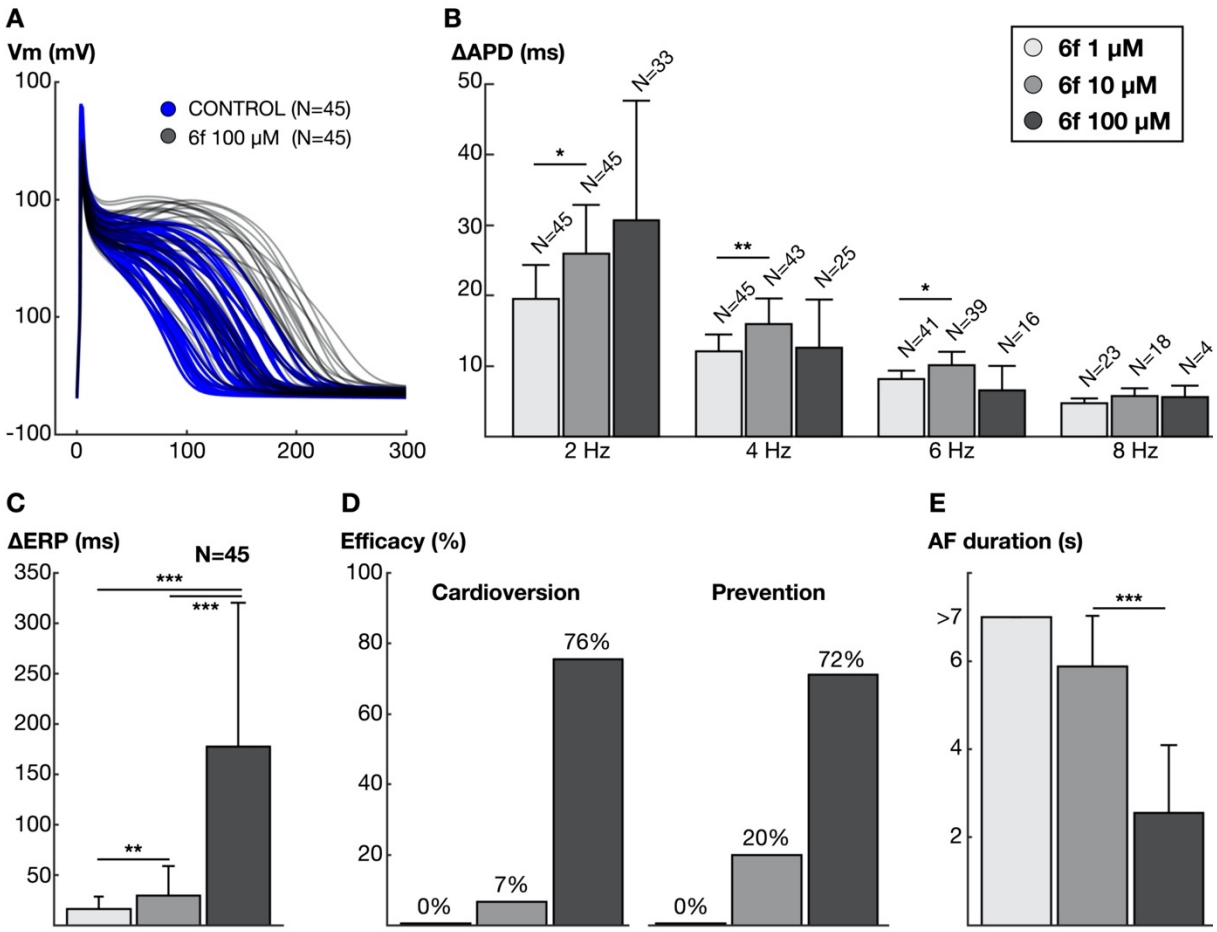


Figure 7.2 Impact of three doses (1, 10 and 100 μM) of compound 6f on single-cell, cable and whole-atria properties. **A)** Action potential traces of N=45 atrial cardiomyocyte models at 2Hz in control conditions and after the application of compound 6f at 100 μM. **B)** Rate-dependent variation of the action potential duration (ΔAPD). Number (N) of atrial cardiomyocyte models able to propagate the stimulus according to the dose applied and the pacing rate. **C)** Dose-dependent increase in the effective refractory period (ΔERP) compared to control conditions in the N=45 atrial cardiomyocyte models. **D)** AF cardioversion and prevention efficacy (i.e., percentage of AF episodes cardioverted or prevented) in the population of 45 virtual-atria models. **E)** AF duration in the 45 virtual-atria models considering that AF episodes are analysed for 7 s of activity.

The application of Compound 6f prolonged the APD at the cellular level (142.2±30.7 vs. 181.6±38.8 for control vs Compound 6f at 100 μM at 2 Hz; N=45; **Figure 7.2A**). The atrial cardiomyocyte models were subsequently paced on a one-dimensional cable to assess propagation properties and refractoriness.

At moderate frequencies (i.e., 2 Hz), the virtual administration of Compound 6f caused a dose-dependent prolongation of the APD. As the pacing frequency increased, fewer cardiomyocyte models were able to propagate the stimulus after applying Compound 6f at 100 µM, due to a longer post-repolarization refractoriness (87% [39/45] vs. 35% [15/45] of cardiomyocyte models propagating the stimulus at 6 Hz after 10 µM vs. 100 µM of compound 6f; **Figure 7.2B**). At these higher rates, the strong I_{Na} inhibition prevailed over I_{Kur} and I_{K2P} block, so that 10 µM prolonged the APD to a larger extent than 100 µM (**Figure 7.2B**; from 4 Hz to 8 Hz).

The dose-dependent prolongation of the post-repolarization refractoriness is illustrated in **Figure 7.2C**. The application of 1 µM, 10 µM and 100 µM of Compound 6f increased the refractory period by 16.3±12.3 ms, 29.3±29.5 ms and 177.6±143.0, respectively, compared to control conditions. This increase in refractoriness caused a proportional increase in the effectiveness of Compound 6f for rhythm control of AF (**Figure 7.2C-D**). Therefore, a dose-dependent increase in AF cardioversion and prevention efficacy were observed for the virtual application of Compound 6f (**Figure 7.2D**). This was also reflected in a larger decrease of AF duration for the highest dose (**Figure 7.2E**).

Figure 7.3 shows a representative AF episode in control conditions and after the virtual administration of 10 and 100 µM of Compound 6f to illustrate the reduction of AF burden with increasing drug dose. The drug is applied 2 s after AF initiation, representing acute AF cardioversion.

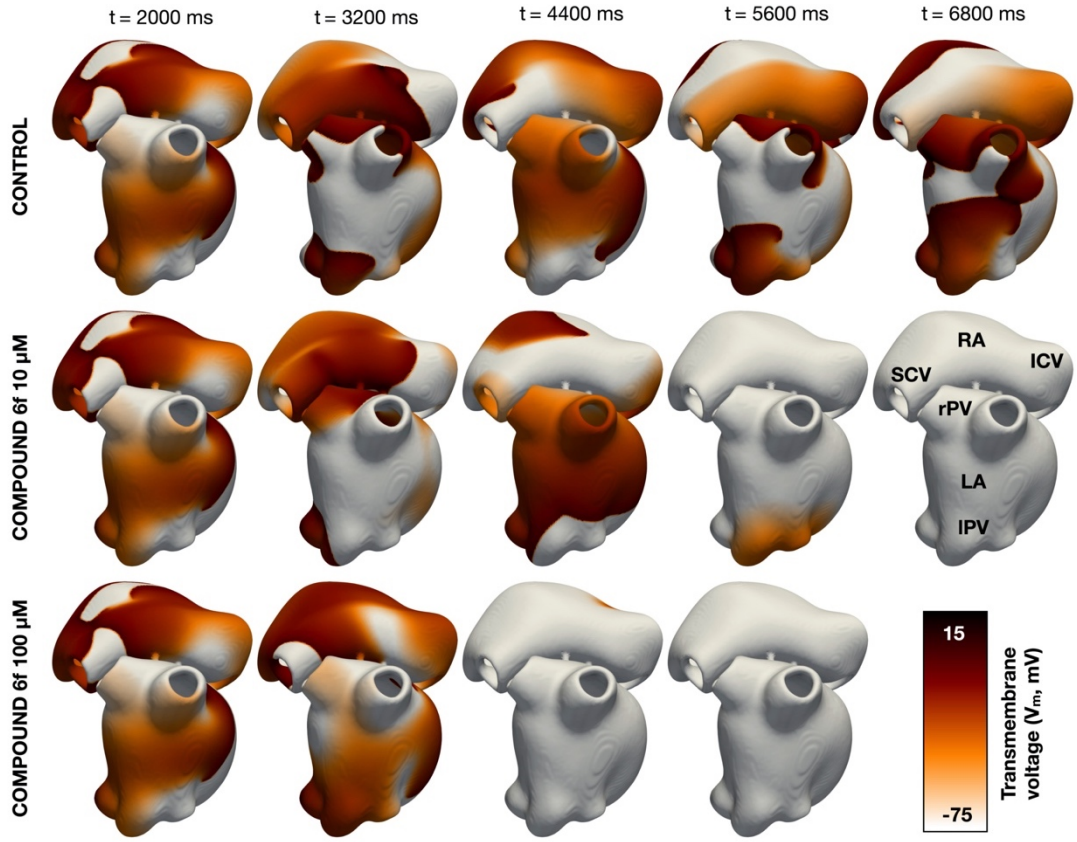


Figure 7.3. Consecutives snapshots of the transmembrane voltage (V_m) for a representative AF episode in control conditions and after the virtual administration of 10 and 100 µM of compound 6f. Abbreviations: RA-LA: right and left atrium; SCV-IVC: superior and inferior cava vein; rPV-lPV: right and left pulmonary veins.

7.4.2. The antiarrhythmic response of Compound 6f (100 μM) is modulated by Na^+ channel density

The ionic current substrate of virtual patients responding to Compound 6f was analysed to identify patient characteristics modulating treatment response. **Figure 7.4** shows a comparison of the ionic current densities between virtual patients responding and not responding to the virtual application of two doses (i.e., 10 and 100 μM) of the drug.

When a 10 μM dose was considered, the drug produced a predominant K^+ current block (**Table 7.1**). Thus, virtual patients responding to 10 μM of Compound 6f presented longer refractoriness (157.3 ± 19.8 vs. 114.6 ± 15.9 ms; virtual responders vs. non-responders), as a result of low I_{K1} and high I_{CaL} (I_{K1}: 0.063±0.037 vs. 0.095±0.045 mS/F; I_{CaL} 0.15±0.06 vs. 0.10±0.04 mS/F; responders vs. non-responders). Conversely, 100 μM of the drug produced a strong I_{Na} inhibition. Virtual patients with I_{Na} up-regulation were less sensitive to I_{Na} block (I_{Na} density: 6.2±2.5 vs. 9.5±1.9 mS/F; responders vs. non-responders).

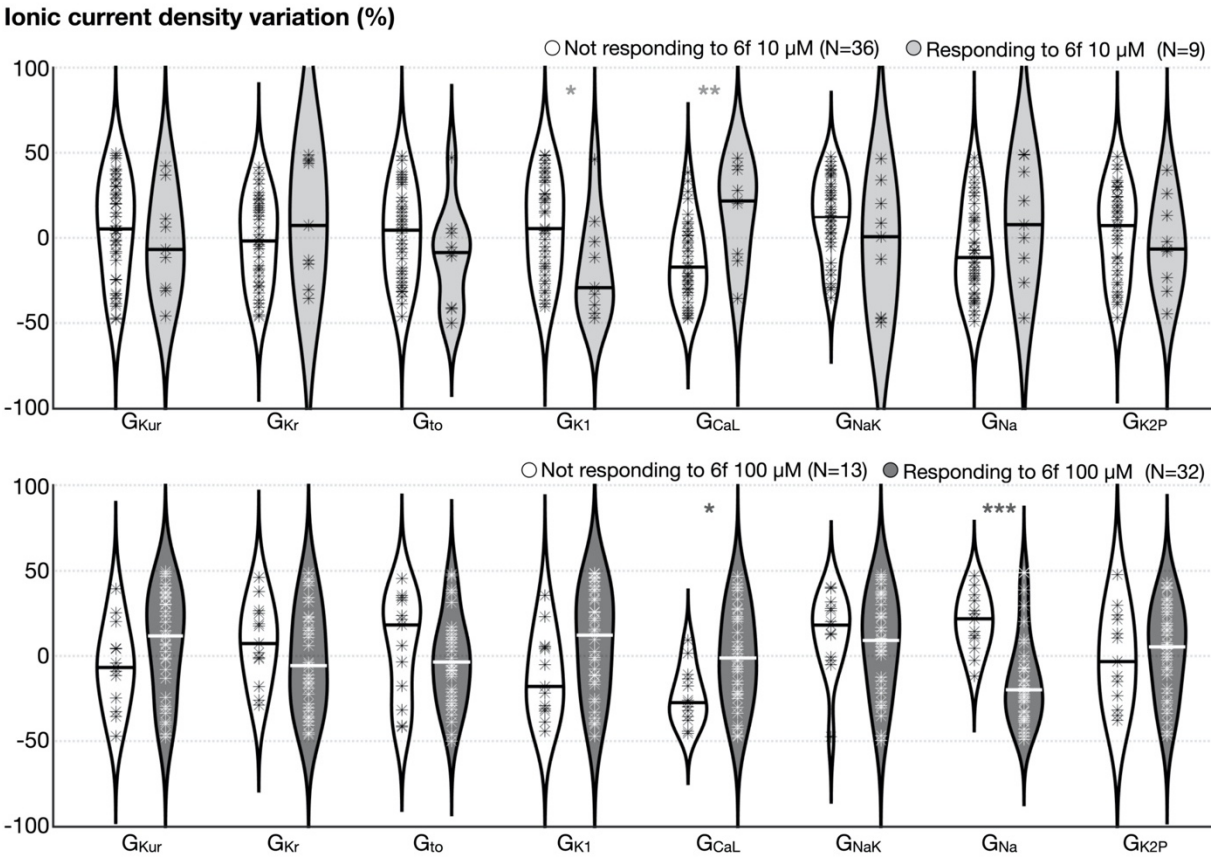


Figure 7.4. Comparison of the ionic current variation (%) between virtual patients responding and not responding to two doses (10 and 100 μM) of compound 6f. Data are expressed as medians and IQR and analysed using Wilcoxon Test. *P<0.05, **P<0.01, ***P<0.001.

7.5. Conclusion

In this study I have assessed the efficacy of three doses of a novel compound for rhythm control of AF. The pharmacological agent, Compound 6f, is based on the structure of a local anaesthetic and, as such, inhibits I_{K2P}, I_{Kur} and I_{Na}. This represents a promising poly-pharmacological strategy, which has been investigated by means of in-silico trials in a population of 45 virtual patients with structurally-healthy atria and varying ionic current densities.

The main finding is that, when applied at high concentration (100 μM), Compound 6f yields high AF cardioversion and prevention efficacy (>70%). This is due to a strong Na^+ channel inhibition, so that patients without I_{Na} up-regulation are expected to present a more favourable response. Conversely, limited success rates are obtained for lower concentrations of the drug (i.e., 1 and 10 μM). At these lower concentrations, Compound 6f exerts a primary K^+ current block. Thus, only those patients with longer refractoriness might benefit from drug treatment.

Overall, Compound 6f represents a promising drug for AF treatment, but further research is needed to investigate whether the strong Na^+ channel inhibition occurs only in the atria (i.e., rate-dependent inhibition of I_{Na}, differences between atrial and ventricular Na^+ channels (Mamoshina, Rodriguez and Bueno-Orovio, 2021), etc.) or, conversely, it could jeopardise ventricular conduction. Moreover, it is unclear how the efficacy of the drug might be modulated by presence of other AF predisposing conditions. Among the later, the remodelling of the atrial tissue structure is a key aspect influencing drug treatment response. Therefore, the following chapter investigates the outcome of pharmacological treatment in a cohort of virtual patients presenting structurally-remodelled atria.

CHAPTER

IN-SILICO TRIALS FOR OPTIMAL SELECTION OF PHARMACOLOGICAL TREATMENT IN VIRTUAL AF PATIENTS WITH LOW VOLTAGE AREAS

8

*As mentioned in **section 2.2.3**, AF patients commonly present an arrhythmogenic structural substrate. In this chapter, I include the assessment of arrhythmogenic structural substrate, through in-silico trials in 800 virtual patients presenting variability in electrophysiology and LVAs (related to structural abnormalities). As in the previous chapters, in this study, I assessed pharmacological treatment for rhythm control of AF, and the original work can be found in: "Dasí et al., (2023), J. Physiol. DOI: 10.1113/JP284730".*

8.1. Summary of the study

The study aimed to conduct in-silico trials in a large population of virtual patients to identify key clinical characteristics to guide optimal selection of antiarrhythmic drugs. For this, AF was induced in 800 virtual patients considering variability in ionic currents and LVA. Sustained AF developed in 494 (62%), characterised by large I_{K1} and I_{NaK} densities (I_{K1} 0.11±0.03 vs. 0.07±0.03 S/mF; I_{NaK} 0.68±0.15 vs. 0.38±26 S/mF; sustained vs. unsustained AF). In virtual patients with severely remodelled left atrium, with LVA extensions of more than 40% in the posterior wall, higher I_{K1} (0.12±0.02 S/mF) was required for AF maintenance, and rotors localised in healthy right atrium. For lower LVA extensions, rotors also anchored to LVA, in virtual patients with short refractoriness (I_{CaL} density 0.08±0.03 S/mF). This atrial refractoriness, modulated by I_{CaL} and I_{Na}, determined pharmacological treatment success for both small and large LVA. Vernakalant was effective in atria presenting long refractoriness (I_{CaL} density 0.13±0.05 S/mF). For short refractoriness, atria with high I_{Na} density (8.92±2.59 S/mF) responded more favourably to amiodarone than flecainide, and the opposite was found in atria with low I_{Na} (5.33±1.41 S/mF). In-silico trials were consistent with clinical trials and identified the inward currents as critical for optimal

stratification of AF patient to pharmacological treatment and, together with the left atrial LVA extension, for accurately phenotyping AF dynamics.

8.2. Introduction

Pharmacological therapy remains a core element of AF management (Heijman, Hohnloser and Camm, 2021). However, as explained in **section 2.3.1**, antiarrhythmic drugs have moderate efficacy. Therefore, improving pharmacological treatment, through tailored therapies that consider individual patient characteristics, is paramount.

As shown in the previous chapters, in-silico trials based on human multiscale modelling and simulation hold potential for unravelling key modulators of successful pharmacological therapy. Thus, the aim of this study is to perform in-silico trials in a large cohort of virtual patients, with variability in the extent of LVAs and membrane kinetics, to identify key determinants of AF treatment that guide the decision-making of optimal pharmacological therapies.

8.3. Methods

8.3.1. Population of virtual AF patients

A population of 800 virtual atria was developed combining a range of LVA distributions and atrial ionic current profiles. **Figure 8.1** illustrates the overall process, and an explanation is provided below.

8.3.1.1. Patient-specific bipolar voltage map

Left atrial bipolar voltage maps were obtained from eight AF patients as described in **section 4.2.2.2**. The left atrial surface of each patient was registered to the left atrium of the Visible Female atria. The voltage data were subsequently interpolated using the nearest neighbour algorithm. Thus, eight human whole-atria models, presenting LVA variability were constructed based on the eight patient maps.

Each whole-atria model was binarized into non-LVA and LVA (i.e., bipolar voltage lower than 0.5 mV in sinus rhythm). The right atrium was considered structurally-healthy to isolate the role of structurally-remodelled left atrium on AF dynamics and pharmacological treatment.

8.3.1.2. Population of whole-atria models

To reflect variability in the patient electrophysiological substrate, each virtual patient was modelled with a specific ionic current profile. As described in **section 4.1.2**, a population of atrial cardiomyocyte models was generated with the CRN model by varying current densities up to ±50%.

Three-hundred cardiomyocyte models were calibrated against experimental data obtained from patients in sinus rhythm and AF (Sánchez *et al.*, 2014). A representative sample of the overall ionic current variability, consisting of 100 atrial cardiomyocyte models, was randomly selected.

The final population of 800 virtual patients was built combining the 100 atrial cardiomyocyte models with the eight LVA distributions. The single-cell properties of each atrial cardiomyocyte model were assigned to the left atrial tissue and modified in other atrial regions, as detailed in **section 4.2.1**. Regional heterogeneities in conduction velocity and anisotropy ratio were likewise considered, setting the longitudinal velocity in the bulk tissue to 80 cm/s, according to patient data.

The LVA remodelling (described in **section 4.2.2.2**) was implemented on top of the specific electrophysiological properties of each virtual patient.

8.3.1.3. AF induction, ECG and dominant frequency maps

AF was induced in the virtual atria by imposing spiral wave re-entries as the initial conditions of the simulation, and AF dynamics were analysed for 7 s of activity. Simulated 8-lead (Leads I, II, V1-V6) ECGs and dominant frequency maps were computed for sustained (>7s) AF episodes. The frequency maps were discretized considering three values: low [10^{th} percentile], middle (10-90^{th} percentile) and high frequency [90^{th} percentile]. High-frequency regions obtained for a given LVA distribution with different ionic profiles were superimposed to generate frequency density maps. The latter maps identified preferential regions of high atrial activity (i.e., AF drivers) for each LVA distribution.

8.3.2. In-silico trials

Virtual patients with sustained (>7s) AF were subjected to the administration of four drugs commonly used for AF treatment (Hindricks *et al.*, 2021). Their administration was modelled 2 seconds from AF initiation and the episode was continued until completion of the original 7 s. The therapy was considered successful if the atria were free of arrhythmic activity before the conclusion of the 7 s. Drug efficacy was defined as the percentage of virtual patients without sustained AF after drug administration.

For each drug, different doses were administered within the therapeutic plasma concentration range: vernakalant 10 and 30 μM (Roy *et al.*, 2004), amiodarone 1.5 and 3.0 μM (Nishimura, Follmer and Singer, 1989), flecainide 1 and 2 μM (Viswanathan *et al.*, 2001), and digoxin 5 and 10 nM (Chamberlain *et al.*, 1970). Digoxin, clinically used for rate control, was also considered for rhythm control of AF (Bueno-Orovio *et al.*, 2014). Flecainide 2 μM considered the high levels of I_{Na} block observed at fast activation rates (~60 to 70% block at 10Hz, (Moreno *et al.*, 2011)). Acute and chronic amiodarone 3.0 μM were modelled with and without I_{CaL} inhibition, respectively. Chronic amiodarone additionally comprised a progressive I_{NaK} (Gray *et al.*, 1998) and I_{K1} block (Guillemare, Marion and Gautier, 2000; Patel, Yan and Kowey, 2009). Drug action was simulated as simple pore-block models and **Table 8.1** collects the ionic current blockade of each treatment.

8.3.3. Clinical decision support system

A decision algorithm was built using the outcome of in-silico trials and patient characteristics. Different from **Chapter 6**, the algorithm consisted of a flow-chart (i.e., not a data-driven model) that assigned

optimal treatment according to the evaluation of key patient characteristics and based on the observation of key results.

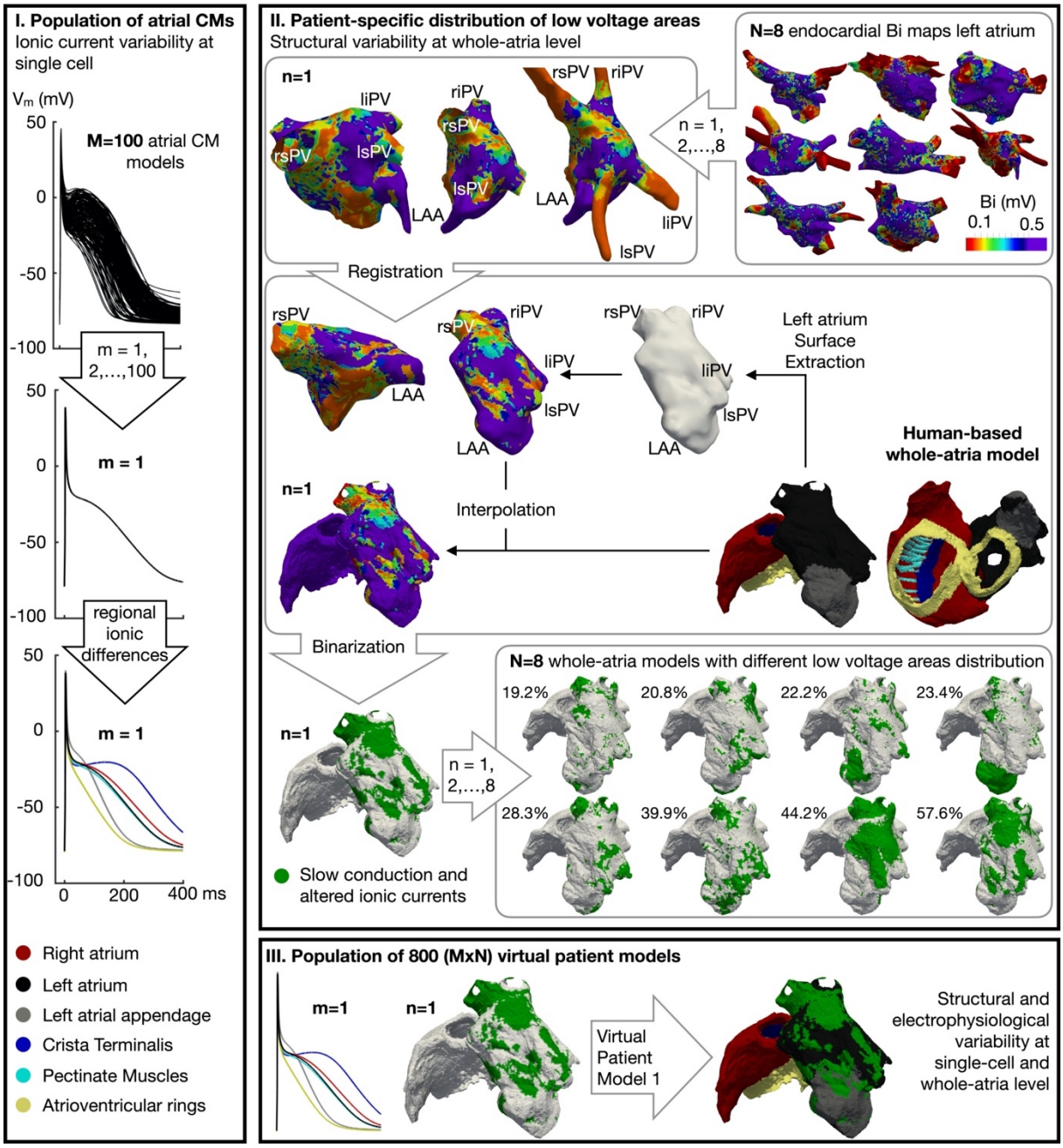


Figure 8.1. Generation of the population of 800 virtual patients. **I.** M=100 atrial cardiomyocyte (CM) models reflecting variability in ionic current densities are developed and scaled in different atrial regions. **II.** N=8 bipolar voltage (Bi) maps of the left atrium are registered to a human-based whole-atria model. The resulting whole-atria models are binarized into LVA (Bi < 0.5 mV) and non-LVA. Abbreviations: LAA: left atrial appendage; rs-ri-ls-li-PV: right superior, right inferior, left superior and right inferior pulmonary vein. **III.** A final population of 800 virtual patient models is generated combining each cardiomyocyte model, scaled in different atrial regions, with each whole-atria model with a specific LVA distribution.

Table 8.1. Ionic current block (%) exerted by the antiarrhythmic drugs modelled in this study.

Drug		Dose	Ionic current block (%)									References
			I_{Kur}	I_{Kr}	I_{to}	I_{K1}	I_{Ks}	I_{CaL}	I_{NaK}	I_{NCX}	I_{Na}	
Amiodarone	Acute	1.5 μM	-	40	-	-	30	30	-	30	20	Loewe et al., 201 4; Sutanto et al., 201 9; Bai, Lu and Zhang, 2020
		3.0 μM	-	65	30	20	50	65	10	50	40	
	Chronic	3.0 μM	-	65	30	20	50	0	10	50	40	
		3.0 μM	-	65	30	40	50	0	25	50	40	(Patel et al., 2009); (Gray et al., 1998); (Guillemare et al., 2000)
		3.0 μM	-	65	30	50	50	0	25	50	40	
Flecainide		1.0 μM	-	30	-	-	-	-	-	-	40	Sutanto et al., 201 9; Bai et al., 202 0;
		2.0 μM	30	60	15	-	-	10	-	-	60	
		2.0 μM	30	60	15	-	-	10	-	-	70	
Vernakalant		10 μM	40	30	40	-	-	-	-	-	10	Loewe et al., 201 5; Sutanto et al., 2019
		30 μM	70	60	60	-	-	20	-	-	30	
Digoxin		5 nM	-	40	-	-	-	-	30	-	-	Bai, Lu and Zhang, 2020
		10 nM	-	50	-	-	-	-	60	-	-	

8.4. Results

8.4.1. AF sustains in virtual atria presenting short refractoriness and high cellular excitability, the latter proportional to the extent of LVAs in the left atrium

Sustained AF (>7s) developed in 494 (62%) of the 800 virtual patient models. **Figure 8.2A** illustrates a representative AF episode and the corresponding ECG. Simulated and clinical recordings shared similar morphology and complexity of fibrillatory-waves (f-waves), as well as comparable AF dominant frequency, supporting the credibility of the simulation results. **Figure 8.2B** characterises the atrial ionic current substrate favouring AF maintenance. The 100 ionic current profiles included in this study have been grouped into three categories: profiles sustaining AF (>7s) for less than 2 LVA distributions (less than 25% of the LVA distributions studied), between 2 and 6 (25-75% of the LVA distributions) and for more than 6 LVA distributions (more than 75% of the LVA distributions). **Figures 8.2C** and **8.2D** show the ionic current substrate needed for AF maintenance as the LVA extension increased.

Twelve ionic current profiles led to unsustained AF in all LVA distributions, whereas 11 perpetuated AF in only 1 out of the 8 (less than 25% of the LVA distributions considered). Ionic profiles leading to low AF sustenance were characterised by significantly high I_{CaL} and low I_{NaK} compared to baseline (i.e., ionic current density variation equal to 0%). I_{NaK} increase and I_{CaL} decrease led to AF developing in more LVA distributions, with the 45 most proarrhythmic profiles (i.e., sustaining AF for more than 75% of the LVA distributions) showing the highest I_{NaK} and the lowest I_{CaL}. The 45 AF-prone ionic current substrates additionally presented I_{to} and I_{K1} up-regulation, which yielded a shorter refractory period

(185.3±56.7 vs. 125.3±18.2 ms; atria with sustained AF for less than 25% vs. more than 75% LVA distributions) and a more negative resting membrane potential (-83.6± 0.4 vs. -84.5±0.4 mV).

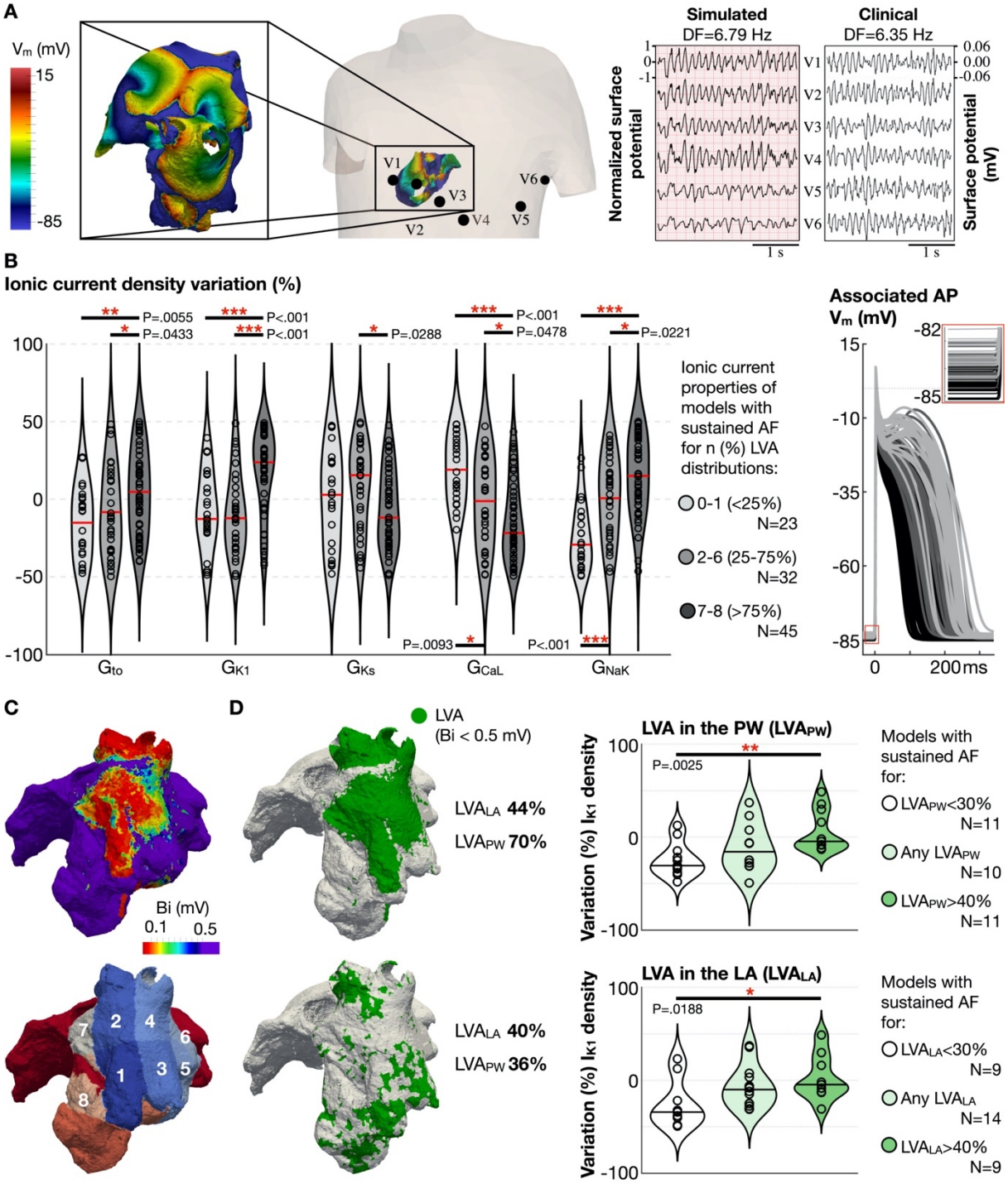


Figure 8.2. Ionic current substrate favouring AF for distinct LVA distributions. **A)** Snapshot of the atrial transmembrane voltage map during AF and location of the atria within the torso (left). Simulated and clinical ECG during AF and dominant frequency (DF) of lead V1 (right, adapted from Lankveld et al., 2016 with permission). **B)** Variation of G_{to}, G_{K1}, G_{Ks}, G_{CaL} and G_{NaK} (%) yielding sustained AF (>7s) for an increasing number of LVA distributions (left), and associated atrial action potential (AP, right). **C)** Bipolar voltage (Bi) map and left atrium parcellation: Estimation of LVAs in the left atrium posterior wall (regions 1-4). **D)** I_{K1} density variation leading to sustained AF for an increasing LVA extension in the left atrium (LVA_{LA}, bottom) and in the left atrial posterior wall (LVA_{PW}, top).

I_{K1} up-regulation was especially needed as the LVA density increased in the left atrium. LVAs were characterised by low cellular excitability (i.e., conduction impairment and reduced I_{Na}, I_{CaL} and I_{K1}). When they occupied a large portion of the left atrium, i.e., extending throughout the entire posterior wall (**Figure 8.2D**, >40% LVAs), sustained AF (> 7 s) could only result from ionic current profiles exhibiting the highest I_{K1}. This is illustrated in the 32 ionic current profiles yielding AF maintenance in 2-6 LVA distributions. From the 32 profiles, 9 sustained AF (> 7 s) primarily in smaller LVA extensions (20-30% LVAs), 9 in larger (40-60% LVAs) and 14 in both. Compared to ionic current profiles sustaining AF in smaller LVAs, those profiles engaging with severe structural remodelling showed a significantly higher I_{K1}. This difference was accentuated when considering the LVA extension in the left atrial posterior wall (**Figure 8.2C**, regions 1-4).

8.4.2. The ionic current dysregulation favouring AF maintenance is identified through ECG metrics, with I_{K1} being the main determinant of AF dominant frequency

To assess whether the ionic density dysregulation presented in **Figure 8.2** could be identified non-invasively, simulated ECGs were computed in the 494 sustained AF (>7s) episodes. **Table 8.2** shows the influence of ionic current dysregulation on five ECG markers (i.e., dominant frequency, organization index, spectral entropy, sample entropy, and relative harmonic energy).

Table 8.2. Effect of ionic current dysregulation on the ECG metrics during AF. Statistical significance with P<.001 highlighted in bold, otherwise P<.05. The number of ECG leads where the ionic current dysregulation increases each biomarker is shown in brackets next to the ionic density, being 8 the maximum.

% LVAs left atrium		Dominant frequency	Organization index	Spectral entropy	Sample entropy	Rel. harmonic energy
Dist. 1	**19.2**	↑**G_{K1}(8)**, ↑G_{NaK}(8), ↑G_{to}(8), ↑G_{Na}(8)	–	–	–	↑G_{Na}(7)
Dist. 2	**20.8**	↑**G_{K1}(8)**, ↑**G_{NaK}(8)**, ↑G_{Na}(4)	–	–	↑G_{NaK}(3)	↑**G_{Na}(7)**
Dist. 3	**22.2**	↑**G_{K1}(8)**, ↑G_{NaK}(8), ↑G_{Na}(8), ↑G_{to}(5)	–	↓G_{to}(4)	↑**G_{NaK}(6)**	↑**G_{Na}(5)**
Dist. 4	**23.4**	↑**G_{K1}(8)**, ↑G_{NaK}(8), ↑G_{to}(6), ↑G_{Na}(6)	↑G_{to}(4)	↑G_{CaL}(3)	↓G_{CaL}(6)	↑G_{Na}(4)
Dist. 5	**28.3**	↑**G_{K1}(8)**, ↑G_{NaK}(8), ↑G_{to}(7)	–	↓**G_{to}(3)**	↑**G_{K1}(5)**, ↑G_{to}(5)	↑**G_{Na}(4)**
Dist. 6	**39.9**	↑**G_{K1}(8)**, ↑G_{NaK}(8), ↑G_{to}(8)	↑**G_{CaL}(4)**	↑**G_{CaL}(6)**, ↑G_{Kur}(4), ↓**G_{to}(3)**	↑G_{to}(5), ↓G_{CaL}(4)	↑**G_{Na}(4)**
Dist. 7	**44.2**	↑**G_{K1}(8)**, ↑G_{NaK}(8), ↑G_{Na}(8), ↑G_{to}(7)	↓G_{NCX}(4)	–	–	↑G_{Na}(4)
Dist. 8	**57.6**	↑**G_{K1}(8)**, ↑G_{to}(8), ↑G_{NaK}(7), ↑G_{Na}(6), ↓G_{CaL}(5)	–	↑G_{CaL}(4)	↓G_{CaL}(5)	–

Overall, dysregulation of I_{CaL}, I_{to}, I_{Na}, I_{NaK} and I_{K1} were associated with variations in ECG metrics (**Table 8.2**). For some LVA distributions, high I_{CaL} and low I_{to} increased the ECG spectral entropy. The spectral entropy relates to the uniformity of fibrillation frequencies and a high value indicates high AF complexity (Zeemering *et al.*, 2018). Elevated I_{CaL} was associated with APD alternans and wavefront

fractionation (**section 6.4.2**), consistent with an increase in AF complexity and the spectral entropy. Conversely, low I_{CaL} and high I_{to} were associated with an elevation of the sample entropy, a measure of predictability and repetitiveness (Zeemering *et al.*, 2018). As such, I_{CaL} down-regulation yielded the formation of localised rotors (see below), which increased AF repetitiveness. High I_{NaK} was also linked to high sample entropy for some LVA distributions, as a result of higher excitability promoting localized re-entrant sources. Lastly, I_{Na} up-regulation increased the relative harmonic energy, indicating low complexity and a dominant role of the main atrial wave (Zeemering *et al.*, 2018).

The ECG dominant frequency was mainly modulated by I_{K1}, with other ionic currents having a cumulative effect (**Table 8.2**). Besides I_{K1} up-regulation, the general analysis identified a higher frequency in atria presenting increased I_{to}, I_{NaK} and I_{Na}. Nevertheless, a thorough patient stratification demonstrated that atria with high I_{to}, I_{NaK} and I_{Na} but control I_{K1}, showed no significantly higher AF frequency than the overall population (**Figure 8.3A**). This is illustrated through two simulated ECG recordings during AF (**Figure 8.3B**), showing high and low frequency f-waves for I_{K1} up- and down-regulation, respectively. Similarly, while faster AF episodes were obtained in atria that additionally presented low I_{CaL}, atria with increased I_{CaL} showed significantly higher AF frequency than the overall population if I_{to}, I_{K1}, I_{NaK}, I_{Na} were up-regulated. As shown in **Figure 8.3A**, the fastest AF episodes were obtained for the combination of increased I_{to}, I_{K1}, I_{NaK}, I_{Na} and decreased I_{CaL}. This ionic current profile yielded the shortest tissue refractoriness (108±10.3 ms), which enabled a fast activation of re-entrant AF drivers (i.e., rotors).

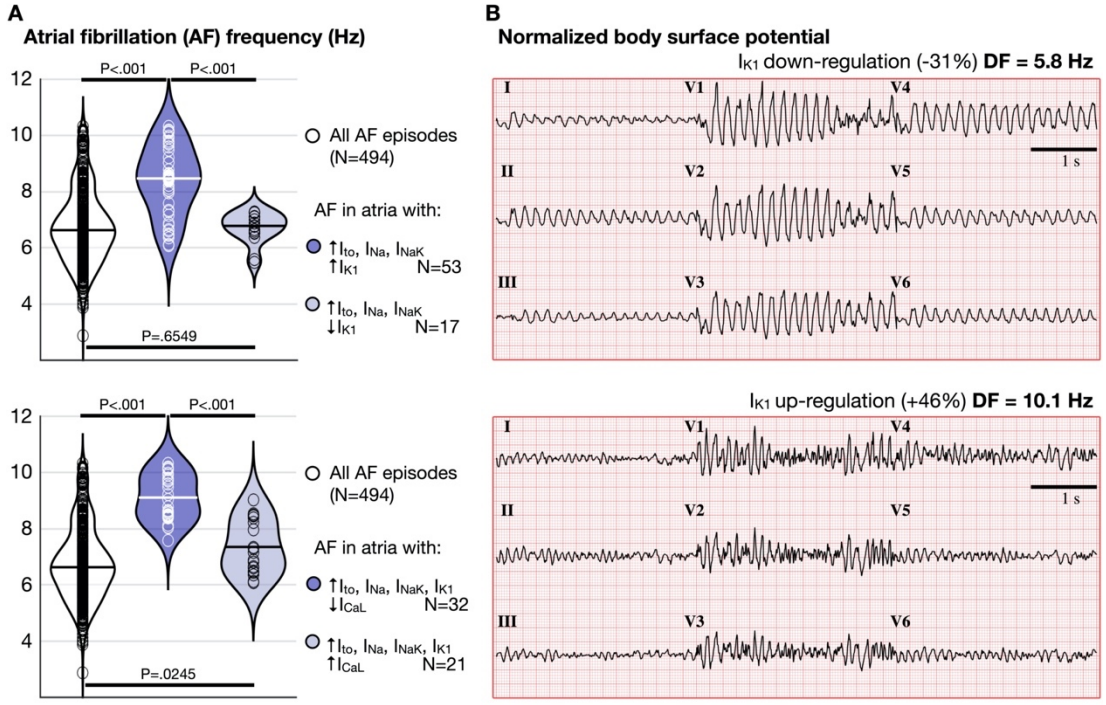


Figure 8.3. Effect of I_{K1} and I_{CaL} on the ECG dominant frequency (DF). **A)** Comparison of AF dominant frequency in atria with I_{to}, I_{NaK} and I_{Na} up-regulation with vs. without I_{K1} up-regulation (top), and with I_{to}, I_{NaK}, I_{Na} and I_{K1} up-regulation with vs. without I_{CaL} down-regulation. **B)** Simulated ECG recordings during AF in virtual atria with low and high I_{K1}.

8.4.3. High frequency rotational activity in structurally-healthy areas coexist with rotors anchored around small and patchy LVAs

Dominant frequency maps were computed in the 494 sustained AF episodes (>7s) to analyse AF dynamics. Each AF episode exhibited a different range of AF frequencies. To enable comparisons on the location of high-frequency regions across multiple AF episodes, every episode was represented by a discrete frequency map. The discrete map was developed by assigning to each cell of the atria one of three possible categories: very low activation frequency (frequencies below 10th percentile for the given AF episode), intermediate (10-90th percentile) and very high activation frequency (above 90th percentile). For each LVA distribution, density maps of high-frequency areas were constructed by superimposing high-frequency values obtained in multiple AF episodes. **Figure 8.4A** illustrates the transmembrane voltage of a representative AF episode and the resulting discrete frequency map. **Figure 8.4B** shows the bipolar voltage and density maps for different LVA distributions.

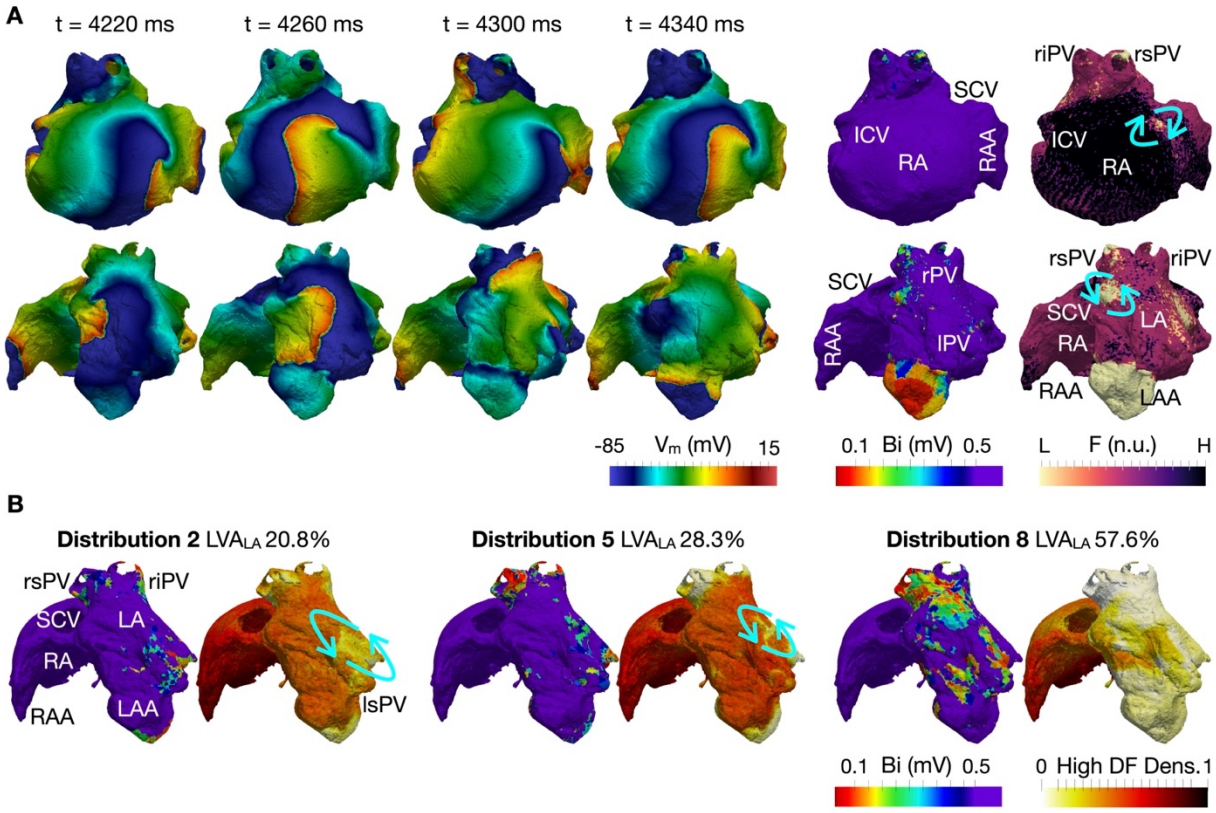


Figure 8.4. Dominant frequency density maps for different LVA distributions. **A)** Consecutive snapshots of the transmembrane voltage (V_m) for a single AF episode. One rotor (top row) is located in the right atrium and another (bottom row) is anchored to a LVA of the left atrium (bipolar voltage, Bi<0.5 mV). The discrete frequency (F, no units) map illustrates the core of the re-entry as a low (L) frequency region and the surroundings as middle and high (H) frequency regions. **B)** Dominant frequency (DF) density maps for three LVA distributions in the left atrium (LVA_{LA}): two with low and one with high LVA density. The blue arrows highlight high frequency regions adjacent to low density regions. Abbreviations. RA-LA: right and left atrium; RAA-LAA: RA and LA appendage; SCV-ICV: superior and inferior cava vein. rPV-lPV: right and left pulmonary veins. rs-ri-ls-li-PV: right superior, right inferior, left superior and left inferior pulmonary vein.

Rotors were not exclusive to the structurally-remodelled substrate. The down-regulation of I_{CaL} and the up-regulation of I_{K1}, I_{to} and I_{NaK} contributed to the stabilization of functional rotors in healthy atrial tissue, appearing primarily in the right atrium (considered in this study as structurally-healthy). Importantly, rotational activity found in structurally-healthy areas coexisted with rotors anchored around LVAs, with the former exhibiting a higher frequency (**Figure 8.4A**). In frequency maps, these rotors appeared as high-frequency regions (i.e., arm of the re-entry), surrounding middle (i.e., border of the core) and low-frequency regions (i.e., core of the re-entry).

Frequency density maps revealed that LVAs were distinguished by low frequency areas (**Figure 8.4B**). However, small and patchy LVAs surrounded by healthy tissue (i.e., LVA distributions 2 and 5) showed high-frequency regions around LVAs (**Figure 8.4B**, blue arrows). The excitability gradient between LVAs and healthy tissue created an arrhythmogenic substrate for rotor anchoring. When LVAs were small, healthy tissue presenting high excitability and short refractoriness (i.e., elevated I_{K1} and reduced I_{CaL}) sustained rotational activity around LVAs (~2 s). Conversely, scattered and large LVA patches (LVA distribution 8) caused an excessive reduction of cellular excitability. Since the right atrium preserved high cellular excitability (i.e., no LVAs), high-frequency sources arising from this chamber prevented the anchoring of rotors in the structurally-remodelled left atrium. Thus, distributions with high percentage of LVAs (distribution 6-8) showed high-frequency regions only in the right atrium.

8.4.4. In-silico drug trials in 494 virtual patients with 4 reference compounds identify the inward currents (I_{CaL} and I_{Na}) as critical for optimal stratification of AF patient to pharmacological treatment

The 494 sustained AF episodes (>7 s) were subject to in-silico trials with 12 pharmacological treatments (i.e., 6.422 simulated AF episodes in total). **Figure 8.5** compares the success rate obtained in-silico and in human clinical trials (**Figure 8.5A**), and the atrial ionic current substrate favouring pharmacological AF prevention (**Figure 8.5B-C**).

Drug efficacy increased proportionally to a dose-dependent prolongation of refractoriness. This was less accentuated for vernakalant, with both doses achieving a similar efficacy despite a greater prolongation of refractoriness after vernakalant 30 μM (+16.5±27.6 vs. +54.0±44.8 ms with respect to control; vernakalant 10 vs. 30 μM). Conversely, a decrease in the refractory period derived from acute amiodarone (–5.0±18.1 and –4.0±18.4 ms; amiodarone 1.5 and 3 μM, respectively), which explained its very low efficacy (**Figure 8.5A**, 0.1-11%). A prolongation of refractoriness (+71.5±71.2 ms compared to control), followed by an increase in prevention efficacy, resulted from applying chronic amiodarone (i.e., 33% efficacy without I_{CaL} block and 72-89% with progressive I_{K1} inhibition). Thus, amiodarone showed the highest prevention efficacy within the tested treatments, consistent with clinical trials (**Figure 8.5A**).

High success rates derived also from 70% I_{Na} block (i.e., flecainide 2 μM) due to a great post-repolarization refractoriness. However, the prolongation of the refractory period and thus, flecainide prevention efficacy, dropped proportionally to a reduction in I_{Na} block (+171.5±164.9 vs. +100.0±131.4 vs. +18.0±35.2 ms; prolongation of the refractory period after 70%, 60%, and 40% I_{Na} block). Similarly, the efficacy of digoxin was proportional to I_{NaK} inhibition. Compared to 30% I_{NaK} block, a 60% inhibition increased 2-fold the refractory period (+22.0±35.0 vs. +53.0±57.7ms) and the efficacy of digoxin (60% I_{NaK} inhibition is considered cardiotoxic, and only calculated to show the main role of I_{NaK} on AF perpetuation).

Interestingly, while pharmacological outcome was largely independent of the extent of LVAs, the atrial ionic current substrate determined treatment success. **Figure 8.5B** analyses the pharmacological outcome (i.e., AF termination vs. non-termination) of three drugs commonly used for rhythm control of AF according to the atrial ionic current profile (88 of the 100 profiles are included in the analysis since 12 failed to sustain AF, **Figure 8.2**). These ionic profiles have been grouped into three categories: profiles with a favourable drug response in all (100%) LVA distributions, in most of them (50-90% of LVA distributions), and in only a few (0-50%). **Figure 8.5C** infers about potential patient stratification by differentiating the ionic current characteristics of atria responding to one drug or another.

Vernakalant lost efficacy in atria with low I_{CaL} and high I_{NaK}. As the major I_{Kur} blocker considered, vernakalant prolonged the refractory period to a lesser extent in atria with low I_{CaL} (+80.0±36.4 vs. +15.8±26.3ms; prolongation of refractoriness in atria responding vs. non-responding to vernakalant). Because models refractory to vernakalant additionally showed high I_{NaK}, they were characterised by higher excitability (refractory period: 159.4±43.3 vs 124.2±17.5 ms; models responding vs. non-responding to vernakalant), so that I_{Kur} inhibition was not sufficient to terminate AF.

Amiodarone was efficacious in most ionic current profiles (65/88, **Figure 8.5B**). However, it failed to prevent AF in virtual atria with the shortest refractoriness (153.4±40.0 vs. 118.3±16.9 ms; atria responding vs. non-responding to amiodarone), due to significant I_{K1} and I_{NaK} up-regulation, and I_{CaL} and I_{NCX} down-regulation.

Finally, flecainide increased post-repolarization refractoriness through I_{Na} inhibition. Therefore, virtual patents presenting I_{Na} up-regulation were less sensitive to I_{Na} block.

The comparison of the ionic current profiles of atria responding to either drug (**Figure 8.5C**) revealed that vernakalant and amiodarone were superior to flecainide for AF termination when I_{Na} was up-regulated. When I_{CaL} and I_{Na} were down-regulated, I_{Na} inhibition was a very effective strategy (as explained above), so that flecainide was the desired approach for AF termination. When comparing amiodarone and vernakalant, vernakalant was favourable for I_{CaL} up-regulation.

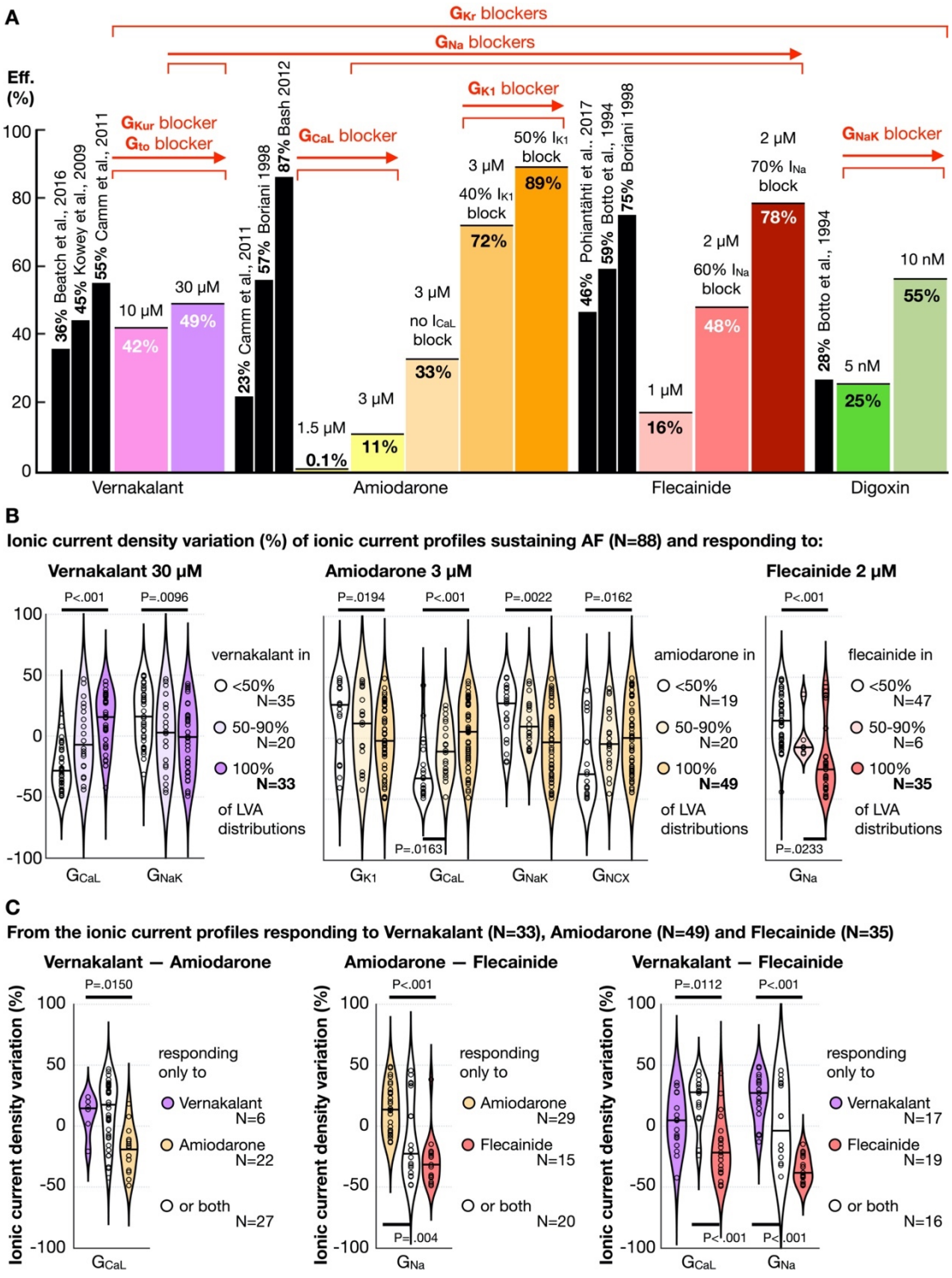


Figure 8.5. In-silico trials over 494 AF episodes with 12 pharmacological treatments. **A)** Comparison between the success rates (Efficacy, Eff.) obtained in-silico (colour bars) and in human clinical trials (black bars). A threshold of 25% block at therapeutic plasma concentration has been considered to group drugs according to the ionic current channel they target. The arrows point towards greater ionic current density block. **B)** Comparison of the ionic current density of virtual patients responding and not responding to pharmacological treatment for a different number of LVA distributions. The three drugs considered are Vernakalant 30 μM, Amiodarone 3 μM without ICaL block and Flecainide 2 μM with 60% INa block. **C)** Comparison of the ionic current densities of virtual patients only responding to drug-A against those only responding to drug-B (where drug-A and drug-B are the three antiarrhythmic drugs shown in panel B). Only ionic current densities presenting significant differences are displayed in the comparisons illustrated in panel B and C.

8.4.5. Decision algorithm for optimal pharmacological treatment selection

Flecainide was the preferred choice for inward current down-regulation. Conversely, for elevated I_{Na}, vernakalant and amiodarone were a better option, the former for high I_{CaL} and the latter for atria presenting the highest cellular excitability (I_{Na} up-regulation with additional I_{CaL} down-regulation). These findings have been used to develop the decision algorithm shown in **Figure 8.6**, considering also that (1) in severely remodelled left atrium, with LVAs covering more than 40% of the posterior wall, sustained AF requires higher I_{K1} and rotors localize in healthy right atrium, and (2) for lower LVA extensions, rotors can also anchor to LVAs for short refractoriness (low I_{CaL}).

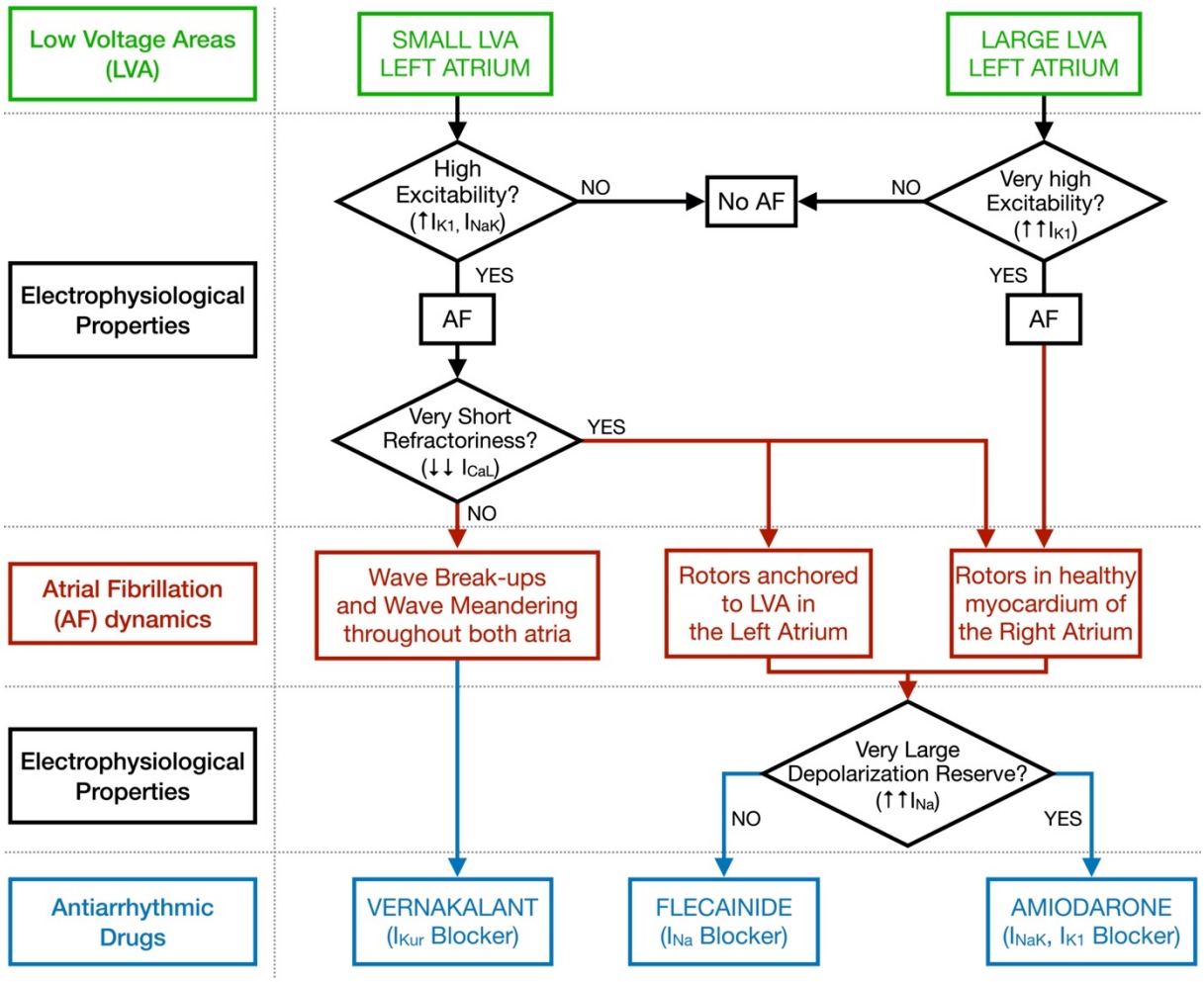


Figure 8.6. Decision algorithm for optimal stratification of virtual AF patients to antiarrhythmic drug therapy.

8.5. Discussion

In this study, in-silico trials were conducted in a large cohort of human atria with electrophysiological and structural variability. Considering electrophysiological variability is crucial for overcoming bias associated with drug effects, since the success of pharmacological therapy depends on the specific ionic current substrate of the atria. Similarly, including structural variability is crucial to represent complex

AF dynamics. As such, I have identified several structural and electrophysiological characteristics that modulate AF mechanisms and management, and have leveraged them to create a decision algorithm for guiding the decision-making of AF therapy.

I have observed that the inward currents (I_{CaL} and I_{Na}) are critical for optimal stratification of AF patient to pharmacological treatment. Notably, as presented in **Chapter 6** and **Annex III**, ECG markers could characterise this ionic current substrate and help with patient stratification.

8.5.1. Pharmacological treatment is influenced by the patients' ionic current substrate

The ionic current substrate, rather than the extent, location or distribution of LVAs, played the most important role on pharmacological AF management. I have shown in **Chapter 6** that the ionic current profile of the atria influences antiarrhythmic drug outcome in structurally healthy-atria. Moreover, several simulation studies (Passini *et al.*, 2016, 2017) have evidenced the relevance of ionic current variability to assess drug-induced myocardial proarrhythmia. This is important as it underlines the possibility of predicting the response to pharmacological treatment using the patients' individual ionic current profile (Capucci *et al.*, 2018).

In the in-silico trials, a success rate of 49% was observed after the virtual administration of vernakalant. A success rate of 65% was obtained in structurally-healthy atria (**section 6.4.4**). The latter results are consistent with a randomized clinical trial conducted in patients with recent-onset AF (Simon *et al.*, 2016), reporting an efficacy of 69% (34/49 patients). As in the present study, lower rates, i.e., 37% (81/221 patients (Roy *et al.*, 2008)), 46% (59/129 patients (Beatch and Mangal, 2016)) and 52% (60/116 patients (Camm *et al.*, 2011)), were obtained when additionally considering persistent AF patients, reflective of a more advanced AF substrate.

I obtained low efficacies for acute modelling of amiodarone (i.e., 0.1-11%). It has been suggested that the high cardioversion of amiodarone results from the long-term accumulation of desethylamiodarone metabolite (Talajic, DeRoode and Nattel, 1987). Other authors advocate for amiodarone-induced I_{Na} inhibition as the primary mechanism involving rotor termination (discussed in **section 6.5.1**). When I modelled amiodarone without I_{CaL} inhibition, a three-fold increase in its prevention efficacy (i.e., 33%) was observed. In a study conducted with rabbit ventricular cardiomyocytes, acute but not chronic exposure to amiodarone inhibited I_{CaL} (Varró, Virág and Papp, 1996). Moreover, even when amiodarone proved to be a strong Ca^{2+} channel blocker experimentally (Nishimura, Follmer and Singer, 1989), the authors suggested that very little block (i.e., 1-2%) would be expected under clinical conditions. Further experimental studies found that chronic treatment with amiodarone reduced I_{NaK} by 33% (Gray *et al.*, 1998) and exerted a strong inhibition of I_{K1} (Guillemare, Marion and Gautier, 2000). I found I_{K1} crucial for AF maintenance (as in **Chapter 6**), so that when chronic amiodarone considered progressive I_{K1} block, success rates of 72-89% were observed, matching clinical trials (Bash *et al.*, 2012).

Virtual flecainide administration also showed consistency between the simulated efficacy, i.e., 48-78%, and the success rate observed in clinical trials, i.e., 46% (46/100 patients (Pohjantähti-Maaroos *et al.*, 2019)), 59% (20/34 patients (Botto *et al.*, 1994)), and 75% (52/69 (Boriani *et al.*, 1998)). Different degrees of I_{Na} inhibition were considered, including high degrees of block observed at fast activation rates (Moreno *et al.*, 2011). Accordingly, I observed an increase in flecainide efficacy with increasing I_{Na} block, particularly in atria with low I_{Na}. In patients with I_{Na} down-regulation, additional I_{Na} inhibition (i.e., flecainide) could pose a risk to the normal electrical conduction. However, the sever I_{Na} block exerted by flecainide in this study would only be expected at very high atrial rates (i.e., those observed during fibrillation). Under these high rates, flecainide application might even result in a complete loss of tissue excitability, as seen in atrial trabeculae after the application of compounds with a strong rate-dependent I_{Na} block (Wettwer *et al.*, 2013). Conversely, a minimal I_{Na} block, and thus preserved conduction, would be expected during normal sinus rhythm (i.e., lower atrial rates).

A similar dose-dependent increase in the success rate derived from progressive I_{NaK} inhibition (i.e., virtual digoxin administration). Digoxin is however administered at low doses, due to the toxicity associated with cardiac glycosides (Bueno-Orovio *et al.*, 2014) Nevertheless, while observational studies have reported an increased mortality with high plasma levels of digoxin (Hindricks *et al.*, 2021), a recent randomized controlled trial reported a lower rate of adverse events with low-dose digoxin compared to bisoprolol (β-blocker) in patients with permanent AF and heart failure (Kotecha *et al.*, 2020). In this study, low-dose digoxin (i.e., 5 nM and 30% INaK inhibition) had only a 25% efficacy, consistent with its current use as rate control, rather than rhythm control (Hindricks *et al.*, 2021). However, digoxin-induced I_{NaK} inhibition and the subsequent excitability reduction, hold potential for terminating re-entrant drivers (as also shown in **Chapter 6**), especially if combined with other antiarrhythmics drugs

8.5.2. Fibrillation drivers are not exclusive of scarred areas

I identified small and patchy LVAs as the preferred location for these re-entrant drivers. The predisposition of rotational activity for LVAs has been widely demonstrated, both in clinical (Honarbakhsh *et al.*, 2019) and simulation studies (Azzolin *et al.*, 2023). This, together with the high prognostic value of LVAs for predicting AF recurrence after catheter ablation (Masuda *et al.*, 2020), led to consider ablation of LVAs as an attractive personalized approach (Junarta *et al.*, 2022). Nevertheless, as mentioned in **section 2.3.2**, only ERASE AF (Huo *et al.*, 2022) has shown superiority to PVI in persistent AF patients, after VOLCANO (Masuda *et al.*, 2020) and STABLE-SR-II (Yang *et al.*, 2022) reported no beneficial impact in neither paroxysmal nor persistent AF, respectively.

Furthermore, presence of LVAs might not necessarily correlate with AF drivers (Kircher *et al.*, 2018). LVAs show low specificity detecting AF sources, with only a small LVA proportion harbouring proarrhythmic potential (Chen *et al.*, 2019). This is, while transient rotational activity might localize

within LVAs, not all LVA regions might be associated with rotational activity. Similarly, in this study I found that large and scattered LVAs had a passive role on AF perpetuation, with high atrial activity arising only within small LVAs.

This is in agreement with previous simulation studies (McDowell *et al.*, 2015; Roney *et al.*, 2016), observing that large degrees of fibrosis prompted wavefront meandering and loss of anchors. However, as opposed to these studies, I did not find spontaneous termination under such conditions, since large LVA infiltration in the left atrium yielded rotor drift towards the right atrium. The latter chamber, modelled as structurally-healthy tissue, always presented high atrial activity (i.e., high-frequency regions). Indeed, I commonly observed atrial activity of higher frequency in structurally-healthy regions, with functional rotors coexisting with rotors anchored to areas of scarring. This has been previously attributed to a hierarchical organization in activation frequency (Atienza *et al.*, 2006), with high-frequency sources most likely harbouring functional rotors (Rodrigo *et al.*, 2014).

The coexistence of rotors in structurally-healthy and structurally-remodelled areas could explain the lack of beneficial impact of LVA ablation in paroxysmal AF patients. In (Masuda *et al.*, 2020), the authors suggested that the presence of LVAs in these patients underlined a natural predisposition to develop an arrhythmogenic substrate, which could promote AF even post-ablation (Masuda *et al.*, 2020). Further explanations considered the primary role of triggered ectopy compared to arrhythmogenic substrate on paroxysmal AF (Masuda *et al.*, 2020; Junarta *et al.*, 2022). Here, however, I present an additional hypothesis to the lack of efficacy of LVA ablation, based on the assumption that the structural substrate is not the only arrhythmogenic perpetuator. As illustrated in this study, re-entrant sources arising in structurally-healthy regions may sustain AF, even when presented together with rotors anchored to structural heterogeneities.

8.5.3. Ionic current dysregulation is crucial for AF maintenance

Several ionic current dysregulations contributed to the stabilization of the above-mentioned functional drivers, namely, the down-regulation of I_{CaL} and the up-regulation of I_{K1}, I_{to} and I_{NaK}. Indeed, atria presenting this ionic current substrate sustained AF irrespective of the LVA distribution. Numerous simulation studies (Morgan *et al.*, 2016; Zahid *et al.*, 2016; Boyle *et al.*, 2019) have regarded fibrosis as the main determinant of AF inducibility, maintenance and overall dynamics. Conversely, in this population of virtual patients, while LVAs influenced AF dynamics, the ionic current substrate played a crucial role. Clinically, AF inducibility and maintenance have proven common in human patients without structural heart disease (Kumar *et al.*, 2012). Therefore, despite the central role of the structural remodelling on AF perpetuation, a more complex interaction between structural and functional perpetuators is likely to dictate AF dynamics (Heijman, Linz and Schotten, 2021).

As in my simulations, previous studies highlighted the role of I_{K1} on rotor stabilization and AF acceleration (Atienza *et al.*, 2006; Pandit and Jalife, 2013). More specifically, decreased I_{CaL} and

increased I_{K1} have been considered the primary electrical remodelling causing a progressive increase in the dominant frequency in paroxysmal AF (Martins *et al.*, 2014). Similarly, I found that I_{K1} up-regulation increased AF dominant frequency, independently of additional ionic current dysregulations. This increase was further exacerbated when combined with I_{CaL} down-regulation, with both ionic current dysregulations yielding high-frequency f-waves in the ECG.

8.6. Conclusion

The in-silico trial conducted in **Chapter 8** has further demonstrated consistency between simulated and clinical results, and that the ionic current substrate of the atria modulates pharmacological treatment. Accordingly, assessing the individual atrial ionic current profile could yield an optimal stratification of patients to specific antiarrhythmic drugs. In this regard, the analysis of the ECG holds potential for non-invisibly characterising the ionic current profile (further evidence provided in **Annex III**).

However, this chapter only considered structurally-remodelled left atrium, since many studies have reported that the extent of LVAs in the left atrium has prognostic value for predicting AF recurrence after pulmonary vein isolation (Masuda *et al.*, 2020). Nevertheless, findings may be determined by the relative distribution of LVAs between the atria, so that future studies should consider accurate LVA infiltration in both the right and left atrium. Similarly, while I considered different LVA distributions in the left atrium, all simulations were performed with the same atrial anatomy. The structural remodelling of the atria is also associated with variations in atrial shape and size. Therefore, the following chapter considers a population of virtual patients with anatomical variability and presence of bi-atrial LVA remodelling.

CHAPTER

IN-SILICO TRIALS GUIDE OPTIMAL STRATIFICATION OF AF PATIENTS TO PHARMACOLOGICAL AND CATHETER ABLATION THERAPIES

9

*As mentioned in **Section 2.3.2**, PVI is the most effective therapy for paroxysmal AF. However, half of patients with persistent AF experience recurrence after PVI, and no consensus is established for second treatments. In this chapter, I conducted in-silico trials with 12 additional treatments in a population of virtual patients presenting AF despite PVI. The population considers human-representative variability, which allows informing the stratification of patients with AF recurrence after PVI to optimal pharmacological and ablation therapies. The original work can be found in: "Dasí et al., (2024), EP Europace. DOI: 10.1093/europace/euae150.*

9.1. Summary of the study

A cohort of 800 virtual patients, with variability in atrial anatomy, electrophysiology, and tissue structure (LVAs), was developed and validated against clinical data from ionic currents to ECG. Virtual patients presenting AF post-PVI underwent 12 secondary treatments. Sustained AF developed in 522 virtual patients after PVI. In-silico trials reproduced the outcome reported in clinical trials and studies and provided mechanistic explanations to treatment success. Second ablation procedures involving left atrial ablation alone showed 55% efficacy, only succeeding in small right atria (<60mL). When additional cavo-tricuspid isthmus ablation was considered, Marshall-Plan sufficed (66% efficacy) for small left atria (<90mL). For bigger left atria, a more aggressive ablation approach was required, such as anterior mitral line (75% efficacy) or posterior wall isolation plus mitral isthmus ablation (77% efficacy). Virtual patients with LVAs greatly benefited from LVA ablation in the left and right atria (100% efficacy). Conversely, in the absence of LVAs, synergistic ablation and pharmacotherapy could terminate AF. In the absence of ablation, the patient's ionic current substrate modulated the response to drugs, being the inward currents critical for optimal stratification to amiodarone or vernakalant.

9.2. Introduction

Persistent AF patients experience 50% recurrence after PVI (Verma *et al.*, 2015), suggesting an additional substrate for arrhythmia beyond pulmonary venous ectopic triggers. Nevertheless, since additional empirical ablation has not demonstrated incremental benefit in large clinical trials (STAR AF II (Verma *et al.*, 2015), or CAPLA (Kistler *et al.*, 2023)), PVI remains the recommended ablation strategy at the first procedure (Betts *et al.*, 2023). In patients who experience AF recurrence despite durable PVI (Benali *et al.*, 2023), there is no consensus regarding the optimal further treatment strategy.

As mentioned in **section 2.3.2**, novel ablation strategies (i.e., Marshall-Plan (Derval *et al.*, 2021), MiLine (Bergonti, Spera, Ferrero, Nsahlai, Bonomi, Boris, *et al.*, 2023), and LVA ablation (Huo *et al.*, 2022)) have shown promising results. However, these strategies rely on extensive ablation lesions or are counter to the paradigm of patient-specific ablation. Thus, the ability to accurately stratify patients with AF recurrence after PVI to those requiring extensive versus minimal substrate modification, those benefitting from empirical versus functional ablation, and those who may be optimally treated only with additional antiarrhythmic drug therapy, would be of tremendous clinical value but remains a major challenge.

The aim of this study was to provide evidence for the optimal stratification of patients with AF recurrence after PVI to 12 state-of-the-art pharmacological and ablation therapies.

9.3. Methods

9.3.1. Overview of study design

A total of 800 virtual AF patients with durable PVI underwent a non-pulmonary vein-based AF induction protocol. The subset with sustained arrhythmia despite PVI were then subjected to 12 independent further treatments for AF (**Figure 9.1**). This served to identify specific subgroups of patients that, based on their clinical characteristics, were most likely to respond to a specific treatment. These clinical features were used to inform a decision algorithm for the optimal stratification of AF patients to specific catheter ablation strategies and/or antiarrhythmic drug therapies.

9.3.2. Virtual AF patients

The cohort of 800 virtual AF patients was designed to have variability in anatomy, electrophysiology, and tissue structure, based on human data and recreating the heterogeneity encountered in clinical practice (**Figure 9.1**). In line with STABLE-SR-II (Yang *et al.*, 2022), one-half of the cohort was modelled without LVAs. These 400 virtual AF patients were developed combining 40 widely-variable ionic current profiles with 10 population-representative atrial anatomies.

Anatomical variability. The atrial anatomies in the virtual cohort were selected to span volume ranges associated with AF recurrence (right and left atrial volume [80, 148] mL and [65, 112] mL, respectively (Lang *et al.*, 2015)). Thus, the 10 atrial anatomies presented in **Section 4.2.2.1** were considered.

Electrophysiological variability. Forty atrial cardiomyocyte profiles were identified to mimic variability in experimental recordings. An initial population of 60 atrial cardiomyocyte models was created as described in **section 4.1.2**. From the initial population, 40 cardiomyocyte models captured the action potential characteristics of right atrial trabeculae from persistent AF patients (Sánchez *et al.*, 2014). Each of these 40 cardiomyocyte models, representative of the right atrial tissue, was scaled to reflect electrophysiological heterogeneities in six atrial regions, as described in **section 4.2.1**. Every virtual patient presented a unique combination of ionic current profile and atrial anatomy, resulting in 400 human bi-atrial models with variability in anatomy and electrophysiology (**Figure 9.1**). Regional heterogeneities in conduction velocity and anisotropy were also included, setting the baseline plane wave velocity to 80 cm/s in the bulk tissue. After considering variability in the ionic current profile (e.g., ±50% variation in I_{Na} density), the population of virtual patients had a conduction velocity in the bulk tissue ranging between 58.8 and 102.5 cm/s (86.9±18.3 cm/s; median ± IQR).

Structural variability. To develop the other half of the cohort, each of the 400 virtual patients was duplicated into a version that considered LVAs. LVAs occupied at least 15% of the left atrium, as this LVA extension has been associated with AF recurrence in patient with persistent AF (Bergonti, Spera, Ferrero, Nsahlai, Bonomi, Tijskens, *et al.*, 2023). Moreover, the same degree of LVAs was modelled in the right atrium, since structural remodelling occurs in both atria (Hopman *et al.*, 2023).

To incorporate LVAs, the bi-atrial electro-anatomical maps of 20 (85% persistent) AF patients (Pope *et al.*, 2021) were registered to the endocardial surface of the bi-atrial statistical shape model. Then, the bipolar voltage data of all 20 patients were superimposed into the same atrial geometry to build a probabilistic LVA map, i.e., identifying those atrial regions most likely to undergo LVA remodelling. These most probable areas were assigned to be LVA until 15% of the left and right atrium was remodelled. Finally, the LVA distribution created in the bi-atrial statistical shape model was extended to the 10 atrial anatomies. **Figure 9.1** shows the 15% LVA extension in the right and left atrium in a representative anatomy. LVAs were simulated as described in **section 4.2.2.2**.

Pulmonary vein isolation and AF induction. To simulate AF recurrence after PVI, the pulmonary veins of virtual patients were isolated before applying the AF induction protocol. PVI was modelled as in (Roney *et al.*, 2022), considering a wide circumferential ablation. For consistency across different atrial anatomies, the circumferential ablation was applied at the minimum distance from the veins that enabled their complete isolation. The ablation lesions were modelled by making cells of the atrial mesh unexcitable.

After the virtual application of PVI, spiral wave re-entries were imposed in the atria as the initial conditions of the simulation and AF dynamics were analysed for 7 s of activity. This protocol, described in **section 4.3**, mimicked AF initiation from non-specific triggers outside the pulmonary veins.

9.3.3. In-silico trials

Virtual patients with uninterrupted arrhythmia (i.e., > 7 s of organized flutter or AF) after PVI were independently subjected to nine ablation strategies and two antiarrhythmic drugs. Two additional drugs were applied after ablation if arrhythmia sustained for all ablation procedures (**Figure 9.1**).

The ablation strategies considered: (i) Posterior wall isolation, PWI (Kistler *et al.*, 2023) (ii) PWI plus mitral isthmus (MI) line, PWI+MI; (iii) PWI+MI plus cavo-tricuspid isthmus line (CTI), PWI+MI+CTI; (iv) Anterior mitral line, MiLine (Bergonti, Spera, Ferrero, Nsahlai, Bonomi, Boris, *et al.*, 2023); (v) MiLine+CTI; (vi) Marshall-Plan (Derval *et al.*, 2021); and (vii-ix) ablations of LVAs in three steps: only isolating LVAs in the left atrium, as in STABLE-SR-II (Yang *et al.*, 2022) and ERASE-AF (Huo *et al.*, 2022), together with CTI block, and with CTI block and right atrial LVA ablation. Two drugs could be applied on top of the ablation procedure: amiodarone 1.5 μM and digoxin 10 nM.

The pharmacological arm considered: (i) amiodarone 3.0 μM; and (ii) vernakalant 30 μM. Drug action was simulated as a simple pore-block model, considering the doses within the therapeutic plasma concentration. **Table 9.1** shows the percentage of ionic current block.

Table 9.1. Ionic current block (%) exerted by the antiarrhythmic drugs.

Treatment (concentrations)	**Ionic current block (%)**								
	I_{Kur}	I_{Kr}	I_{to}	I_{K1}	I_{Ks}	I_{CaL}	I_{NaK}	I_{NCX}	I_{Na}
Amiodarone (1.5 μM)	-	40	-	-	30	-	-	30	20
Amiodarone (3.0 μM)	-	70	30	20	50	-	40	50	50
Vernakalant (30 μM)	70	60	70	-	-	20	-	-	70
Digoxin (5 nM)	-	-	-	-	-	-	30	-	-

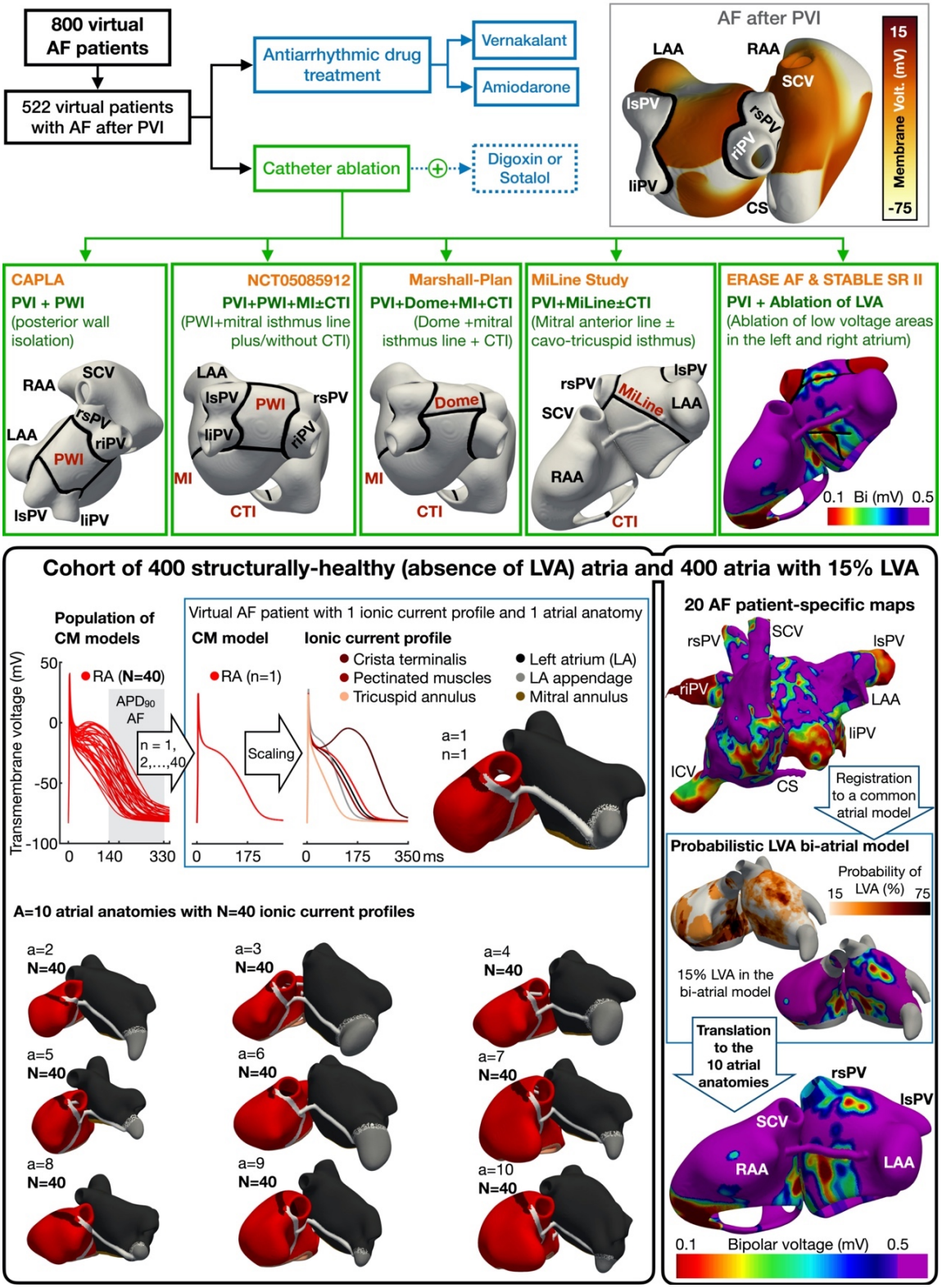


Figure 9.1. Top) Study design: virtual patients with AF despite PVI are subjected to second procedure treatments. **Bottom)** Population of 400 virtual patients with absence of LVAs: Forty cardiomyocyte (CM) models, representative of right atrial tissue, are considered. The 40 ionic current profiles, with consideration of regional heterogeneities, are used to populate 10 atrial anatomies, resulting in 400 human atria. The cohort is extended to 800 virtual patients by adding LVAs into each of the 400 atria, using a probabilistic LVA map derived from 20 AF patients. A representative model with 15% LVA extension in the right and left atrium is shown. Abbreviations. **RA-LA**: right and left atrium; **RAA-LAA**: RA and LA appendage; **SCV-ICV**: superior and inferior cava vein; **rs-ri-ls-li-PV**: right superior, right inferior, left superior and left inferior pulmonary vein; **CS**: coronary sinus.

9.4. Results

9.4.1. Primary outcome

Sustained arrhythmia (i.e., organized flutter or AF) occurred in 522 (65%) virtual patients despite PVI (243 and 279 with absence and presence of LVA, respectively; the type of arrhythmia observed with and without LVAs is explained below). **Table 9.2** summarizes the efficacy of each treatment according to presence of LVAs, and compares the efficacy obtained in-silico and in clinical studies.

Table 9.2. Efficacy of second strategies according to presence of LVAs. Comparison between in-silico and clinical trials. Abbreviations. **PWI**: Posterior wall isolation; **MI**: Mitral isthmus ablation; **CTI**: Cavo-tricuspid isthmus ablation; **MiLine**: Anterior mitral line; **LVA_{LA}–LVA_{RA}**: Ablation of LVAs in the left (LA) and right atrium (RA).

Treatment	Number of patients free from arrhythmia after treatment (N (%))				
	In-silico trials			Clinical trials /studies	
	absence LVAs (N=243)	presence LVAs (N=279)	Total (N=522)	N (%)	Name
Amiodarone	160 (66%)	140 (50%)	**300 (57%)**	65 (61%)	AMIO-CAT
Vernakalant	135 (56%)	163 (58%)	**298 (57%)**	60 (52%)	AVRO
PWI	10 (4%)	0 (0%)	**10 (2%)**	89 (52%)	CAPLA
PWI+MI	127 (52%)	146 (52%)	**273 (52%)**		
PWI+MI+CTI	187 (77%)	217 (78%)	**404 (77%)**	147 (74%) 36 (80%)	Li et al., 2023 Davong et al., 2023
Marshall-Plan	182 (75%)	170 (61%)	**352 (67%)**	54 (72%)	Marshall-Plan
MiLine	130 (53%)	152 (54%)	**282 (54%)**	69 (63%)	MiLine Study
MiLine+CTI	186 (77%)	206 (74%)	**392 (75%)**		
LVA_{LA}	-	**156 (56%)**	-	29 (57%) 46 (65%)	ERASE-AF STABLE-SR-II
LVA_{LA}+CTI	-	222 (80%)	-	-	-
$LVA_{LA\text{-}RA}$+CTI	-	279 (100%)	-	-	-

In the cohort of 552 virtual patients with AF after PVI, additional PWI had no incremental benefit, in agreement with CAPLA (Kistler *et al.*, 2023), and arrhythmia only stopped in 2% of cases. Higher success rates were observed when PWI was applied together with mitral isthmus (PWI+MI) and cavo-tricuspid isthmus ablation (PWI+MI+CTI): 52% and 77%, respectively. Similar efficacies derived from the virtual application of MiLine and MiLine+CTI: 54% and 75%, in agreement with 63% reported clinically (Bergonti, Spera, Ferrero, Nsahlai, Bonomi, Boris, *et al.*, 2023). Virtual Marshall-Plan prevented 67% of AF cases, comparable to 72% observed in human patients (Derval *et al.*, 2021). Finally, LVA ablation was applied in the 279 virtual patients with LVA remodelling, and 56%, 80% and 100% efficacy were observed for LVA ablation in the left atrium (LVALA), together with cavo-tricuspid isthmus block (LVA_{LA}+CTI) and LVA ablation in the right and left atrium (LVA_{LA}+CTI+LVA_{RA}), respectively. Regarding the antiarrhythmic drug arm, both amiodarone and

vernakalant had a success rate of 57%, as observed clinically (Hindricks *et al.*, 2021). The credibility of in-silico trials is supported by the overall agreement with the efficacy reported in clinical trials.

9.4.2. Arrhythmia despite PVI

Two-hundred forty-three virtual patients with absence of LVAs had inducible arrhythmia despite PVI. In 57% (137 of the 243) this was an organised atypical flutter around the rings of the isolated veins, whilst in 43% it was AF. AF was facilitated by shorter tissue refractoriness (172.3±13.0 vs. 230.6±47.7 ms; virtual patients with AF vs. flutter, respectively; mean ± SD) and a larger right atrium (i.e., AF proportion increased by 0.21% per mL increase in right atrial volume). The latter enabled sustained arrhythmia in virtual patients with faster conduction velocity (95.0±6.1 vs. 75.3±5.7 cm/s; mean wave velocity in the bulk tissue observed in virtual patients with right atrial volume bigger vs. smaller than 90 mL, respectively).

LVA remodelling increased the proportion of virtual patients sustaining AF to 60% (166 of the 279), whilst the remaining 40% had organized flutter. **Figure 9.2** illustrates representative LVAs in the left and right atrium associated with lower and higher proarrhythmic potential. An increase in arrhythmia complexity owed to a higher amount of pathological conduction patterns located in LVAs. Furthermore, the proarrhythmic potential of LVAs depended on the atrial refractoriness, modulated by the ionic current variability and the resulting electrophysiological substrate.

AF drivers (i.e., sources of electrical activity with the fastest activation time) were observed within LVAs only in virtual patients with the shortest refractoriness (168.5±12.1 ms). When these patients additionally presented slower conduction velocity (75.3±5.7 cm/s), rotors anchored to smaller LVAs (**Figure 9.2, top**). On the other hand, rotors were observed in bigger LVAs (**Figure 9.2, middle**) for virtual patients with higher conduction velocity (95.0±6.1 cm/s). Throughout the population, rotors only anchored to dense and more spherical LVAs that presented healthy myocardium in their surroundings (**Figure 9.2, bottom**). In virtual patients with longer refractoriness (237.8±46.6 ms), drivers were observed in healthy myocardium, and LVAs contributed to AF perpetuation by creating localized irregular activity (i.e., changes of wavefront direction). In these patients, AF maintenance and the success of ablation therapy were determined by the right and left atrial volumes, as discussed below.

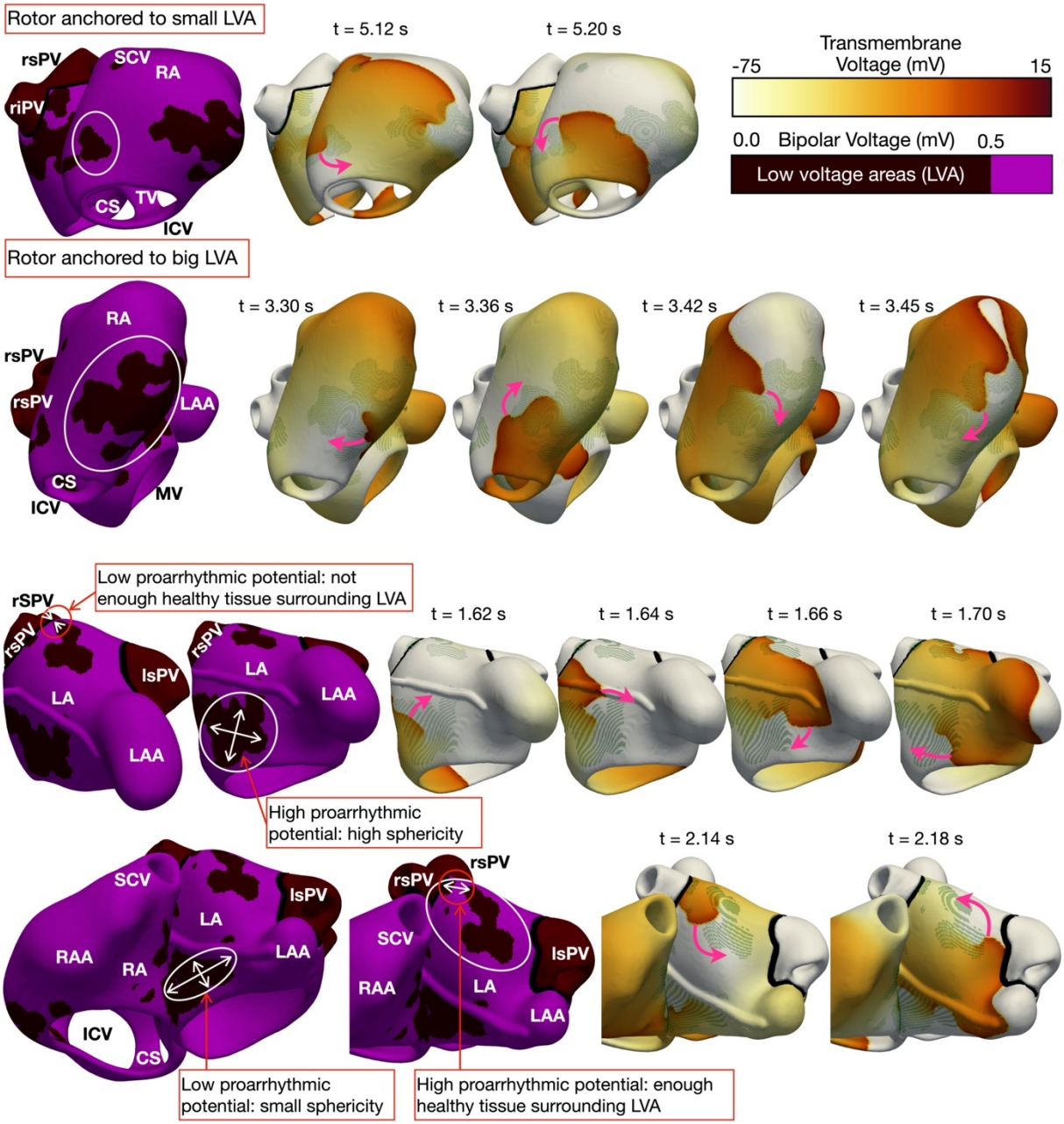


Figure 9.2. Proarrhythmic potential of LVAs. Re-entrant drivers anchored to smaller LVAs in virtual patients with short refractoriness and slow conduction velocity. Virtual patients with higher conduction velocity showed rotors within bigger LVAs. Rotors only anchored to LVAs that presented enough healthy myocardium in their surroundings. Higher proarrhythmic potential derived from more spherical rather than elongated LVA shapes. Abbreviations. **RA-LA**: right and left atrium; **RAA-LAA**: RA and LA appendage; **SCV-ICV**: superior and inferior cava vein; **rs-ri-ls-li-PV**: right superior, right inferior, left superior and left inferior pulmonary vein; **MV-TV**: mitral and tricuspid valve; **CS**: coronary sinus.

9.4.3. Catheter ablation as second procedure treatment

The success of second ablation procedures was determined by the extent of bi-atrial enlargement and presence of LVAs. Thus, positive ablation outcomes derived from targeting anatomic and functional structures in the left and right atrium. Indeed, the importance of additional right atrial ablation is evidenced by comparing the efficacy of strategies that considered CTI ablation (**Table 9.2**).

Additional benefit of cavo-tricuspid isthmus block. Fifty percent of virtual patients presented sustained arrhythmia when only left atrial ablation was considered, regardless of the ablation extent (52%, 54% and 56% arrhythmia freedom after PWI+MI, MiLine and LVA_{LA} ablation, respectively). As explained below, small differences in the efficacy of these strategies regarded whether drivers could still arise in the left atrium post-ablation. Patients with sustained arrhythmia after left atrial ablation were characterized by bigger right atria: no arrhythmia was observed for right atrial volumes lower than 60 mL, and a 40% probability of sustained arrhythmia arose for volumes higher than 100 mL. These patients additionally presented short refractoriness (172.3±13.0 ms), so that right atrial drivers could still perpetuate AF after extensive left atrial ablation.

On the other hand, 67-80% efficacy derived from additionally considering CTI block (67%, 77%, 75% and 80% arrhythmia freedom after Marshall-Plan, PWI+MI+CTI, MiLine+CTI and LVA_{LA}+CTI, respectively). Noteworthy, only 10% of virtual patients where CTI block was successful had originally flutter alone. The other 90% showed a stable macro-re-entry, anchored to an anatomical structure of the right atrium, which potentiated other forms of complex arrhythmias such as unstable rotors anchored to LVAs (**Figure 9.3A**), meandering throughout the right atrial body (**Figure 9.3B**) or breaking into wavelets (**Figure 9.3C**). When the macro-re-entry was eliminated through CTI block, unstable rotors spontaneously vanished.

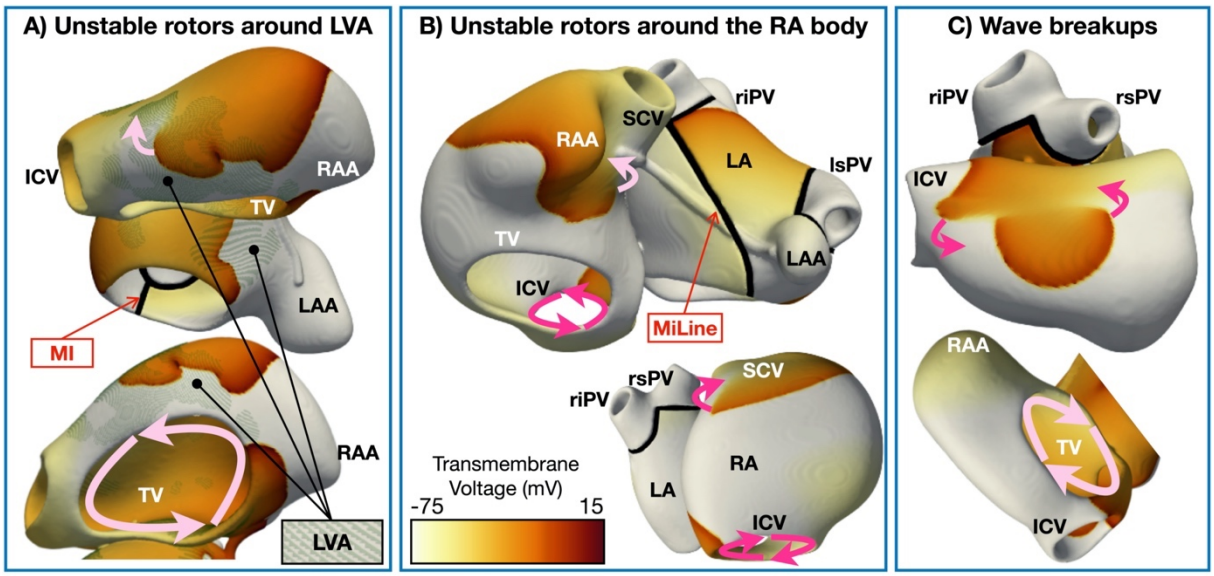


Figure 9.3. Snapshots of complex arrhythmias sustained by the presence of a macro-re-entrant circuit. The arrows show the direction of rotation. One arrow represents unstable rotors (i.e., rotors that vanish if the macro-re-entry is terminated), and two arrows a macro-re-entrant circuit. Abbreviations. **RA-LA**: right and left atrium; **RAA-LAA**: RA and LA appendage; **TV**: tricuspid valve; **SCV-ICV**: superior and inferior cava vein; **rs-ri-ls-li-PV**: right superior, right inferior, left superior and left inferior pulmonary vein; **MiLine:** anterior mitral line of block; **MI:** mitral isthmus line of block.

When CTI block was applied, the success of left atrial ablation depended on the ablation strategy considered, tissue refractoriness and presence of LVAs. **Figures 9.4A-D** illustrate representative

examples of unsuccessful ablation for the ablation strategies that considered CTI block. **Figure 9.4E** shows the number of virtual patients with left vs. right atrial drivers, while **Figure 9.4F** separates the latter between drivers anchored to LVAs or drivers present in healthy myocardium of the right atrium.

Marshall-Plan. Marshall-Plan had a 75% efficacy in virtual patients with absence of LVAs (**Table 9.2**). The lines of block considered by Marshall-Plan (i.e., dome and mitral isthmus) prevented all arrhythmias in virtual patients with a left atrial volume lower than 90 mL. However, since no ablation lines were applied in the roof or anterior wall, where rotors preferentially located (**Figure 9.4Ai-ii**), the proportion of AF increased by 0.15% per mL increase in left atrial volume. The efficacy of Marshall-Plan worsened with LVA presence (61%, **Table 9.2**), since more virtual patients presented drivers anchored to LVAs in the left atrial anterior wall (**Figure 9.4Aii**). In total, 24 and 69 virtual patients with absence and presence of LVAs, respectively, presented drivers in the left atrium.

MiLine+CTI. Compared to Marshall-Plan, anterior mitral line prevented the formation of rotors in the anterior wall of the left atrium for both patients with absence and presence of LVAs. However, after applying MiLine, 6 and 24 virtual patients with absence and presence of LVA, respectively, still presented left atrial drivers. The 6 virtual patients with absence of LVAs had a left atrial volume bigger than 140 mL, which facilitated rotor anchoring in the posterior wall (**Figure 9.4Bi**). The 24 virtual patients with LVAs had varying left atrial sizes (100.5±54.5 mL), but all of them presented very short refractoriness (168.5±12.1 ms). Rotors also appeared in the posterior wall, anchored to small LVAs (**Figure 9.4Bii**). For longer refractoriness, MiLine was very effective even for large left atria.

PWI+MI+CTI. When applied with cavo-tricuspid isthmus block, posterior wall isolation plus mitral isthmus ablation had a similar efficacy in virtual patients with absence and presence of LVA: 77 and 78%, respectively. In the absence of LVAs, drivers were mainly located in the right atrium, but unstable rotors appeared in the anterior wall of the left atrium (**Figure 9.4Ci**). In this subgroup, the proportion of AF increased with increasing right atrial volume (0.16%/mL). Conversely, in the subgroup of virtual patients with LVAs, 18 presented stable left atrial drivers in the anterior wall (**Figure 9.4Cii**).

LVA_{LA}+CTI. Ablation of LVAs prevented all left atrial drivers, showing the highest success rate in the subgroup of virtual patients with LVAs. Fifty-seven patients still had sustained arrhythmia, due to right atrial drivers (**Figure 9.4Dii**, **9.4E**).

Arrhythmia despite left atrial ablation and cavo-tricuspid isthmus block. Despite extensive left atrial ablation and CTI block, these four strategies had an efficacy of 67-80% since drivers could still arise primarily in the right atrium (**Figure 9.4E**). In the subgroup of patients with presence of LVAs, drivers were mostly anchored to LVAs (**Figure 9.4F**). Furthermore, even when drivers located in healthy myocardium of the right atrium, LVAs helped perpetuating the arrhythmia. Consequently, a prevention of 100% was observed after ablating LVAs in the right and left atria plus additional CTI block.

In the subgroup with absence of LVA, 56-61 virtual patients presented right atrial drivers despite left atrial ablation and CTI block (**Figure 9.4E**). In this subgroup no further ablation was considered, since non-focal rotors meandered throughout the right atrial body. Conversely, additional pharmacological treatment successfully stopped the arrhythmias. Low dose amiodarone (i.e., 40% I_{Kr} inhibition) was successful in virtual patients with absence of LVAs when applied on top of the ablation.

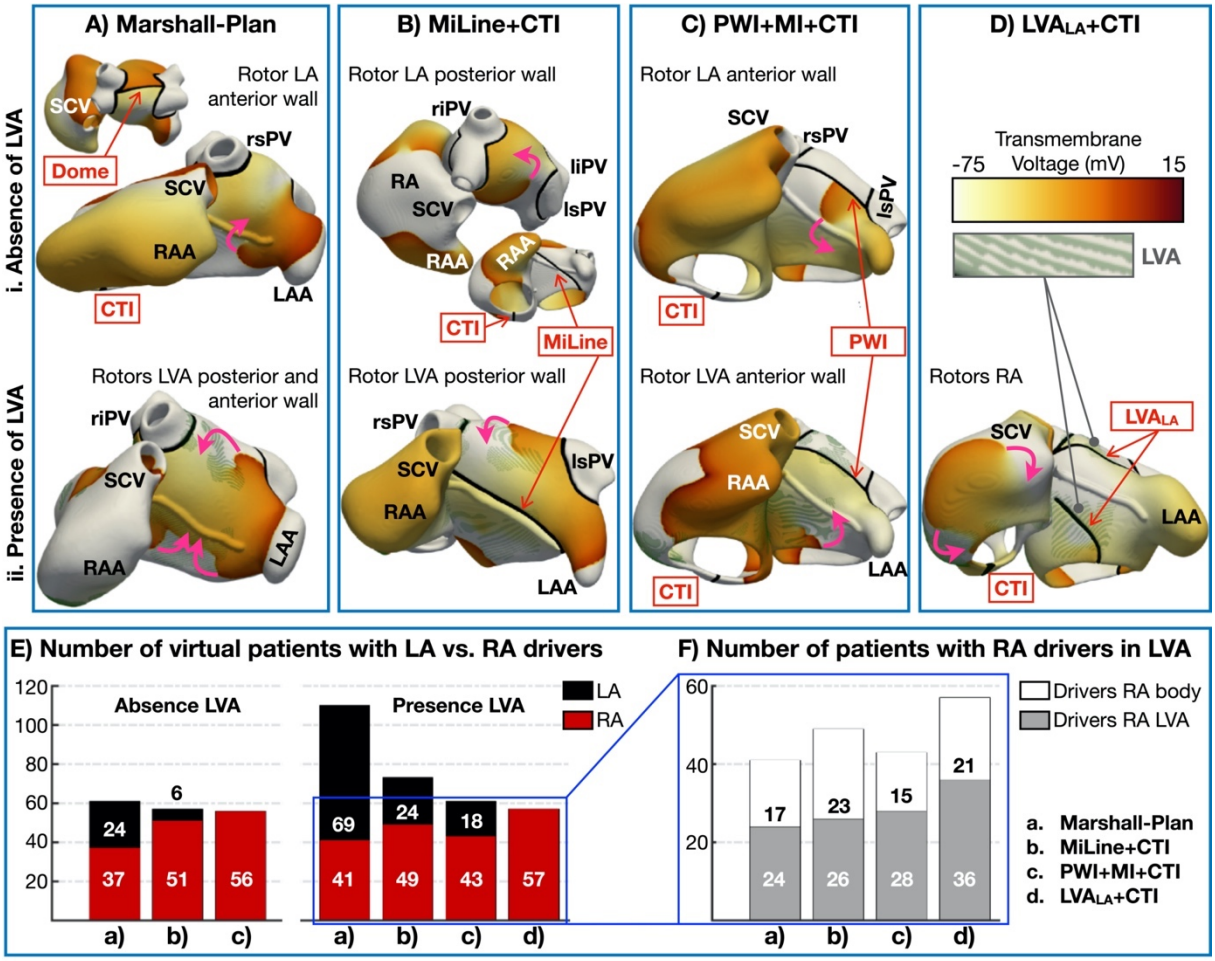


Figure 9.4. Examples of unsuccessful ablation for the strategies considering CTI block. **A)** Re-entrant drivers (the arrows show the direction of rotation) in the anterior and posterior wall of the left atrium after Marshall-Plan. **B)** Rotors in the posterior wall after anterior mitral line (MiLine). **C)** Drivers in the anterior wall after posterior wall isolation and mitral isthmus ablation (PWI+MI). **D)** Ablation of LVAs in the left atrium (LVA_{LA}) prevents left atrial drivers, but right atrial drivers may exist. **E)** Number of virtual patients presenting left atrial vs. right atrial drivers**. F)** Number of virtual patients with right atrial drivers in healthy myocardium vs. anchored to LVA. Abbreviations. **RA-LA**: Right and left atrium; **RAA-LAA**: RA and LA appendage; **SCV-ICV**: Superior and sinferior cava vein; **rs-ri-ls-li-PV**: Right superior, right inferior, left superior and left inferior pulmonary vein.

9.4.4. Antiarrhythmic drugs as second procedure treatment

When antiarrhythmic drugs were virtually-tested post-PVI in the absence of further ablation procedures, the ionic current substrate of the atria determined the response to pharmacological treatment.

Amiodarone. Amiodarone prevented all arrhythmia in atria presenting longer refractoriness (230.7±51.4 ms), resulting from higher I_{CaL} density (0.13±0.08 vs. 0.08±0.02 S/mF; responders vs. non-responders; median ± IQR). For shorter refractoriness, the success rate of amiodarone was also influenced by the structural substrate (i.e., atrial volume and LVA infiltration). LVA infiltration hampered amiodarone efficacy (66% and 50% for absence and presence of LVAs, respectively). Moreover, 88% (73/83) and 82% (114/139) of non-responders with absence and presence of LVAs, respectively, were characterized by a bi-atrial volume bigger than 200 mL. Thus, amiodarone was less efficacious in virtual patients with short refractoriness, big atria and presence of LVAs.

Vernakalant. Vernakalant increased post-repolarization refractoriness through I_{Na} block and thus, virtual patients with I_{Na} up-regulation were less likely to respond to vernakalant (5.2±1.8 vs. 9.1±1.8 S/mF; responders vs. non-responders). Unlike amiodarone, the efficacy of vernakalant was not influenced by atrial size or LVA infiltration (56% and 58% efficacy for absence and presence of LVA, respectively), but by the excitability (i.e., I_{Na} expression) of virtual AF patients.

9.4.5. Key patient characteristics and proposed decision algorithm

Decision trees. In an attempt to rationalise the findings of our large-scale simulation study, three decision trees were built: one for the selection of optimal ablation therapy in virtual patients with absence of LVA, one considering ablation in virtual patients with LVA, and one for optimal drug therapy in the entire cohort. In all three cases, key patient characteristics were used as features. Therefore, the complete dataset considered 522 items (i.e., 522 virtual patients with sustained AF), and 12 attributes (i.e., nine ionic current densities, right and left atrial volumes, and tissue refractoriness). The datasets for ablation therapy considered the same number of attributes (i.e., patient characteristics) but included 243 and 279 items for virtual patients with absence and presence of LVA, respectively. The vector of labels was constructed by assigning to each virtual patient (i.e., rows) the least aggressive treatment that terminated AF (e.g., the strategy that considered less tissue ablated).

Figure 9.5 illustrates decision algorithms built using the entire dataset of features and the MATLAB function *fitctree*. In this scenario, the trees included many branches (especially for ablation of virtual patients without LVA), since the algorithm tried to provide optimal stratification for every virtual patient in the dataset (i.e., overfitting). However, a careful examination of the trees allowed identifying key patient characteristics determining optimal stratification. For example, in both ablation trees, virtual patients with a right atrial volume below 61 mL or longer tissue refractoriness (>195–200 ms) were stratified to left atrial ablation alone (**Figure 9.5,** LVA_{LA} and MiLine). This is not surprising since, as mentioned in **Section 9.4.2**, virtual patients with long tissue refractoriness presented atypical flutter in the left atrium. Moreover, larger right atria prompted the appearance of rotors in this chamber.

Therefore, virtual patients with LVA and bigger right atria (>61 mL) were stratified to additional CTI, which could be applied alone or together with LVA ablation in the right atrium (LVA_{RA}). In this sense,

the algorithm identified a refractory period shorter than 165–175 ms for selecting the most aggressive approach (LVA_{LA}+CTI+LVA_{RA}).

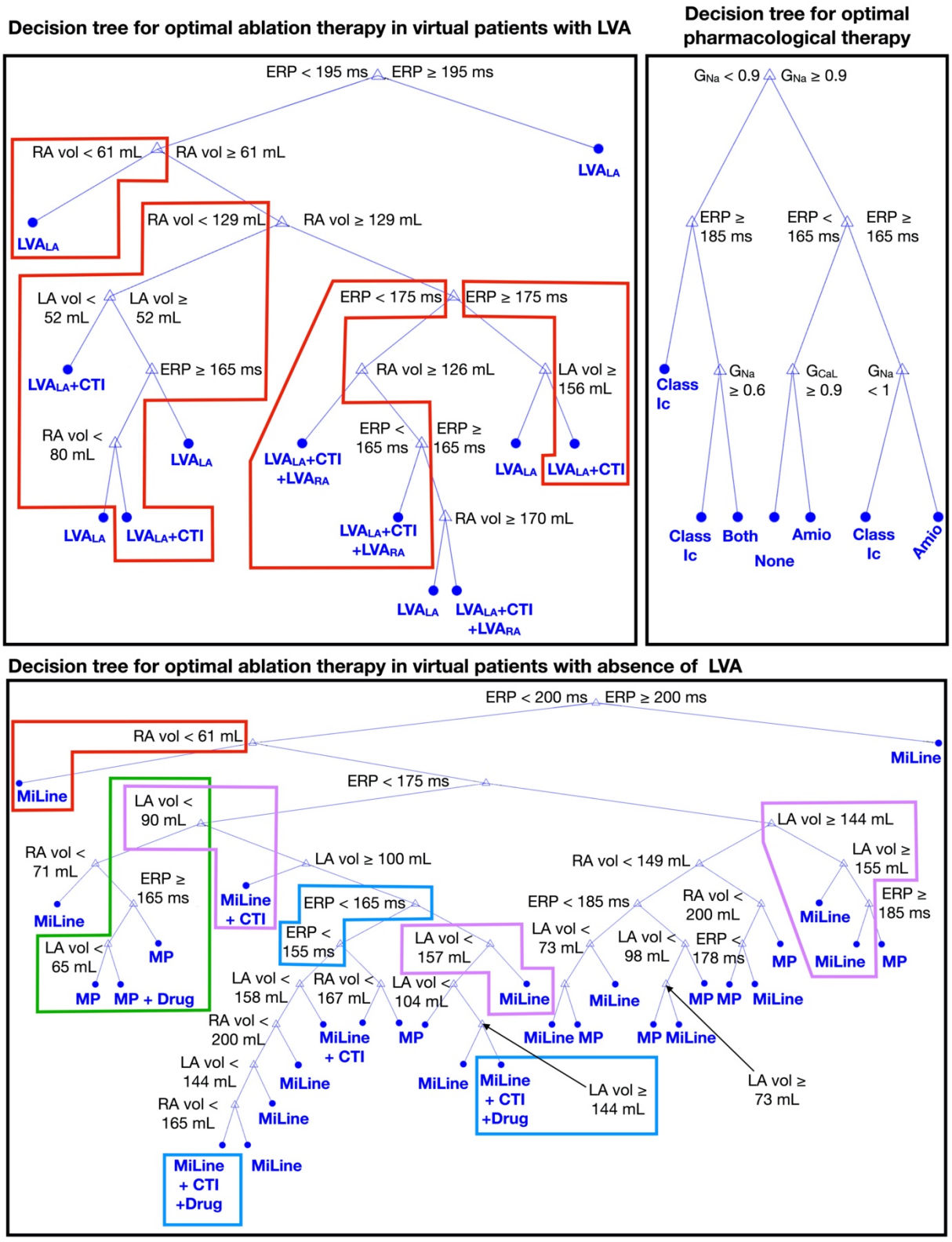


Figure 9.5. Data-driven decision algorithm for optimal stratification of persistent AF patients to catheter ablation and antiarrhythmic drug therapy. Abbreviations as in Table 9.2. The decision tree for optimal pharmacological treatment considers the scaling factors (dimensionless) applied to the ionic current densities.

In virtual patients with absence of LVA and larger right atrial volumes (> 61 mL), a left atrial volume below 90 mL was indicative of successful Marshall-Plan (**Figure 9.5**, green box). Moreover, combined Marshall-Plan and pharmacological treatment was selected in virtual patients with a refractory period below 165 ms. On the other hand, larger left atrial volumes (>90 mL) suggested a more aggressive ablation in the left atrium (i.e., MiLine). Indeed, the algorithm repeatedly identified MiLine or MiLine+CTI as the ideal strategy in virtual patients with very large left atrial volumes (**Figure 9.5**, purple boxes). Similar to Marshall-Plan, virtual patients with shorter refractory periods (<165 ms) were stratified to combined MiLine+CTI and pharmacological therapy (**Figure 9.5**, blue boxes).

When pharmacological therapy was applied alone, the decision algorithm reiterated the results presented in **Section 9.4.4**. Virtual patients with I_{Na} up-regulation (scaling factor for $G_{Na} > 1.0$) were stratified to Class Ic antiarrhythmics, and amiodarone was selected in virtual patients presenting longer refractoriness (>165 ms) and I_{CaL} up-regulation (scaling factor for $G_{CaL} > 0.9$).

Random Forest. The complete datasets used in **Figure 9.5** were subsequently split into 70-30% training and testing data, respectively, through a hold-out cross-validation approach. A Random Forest classifier was trained using MATLAB's function TreeBagger. Fifty trees were included in the forest, and the prediction accuracy of the resulting classifier was assessed using the testing set.

After considering 10-fold cross-validation, prediction accuracies of 60-70% and of 70-80% were obtained for the optimal stratification to catheter and pharmacological therapy, respectively. Noteworthy, higher accuracies would have been obtained if the labels considered, not only the least aggressive treatment that terminated AF but also, all treatments resulting in AF termination for a given virtual patient. This, however, would have greatly increased the complexity of the generated trees.

In this sense, **Figure 9.6** illustrates an updated decision algorithm, resulting from the combination of the results presented in **Figure 9.5** (i.e., machine learning) and the subjective assessment of key aspects not captured by the machine learning approach (i.e., natural learning). **Figure 9.6** has been developed in order to provide an optimal stratification of the virtual patients considered in this study, and can be further evaluated with additional clinical evidence in successive iterations.

Based on the simulation results, we propose that the algorithm first evaluates the presence of LVA (i.e., **Figure 9.6–**- right arm of the algorithm), since their ablation yielded the highest prevention efficacy. Patients with LVA and smaller right atria (<60 mL) benefit from LVA ablation in the left atria alone. Conversely, right atrial ablation is required for bigger right atria. Patients with a right atrial volume above 60 mL and short ERP (<170 ms) are optimally treated with LVA ablation in both the left and right atria, with additional CTI block to prevent flutter-derived more complex arrhythmias (**Figure 9.3**). In patients with big right atria but longer ERP, CTI block and LVA ablation in the left atrium are sufficient to stop AF maintenance.

In the absence of LVA (i.e., **Figure 9.6** – left arm of the algorithm), the optimal empirical ablation strategy is also dictated by the atrial volume. Atrial flutter is observed in patients with small right (< 60 mL) and left atria (< 90 mL). Thus, ablation should attempt to eliminate the specific re-entrant circuit. For bigger right atria (> 60 mL), additional CTI ablation improvs AF prevention. Accordingly, within the strategies considering CTI block, Marshall-Plan is sufficient for small left atria (< 90 mL), but a more extensive ablation, such as MiLine+CTI or PWI+MI+CTI, is required as the left atrial volume increases. In the cases of big left atria and small right atria (< 60 mL), the latter strategies without CTI line (i.e., MiLine and PWI+MI) succeed in preventing AF maintenance.

Noteworthy, patients with absence of LVA but short ERP (< 170 ms) require synergistic pharmacological (i.e., low-dose amiodarone) and ablation therapy. The optimal stratification to ablation strategies is still dependent on the atrial volumes, as with patients with long ERP, but additional antiarrhythmic drugs are needed to prevent AF maintenance.

When administered without catheter ablation, the efficacy of pharmacotherapy is determined by the patient's electrophysiological profile, being the inward currents (i.e., I_{Na} and I_{CaL}) critical for optimal selection of amiodarone or class Ic agents (i.e., vernakalant). Due to the current inability to characterise the patient's ionic current profile on the fly, the stratification to antiarrhythmic drugs in **Figure 9.6** has been represented with dashed lines.

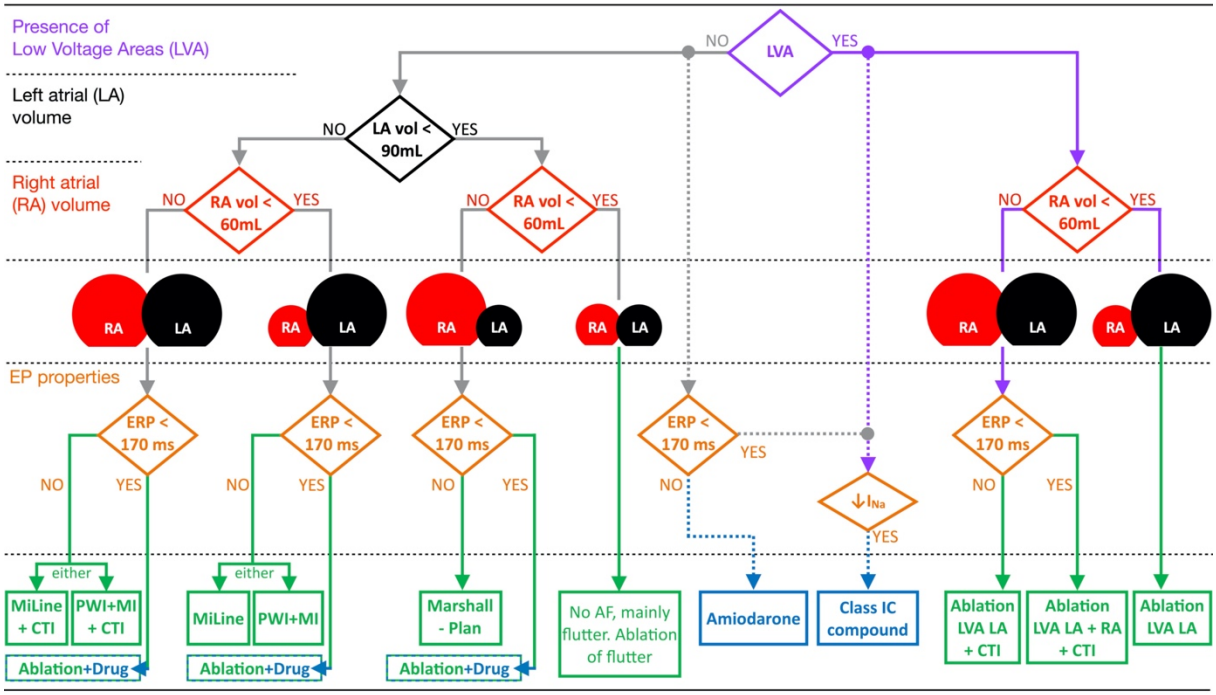


Figure 9.6. Decision algorithm for optimal stratification of persistent AF patients to catheter ablation and antiarrhythmic drug therapy. Abbreviations as in Table 9.2.

9.5. Discussion

In this study AF maintenance was evaluated in a population of 800 virtual patients presenting variability in anatomy, electrophysiology and tissue structure. In this cohort, 522 virtual patients had inducible arrhythmia after PVI, and were subjected to in-silico trials with 12 ablation and pharmacological treatments. Key findings are: (i) Ablation strategies that only consider the left atrium have 52-56% efficacy, and only succeed in virtual patients with small right atria (< 60 mL). (ii) With right atrial ablation (i.e., CTI block), Marshall-Plan is sufficient for patients with small left atria (< 90 mL). Conversely, for larger left atria, a more aggressive ablation approach is required, such as anterior mitral line (MiLine) or posterior wall isolation and mitral isthmus ablation (PWI+MI). (iii) When patients present LVA, ablation of LVAs in both the left and right atrium has the highest efficacy. (iv) Conversely, patients with absence of LVAs that present arrhythmia despite right and left atrial ablation benefit from additional pharmacological therapy (i.e., low-dose amiodarone). (v) In the absence of catheter ablation, the efficacy of antiarrhythmic drugs is determined by the patient's electrophysiological profile, being the inward currents (i.e., I_{Na} and I_{CaL}) critical for optimal selection of amiodarone or vernakalant.

9.5.1. In-silico trials using modelling and simulation for optimal AF treatment

Computer modelling and simulation has been widely used for testing optimal ablation therapies of in virtual cohorts. Early work by (Hwang *et al.*, 2014) showed the feasibility of applying virtual ablation in a cohort of 20 virtual atria reconstructed from CT images of 20 (80% persistent) AF patients. The authors virtually-tested three empirical ablations strategies and, in agreement with our study, concluded that PVI applied together with roof, floor and anterior mitral line had the highest antiarrhythmic efficacy. This work preceded a prospective clinical trial by the same group (Shim *et al.*, 2017), in which 108 (78% persistent) AF patients were randomly assigned to receive in-silico guided or standard-of-care ablation. In the in-silico ablation group, the patient's left atrium was reconstructed and five ablation strategies were assessed. The strategy yielding the fastest AF termination in-silico was selected as optimal therapy and applied in the actual patient. The study obtained non-inferiority of in-silico guided ablation and showcased in-silico trials for guiding the selection of optimal AF therapies.

Further simulation studies (Roney *et al.*, 2020; Azzolin *et al.*, 2023) included personalization of both the left atrial geometry and the patient-specific fibrotic distribution. Thus, the authors additionally assessed virtual ablation of structurally-remodelled substrate (i.e., LVAs or fibrosis derived from late gadolinium-enhancement MRI), which showed higher success rates than empirical ablation. Both studies demonstrated that targeting AF-perpetuating areas (i.e., drivers), yielded the greatest freedom from arrhythmia (i.e., 46% (Roney *et al.*, 2020) and 40-80% (Azzolin *et al.*, 2023)). In our study, we have also observed the importance of LVA ablation for driver termination. However, after complete isolation of left atrial drivers, we found that right atrial drivers sustained AF in ~40% of cases, not considered in the above-mentioned studies. The importance of right atrial ablation has been illustrated

by (Roney *et al.*, 2023), in which bi-atrial ablation of fibrosis proved superior to left atrial ablation alone. This was further supported by (Boyle *et al.*, 2019) in which the optimal ablation of drivers in both atrial chambers is now being tested in a randomized clinical trial (NCT04101539). In this study, 100 AF patients are expected to undergo simulation-driven ablation, compared to the 800 virtual patients included in our pilot study.

While all these works aimed to develop "digital twins" of the atria for precision medicine, they included no variability in atrial electrophysiology. Failing to consider accurate tissue repolarization properties might lead to believe (among others) that re-entrant AF drivers exclusively localize within regions of structurally-remodelled tissue (Azzolin *et al.*, 2023). In our study, variability in ionic current profiles was considered, resulting in a whole spectrum of AF dynamics (i.e., focal re-entrant drivers anchored to LVA, wave break-ups, unstable and meandering rotors etc.) for the same atrial anatomy and LVA distribution. As shown in this population-based study, including variability in atrial electrophysiological properties is crucial for both accurately phenotyping AF dynamics and properly stratifying patients to optimal ablation and, specifically, pharmacological therapies.

The latter concept, patient stratification, is another aspect largely disregarded in both simulation and clinical studies. The "one-size fits all" approach that is currently adopted for rhythm control of AF, and the search for one best treatment, might explain the high recurrence rates reported in persistent AF patients. Conversely, we have shown that the efficacy of AF therapy could be improved if optimal patient stratification, based on key patient characteristics, is considered.

9.5.2. Efficacy of Efficacy of in-silico vs. clinical trials

Overall agreement between simulated and clinical results was observed, supporting credibility of the in-silico trials. This is important since the results of clinical trials might be confounded by lack of lesion durability, and failure could be due to healing and gaps in lines, rather than ineffective ablation strategy. Conversely, 100% lesion effectiveness is guaranteed in-silico. Still, small differences were observed between clinical and simulated results due to procedural differences. For example, most clinical studies considered first procedure treatments. Therefore, the proposed strategy comprised the efficacy derived from the elimination of pulmonary vein triggers (PVI), plus the added benefit of further lines of block (PVI+). Conversely, our in-silico trials considered second procedure treatments, in which non-pulmonary vein triggers were imposed in every virtual patient. Thus, PVI had no additional benefit, which explained the lower efficacies generally observed in-silico.

This was the case for the virtual application of **posterior wall isolation**. A 52% efficacy was observed in persistent AF patients treated with PWI in CAPLA (Kistler *et al.*, 2023), as compared to 2% obtained in our study. The posterior wall shares a common embryological origin with the pulmonary veins and thus, it is believed to be a focus of triggered activity. Accordingly, the high success of PVI+PWI might be attributed to a complete elimination of ectopy. In our study, we mimicked a situation in which triggers

arose everywhere in the atria, which could explain the low efficacy of simulated PWI. In agreement with clinical studies (Saad and Slater, 2014), we observed a high proportion (51%) of virtual patients with mitral isthmus dependent flutter after PWI.

Therefore, an important increase in the success rate derived from the virtual application of posterior wall isolation together with **mitral isthmus ablation**. Efficacies of 73.5% and 80% have been reported clinically after PWI+MI in a retrospective (Li *et al.*, 2023) and a small prospective study (Davong *et al.*, 2023). In the former study, 30 (15%) persistent AF patients treated with PWI+MI additionally received ablation of atrial isthmus, including the tricuspid isthmus, and in the latter study, CTI ablation was applied in 6 (13%) patients. Consistent with the clinical results, we observed 77% efficacy when PWI+MI+CTI was considered.

A similar success rate (75%) derived from the virtual application of **anterior mitral line** and CTI ablation. When MiLine was applied alone, 282 (54%) virtual patients were free of arrhythmia. While a higher efficacy (62.7%) was observed clinically in a cohort of 110 persistent AF patients (Bergonti, Spera, Ferrero, Nsahlai, Bonomi, Boris, *et al.*, 2023), 59 of them were treated with additional lines of block (50 with posterior wall isolation and 9 roof line). Moreover, the patients in this clinical study were carefully selected, so that MiLine was only applied in those presenting large LVAs in the left atrial anterior wall. In this case, MiLine regarded a patient-tailored approach, rather than an empirical ablation. Consistent with the clinical study, we observed absence of AF drivers anchored to LVAs in the left atrial anterior wall after the virtual application of MiLine.

In this sense, a complete elimination of LVA-dependent drivers derived from **LVA ablation** in both atrial chambers. When LVA ablation was applied only in the left atrium, we observed a 56% success rate, consistent with ERASE-AF (Huo *et al.*, 2022). In the latter, from 51 patients with presence of LVAs that underwent LVA ablation, 29 (57%) were free from arrhythmia. A slightly higher efficacy (65%) was observed in STABLE-SR-II (Yang *et al.*, 2022), where recurrence occurred in 25 out of 71 patients with presence of LVA. This might be attributed to the fact that not all LVAs harbour proarrhythmic potential, as shown in this study, and PVI might be enough for preventing arrhythmia.

A slightly higher efficacy was also observed for **Marshall-Plan** in a prospective study (Derval *et al.*, 2021) compared to our simulations (72% vs. 67%, respectively). The ablation set of Marshall-Plan was the hardest to reproduce, since the vein of Marshall ethanol infusion could not be accurately modelled in-silico. In VENUS (Valderrábano *et al.*, 2020), adding vein of Marshall ethanol infusion proved to reduce recurrence compared to PVI alone, which could explain the slightly lower efficacy of Marshall-Plan observed in-silico. Nevertheless, since we incorporated mitral isthmus ablation, comparable efficacies of 67% and 72% (54/75) derived from our simulations and clinically (Derval *et al.*, 2021). In the prospective study, 79% freedom from arrhythmia was observed in 68 patients presenting a complete lesion set, consistent with the efficacy that we observed in virtual patients with absence of LVAs (75%).

No subgroup analysis or proportion of LVAs is reported in the clinical study for comparison with our simulations.

Likewise for pharmacological therapy, the success rate obtained after virtual administration of amiodarone post-PVI (57%) agrees with the 61% (65/107) reported in AMIO-CAT (Darkner *et al.*, 2014), a randomized clinical trial assessing whether the short-term use of amiodarone after catheter ablation could prevent early recurrence. The slightly higher efficacy observed in the clinical study might be due to the fact that PVI only was performed in 75% of patients, with the other 25% receiving additional ablation lines. Overall, the excellent agreement between in-silico and clinical trials is improved when the different procedural aspects are also taken into account.

9.6. Conclusion

In this study, we demonstrate that simulations using populations of 800 virtual patients can reproduce findings of randomized clinical trials for 12 AF therapies, including ablation and pharmacological therapy. The work presented provides scientific insights and knowledge on how specific patient characteristics, easily obtained during routine clinical interventions, can guide an optimal stratification of patients to pharmacological treatment and catheter ablation. In addition to the methodological novelty and scientific findings into AF therapies, an outcome of this study is to propose a decision algorithm for stratification of AF patients to optimal treatments based on these patient characteristics. The algorithm is based on computational results and the validation of the methodological framework and the decision algorithm with further clinical data would be needed. This could lead, in the future, to improving the efficacy of AF treatment and reinforce the integration of in-silico trials into clinical practice. Further discussion on this topic is presented in the following chapter when analysing the contributions of this thesis and future lines of work.

CHAPTER

10 CONCLUSIONS AND FUTURE WORK

In this thesis I aimed to provide a computational framework for in-silico trials in large cohorts of virtual patients and produce digital evidence for stratifying patients with AF to optimal therapies. The framework allowed investigating the efficacy of pharmacological and ablation treatments in large population of virtual AF patients and identifying patient characteristics dictating treatment response. Accordingly, the in-silico trials results informed clinical decision algorithms for optimal patient stratification to AF therapies.

10.1. Main thesis contributions

The main contribution of this thesis is the development of a methodological framework based on in-silico trials for evaluating AF therapy in large populations of virtual atria. For the first time, I show arrhythmia dynamics and response to treatment in large cohorts of virtual patients that mimic the great variability observed in clinical practice for characteristics such as electrophysiology, anatomy and tissue structure. I have demonstrated that including such variability is crucial to extrapolate in-silico trials findings to the design and interpretation of clinical trials, as evidenced by the overall agreement between clinical and simulated results in this thesis.

From a clinical perspective, several findings of AF mechanisms and management are generated in this thesis (summarized in **Section 10.2**), resulting in **five first-author journal publications and many conference proceedings**. Most importantly, I have identified specific patient characteristics that dictate treatment success and provided mechanistic explanations for treatment failure. The digital evidence obtained from the in-silico trials has informed decision algorithms to guide patient stratification to optimal AF treatments. This methodological framework can be used to evaluate further treatments for AF, or for other cardiac diseases, highlighting a rout for direct translation of human modelling and simulation into clinical practice and the importance of my work for Precision Medicine.

From a methodological perspective, this thesis represents a compendium of the largest multi-scale computational studies reported to date, including more than 16.600 multi-scale simulations of pharmacological and ablation therapy for AF: 3110 multi-scale simulations (1000 under control conditions and 2110 after application of 10 drug treatments) in **Chapter 6**; 6728 simulations (800 under control conditions and 5928 after application of 12 pharmacological therapies) in **Chapter 8**; and 7064 multi-scale simulations (800 under control conditions and 6264 after application of 12 catheter ablation strategies) in **Chapter 9**. This substantially advances the state-of-the-art compared to previous studies simulating drug therapy in 275 simulations (Hwang et al., 2021) and ablation therapies in 1100 simulations (Roney et al., 2022).

Therefore, the validation of the computational framework and the resulting decision algorithm with clinical data has broad implication for treatment personalisation, since it could serve as the basis for stratifying AF patients to optimal treatments based on patient characteristics.

10.2. Summary of main findings

Throughout the thesis, AF inducibility and maintenance have been evaluated in large populations of virtual patients with variability in relevant clinical features. In structurally-healthy atria (i.e., absence of heterogeneities in tissue structure and atrial enlargement) AF inducibility is favoured by discordant APD alternans. These alternans appear near the ectopic focus (e.g., the pulmonary veins), and result from steep electrical restitution (occurring for elevated I_{CaL}) and high excitability (due to increased I_{K1}). In these cases of elevated I_{CaL}, localized rotors are absent, and wavefront meandering, transient rotors and wave breakups rule AF dynamics. Thus, AF maintenance is only enabled in virtual patients with considerable I_{K1} and I_{NaK} up-regulation, which confer high excitability. These patients with elevated I_{CaL} show high spectral entropy on the f-waves (i.e., fibrillatory waves on the ECG). The high spectral entropy indicates high AF complexity, consistent with wavefront fractionation.

Conversely, when virtual patients present decreased I_{CaL} and increased I_{K1} and I_{NaK}, stable micro-reentries can be observed. AF maintenance is common in these patients, and localized rotors anchor both to structurally-remodelled substrate (i.e., LVAs) and to healthy myocardium. The formation of localized re-entries increases the predictability and repetitiveness of AF. Thus, these virtual patients show elevated sample entropy on the f-waves. Moreover, as shown in clinical studies, I observed that low I_{CaL} and high I_{K1} and I_{NaK} yield the fastest AF episodes (i.e., highest ECG dominant frequency). The analysis of the ECG during sinus rhythm (**Annex III**) further demonstrated a relationship between these ionic currents and changes on the ECG. As such, I identified I_{K1} as the main modulator of the T_a-wave duration (i.e., atrial repolarization), and I_{NaK} determines the T_a-wave amplitude. This is important since an accurate, non-invasive characterisation of I_{K1} and I_{NaK} density could help planning safer and more efficacious AF treatments with I_{K1} and I_{NaK} inhibitors.

Indeed, I have shown that inhibiting both currents represents an effective pharmacological approach, since it prolongs atrial refractoriness. This atrial refractoriness, additionally modulated by I_{CaL} and I_{Na}, determines pharmacological treatment success for both structurally-healthy and structurally-remodelled atria. Vernakalant is effective in atria presenting long refractoriness (i.e., elevated I_{CaL}), when simulated as a Class III inhibitor (i.e., antiarrhythmic effect due to I_{Kur} block). For shorter refractoriness, virtual patients with high I_{Na} density respond more favourably to amiodarone. Conversely, I have consistently observed that compounds that exert a primary I_{Na} inhibition (i.e., flecainide, Compound 6f and vernakalant when simulated as a strong Na^+ channel inhibitor) are more efficacious in virtual patients without I_{Na} up-regulation. Thus, an accurate estimation of I_{Na} density might be crucial for improving drug efficacy. In this sense, I have shown in **Annex III** that I_{Na} is the main modulator of the P-wave duration, which might serve for its non-invasive characterisation.

As can be appreciated, in this work I have provided direct evidence that the ionic current profile of the atria modulates the success of pharmacological treatment. Conversely, while the ionic current substrate greatly influences AF dynamics, I have observed that the outcomes of catheter ablation therapy are mainly determined by the presence of heterogeneities in the tissue structure (i.e., presence of LVAs) and the bi-atrial size (i.e., left and right atrial volume).

Accordingly, I found that ablation strategies that only consider the left atrium have 52-56% efficacy, and succeed in virtual patients with small right atrium. When minimal right atrial ablation is considered (i.e., CTI block), Marshall-Plan is sufficient for patients with small left atria. Conversely, for large left atria, a more aggressive ablation approach is required, such as anterior mitral line or posterior wall isolation and mitral isthmus ablation. However, these strategies might not be sufficient if patients present LVAs. I have identified that after applying a roof line (e.g., posterior wall isolation), rotors can still appear in the anterior wall of the left atrium. Similarly, if only an anterior mitral line is applied, then rotors can appear at the posterior wall. When applying a dome line (e.g., Marshall-Plan), rotors can appear both in the anterior and posterior walls.

Therefore, ablation of LVAs in both the left and right atrium might have the highest efficacy, especially in patients that present rotors anchored in LVAs (i.e., short refractoriness derived from low I_{CaL}). Conversely, patients with absence of LVAs that presented arrhythmia despite right and left atrial ablation, benefit from additional pharmacological therapy. Indeed, the synergy of pharmacological therapy and catheter ablation is the most effective approach, especially for patients with the shortest refractoriness (low I_{CaL} and high I_{NaK} and I_{K1}).

10.3. Limitations and future work

This thesis proposes an in-silico trial framework, applied to study several AF treatments in large populations of virtual patients. Given the large scale of the studies presented in this thesis (more than 16,600 multi-scale simulations), a compromise was reached between the total number of simulations

and the time per simulation (i.e., 7 seconds). At baseline conditions (i.e., no treatment simulation), virtual patients with sustained AF over 7 s also present AF maintenance for 30 s. Moreover, since pharmacokinetics (i.e., time course of drug absorption and bioavailability in the organisms) are not included in the drug modelling, the simulated interventions produce an immediate effect. Thus, in-silico trials can predict within a very short time whether a drug might be effective terminating an arrhythmia.

Likewise, since human modelling and simulation allows a perfect control over the parameters of interest, a mechanistic explanation can be provided for treatment success. In this sense, I have illustrated throughout the thesis that virtual patients responding to drug treatment experienced a significant prolongation of the ERP after drug application, which failed to happen in those patients not responding. Similarly, virtual patients not responding to an ablation strategy presented stable rotors in the atria, which remained unmodified during the entire duration of the AF episode. The significant difference in ERP prolongation between responders vs. non-responders and the stable AF dynamics seen in non-responder patients after simulated drug treatment and ablation therapy is reassuring that longer simulation times would unlikely change the outcomes of the study. That being said, my future studies should attempt to analyse whether 7 s of simulated AF is representative of the follow-up time reported in clinical trials and thus, if could be used to predict AF cardioversion or recurrence clinically.

With this thesis, I have proposed two decision algorithms in an attempt to rationalise the large amount of data generated and initiate the process of clinical translation. In their current version, the proposed decision algorithms have not been validated with prospective clinical data, since clinical validation was out of scope of the current thesis. Instead, I have developed a computational framework and provided the tools for in-silico trials, so that the path towards clinical translation could start (plans for validation are currently ongoing; see following section).

Lastly, the algorithms that I presented largely rely on invasive electro-anatomical mapping. For future studies, I have to consider that an ideal tissue characterisation derives from combining several mapping modalities and clinical data. Thus, further work should complement invasive mapping with other non-invasive image techniques (e.g., late-gadolinium enhanced magnetic resonance imaging).

10.4. Thesis outlook

Building on the simulations already conducted, now I aim to translate the developed research tool to clinical practice. Bridging the gap between in-silico results and clinical impact requires being immersed in the clinic and understanding clinical requirements. Thus, the immediate step in this direction is the validation of the theoretical findings and the methodological framework with appropriate clinical data. For this, I applied, and have been already granted, the ERPSC (Engineering and Physical Sciences Research Council) Impact Acceleration Award. This award provides support for accelerating the impact of research beyond academia, and thus it constitutes a perfect scheme to achieve clinical impact.

Therefore, for the duration of one year I will partner with three hospital centres, with access to clinical experience and data to validate the theoretical work, as well as highly relevant expertise. This will build confidence in human in-silico trials towards precision medicine and facilitate its dissemination to other clinical centres. Eventually, it could impact future guidelines of AF treatment, highlighting the power of modelling and simulation as an assisting tool for optimal treatment selection.

CHAPTER

11

REFERENCES

Aguilar, M. *et al.* (2021) 'New aspects of endocrine control of atrial fibrillation and possibilities for clinical translation', *Cardiovascular Research*, 117(7), pp. 1645–1661. DOI: 10.1093/cvr/cvab080.

Alcaraz, R. *et al.* (2011) 'Classification of Paroxysmal and Persistent Atrial Fibrillation in Ambulatory ECG Recordings', *IEEE Transactions on Biomedical Engineering*, 58(5), pp. 1441–1449. DOI: 10.1109/TBME.2011.2112658.

Atienza, F. *et al.* (2006) 'Activation of Inward Rectifier Potassium Channels Accelerates Atrial Fibrillation in Humans', *Circulation*, 114(23), pp. 2434–2442. DOI: 10.1161/CIRCULATIONAHA.106.633735.

Azzolin, L. *et al.* (2023) 'Personalized ablation vs. conventional ablation strategies to terminate atrial fibrillation and prevent recurrence', *EP Europace*, 25(1), pp. 211–222. DOI: 10.1093/europace/euac116.

Bai, J. *et al.* (2020) 'In silico investigation of the mechanisms underlying atrial fibrillation due to impaired Pitx2', *PLOS Computational Biology*, 16(2), p. e1007678. DOI: 10.1371/journal.pcbi.1007678.

Bai, J. *et al.* (2021) 'In Silico Assessment of Class I Antiarrhythmic Drug Effects on Pitx2-Induced Atrial Fibrillation: Insights from Populations of Electrophysiological Models of Human Atrial Cells and Tissues', *International Journal of Molecular Sciences*, 22(3), p. 1265. DOI: 10.3390/ijms22031265.

Bai, J., Lu, Y. and Zhang, H. (2020) 'In silico study of the effects of anti-arrhythmic drug treatment on sinoatrial node function for patients with atrial fibrillation', *Scientific Reports*, 10(1), p. 305. DOI: 10.1038/s41598-019-57246-5.

Bash, L.D. *et al.* (2012) 'Systematic Review and Meta-analysis of the Efficacy of Cardioversion by Vernakalant and Comparators in Patients with Atrial Fibrillation', *Cardiovascular Drugs and Therapy*, 26(2), pp. 167–179. DOI: 10.1007/s10557-012-6374-4.

Beatch, G.N. and Mangal, B. (2016) 'Safety and efficacy of vernakalant for the conversion of atrial fibrillation to sinus rhythm; a phase 3b randomized controlled trial', *BMC Cardiovascular Disorders*, 16(1), p. 113. DOI: 10.1186/s12872-016-0289-0.

Benali, K. *et al.* (2023) 'Recurrences of Atrial Fibrillation Despite Durable Pulmonary Vein Isolation: The PARTY-PVI Study', *Circulation: Arrhythmia and Electrophysiology*, 16(3). DOI: 10.1161/CIRCEP.122.011354.

Bergonti, M., Spera, F.R., Ferrero, T.G., Nsahlai, M., Bonomi, A., Boris, W., *et al.* (2023) 'Anterior mitral line in patients with persistent atrial fibrillation and anterior scar: A multicenter matched comparison—The MiLine study', *Heart Rhythm*, 20(5), pp. 658–665. DOI: 10.1016/j.hrthm.2023.01.009.

Bergonti, M., Spera, F.R., Ferrero, T.G., Nsahlai, M., Bonomi, A., Tijskens, M., *et al.* (2023) 'Characterization of Atrial Substrate to Predict the Success of Pulmonary Vein Isolation: The Prospective, Multicenter MASH-AF II (Multipolar Atrial Substrate High Density Mapping in Atrial Fibrillation) Study', *Journal of the American Heart Association*, 12(1). DOI: 10.1161/JAHA.122.027795.

Betts, T.R. *et al.* (2023) 'Treatment of pathophysiologic propagation outside of the pulmonary veins in retreatment of atrial fibrillation patients: RECOVER AF study', *Europace*, 25(5). DOI: 10.1093/europace/euad097.

Boriani, G. *et al.* (1998) 'Conversion of Recent-Onset Atrial Fibrillation to Sinus Rhythm: Effects of Different Drug Protocols', *Pacing and Clinical Electrophysiology*, 21(11), pp. 2470–2474. DOI: 10.1111/j.1540-8159.1998.tb01203.x.

Boriani, G. *et al.* (2004) 'Pharmacological Cardioversion of Atrial Fibrillation', *Drugs*, 64(24), pp. 2741–2762. DOI: 10.2165/00003495-200464240-00003.

Botto, G.L. *et al.* (1994) 'Regular Ventricular Rhythms Before Conversion of Recent Onset Atrial Fibrillation to Sinus Rhythm', *Pacing and Clinical Electrophysiology*, 17(11), pp. 2114–2117. DOI: 10.1111/j.1540-8159.1994.tb03810.x.

Boyle, P.M. *et al.* (2019) 'Computationally guided personalized targeted ablation of persistent atrial fibrillation', *Nature Biomedical Engineering*, 3(11), pp. 870–879. DOI: 10.1038/s41551-019-0437-9.

Britton, O.J. *et al.* (2013) 'Experimentally calibrated population of models predicts and explains intersubject variability in cardiac cellular electrophysiology', *Proceedings of the National Academy of Sciences*, 110(23). DOI: 10.1073/pnas.1304382110.

Bueno-Orovio, A. *et al.* (2014) 'Na/K pump regulation of cardiac repolarization: insights from a systems biology approach', *Pflügers Archiv – European Journal of Physiology*, 466(2), pp. 183–193. DOI: 10.1007/s00424-013-1293-1.

Burashnikov, A. *et al.* (2007) 'Atrium-Selective Sodium Channel Block as a Strategy for Suppression of Atrial Fibrillation', *Circulation*, 116(13), pp. 1449–1457. DOI: 10.1161/CIRCULATIONAHA.107.704890.

Burashnikov, A. *et al.* (2012) 'Rate-Dependent Effects of Vernakalant in the Isolated Non-Remodeled Canine Left Atria Are Primarily Due to Block of the Sodium Channel', *Circulation: Arrhythmia and Electrophysiology*, 5(2), pp. 400–408. DOI: 10.1161/CIRCEP.111.968305.

Burashnikov, A., Belardinelli, L. and Antzelevitch, C. (2012) 'Atrial-Selective Sodium Channel Block Strategy to Suppress Atrial Fibrillation: Ranolazine versus Propafenone', *Journal of Pharmacology and Experimental Therapeutics*, 340(1), pp. 161–168. DOI: 10.1124/jpet.111.186395.

Camm, A.J. *et al.* (2011) 'A Randomized Active-Controlled Study Comparing the Efficacy and Safety of Vernakalant to Amiodarone in Recent-Onset Atrial Fibrillation', *Journal of the American College of Cardiology*, 57(3), pp. 313–321. DOI: 10.1016/j.jacc.2010.07.046.

Camm, A.J. *et al.* (2019) 'A randomized, double-blind, placebo-controlled trial assessing the efficacy of S66913 in patients with paroxysmal atrial fibrillation', *European Heart Journal – Cardiovascular Pharmacotherapy*, 5(1), pp. 21–28. DOI: 10.1093/ehjcvp/pvy022.

Capucci, A. *et al.* (2018) 'Emerging pharmacotherapies for the treatment of atrial fibrillation', *Expert Opinion on Emerging Drugs*, 23(1), pp. 25–36. DOI: 10.1080/14728214.2018.1446941.

Carbonell-Pascual, B. *et al.* (2016) 'Comparison between Hodgkin–Huxley and Markov formulations of cardiac ion channels', *Journal of Theoretical Biology*, 399, pp. 92–102. DOI: 10.1016/j.jtbi.2016.03.039.

Chamberlain, D.A. *et al.* (1970) 'Plasma Digoxin Concentrations in Patients with Atrial Fibrillation', *BMJ*, 3(5720), pp. 429–432. DOI: 10.1136/bmj.3.5720.429.

Chen, J. *et al.* (2019) 'Extent and spatial distribution of left atrial arrhythmogenic sites, late gadolinium enhancement at magnetic resonance imaging, and low-voltage areas in patients with persistent atrial fibrillation: comparison of imaging vs. electrical parameters of fibrosis and arrhythmogenesis', *EP Europace*, 21(10), pp. 1484–1493. DOI: 10.1093/europace/euz159.

Connolly, S.J. *et al.* (2011) 'Dronedarone in High-Risk Permanent Atrial Fibrillation', *New England Journal of Medicine*, 365(24), pp. 2268–2276. DOI: 10.1056/NEJMoa1109867.

Courtemanche, M., Ramirez, R.J. and Nattel, S. (1998) 'Ionic mechanisms underlying human atrial action potential properties: insights from a mathematical model', *American Journal of Physiology-Heart and Circulatory Physiology*, 275(1), pp. H301–H321. DOI: 10.1152/ajpheart.1998.275.1.H301.

Coveney, S., Cantwell, C. and Roney, C. (2022) 'Atrial conduction velocity mapping: clinical tools, algorithms and approaches for understanding the arrhythmogenic substrate', *Medical & Biological Engineering & Computing*, 60(9), pp. 2463–2478. DOI: 10.1007/s11517-022-02621-0.

Cytrynbaum, E. and Keener, J.P. (2002) 'Stability conditions for the traveling pulse: Modifying the restitution hypothesis', *Chaos: An Interdisciplinary Journal of Nonlinear Science*, 12(3), pp. 788–799. DOI: 10.1063/1.1503941.

Darkner, S. *et al.* (2014) 'Recurrence of arrhythmia following short-term oral AMIOdarone after CATheter ablation for atrial fibrillation: a double-blind, randomized, placebo-controlled study (AMIO-CAT trial)', *European Heart Journal*, 35(47), pp. 3356–3364. DOI: 10.1093/eurheartj/ehu354.

Davong, B. *et al.* (2023) 'Pulsed-Field Ablation on Mitral Isthmus in Persistent Atrial Fibrillation', *JACC: Clinical Electrophysiology*, 9(7), pp. 1070–1081. DOI: 10.1016/j.jacep.2023.03.021.

Deo, M. *et al.* (2013) 'KCNJ2 mutation in short QT syndrome 3 results in atrial fibrillation and ventricular proarrhythmia', *Proceedings of the National Academy of Sciences*, 110(11), pp. 4291–4296. DOI: 10.1073/pnas.1218154110.

Derval, N. *et al.* (2021) 'Marshall bundle elimination, Pulmonary vein isolation, and Line completion for Anatomical ablation of persistent atrial fibrillation (Marshall-PLAN): Prospective, single-center study', *Heart Rhythm*, 18(4), pp. 529–537. DOI: 10.1016/j.hrthm.2020.12.023.

Dobrev, D. and Ravens, U. (2003) 'Remodeling of cardiomyocyte ion channels in human atrial fibrillation', *Basic Research in Cardiology*, 98(3), pp. 137–148. DOI: 10.1007/s00395-003-0409-8.

Dukes, I.D. and Williams, E.M.V. (1984) 'The multiple modes of action of propafenone', *European Heart Journal*, 5(2), pp. 115–125. DOI: 10.1093/oxfordjournals.eurheartj.a061621.

Filgueiras-Rama, D. *et al.* (2012) 'Chloroquine Terminates Stretch-Induced Atrial Fibrillation More Effectively Than Flecainide in the Sheep Heart', *Circulation: Arrhythmia and Electrophysiology*, 5(3), pp. 561–570. DOI: 10.1161/CIRCEP.111.966820.

Fox, J.J., Bodenschatz, E. and Gilmour, R.F. (2002) 'Period-Doubling Instability and Memory in Cardiac Tissue', *Physical Review Letters*, 89(13), p. 138101. DOI: 10.1103/PhysRevLett.89.138101.

Garfinkel, A. *et al.* (2000) 'Preventing ventricular fibrillation by flattening cardiac restitution', *Proceedings of the National Academy of Sciences*, 97(11), pp. 6061–6066. DOI: 10.1073/pnas.090492697.

Gharaviri, A. *et al.* (2021) 'Synergistic antiarrhythmic effect of inward rectifier current inhibition and pulmonary vein isolation in a 3D computer model for atrial fibrillation', *EP Europace*, 23(Supplement_1), pp. i161–i168. DOI: 10.1093/europace/euaa413.

Gima, K. and Rudy, Y. (2002) 'Ionic Current Basis of Electrocardiographic Waveforms', *Circulation Research*, 90(8), pp. 889–896. DOI: 10.1161/01.RES.0000016960.61087.86.

Gong, Y. *et al.* (2007) 'Mechanism Underlying Initiation of Paroxysmal Atrial Flutter/Atrial Fibrillation by Ectopic Foci', *Circulation*, 115(16), pp. 2094–2102. DOI: 10.1161/CIRCULATIONAHA.106.656504.

Grandi, E. *et al.* (2011) 'Human Atrial Action Potential and Ca $^{2+}$ Model', *Circulation Research*, 109(9), pp. 1055–1066. DOI: 10.1161/CIRCRESAHA.111.253955.

Gray, D.F. *et al.* (1998) 'Amiodarone inhibits the Na(+)-K+ pump in rabbit cardiac myocytes after acute and chronic treatment.', *The Journal of pharmacology and experimental therapeutics*, 284(1), pp. 75–82.

de Groot, N. *et al.* (2016) 'Direct Proof of Endo-Epicardial Asynchrony of the Atrial Wall During Atrial Fibrillation in Humans', *Circulation: Arrhythmia and Electrophysiology*, 9(5). DOI: 10.1161/CIRCEP.115.003648.

Guillemare, E., Marion, A. and Gautier, P. (2000) 'Inhibitory Effects of Dronedarone on Muscarinic K+ Current in Guinea Pig Atrial Cells', *Journal of Cardiovascular Pharmacology*, 36(6), pp. 802–805.

Haïssaguerre, M. *et al.* (1998) 'Spontaneous Initiation of Atrial Fibrillation by Ectopic Beats Originating in the Pulmonary Veins', *New England Journal of Medicine*, 339(10), pp. 659–666. DOI: 10.1056/NEJM199809033391003.

Haïssaguerre, M. *et al.* (1999) 'Spontaneous Initiation of Atrial Fibrillation by Ectopic Impulses Originating in the Pulmonary Veins', *Cardiology in Review*, 7(2), p. 65. DOI: 10.1097/00045415-199903000-00006.

Haissaguerre, M. *et al.* (2016) 'Intermittent drivers anchoring to structural heterogeneities as a major pathophysiological mechanism of human persistent atrial fibrillation', *The Journal of Physiology*, 594(9), pp. 2387–2398. DOI: 10.1113/JP270617.

Hanna, P. *et al.* (2021) 'Neuroscientific therapies for atrial fibrillation', *Cardiovascular Research*, 117(7), pp. 1732–1745. DOI: 10.1093/cvr/cvab172.

Hatem, S. *et al.* (1992) 'Differential effects of quinidine and flecainide on plateau duration of human atrial action potential', *Basic Research in Cardiology*, 87(6), pp. 600–609. DOI: 10.1007/BF00788670.

Heijman, J., Hohnloser, S.H. and Camm, A.J. (2021) 'Antiarrhythmic drugs for atrial fibrillation: lessons from the past and opportunities for the future', *EP Europace*, 23(Supplement_2), pp. ii14–ii22. DOI: 10.1093/europace/euaa426.

Heijman, J., Linz, D. and Schotten, U. (2021) 'Dynamics of Atrial Fibrillation Mechanisms and Comorbidities', *Annual Review of Physiology*, 83(1), pp. 83–106. DOI: 10.1146/annurev-physiol-031720-085307.

Hill, A. V (1910) 'The possible effects of the aggregation of the molecules of haemoglobin on its dissociation curves', *The Journal of Physiology*, 40(suppl), pp. i–vii. DOI: 10.1113/jphysiol.1910.sp001386.

Hindricks, G. *et al.* (2021) '2020 ESC Guidelines for the diagnosis and management of atrial fibrillation developed in collaboration with the European Association for Cardio-Thoracic Surgery (EACTS)', *European Heart Journal*, 42(5), pp. 373–498. DOI: 10.1093/eurheartj/ehaa612.

Ho, S.Y. *et al.* (2001) 'Architecture of the pulmonary veins: relevance to radiofrequency ablation', *Heart*, 86(3), pp. 265–270. DOI: 10.1136/heart.86.3.265.

Ho, S.Y., Cabrera, J.A. and Sanchez-Quintana, D. (2012) 'Left Atrial Anatomy Revisited', *Circulation: Arrhythmia and Electrophysiology*, 5(1), pp. 220–228. DOI: 10.1161/CIRCEP.111.962720.

Hodgkin, A.L. and Huxley, A.F. (1952a) 'A quantitative description of membrane current and its application to conduction and excitation in nerve', *The Journal of Physiology*, 117(4), pp. 500–544. DOI: 10.1113/jphysiol.1952.sp004764.

Hodgkin, A.L. and Huxley, A.F. (1952b) 'Currents carried by sodium and potassium ions through the membrane of the giant axon of Loligo', *The Journal of Physiology*, 116(4), pp. 449–472. DOI: 10.1113/jphysiol.1952.sp004717.

Hodgkin, A.L. and Huxley, A.F. (1952c) 'The components of membrane conductance in the giant axon of Loligo', *The Journal of Physiology*, 116(4), pp. 473–496. DOI: 10.1113/jphysiol.1952.sp004718.

Hodgkin, A.L. and Huxley, A.F. (1952d) 'The dual effect of membrane potential on sodium conductance in the giant axon of Loligo', *The Journal of Physiology*, 116(4), pp. 497–506. DOI: 10.1113/jphysiol.1952.sp004719.

Hohnloser, S.H. *et al.* (2009) 'Effect of Dronedarone on Cardiovascular Events in Atrial Fibrillation', *New England Journal of Medicine*, 360(7), pp. 668–678. DOI: 10.1056/NEJMoa0803778.

Honarbakhsh, S. *et al.* (2019) 'Left atrial scarring and conduction velocity dynamics: Rate dependent conduction slowing predicts sites of localized reentrant atrial tachycardias', *International Journal of Cardiology*, 278, pp. 114–119. DOI: 10.1016/j.ijcard.2018.10.072.

Hopman, L.H.G.A. *et al.* (2023) 'Right atrial function and fibrosis in relation to successful atrial fibrillation ablation', *European Heart Journal – Cardiovascular Imaging*, 24(3), pp. 336–345. DOI: 10.1093/ehjci/jeac152.

van Hunnik, A. *et al.* (2016) 'Antiarrhythmic effect of vernakalant in electrically remodeled goat atria is caused by slowing of conduction and prolongation of postrepolarization refractoriness', *Heart Rhythm*, 13(4), pp. 964–972. DOI: 10.1016/j.hrthm.2015.12.009.

Huo, Y. *et al.* (2022) 'Low-Voltage Myocardium-Guided Ablation Trial of Persistent Atrial Fibrillation', *NEJM Evidence*, 1(11). DOI: 10.1056/EVIDoa2200141.

Hwang, M. *et al.* (2014) 'Virtual ablation for atrial fibrillation in personalized in-silico three-dimensional left atrial modelling: Comparison with clinical catheter ablation', *Progress in Biophysics and Molecular Biology*, 116(1), pp. 40–47. DOI: 10.1016/j.pbiomolbio.2014.09.006.

Hwang, M. *et al.* (2021) 'Computational Modeling for Antiarrhythmic Drugs for Atrial Fibrillation According to Genotype', *Frontiers in Physiology*, 12, pp. 650449. DOI: 10.3389/fphys.2021.650449.

Jadidi, A.S. *et al.* (2016) 'Ablation of Persistent Atrial Fibrillation Targeting Low-Voltage Areas With Selective Activation Characteristics', *Circulation: Arrhythmia and Electrophysiology*, 9(3). DOI: 10.1161/CIRCEP.115.002962.

Jalife, J. (2011) 'Deja vu in the theories of atrial fibrillation dynamics', *Cardiovascular Research*, 89(4), pp. 766–775. DOI: 10.1093/cvr/cvq364.

Jalife, J. and Kaur, K. (2015) 'Atrial remodeling, fibrosis, and atrial fibrillation', *Trends in Cardiovascular Medicine*, 25(6), pp. 475–484. DOI: 10.1016/j.tcm.2014.12.015.

Jayaraman, S. *et al.* (2015) 'Unmasking of atrial repolarization waves using a simple modified limb lead system', *The Anatolian Journal of Cardiology*, 15(8), pp. 605–610. DOI: 10.5152/akd.2014.5695.

Ji, Y. *et al.* (2017) 'The inward rectifier current inhibitor PA-6 terminates atrial fibrillation and does not cause ventricular arrhythmias in goat and dog models', *British Journal of Pharmacology*, 174(15), pp. 2576–2590. DOI: 10.1111/bph.13869.

John Hall (1946) *Guyton and Hall textbook of medical physiology*. 12th edn. Philadelphia: Elsevier.

Jones, N.R. *et al.* (2020) 'Screening for atrial fibrillation: a call for evidence', *European Heart Journal*, 41(10), pp. 1075–1085. DOI: 10.1093/eurheartj/ehz834.

Junarta, J. *et al.* (2022) 'Low-voltage area substrate modification for atrial fibrillation ablation: a systematic review and meta-analysis of clinical trials', *EP Europace*, 24(10), pp. 1585–1598. DOI: 10.1093/europace/euac089.

Kany, S. *et al.* (2021) 'Genetics of atrial fibrillation—practical applications for clinical management: if not now, when and how?', *Cardiovascular Research*, 117(7), pp. 1718–1731. DOI: 10.1093/cvr/cvab153.

Karma, A. (1994) 'Electrical alternans and spiral wave breakup in cardiac tissue', *Chaos: An Interdisciplinary Journal of Nonlinear Science*, 4(3), pp. 461–472. DOI: 10.1063/1.166024.

Karma, A. (2000) 'New paradigm for drug therapies of cardiac fibrillation', *Proceedings of the National Academy of Sciences*, 97(11), pp. 5687–5689. DOI: 10.1073/pnas.97.11.5687.

Kircher, S. *et al.* (2018) 'Individually tailored vs. standardized substrate modification during radiofrequency catheter ablation for atrial fibrillation: a randomized study', *EP Europace*, 20(11), pp. 1766–1775. DOI: 10.1093/europace/eux310.

Kishima, H. *et al.* (2020) 'Is the abnormal conduction zone of the left atrium a precursor to a low voltage area in patients with atrial fibrillation?', *Journal of Cardiovascular Electrophysiology*, 31(11), pp. 2874–2882. DOI: 10.1111/jce.14744.

Kistler, P.M. *et al.* (2023) 'Effect of Catheter Ablation Using Pulmonary Vein Isolation With vs Without Posterior Left Atrial Wall Isolation on Atrial Arrhythmia Recurrence in Patients With Persistent Atrial Fibrillation', *JAMA*, 329(2), p. 127. DOI: 10.1001/jama.2022.23722.

Koller, M.L., Riccio, M.L. and Jr., R.F.G. (1998) 'Dynamic restitution of action potential duration during electrical alternans and ventricular fibrillation', *American Journal of Physiology-Heart and Circulatory Physiology*, 275(5), pp. H1635–H1642. DOI: 10.1152/ajpheart.1998.275.5.H1635.

Kornej, J. *et al.* (2021) 'New biomarkers from multiomics approaches: improving risk prediction of atrial fibrillation', *Cardiovascular Research*, 117(7), pp. 1632–1644. DOI: 10.1093/cvr/cvab073.

Kotecha, D. *et al.* (2020) 'Effect of Digoxin vs Bisoprolol for Heart Rate Control in Atrial Fibrillation on Patient-Reported Quality of Life', *JAMA*, 324(24), p. 2497. DOI: 10.1001/jama.2020.23138.

Kottkamp, H. (2013) 'Human atrial fibrillation substrate: towards a specific fibrotic atrial cardiomyopathy', *European Heart Journal*, 34(35), pp. 2731–2738. DOI: 10.1093/eurheartj/eht194.

Krijthe, B.P. *et al.* (2013) 'Projections on the number of individuals with atrial fibrillation in the European Union, from 2000 to 2060', *European Heart Journal*, 34(35), pp. 2746–2751. DOI: 10.1093/eurheartj/eht280.

Krummen, D.E. *et al.* (2012) 'Mechanisms of Human Atrial Fibrillation Initiation', *Circulation: Arrhythmia and Electrophysiology*, 5(6), pp. 1149–1159. DOI: 10.1161/CIRCEP.111.969022.

Kuck, K.-H. *et al.* (2016) 'Cryoballoon or Radiofrequency Ablation for Paroxysmal Atrial Fibrillation', *New England Journal of Medicine*, 374(23), pp. 2235–2245. DOI: 10.1056/NEJMoa1602014.

Kumar, S. *et al.* (2012) 'Atrial Fibrillation Inducibility in the Absence of Structural Heart Disease or Clinical Atrial Fibrillation', *Circulation: Arrhythmia and Electrophysiology*, 5(3), pp. 531–536. DOI: 10.1161/CIRCEP.111.968859.

Lang, R.M. *et al.* (2015) 'Recommendations for Cardiac Chamber Quantification by Echocardiography in Adults: An Update from the American Society of Echocardiography and the European Association of Cardiovascular Imaging', *European Heart Journal – Cardiovascular Imaging*, 16(3), pp. 233–271. DOI: 10.1093/ehjci/jev014.

Lankveld, T. *et al.* (2016) 'Systematic analysis of ECG predictors of sinus rhythm maintenance after electrical cardioversion for persistent atrial fibrillation', *Heart Rhythm*, 13(5), pp. 1020–1027. DOI: 10.1016/j.hrthm.2016.01.004.

Lawson, BAJ et al. (2018) 'Unlocking data sets by calibrating populations of models to data density: A study in atrial electrophysiology'. *Science Advance*, 4, p. e1701676. DOI: 10.1126/sciadv.1701676.

Lee, K.S. (1992) 'Ibutilide, a new compound with potent class III antiarrhythmic activity, activates a slow inward Na+ current in guinea pig ventricular cells.', *The Journal of pharmacology and experimental therapeutics*, 262(1), pp. 99–108.

Lee, K.S. and Lee, E.W. (1998) 'Ionic mechanism of ibutilide in human atrium: evidence for a drug-induced Na+ current through a nifedipine inhibited inward channel.', *The Journal of pharmacology and experimental therapeutics*, 286(1), pp. 9–22.

Lei, M. *et al.* (2018) 'Modernized Classification of Cardiac Antiarrhythmic Drugs', *Circulation*, 138(17), pp. 1879–1896. DOI: 10.1161/CIRCULATIONAHA.118.035455.

Li, X. *et al.* (2023) 'Efficacy and Safety Ablation Index-Guided High-Energy Linear Ablation for Persistent Atrial Fibrillation: PVI Plus Linear Ablation of Mitral Isthmus and Posterior Box Isolation', *Journal of Clinical Medicine*, 12(2), p. 619. DOI: 10.3390/jcm12020619.

Liang, Z. *et al.* (2021) 'New method and electrophysiological characteristics of LA posterior wall isolation in persistent atrial fibrillation', *Pacing and Clinical Electrophysiol*ogy, 44, pp. 1691–1700. DOI: 10.1111/pace.14220.

Liberos, A. *et al.* (2016) 'Balance between sodium and calcium currents underlying chronic atrial fibrillation termination: An in silico intersubject variability study', *Heart Rhythm*, 13(12), pp. 2358–2365. DOI: 10.1016/j.hrthm.2016.08.028.

Loewe, A. *et al.* (2014) 'In-silico assessment of the dynamic effects of amiodarone and dronedarone on human atrial patho-electrophysiology', *EP Europace*, 16(suppl_4), pp. iv30–iv38. DOI: 10.1093/europace/euu230.

Loewe, A. *et al.* (2015) 'Understanding the cellular mode of action of vernakalant using a computational model: answers and new questions', *Current Directions in Biomedical Engineering*, 1(1), pp. 418–422. DOI: 10.1515/cdbme-2015-0101.

Maleckar, M.M. *et al.* (2009) 'K+ current changes account for the rate dependence of the action potential in the human atrial myocyte', *American Journal of Physiology-Heart and Circulatory Physiology*, 297(4), pp. H1398–H1410. DOI: 10.1152/ajpheart.00411.2009.

Mamoshina, P., Rodriguez, B. and Bueno-Orovio, A. (2021) 'Toward a broader view of mechanisms of drug cardiotoxicity', *Cell Reports Medicine*, 2(3), p. 100216. DOI: 10.1016/j.xcrm.2021.100216.

Margara, F. *et al.* (2022) 'Mechanism based therapies enable personalised treatment of hypertrophic cardiomyopathy', *Scientific Reports*, 12(1), p. 22501. DOI: 10.1038/s41598-022-26889-2.

Martins, R.P. *et al.* (2014) 'Dominant Frequency Increase Rate Predicts Transition from Paroxysmal to Long-Term Persistent Atrial Fibrillation', *Circulation*, 129(14), pp. 1472–1482. DOI: 10.1161/CIRCULATIONAHA.113.004742.

Masuda, M. *et al.* (2020) 'Additional Low-Voltage-Area Ablation in Patients With Paroxysmal Atrial Fibrillation: Results of the Randomized Controlled VOLCANO Trial', *Journal of the American Heart Association*, 9(13). DOI: 10.1161/JAHA.120.015927.

Matene, E. and Jacquemet, V. (2012) 'Fully automated initiation of simulated episodes of atrial arrhythmias', *Europace*, 14(suppl 5), pp. v17–v24. DOI: 10.1093/europace/eus271.

McDowell, K.S. *et al.* (2015) 'Virtual Electrophysiological Study of Atrial Fibrillation in Fibrotic Remodeling', *PLOS ONE*, 10(2), p. e0117110. DOI: 10.1371/journal.pone.0117110.

Mikhailov, A. V. *et al.* (2021) 'Comprehensive evaluation of electrophysiological and 3D structural features of human atrial myocardium with insights on atrial fibrillation maintenance mechanisms', *Journal of Molecular and Cellular Cardiology*, 151, pp. 56–71. DOI: 10.1016/j.yjmcc.2020.10.012.

Miyamoto, K. *et al.* (2009) 'Bipolar electrogram amplitudes in the left atrium are related to local conduction velocity in patients with atrial fibrillation', *Europace*, 11(12), pp. 1597–1605. DOI: 10.1093/europace/eup352.

Monfredi, O. and Boyett, M.R. (2015) 'Sick sinus syndrome and atrial fibrillation in older persons — A view from the sinoatrial nodal myocyte', *Journal of Molecular and Cellular Cardiology*, 83, pp. 88–100. DOI: 10.1016/j.yjmcc.2015.02.003.

Moreno, J.D. *et al.* (2011) 'A Computational Model to Predict the Effects of Class I Anti-Arrhythmic Drugs on Ventricular Rhythms', *Science Translational Medicine*, 3(98). DOI: 10.1126/scitranslmed.3002588.

Morgan, R. *et al.* (2016) 'Slow Conduction in the Border Zones of Patchy Fibrosis Stabilizes the Drivers for Atrial Fibrillation: Insights from Multi-Scale Human Atrial Modeling', *Frontiers in Physiology*, 7. DOI: 10.3389/fphys.2016.00474.

Muszkiewicz, A. *et al.* (2016) 'Variability in cardiac electrophysiology: Using experimentally-calibrated populations of models to move beyond the single virtual physiological human paradigm', *Progress in Biophysics and Molecular Biology*, 120(1–3), pp. 115–127. DOI: 10.1016/j.pbiomolbio.2015.12.002.

Muszkiewicz, A. *et al.* (2018) 'From ionic to cellular variability in human atrial myocytes: an integrative computational and experimental study', *American Journal of Physiology-Heart and Circulatory Physiology*, 314(5), pp. H895–H916. DOI: 10.1152/ajpheart.00477.2017.

Nagel, C., Schuler, S., *et al.* (2021) 'A bi-atrial statistical shape model for large-scale in silico studies of human atria: Model development and application to ECG simulations', *Medical Image Analysis*, 74, p. 102210. DOI: 10.1016/j.media.2021.102210.

Nagel, C. *et al.* (2021) 'Non-Invasive and Quantitative Estimation of Left Atrial Fibrosis Based on P Waves of the 12-Lead ECG—A Large-Scale Computational Study Covering Anatomical Variability', *Journal of Clinical Medicine*, 10(8), p. 1797. DOI: 10.3390/jcm10081797.

Nairn, D. *et al.* (2020) 'Comparison of Unipolar and Bipolar Voltage Mapping for Localization of Left Atrial Arrhythmogenic Substrate in Patients with Atrial Fibrillation', *Frontiers in Physiology*, 11, p. 575846. DOI: 10.3389/fphys.2020.575846.

Narayan, S.M. *et al.* (2008) 'Repolarization and Activation Restitution Near Human Pulmonary Veins and Atrial Fibrillation Initiation', *Journal of the American College of Cardiology*, 52(15), pp. 1222–1230. DOI: 10.1016/j.jacc.2008.07.012.

Nattel, S. (2002) 'New ideas about atrial fibrillation 50 years on', *Nature*, 415(6868), pp. 219–226. DOI: 10.1038/415219a.

Nattel, S. (2013) 'Paroxysmal Atrial Fibrillation and Pulmonary Veins: Relationships Between Clinical Forms and Automatic Versus Re-entrant Mechanisms', *Canadian Journal of Cardiology*, 29(10), pp. 1147–1149. DOI: 10.1016/j.cjca.2013.07.797.

Nattel, S. *et al.* (2021) 'Challenges and opportunities in improving the management of atrial fibrillation: recent research advances and their clinical translation', *Cardiovascular Research*, 117(7), pp. 1609–1611. DOI: 10.1093/cvr/cvab170.

Nattel, S. and Dobrev, D. (2017) 'Controversies About Atrial Fibrillation Mechanisms', *Circulation Research*, 120(9), pp. 1396–1398. DOI: 10.1161/CIRCRESAHA.116.310489.

Niederer, S.A. *et al.* (2011) 'Verification of cardiac tissue electrophysiology simulators using an *N*-version benchmark', *Philosophical Transactions of the Royal Society A: Mathematical, Physical and Engineering Sciences*, 369(1954), pp. 4331–4351. DOI: 10.1098/rsta.2011.0139.

Nishimura, M., Follmer, C.H. and Singer, D.H. (1989) 'Amiodarone blocks calcium current in single guinea pig ventricular myocytes.', *The Journal of pharmacology and experimental therapeutics*, 251(2), pp. 650–9.

Njoku, A. *et al.* (2018) 'Left atrial volume predicts atrial fibrillation recurrence after radiofrequency ablation: a meta-analysis', *EP Europace*, 20(1), pp. 33–42. DOI: 10.1093/europace/eux013.

Noble, D. (1962) 'A modification of the Hodgkin-Huxley equations applicable to Purkinje fibre action and pacemaker potentials', *The Journal of Physiology*, 160(2), pp. 317–352. DOI: 10.1113/jphysiol.1962.sp006849.

Nolasco, J.B. and Dahlen, R.W. (1968) 'A graphic method for the study of alternation in cardiac action potentials.', *Journal of Applied Physiology*, 25(2), pp. 191–196. DOI: 10.1152/jappl.1968.25.2.191.

O'Hara, G. *et al.* (1992) 'Effects of flecainide on the rate dependence of atrial refractoriness, atrial repolarization and atrioventricular node conduction in anesthetized dogs', *Journal of the American College of Cardiology*, 19(6), pp. 1335–1342. DOI: 10.1016/0735-1097(92)90342-K.

Oshikawa, N. *et al.* (2001) 'Frequency-dependent electrophysiological effect of ibutilide on human atrium and ventricle', *Journal of Interventional Cardiac Electrophysiology*, 5(1), pp. 81–87. DOI: 10.1023/A:1009866126492.

Pandit, S. V. *et al.* (2005) 'Ionic Determinants of Functional Reentry in a 2-D Model of Human Atrial Cells During Simulated Chronic Atrial Fibrillation', *Biophysical Journal*, 88(6), pp. 3806–3821. DOI: 10.1529/biophysj.105.060459.

Pandit, S. V. and Jalife, J. (2013) 'Rotors and the Dynamics of Cardiac Fibrillation', *Circulation Research*, 112(5), pp. 849–862. DOI: 10.1161/CIRCRESAHA.111.300158.

Passini, E. *et al.* (2016) 'Mechanisms of pro-arrhythmic abnormalities in ventricular repolarisation and anti-arrhythmic therapies in human hypertrophic cardiomyopathy', *Journal of Molecular and Cellular Cardiology*, 96, pp. 72–81. DOI: 10.1016/j.yjmcc.2015.09.003.

Passini, E. *et al.* (2017) 'Human In Silico Drug Trials Demonstrate Higher Accuracy than Animal Models in Predicting Clinical Pro-Arrhythmic Cardiotoxicity', *Frontiers in Physiology*, 8. DOI: 10.3389/fphys.2017.00668.

Pastore, J.M. *et al.* (1999) 'Mechanism Linking T-Wave Alternans to the Genesis of Cardiac Fibrillation', *Circulation*, 99(10), pp. 1385–1394. DOI: 10.1161/01.CIR.99.10.1385.

Patel, C., Yan, G.-X. and Kowey, P.R. (2009) 'Dronedarone', *Circulation*, 120(7), pp. 636–644. DOI: 10.1161/CIRCULATIONAHA.109.858027.

Peyronnet, R. and Ravens, U. (2019) 'Atria-selective antiarrhythmic drugs in need of alliance partners', *Pharmacological Research*, 145, p. 104262. DOI: 10.1016/j.phrs.2019.104262.

Platonov, P.G. (2012) 'P-Wave Morphology: Underlying Mechanisms and Clinical Implications', *Annals of Noninvasive Electrocardiology*, 17(3), pp. 161–169. DOI: 10.1111/j.1542-474X.2012.00534.x.

Pohjantähti-Maaroos, H. *et al.* (2019) 'Intravenous vernakalant in comparison with intravenous flecainide in the cardioversion of recent-onset atrial fibrillation', *European Heart Journal: Acute Cardiovascular Care*, 8(2), pp. 114–120. DOI: 10.1177/2048872617728558.

Pope, M.T. *et al.* (2022) 'Clinical utility of non-contact charge density 'SuperMap' algorithm for the mapping and ablation of organized atrial arrhythmias', *EP Europace*, 24, pp. 747–754. DOI: 10.1093/europace/euab271.

Pope, M.T. *et al.* (2021) 'Spatial and temporal variability of rotational, focal, and irregular activity: Practical implications for mapping of atrial fibrillation', *Journal of Cardiovascular Electrophysiology*, 32(9), pp. 2393–2403. DOI: 10.1111/jce.15170.

Qu, Z. (2010) 'T-wave alternans and arrhythmogenesis in cardiac diseases', *Frontiers in Physiology*, 1. DOI: 10.3389/fphys.2010.00154.

Qu, Z., Weiss, J.N. and Garfinkel, A. (1999) 'Cardiac electrical restitution properties and stability of reentrant spiral waves: a simulation study', *American Journal of Physiology-Heart and Circulatory Physiology*, 276(1), pp. H269–H283. DOI: 10.1152/ajpheart.1999.276.1.H269.

Quinteiro, R.A. and Biagetti, M.O. (1994) 'Chronic Versus Acute Effects of Amiodarone on the Vmax-Conduction Velocity Relationship and on the Space Constant in Canine Myocardium', *Journal of Cardiovascular Pharmacology*, 24(1), pp. 122–132. DOI: 10.1097/00005344-199407000-00020.

Ravens, U. and Cerbai, E. (2008) 'Role of potassium currents in cardiac arrhythmias', *Europace*, 10(10), pp. 1133–1137. DOI: 10.1093/europace/eun193.

Reisinger, J. *et al.* (2004) 'Flecainide versus ibutilide for immediate cardioversion of atrial fibrillation of recent onset', *European Heart Journal*, 25(15), pp. 1318–1324. DOI: 10.1016/j.ehj.2004.04.030.

Rodrigo, M. *et al.* (2014) 'Body surface localization of left and right atrial high-frequency rotors in atrial fibrillation patients: A clinical-computational study', *Heart Rhythm*, 11(9), pp. 1584–1591. DOI: 10.1016/j.hrthm.2014.05.013.

Romero, L. *et al.* (2009) 'Impact of ionic current variability on human ventricular cellular electrophysiology', *American Journal of Physiology-Heart and Circulatory Physiology*, 297(4), pp. H1436–H1445. DOI: 10.1152/ajpheart.00263.2009.

Roney, C.H. *et al.* (2016) 'Modelling methodology of atrial fibrosis affects rotor dynamics and electrograms', *EP Europace*, 18(suppl_4), pp. iv146–iv155. DOI: 10.1093/europace/euw365.

Roney, C.H. *et al.* (2020) 'In silico Comparison of Left Atrial Ablation Techniques That Target the Anatomical, Structural, and Electrical Substrates of Atrial Fibrillation', *Frontiers in Physiology*, 11. DOI: 10.3389/fphys.2020.572874.

Roney, C.H. *et al.* (2022) 'Predicting Atrial Fibrillation Recurrence by Combining Population Data and Virtual Cohorts of Patient-Specific Left Atrial Models', *Circulation: Arrhythmia and Electrophysiology*, 15(2). DOI: 10.1161/CIRCEP.121.010253.

Roney, C.H. *et al.* (2023) 'PO-01-215 Atrial fibrillation outcome is improved by biatrial substrate ablation in a large virtual trial', *Heart Rhythm*, 20(5), pp. S164–S165. DOI: 10.1016/j.hrthm.2023.03.533.

Roy, D. *et al.* (2004) 'A randomized, controlled trial of RSD1235, a novel anti-arrhythmic agent, in the treatment of recent onset atrial fibrillation', *Journal of the American College of Cardiology*, 44(12), pp. 2355–2361. DOI: 10.1016/j.jacc.2004.09.021.

Roy, D. *et al.* (2008) 'Vernakalant Hydrochloride for Rapid Conversion of Atrial Fibrillation', *Circulation*, 117(12), pp. 1518–1525. DOI: 10.1161/CIRCULATIONAHA.107.723866.

Saad, E.B. and Slater, C. (2014) 'Complete Isolation of the Left Atrial Posterior Wall (Box Lesion) to Treat Longstanding Persistent Atrial Fibrillation.', *Journal of atrial fibrillation*, 7(4), p. 1174. DOI: 10.4022/jafib.1174.

Sachetto Oliveira, R. *et al.* (2012) 'An Adaptive Mesh Algorithm for the Numerical Solution of Electrical Models of the Heart', in, pp. 649–664. DOI: 10.1007/978-3-642-31125-3_49.

Sachetto Oliveira, R. *et al.* (2018) 'Performance evaluation of GPU parallelization, space-time adaptive algorithms, and their combination for simulating cardiac electrophysiology', *International Journal for Numerical Methods in Biomedical Engineering*, 34(2), p. e2913. DOI: 10.1002/cnm.2913.

Sachetto Oliveira, R., Alonso, S. and dos Santos, R.W. (2018) 'Killing Many Birds With Two Stones: Hypoxia and Fibrosis Can Generate Ectopic Beats in a Human Ventricular Model', *Frontiers in Physiology*, 9. DOI: 10.3389/fphys.2018.00764.

Sánchez, C. *et al.* (2014) 'Inter-Subject Variability in Human Atrial Action Potential in Sinus Rhythm versus Chronic Atrial Fibrillation', *PLoS ONE*, 9(8), p. e105897. DOI: 10.1371/journal.pone.0105897.

Sánchez, C. *et al.* (2017) 'Atrial Fibrillation Dynamics and Ionic Block Effects in Six Heterogeneous Human 3D Virtual Atria with Distinct Repolarization Dynamics', *Frontiers in Bioengineering and Biotechnology*, 5. DOI: 10.3389/fbioe.2017.00029.

Sarkar, A.X., Christini, D.J. and Sobie, E.A. (2012) 'Exploiting mathematical models to illuminate electrophysiological variability between individuals', *The Journal of Physiology*, 590(11), pp. 2555–2567. DOI: 10.1113/jphysiol.2011.223313.

van Schie, M.S. *et al.* (2021) 'Identification of Low-Voltage Areas: A Unipolar, Bipolar, and Omnipolar Perspective', *Circulation: Arrhythmia and Electrophysiology*, 14(7). DOI: 10.1161/CIRCEP.121.009912.

Schmitt, C. *et al.* (2002) 'Biatrial multisite mapping of atrial premature complexes triggering onset of atrial fibrillation', *The American Journal of Cardiology*, 89(12), pp. 1381–1387. DOI: 10.1016/S0002-9149(02)02350-0.

Schüttler, D. *et al.* (2020) 'Animal Models of Atrial Fibrillation', *Circulation Research*, 127(1), pp. 91–110. DOI: 10.1161/CIRCRESAHA.120.316366.

Scott Jr, L. *et al.* (2021) 'NLRP3 inflammasome is a key driver of obesity-induced atrial arrhythmias', *Cardiovascular Research*, 117(7), pp. 1746–1759. DOI: 10.1093/cvr/cvab024.

Seemann, G. *et al.* (2006) 'Heterogeneous three-dimensional anatomical and electrophysiological model of human atria', *Philosophical Transactions of the Royal Society A: Mathematical, Physical and Engineering Sciences*, 364(1843), pp. 1465–1481. DOI: 10.1098/rsta.2006.1781.

Shim, J. *et al.* (2017) 'Virtual In-Silico Modeling Guided Catheter Ablation Predicts Effective Linear Ablation Lesion Set for Longstanding Persistent Atrial Fibrillation: Multicenter Prospective Randomized Study', *Frontiers in Physiology*, 8. DOI: 10.3389/fphys.2017.00792.

Simon, A. *et al.* (2016) 'Vernakalant is superior to ibutilide for achieving sinus rhythm in patients with recent-onset atrial fibrillation: a randomized controlled trial at the emergency department', *Europace*, p. euw052. DOI: 10.1093/europace/euw052.

Singh, B.N. *et al.* (2007) 'Dronedarone for Maintenance of Sinus Rhythm in Atrial Fibrillation or Flutter', *New England Journal of Medicine*, 357(10), pp. 987–999. DOI: 10.1056/NEJMoa054686.

Spach, M.S. and Dolber, P.C. (1986) 'Relating extracellular potentials and their derivatives to anisotropic propagation at a microscopic level in human cardiac muscle. Evidence for electrical uncoupling of side-to-side fiber connections with increasing age.', *Circulation Research*, 58(3), pp. 356–371. DOI: 10.1161/01.RES.58.3.356.

Staerk, L. *et al.* (2017) 'Atrial Fibrillation Epidemiology, Pathophysiology, and Clinical Outcomes', *Circulation Research*, 120(9), pp. 1501–1517. DOI: 10.1161/CIRCRESAHA.117.309732.

Sun, W., Sarma, J.S.M. and Singh, B.N. (1999) 'Electrophysiological Effects of Dronedarone (SR33589), a Noniodinated Benzofuran Derivative, in the Rabbit Heart', *Circulation*, 100(22), pp. 2276–2281. DOI: 10.1161/01.CIR.100.22.2276.

Sun, W., Sarma, J.S.M. and Singh, B.N. (2002) 'Chronic and Acute Effects of Dronedarone on the Action Potential of Rabbit Atrial Muscle Preparations: Comparison With Amiodarone', *Journal of Cardiovascular Pharmacology*, 39(5), pp. 677–684. DOI: 10.1097/00005344-200205000-00008.

Sutanto, H. *et al.* (2019) 'Maastricht antiarrhythmic drug evaluator (MANTA): A computational tool for better understanding of antiarrhythmic drugs', *Pharmacological Research*, 148, p. 104444. DOI: 10.1016/j.phrs.2019.104444.

Suzuki, T. *et al.* (2013) 'Atrial selectivity in Na+channel blockade by acute amiodarone', *Cardiovascular Research*, 98(1), pp. 136–144. DOI: 10.1093/cvr/cvt007.

Talajic, M., DeRoode, M.R. and Nattel, S. (1987) 'Comparative electrophysiologic effects of intravenous amiodarone and desethylamiodarone in dogs: evidence for clinically relevant activity of the metabolite.', *Circulation*, 75(1), pp. 265–271. DOI: 10.1161/01.CIR.75.1.265.

Tamargo, J. *et al.* (2004) 'Pharmacology of cardiac potassium channels', *Cardiovascular Research*, 62(1), pp. 9–33. DOI: 10.1016/j.cardiores.2003.12.026.

The Digitalis in Acute Atrial Fibrillation (DAAF) Trial Group (1997) 'Intravenous digoxin in acute atrial fibrillation: Results of a randomized, placebo-controlled multicentre trial in 239 patients', *European Heart Journal*, 18(4), pp. 649–654. DOI: 10.1093/oxfordjournals.eurheartj.a015311.

Vagos, M. *et al.* (2018) 'Computational Modeling of Electrophysiology and Pharmacotherapy of Atrial Fibrillation: Recent Advances and Future Challenges', *Frontiers in Physiology*, 9. DOI: 10.3389/fphys.2018.01221.

Valderrábano, M. *et al.* (2020) 'Effect of Catheter Ablation With Vein of Marshall Ethanol Infusion vs Catheter Ablation Alone on Persistent Atrial Fibrillation', *JAMA*, 324(16), p. 1620. DOI: 10.1001/jama.2020.16195.

Varró, A., Virág, L. and Papp, J.Gy. (1996) 'Comparison of the chronic and acute effects of amiodarone on the calcium and potassium currents in rabbit isolated cardiac myocytes', *British Journal of Pharmacology*, 117(6), pp. 1181–1186. DOI: 10.1111/j.1476-5381.1996.tb16713.x.

Verheule, S. *et al.* (2013) 'Loss of Continuity in the Thin Epicardial Layer Because of Endomysial Fibrosis Increases the Complexity of Atrial Fibrillatory Conduction', *Circulation: Arrhythmia and Electrophysiology*, 6(1), pp. 202–211. DOI: 10.1161/CIRCEP.112.975144.

Verma, A. *et al.* (2015) 'Approaches to Catheter Ablation for Persistent Atrial Fibrillation', *New England Journal of Medicine*, 372(19), pp. 1812–1822. DOI: 10.1056/NEJMoa1408288.

Verma, A. *et al.* (2022) 'First-in-Human Experience and Acute Procedural Outcomes Using a Novel Pulsed Field Ablation System: The PULSED AF Pilot Trial', *Circulation: Arrhythmia and Electrophysiology*, 15(1). DOI: 10.1161/CIRCEP.121.010168.

Viceconti, M. *et al.* (2021) 'In silico trials: Verification, validation and uncertainty quantification of predictive models used in the regulatory evaluation of biomedical products', *Methods*, 185, pp. 120–127. DOI: 10.1016/j.ymeth.2020.01.011.

Virag, N. *et al.* (2002) 'Study of atrial arrhythmias in a computer model based on magnetic resonance images of human atria', *Chaos: An Interdisciplinary Journal of Nonlinear Science*, 12(3), pp. 754–763. DOI: 10.1063/1.1483935.

Viswanathan, P.C. *et al.* (2001) 'Gating-Dependent Mechanisms for Flecainide Action in *SCN5A* -Linked Arrhythmia Syndromes', *Circulation*, 104(10), pp. 1200–1205. DOI: 10.1161/hc3501.093797.

Wang, A. *et al.* (2019) 'Atrial Fibrillation and Diabetes Mellitus', *Journal of the American College of Cardiology*, 74(8), pp. 1107–1115. DOI: 10.1016/j.jacc.2019.07.020.

Wang, J. *et al.* (1993) 'Comparative mechanisms of antiarrhythmic drug action in experimental atrial fibrillation. Importance of use-dependent effects on refractoriness.', *Circulation*, 88(3), pp. 1030–1044. DOI: 10.1161/01.CIR.88.3.1030.

Wang, L. *et al.* (2007) 'Cardiac Glycosides as Novel Inhibitors of Human *Ether-a-go-go* -Related Gene Channel Trafficking', *Journal of Pharmacology and Experimental Therapeutics*, 320(2), pp. 525–534. DOI: 10.1124/jpet.106.113043.

Wang, Z., Feng, J. and Nattel, S. (1995) 'Idiopathic atrial fibrillation in dogs: Electrophysiologic determinants and mechanisms of antiarrhythmic action of flecainide', *Journal of the American College of Cardiology*, 26(1), pp. 277–286. DOI: 10.1016/0735-1097(95)90845-F.

Wang, Z.G. *et al.* (1990) 'Effects of flecainide and quinidine on human atrial action potentials. Role of rate-dependence and comparison with guinea pig, rabbit, and dog tissues.', *Circulation*, 82(1), pp. 274–283. DOI: 10.1161/01.CIR.82.1.274.

Wazni, O.M. *et al.* (2021) 'Cryoballoon Ablation as Initial Therapy for Atrial Fibrillation', *New England Journal of Medicine*, 384(4), pp. 316–324. DOI: 10.1056/NEJMoa2029554.

Wettwer, E. *et al.* (2013) 'The new antiarrhythmic drug vernakalant: ex vivo study of human atrial tissue from sinus rhythm and chronic atrial fibrillation', *Cardiovascular Research*, 98(1), pp. 145–154. DOI: 10.1093/cvr/cvt006.

White, J.D. *et al.* (2019) 'MeshMonk: Open-source large-scale intensive 3D phenotyping', *Scientific Reports*, 9(1), p. 6085. DOI: 10.1038/s41598-019-42533-y.

Wiedmann, F. *et al.* (2020) 'Pharmacologic TWIK-Related Acid-Sensitive K+ Channel (TASK-1) Potassium Channel Inhibitor A293 Facilitates Acute Cardioversion of Paroxysmal Atrial Fibrillation in a Porcine Large Animal Model', *Journal of the American Heart Association*, 9(10). DOI: 10.1161/JAHA.119.015751.

Wijffels, M.C.E.F. *et al.* (1995) 'Atrial Fibrillation Begets Atrial Fibrillation', *Circulation*, 92(7), pp. 1954–1968. DOI: 10.1161/01.CIR.92.7.1954.

Wilhelms, M. *et al.* (2013) 'Benchmarking electrophysiological models of human atrial myocytes', *Frontiers in Physiology*, 3. DOI: 10.3389/fphys.2012.00487.

Yang, G. *et al.* (2022) 'Circumferential Pulmonary Vein Isolation Plus Low-Voltage Area Modification in Persistent Atrial Fibrillation', *JACC: Clinical Electrophysiology*, 8(7), pp. 882–891. DOI: 10.1016/j.jacep.2022.03.012.

Zahid, S. *et al.* (2016) 'Patient-derived models link re-entrant driver localization in atrial fibrillation to fibrosis spatial pattern', *Cardiovascular Research*, 110(3), pp. 443–454. DOI: 10.1093/cvr/cvw073.

Zeemering, S. *et al.* (2018) 'The electrocardiogram as a predictor of successful pharmacological cardioversion and progression of atrial fibrillation', *EP Europace*, 20(7), pp. e96–e104. DOI: 10.1093/europace/eux234.

Zink, M.D. *et al.* (2022) 'Extended ECG Improves Classification of Paroxysmal and Persistent Atrial Fibrillation Based on P- and f-Waves', *Frontiers in Physiology*, 13. DOI: 10.3389/fphys.2022.779826.

CHAPTER

ANNEX: BENCHMARK OF CARDIAC CELLULAR ELECTROPHYSIOLOGY

I

In this chapter I present a modified computational benchmark of cardiac electrophysiology, that was conducted to verify the convergence of MonoAlg3D in the setting of atrial simulations.

I.1. Definition of the modified benchmark problem

As proposed by (Niederer *et al.,* 2011) the monodomain equation of the transmembrane voltage was solved on a slab geometry of size 20×7×3 cm^3. An anisotropic conductivity tensor was defined considering the longitudinal-transversal ratio presented in **Table 4.1** (**Chapter 4**). The longitudinal velocity was set to 60 cm/s (i.e., the slowest considered in this thesis), with a transversal to longitudinal ratio of 1:2 (**Table 4.1**). Simulations were performed with the CRN model, which was solved with an adaptive Euler method (second order accurate). The minimum and maximum time steps were set to dt = 0.0001 and dt = 0.01, respectively, with the latter also used for the system of partial differential equations. Different mesh element sizes, ranging from 0.1 to 0.5 mm, were tested to find a compromise between accuracy and computational cost. Other parameters were defined as in (Sachetto Oliveira *et al.*, 2018), namely $\beta = 1400 cm^{-1}$ and $C_m = 1\ \mu F \cdot cm^{-1}$.

An external stimulus of 50 mA/cm^3 during 2 ms was applied on a cubic region of 1.5×1.5×1.5 mm^3, located in one corner of the slab tissue. Following electrical propagation, the conduction velocity was computed across the diagonal of the slab (**Figure I.1**)

I.2. Results

Figure I.1 illustrates a representation of the slab geometry and the local activation times. The latest activation time was 34, 35, 36, 37 and 39 ms for the geometries with element sizes from 0.1 to 0.5 mm, respectively (**Figure I.1**). This resulted in conduction velocities (computed in the farthest point) of 54.9, 57.8, 59.4, 61.1, and 62.9 cm/s. Thus, an element size of 0.4 mm was the longest (i.e., coarsest mesh) that yielded a conduction velocity loss below 10% compared to the finest mesh. This element size has been adopted for conducting multi-scale simulations.

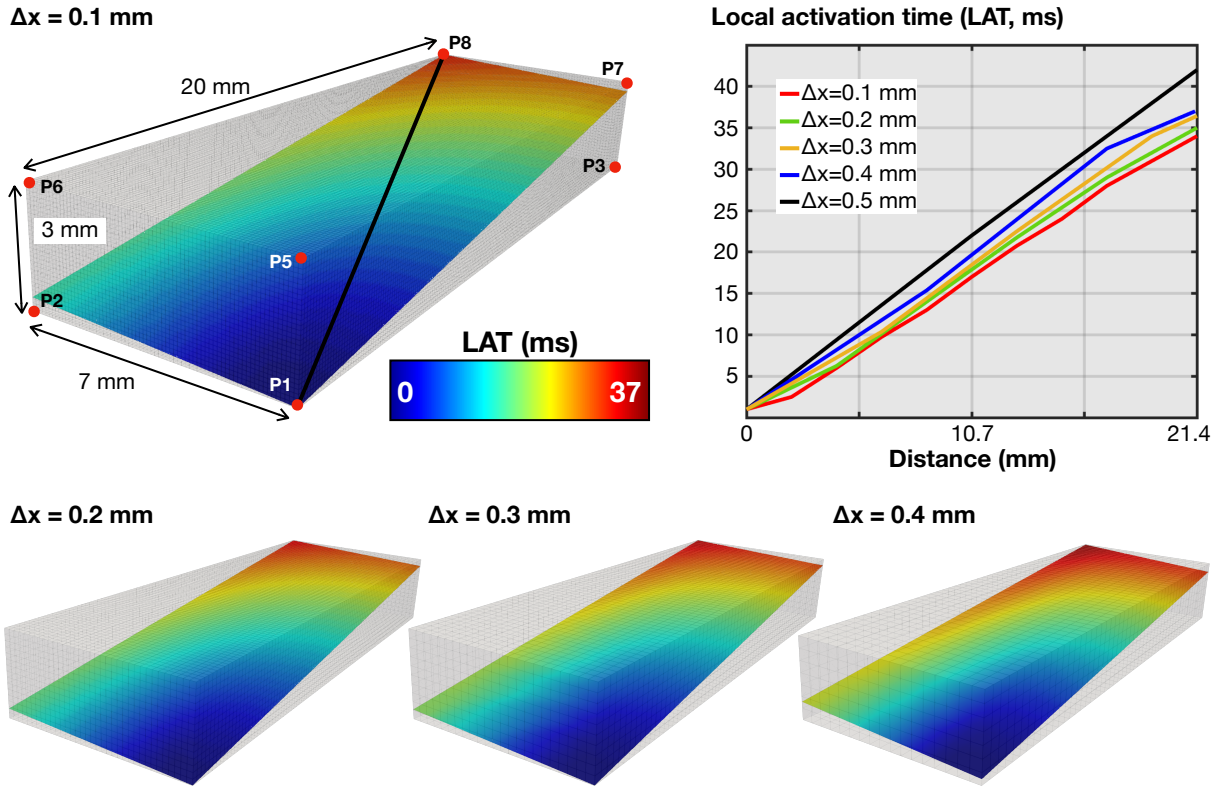


Figure I.1. Schematic representation of the slab geometry used to solve the benchmark problem. Plots of the activation time are evaluated across the line from P1 to P8. Plots of the activation along the plane shown are provided for four meshes with different element length (0.1, 0.2, 0.4 and 0.5 mm).

CHAPTER

ANNEX: SUPPLEMENTAL INFORMATION FOR CHAPTER 5

II

*This chapter covers additional, yet fundamental, material for this thesis, that has been presented in **Chapter 6** as supplemental information.*

II.1. Supplemental methods

II.1.1. APD and conduction velocity restitution

The APD restitution was obtained by both standard S1S2 and dynamic protocols. The standard S1S2 protocol was computed in a single-cell environment and consisted of 50 S1 stimuli applied at a specific cycle length followed by an extra S2 stimulus. Six different cycle lengths (700, 600, 500, 400, 300 and 250 ms) were employed for the S1 stimuli. The S2 stimulus started at the same cycle length than the last S1 and was decreased by 50 ms from 700 to 400 ms, by 20 ms from 400 to 300 ms, and by 10 ms from 300 ms until the previous diastolic interval was lower than zero.

The dynamic restitution protocol was computed using an isotropic cable (40000×100×100 μm) as in (Wilhelms *et al.*, 2013). Five consecutive beats were paced at one side of the cable at decreasing cycle length, following the same interval progression as for the standard S1S2 protocol. Cardiomyocyte models were previously paced for 50 beats in a single-cell environment, so they could adapt to the different cycle lengths. To detect APD alternans, the last two APDs were recorded.

The conduction velocity restitution was computed during the dynamic restitution protocol. For this, the distance travelled by the wavefront was divided by the time at which the cell located at three-quarters down the cable reached the maximum depolarization upstroke. The diffusion coefficient was adjusted to obtain a CV of 60 cm/s (Sánchez *et al.*, 2017).

II.2. Supplemental results

II.2.1. Discordant APD alternans and AF inducibility

Figure II.1A illustrates the sequence of atrial depolarization during sinus rhythm. The transmembrane voltage is recorded at three sites of the posterior wall of the left atrium during the last sinus rhythm beat and the first two S2 stimuli in the burst (**Figure II.1A**, right). **Figure II.1B** (top) shows the APD alternans map obtained subtracting the APD of the last sinus rhythm beat to the APD of the first S2 stimulus. The identity line (white) separates regions alternating in a short-long pattern (green) from those showing a long-short APD alternation (purple). **Figure II.1B** (bottom) depicts snapshots of the transmembrane voltage following the second S2 stimulus, highlighting conduction block and re-entry.

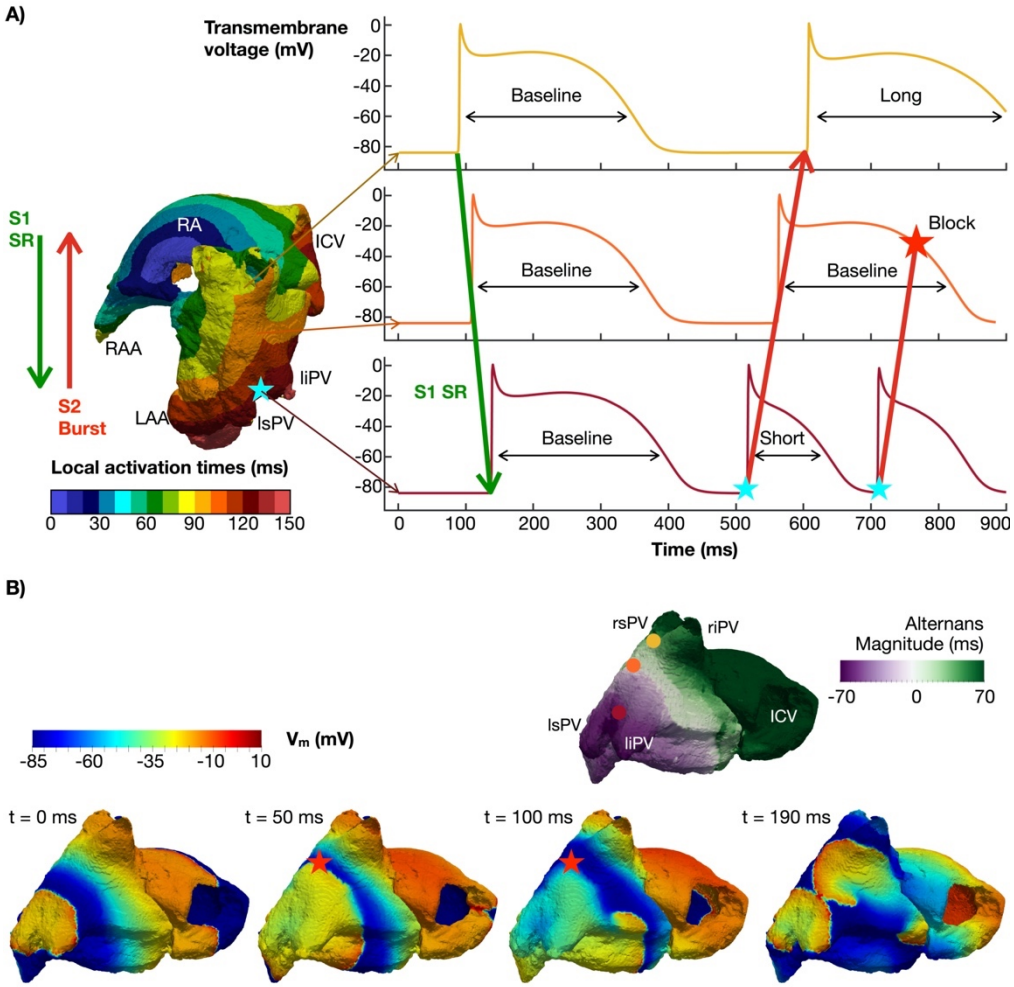


Figure II.1. Discordant alternants favouring AF inducibility. **A)** Local activation times (LAT) during sinus rhythm and time course of the transmembrane voltage (V_m) at three sites of the posterior wall of the left atrium. The application of the burst pacing inverts the activation sequence at the latter. The green arrow represents the direction of wavefront propagation during sinus rhythm (SR) and the red one during burst pacing. **B)** APD alternans map, showing discordant alternation: purple regards long-short alternation and green short-long alternation. The colour dots correspond to the representative action potential traces shown in A), illustrating short-long alternation (yellow dot), long-short alternation (red dot) and no alternation (orange dot placed at the line of identity). Snapshots of Vm following the second S2 stimuli in the burst. The cyan star represents the location of the burst pacing and the red star conduction block.

During sinus rhythm, the wavefront travelled from the right pulmonary veins, throughout the posterior wall, to the left pulmonary veins, as illustrated through local activation time map in **Figure II.1A**. The application of the burst pacing inverted the sequence of activation (red arrow) and the left pulmonary veins were firstly depolarized. Since the left pulmonary veins were lastly depolarized during sinus rhythm but first during ectopic stimulation, a very short diastolic interval arose. This, in turn, yielded a very short APD, so that regions near the left pulmonary veins alternated with a long-short pattern. Following the same reasoning, regions close to the right pulmonary veins presented a very long diastolic interval, which led to a very long APD. These regions alternated with a short-long pattern. Along both regions, a third region presented the same APD during the first S2 stimulus than during SR.

This led to discordant alternans, characterized by adjacent regions alternating with opposing APD phase. In this scenario, when the following S2 stimulus was applied, only those regions that presented short APD (**Figure II.1B**, red dot) were able to propagate the wavefront. Conduction block (red star) arose in regions with long APD (**Figure II.1B**, yellow dot), yielding re-entry and AF initiation. The steep restitution properties that favoured APD alternans additionally facilitated AF maintenance.

II.2.2. Comparison of drug effects between simulated and experimental result, and between simulated results obtained with different cell models

Figure II.2A compares the percentage (%) of APD variation obtained after drug action with respect to control conditions in-silico and in-vitro. Corresponding results were obtained for APD change between simulated drug action and experimental data, with further validation, illustrating rate-dependence alterations in APD, conduction velocity and maximum upstroke velocity provided in **Table II.1**.

Moreover, **Figure II.2B** shows a comparison of APD variation after drug action between the CRN, Grandi-Bers and Maleckar-Trayanova models. Although consistent trends were observed for the antiarrhythmic drugs tested in all three ionic models, the Grandi-Bers and Maleckar-Trayanova models showed a higher sensitivity to I_{Kur} inhibition than the CRN model, which presented a greater APD prolongation after I_{Kr} block. This is due to a predominant contribution of I_{Kur} on the cellular repolarization of the former, and a minor I_{Kr} and I_{Ks} role (Maleckar *et al.*, 2009). Thus, repeating the in-silico trials with the Grandi-Bers or Maleckar-Trayanova models would be expected to yield an even higher efficacy for I_{Kur} blockers than that already shown in **Figure 6.5** (**Chapter 6**).

II.2.3. Dynamic APD restitution and effective refractory period after drug action

Figure II.3 illustrates the dynamic APDR curve (**Figure II.3A**) and refractor period prior and after drug action (**Figure II.3B**). These biomarkers have been computed for 49 virtual AF patients that developed sustained AF. **Figure II.3C** shows consecutives snapshots of a representative AF episode after amiodarone application and I_{K1} inhibition. Unstable rotors in control conditions became stable and local rotors after the virtual application of amiodarone. I_{K1} inhibition terminated the AF episode.

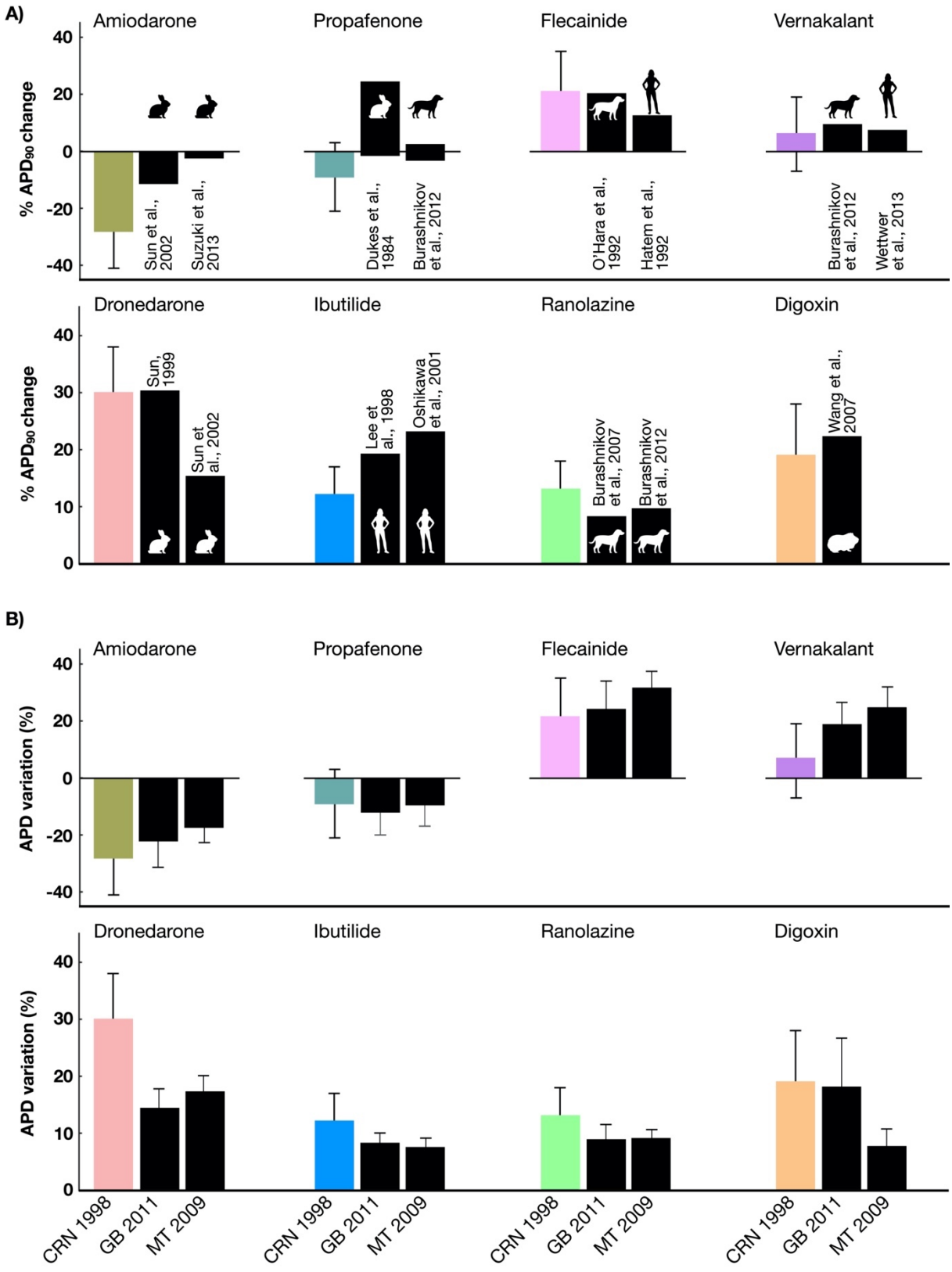


Figure II.2. **A)** Percentage (%) of APD_{90} variation after drug application with respect to control conditions, in-silico (color bars) and in-vitro (black bars, error bars in-vitro not available). **B)** Comparison of the APD variation in-silico between the CRN model, Grandi-Bers (GB 2011) and Maleckar-Trayanova (MT 2009) models.

Table II.1. Comparison of the rate-dependent effects of different drugs in-silico (labelled as "This thesis") and in-vitro (previously published). The in-silico results are obtained from the virtual patient with sustained AF, before ("Control") and after drug modelling. For the in-vitro results, data are presented in parentheses if the authors reported the dose-dependent effects of a drug. The symbol (*) is added in those cases that the cycle length was not exactly the one considered in this table but similar. In both in-silico and in-vitro, data are presented as mean ± standard deviation. The standard deviation is not reported in-vitro if data were not available.

	Study	**APD (ms)**			**CV (cm/s)**			**Vmax (mV/ms)**		
	Cycle Length (ms)	**1000**	**500**	**300**	**1000**	**500**	**300**	**1000**	**500**	**300**
Control	This thesis	276 ± 31	252 ± 35	199 ± 25	63 ± 5	63 ± 5	60 ± 6	211± 3	208 ± 30	162 ± 50

Drug	**Study**	**Species**	**APD Change (%)**			**CV Change (%)**			**Vmax Change (%)**		
			1000	**500**	**300**	**1000**	**500**	**300**	**1000**	**500**	**300**
Amiodarone	This thesis		-28 ± 13	-29 ± 6	-18 ± 7	-12 ± 1	-13 ± 1	-6 ± 11	-21 ± 1	-21 ± 1	-13 ± 5
	(Quinteiro and Biagetti, 1994)	Dog	–	–	–	-2	-3	-5	-4	-11	-21
	(Sun, Sarma and Singh, 1999)	Rabbit	-11	-11	-8	–	–	–	-7	-8	-8
	(Suzuki *et al.*, 2013)	Rabbit	-2	–	–	–	–	-19 ± 4	–	–	–
Dronedarone	This thesis		30 ± 8	19 ± 12	28 ± 23	-5 ± 1	-5 ± 2	-5 ± 3	-9 ± 1	-12 ± 4	-13 ± 6
	(Sun, Sarma and Singh, 1999)	Rabbit	[27, 30]*	[15, 20]*	[5, 12]	–	–	–	–	–	–
	(Sun, Sarma and Singh, 2002)	Rabbit	15	15	17				-6	-7	-6
Flecainide	This thesis		21 ± 14	22 ± 9	29 ± 14	-13 ± 1	-12 ± 1	-16 ± 4	-23 ± 1	-24 ± 2	-65 ± 30
	(Wang *et al.*, 1990)	Human	6 ± 3	–	27 ± 12	–	–	–	- 28	–	-50
	(O'Hara *et al.*, 1992)	Dog	–	[5 , 20]	[7, 39]	–	–	–	–	–	–
	(Hatem *et al.*, 1992)	Human	12*	–	–	–	–	–	- 21*	–	–
	(Wang, Feng and Nattel, 1995)	Dog	–	–	–	–	- 8*	- 11	–	–	–
	(van Hunnik *et al.*, 2016)	Goat	–	–	–	–	[-12, -24]*	[-16, -33]*	–	–	–

Table II.1. (Continuation).

Drug	Study	Species	APD Change (%)			CV Change (%)			Vmax Change (%)		
			1000	500	300	1000	500	300	1000	500	300
Propafenone	This thesis		0 ± 21	-9 ± 12	-7 ± 9	-10 ± 1	-10 ± 1	5 ± 9	-19 ± 1	-19 ± 1	-32 ± 50
	(Dukes and Williams, 1984)	Rabbit	–	[-1, 24]	–	–	[-15, -24]	–	_	[-7, -77]	–
	(Wang *et al.*, 1993)	Dog	–	–	–	–	–	-29 ± 4	_	–	–
	(Burashnikov, Belardinelli and Antzelevitch, 2012)	Dog	–	[0, 2]	[-2, 0]					[-15, -41]	[-30, -77]
Ranolazine	This thesis		12 ± 7	6 ± 6	4 ± 8	-2 ± 1	-2 ± 1	-1 ± 5	-3 ± 1	-4 ± 1	-17 ±7
	(Burashnikov *et al.*, 2007)	Dog	–	8	–	–	-16	-35	–	-24 ± 5	–
	(Burashnikov, Belardinelli and Antzelevitch, 2012)	Dog	–	9	11	–	–	–	–	-26 ± 6	-57 ± 17
	(Burashnikov *et al.*, 2012)	Dog	7	5	8	–	–	–	–	-23 ± 13	-48 ± 18
Vernakalant	This thesis		6 ± 13	11 ± 13	11 ± 11	-5 ± 1	-4 ± 1	-6 ± 6	-7 ± 1	-8 ± 1	-15 ± 34
	(Burashnikov *et al.*, 2012)	Dog	9	7	4	–	–	–	–	-20 ± 12	-22 ± 8
	(Wettwer *et al.*, 2013)	Human	7	–	11	–	–	–	-23 ± 7	–	-32 ± 5
	(van Hunnik *et al.*, 2016)	Goat	–	–	–	–	[-15, -18]	[-15, -21]	–	–	–
Ibutilide	This thesis		13 ± 5	10 ± 7	12 ± 7	0	0	0	0 ± 1	0	0
	(Lee, 1992)	Guinea pigs	–	[5, 39]*	–	–	–	–	–	–	–
	(Lee and Lee, 1998)	Human	[4, 19]	–	–	–	–	–	–	–	–
	(Oshikawa *et al.*, 2001)	Human	–	23*	24*	–	–	–	–	–	–
Digoxin	This thesis		19 ± 9	21 ± 8	26 ± 6	0	0	-5 ± 8	-2 ± 1	-3 ± 3	-44 ± 76
	(Wang *et al.*, 2007)	Guinea pig	[22, 100]*	–	–	–	–	–	–	–	–

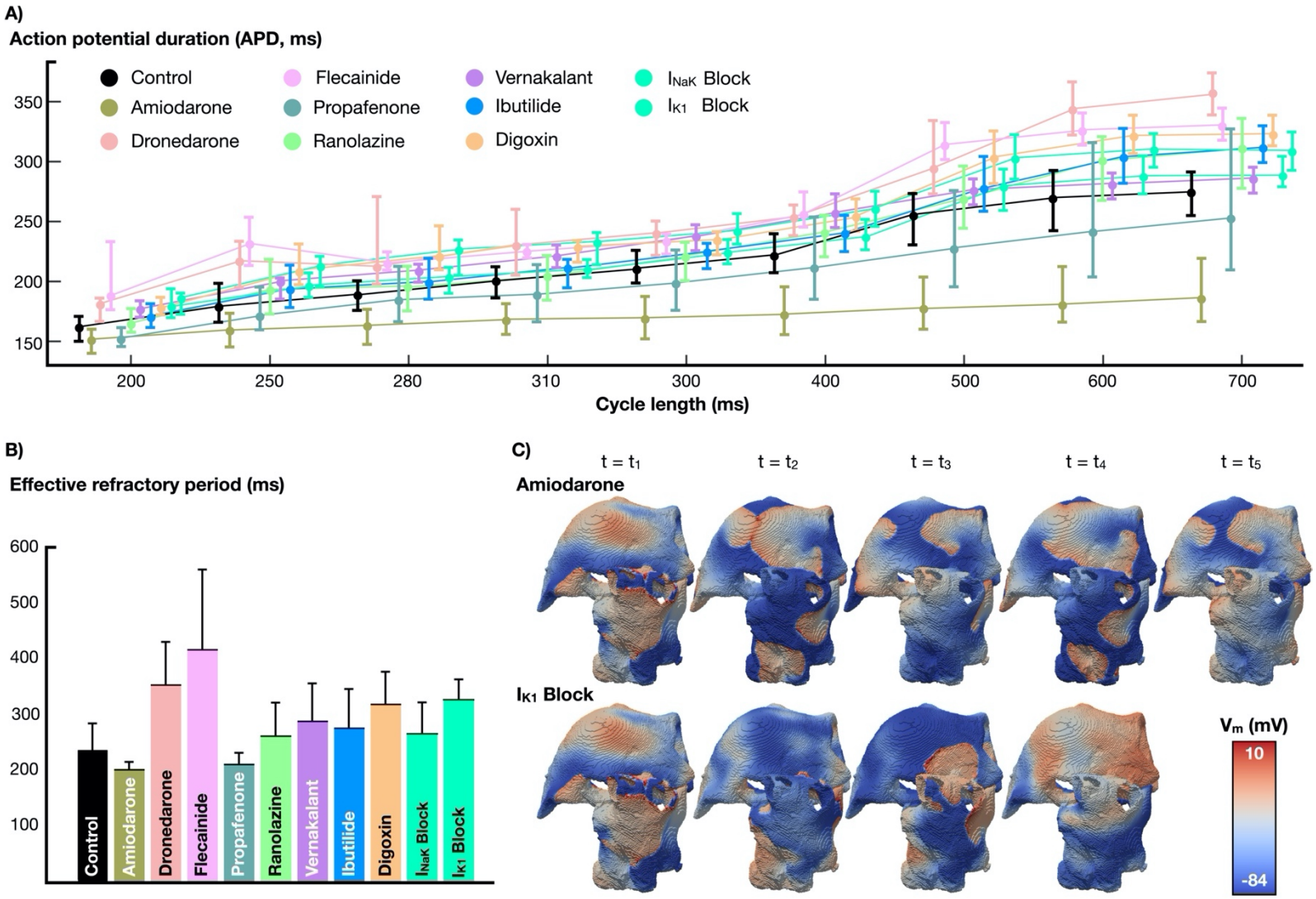


Figure II.3. **A)** Dynamic APD restitution in control conditions and after simulated drug effects for virtual patients with sustained AF. **B)** Comparison of the effective refractory period in control conditions and after drug application. **C)** Consecutive snapshots of a representative AF episode after amiodarone and I_{K1} inhibition.

CHAPTER

ANNEX: ECG ANALYSIS REVEALS IONIC CURRENT DYSREGULATION RELEVANT FOR AF

III

*In **Chapter 6** I have suggested that the ECG might contain information of the atrial ionic current properties. In **Chapter 8** I have shown that ECG biomarkers of virtual AF patients might reflect ionic current dysregulations. This chapter further assesses the extent of atrial ionic information embedded in the ECG, by analyzing ECG biomarkers computed during sinus rhythm. The original work can be found in "Dasí et al., (2022), CinC. DOI: 10.22489/CinC.2022.083".*

III.1. Summary of the study

For conducting this study, a dataset of 1,000 simulated ECGs was computed using a population of virtual patients with 200 individual ionic profiles and 5 different torso-atria orientations. A regression neural network was built to predict key atrial ionic conductances based on P- and T_a-wave biomarkers (ECG waves during the atrial depolarization and repolarization, respectively).

The neural network predicted, with >80% precision, the density of seven ionic currents relevant for AF, namely, I_{Kur}, I_{Kr}, I_{to}, I_{K1}, I_{CaL}, I_{NaK} and I_{Na}. These ionic densities were identified through the P- (i.e., I_{Na}), T_a- (i.e., I_{K1}, I_{NaK}) or both waves (i.e., I_{Kur}, I_{Kr}, I_{to}, I_{CaL}), providing a non-invasive characterisation of atrial electrophysiology. This could improve patient stratification for pharmacological AF treatment.

III.2. Introduction

Pharmacological treatment is a fundamental pillar of AF management. Nevertheless, antiarrhythmic drugs are usually contraindicated given proarrhythmia and cardiotoxicity (Hindricks *et al.*, 2021). Importantly, while proarrhythmic toxicity has been strongly associated with the ionic current profile of the patient (Passini *et al.*, 2017), the latter has so far not been considered for treatment personalization. As shown in **Chapters 6-9**, the ionic current profile is also expected to influence antiarrhythmic drug efficacy, so that neglecting it could explain the limited success of pharmacological treatment for AF and the high rate of cardiotoxic adverse events.

Ignoring the atrial ionic current profile might be due to the inability for its non-invasive characterisation. Nevertheless, previous studies have observed that analysing the ECG might reveal atrial conduction properties, the clinical stage of AF (Zink *et al.*, 2022) or the percentage of atrial fibrosis (Nagel, Luongo, *et al.*, 2021). Thus, as hypothesized in **Chapter 6** and **Chapter 8**, the ECG might also contain information on the ionic current properties. Identifying the atrial ionic substrate non-invasively could improve pharmacological treatment personalization, cardiac safety and efficacy. Accordingly, this study aims to assess the prognostic value of the ECG for inferring the atrial ionic current profile.

III.3. Methods

A dataset of 1,000 ECGs, computed in a population of 200 virtual patients and considering 5 torso-atria orientations (**Figure III.1**), was used to predict the ionic current profile of the atria. The methodology from single cell to body surface level is described below.

III.3.1. Population of virtual patients

A population of 300 atrial cardiomyocyte models was developed as described in **section 4.1.2**. Key conductances and permeabilities of the CRN model were sampled up to ±50% of their control values to capture ionic current variability. The candidate population underwent subsequent calibration, resulting in 200 atrial cardiomyocyte models (**Figure III.1C**).

Every cardiomyocyte model populated one whole-atria model (Visible Female atria), by assigning the single-cell properties to the left atrial tissue and scaling them in the remaining atrial regions (**Figure III.1B**). The longitudinal conduction velocity in the bulk tissue was set to 80 cm/s.

Sinus rhythm was simulated in the cohort of 200 virtual patients for 5 beats, starting with the steady-state conditions at single cell.

III.3.2. ECG analysis and regression with neural networks

Standard 12-lead and extended 15-lead (Zink *et al.*, 2022) ECGs (**Figure III.1A**) were computed for the sixth sinus beat, as described in **section 4.4.2**. The atrial geometry was rotated ±30º around the y- and z-axis, resulting in 5 ECG calculations per virtual patient. Six biomarkers, namely duration, amplitude, area, Shannon entropy, sample entropy and complexity (Zink *et al.*, 2022), were calculated lead-wise from the P- and T_a-wave. Three additional biomarkers were obtained for the P-wave: actual duration (as the last activation time extracted from the simulations), dispersion and V1 terminal force.

A complete dataset was generated considering the P- and T_a-wave biomarkers from 1,000 ECGs (ECG for 200 virtual patients with 5 torso-atria orientations). The dataset was partitioned into four sub-datasets to compare the prognostic value of P- vs. T_a-wave and 12- vs. 15-lead ECG for predicting the ionic current densities of the atria.

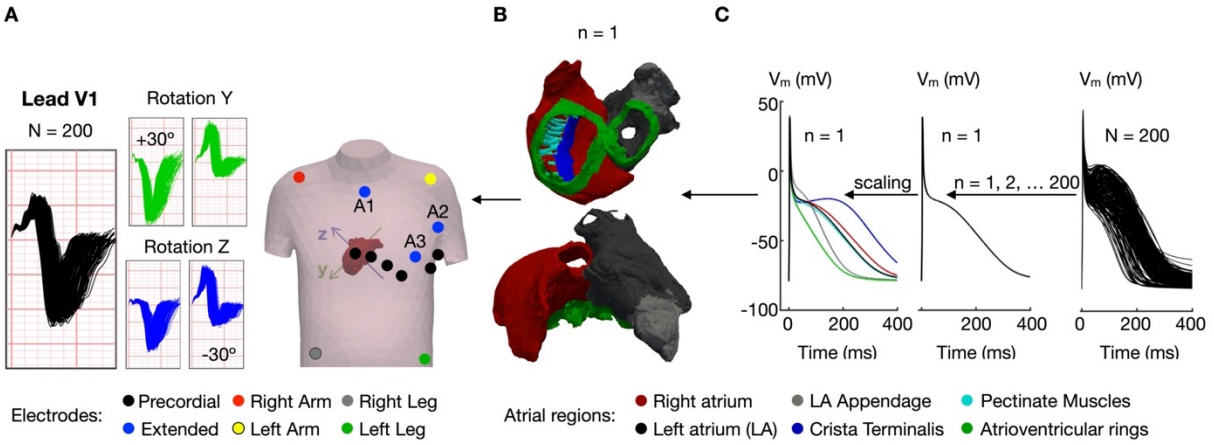


Figure III.1. A) 1,000 simulated ECGs (example of lead V1) considering 5 torso-atria orientations (±30 rotation in the Y and Z axis) and 200 virtual patients with **B)** electrophysiological heterogeneities in different atrial regions and **C)** ionic current variability (200 different cardiomyocyte models).

A regression neural network was built in MATLAB as in (Nagel, Schuler, *et al.*, 2021), considering one hidden layer of 10 neurons. The network was trained 10 times using Bayesian regularisation, with random train-validation-test splits for 1000 epochs each. Thus, 70-15-15% of the entire dataset were randomly allocated for training, validation and testing, respectively. The performance of the neural network was assessed through the root mean squared error. Furthermore, a multi-class classification problem was set by grouping the ionic current distribution into low ([–50, –20] %), middle ((–20, +20) %) or high ([+20, +50] %) ionic density variation, allowing evaluation of precision and recall.

III.4. Results and discussion

III.4.1. I_{Na} and I_{K1} modulate P- and T_a-wave duration, respectively

Figure III.2A illustrates the influence of I_{Na} and I_{K1} on the P- and T_a-wave, and the neural network prediction of their ionic densities.

I_{Na} and I_{K1} were markedly associated with the P- and T_a-wave duration, respectively, with their up-regulation causing a prominent wave shortening (**Figure III.2A**). Accordingly, the neural network predicted their ionic current density with an error below 5%.

III.4.2. I_{Kr} and I_{NaK} determine the amplitude and complexity of the T_a-wave

Figure III.2B illustrates the prediction of I_{Kr}, I_{to} and I_{NaK} densities. Average errors below 12% were obtained for all three currents, as they were key modulators of the T_a-wave.

T_a-wave amplitude and area showed a proportional relationship with I_{NaK}, with high I_{NaK} density causing large T_a-waves in the precordial leads (**Figure III.2B**). The amplitude was to a lower extent associated with I_{Kr}, although I_{Kr} primarily influenced the signal complexity. As such, elevated I_{Kr} yielded less

complex T_a-waves, (i.e., characterized by fewer local peaks), potentially due to a more homogeneous cellular repolarization.

I_{to} influenced both P- and T_a-wave biomarkers. While high I_{to} density increased T_a-wave sample entropy, it reduced P-wave Shannon entropy. Moreover, elevated I_{to} decreased P-wave amplitude and area, due to a reduction in the action potential amplitude. However, as mentioned above, P-wave biomarkers showed a predominant relationship with I_{Na}.

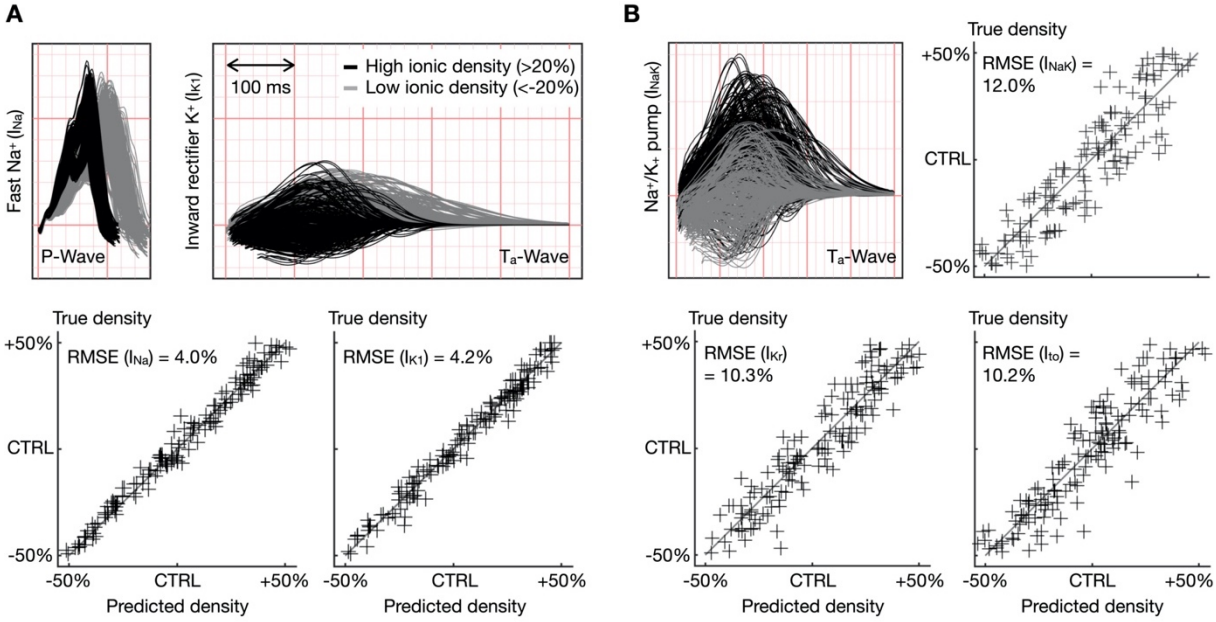


Figure III.2. **A)** Effects of I_{Na} and I_{K1} on the P- and T_a-wave (lead V6 on the ECG). Performance of the neural network, measured using the root mean squared error (RMSE), for the prediction of I_{Na} and I_{K1} density. **B)** Effects of I_{NaK} on the T_a-wave amplitude (lead V6) and prediction (RMSE) of I_{NaK}, I_{Kr} and I_{to} density. Abbreviations. CTRL: Control ionic current density.

III.4.3. ECG metrics identify ionic current dysregulation relevant to pharmacological AF management

Figure III.3 illustrates precision, recall and confusion matrix for the classification of I_{Kur}, I_{CaL}, I_{Kr}, I_{K1}, I_{NaK} and I_{Na} density, using P- and T_a-wave biomarkers from the 12-lead ECG.

As anticipated in **Figure III.2**, very high precision and recall were obtained for I_{Na} classification. As explained in **Chapters 7-9**, the efficacy of class Ic agents (e.g., flecainide) or other compounds that exert a strong Na^+ channel inhibition (e.g., compound 6f) is influenced by the baseline I_{Na} density of each patient. Therefore, an accurate estimation of the latter could be crucial for improving drug efficacy.

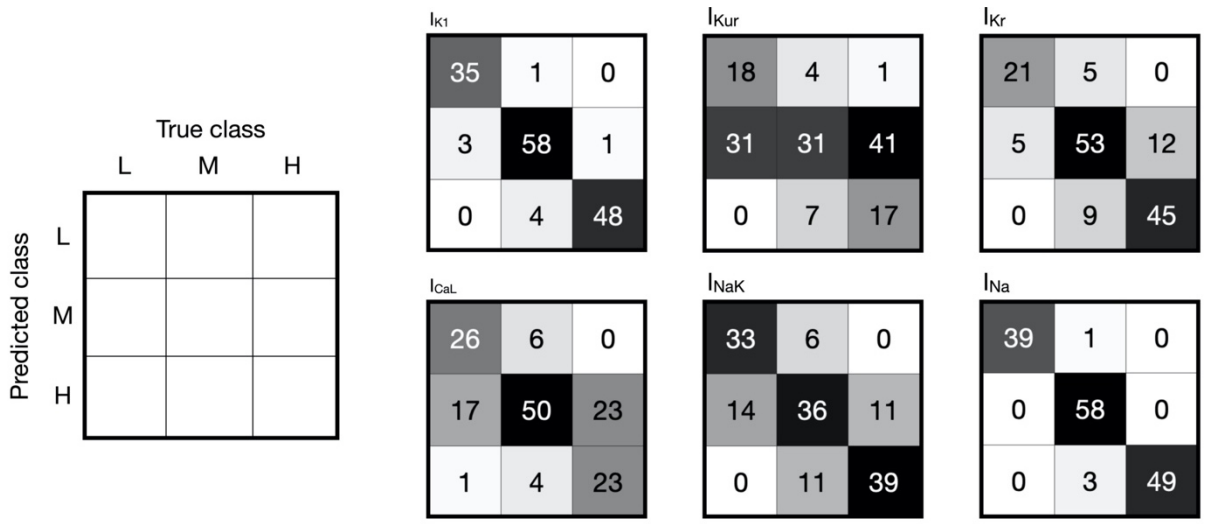
Similarly, in **Chapter 6** and **Chapter 8** I have presented the high AF cardioversion and prevention efficacy that derives from blocking I_{K1} and I_{NaK}. Both current are thought to be increased during AF. Thus, their inhibition represents a well-established approach for AF termination (Filgueiras-Rama *et al.*, 2012; Bueno-Orovio *et al.*, 2014). Paradoxically, repolarization abnormalities, such as early and delayed

afterdepolarizations (Bueno-Orovio *et al.*, 2014), and increased automaticity (Filgueiras-Rama *et al.*, 2012) have been documented after I_{NaK} and I_{K1} block, respectively. Accordingly, an accurate, non-invasive characterisation of I_{K1} and I_{NaK} density (as illustrated in **Figure III.3**) could help planning safer and more efficacious AF pharmacological treatments with I_{K1} and I_{NaK} inhibitors.

Multiple antiarrhythmic drugs, such as amiodarone, dronedarone and ibutilide, block I_{Kr}, I_{Kur} or both. Pharmacological I_{Kr} inhibitors are used with caution, given potential QT prolongation and risk for ventricular proarrhythmia. Accordingly, knowing the atrial I_{Kr} density (**Figure III.3**: precision and recall around 80%), could be used to estimate the ventricular I_{Kr} density and reduce the number of proarrhythmic adverse events (though atrial and ventricular ionic current densities might differ).

Still, the lack of safety associated with I_{Kr} blockers made AF pharmacological treatment to consider atrial-selective targets, such as I_{Kur}. I_{Kur} inhibition, however, has shown limited efficacy in clinical trials, potentially due to I_{Kur} down-regulation in AF patients (Heijman, Hohnloser and Camm, 2021). Similarly, **Chapter 6** showed that I_{Kur} block was more effective in virtual patients with higher I_{Kur}. Thus, estimating I_{Kur} density with high precision, as shown in **Figure III.3**, could enable a better use of I_{Kur} inhibitors.

Finally, high precision was also obtained for the classification of I_{CaL} down-regulation. As shown in **Chapter 8**, I_{CaL} density might be crucial for optimal stratification of patients to pharmacological treatment. Thus, estimating I_{CaL} represents an important step into precision medicine.



Ionic current density	High Density (>20%)		Low Density (<-20%)	
	Precision	Recall	Precision	Recall
I_{Kur}	0.71	0.29	0.78	0.37
I_{Kr}	0.83	0.79	0.81	0.81
I_{K1}	0.92	0.98	0.97	0.92
I_{CaL}	0.82	0.50	0.81	0.59
I_{NaK}	0.78	0.78	0.85	0.70
I_{Na}	0.94	1.00	0.97	1.00

Figure III.3. Confusion matrix, precision and recall for the multi-class classification of I_{Kur}, I_{Kr}, I_{K1}, I_{CaL}, I_{NaK} and I_{Na} density. Abbreviations: L-M-H: Low, middle and high density.

III.4.4. Both P- and T_a-wave are needed for characterizing the atrial ionic profile

The classification error (i.e., root mean square error) differed less than 1% when the neural network was trained with the standard 12-lead ECG or the augmented 15-lead, with the latter adding marginal gain. However, the prediction of all ionic densities required biomarkers from the P- (i.e., I_{Na}) T_a- (i.e., I_{K1}, I_{NaK}), or both waves (i.e., I_{to}, I_{Kr}, I_{Kur}, I_{CaL}). This poses the question as to whether the T_a-wave could be obtained through improved electrode configurations that unmask the atrial repolarization (Jayaraman *et al.*, 2015), without needing adenosine administration.

III.5. Conclusion

The ionic current profile of the atria has been non-invasively characterized in a cohort of 200 virtual patients, showing that ionic current dysregulations critical for pharmacological AF management can be identified through the analysis of the P- and T_a-wave. All simulations were conducted using the same atrial geometry and electrode positions. However, the size and shape of the atria, structural heterogeneities (i.e., atrial fibrosis) and the distance of the electrodes with respect to the heart are known factors that influence the duration and amplitude of ECG waves (Nagel, Schuler, *et al.*, 2021).

Therefore, although further work is needed to take these parameters into account, the non-invasive characterisation of the atrial ionic profile could improve patient stratification, cardiac safety and the efficacy of AF pharmacological treatment.